GDAŃSK UNIVERSITY OF TECHNOLOGY

FACULTY OF CHEMISTRY

The author of the PhD dissertation: Mariusz Wtulich

Scientific discipline: Materials Engineering

DOCTORAL DISSERTATION

Title of PhD dissertation:

Modification of TiO_2 nanotubes as photoanodes for enhanced oxygen evolution reaction (OER) activity

Title of PhD dissertation (in Polish):

Modyfikacja nanorurek TiO_2 jako fotoanod o zwiększonej aktywności w reakcji wydzielania tlenu (OER)

Supervisor *signature*
Prof. Anna Lisowska-Oleksiak, PhD, D.Sc.

Gdańsk, 2026

GDAŃSK UNIVERSITY OF TECHNOLOGY | FACULTY OF CHEMISTRY

STATEMENT

The author of the PhD dissertation: Mariusz Wtulich
I, the undersigned, agree that my PhD dissertation, entitled: Semiconductor photoanodes active under solar illumination may be used for scientific or didactic purposes.[11]

Gdańsk, ...
signature of the PhD student

Aware of criminal liability for violations of the Act of 4th February 1994 on Copyright and Related Rights (Journal of Laws 2006, No. 90, item 631) and disciplinary actions set out in the Law on Higher Education (Journal of Laws 2012, item 572 with later amendments),[22]as well as civil liability, I declare, that the submitted PhD dissertation is my own work.

I declare, that the submitted PhD dissertation is my own work performed under and in cooperation with the supervision of Anna Lisowska-Oleksiak.

This submitted PhD dissertation has never been the basis of an official procedure associated with the awarding of a PhD degree.

All the information contained in the above thesis which is derived from written and electronic sources is documented in a list of relevant literature in accordance with art. 34 of the Copyright and Related Rights Act.

I confirm that this PhD dissertation is identical to the attached electronic version.

Gdańsk, ...
signature of the PhD student

I, the undersigned, agree to include an electronic version of the above PhD dissertation in the open, institutional, digital repository of Gdańsk University of Technology, Pomeranian Digital Library, and for it to be submitted to the processes of verification and protection against misappropriation of authorship.

Gdańsk, ...
signature of the PhD student

---

[1] Decree of Rector of Gdansk University of Technology No. 34/2009 of 9th November 2009, TUG archive instruction addendum No. 8.

[2] Act of 27th July 2005, Law on Higher Education: Chapter 7, Criminal responsibility of PhD students, Article 226.

GDAŃSK UNIVERSITY OF TECHNOLOGY | FACULTY OF CHEMISTRY

Description of the doctoral dissertation

The Author of the PhD dissertation: Mariusz Wtulich

Title of PhD dissertation: Modification of TiO_2 nanotubes as photoanodes for enhanced oxygen evolution reaction (OER) activity

Title of PhD dissertation in Polish: Modyfikacja nanorurek TiO_2 jako fotoanod o zwiększonej aktywności w reakcji wydzielania tlenu (OER)

Language of PhD dissertation: English

Supervision: Prof. Anna Lisowska-Oleksiak, PhD, D.Sc.

Date of doctoral defense: …

Keywords of PhD dissertation in Polish: nanorurki TiO_2, rozkład wody, kokatalizatory fotoelektroutlenianie, OER,

Keywords of PhD dissertation in English: TiO_2 nanotubes, water splitting, cocatalysts, photoelectrooxidation, OER

Summary of PhD dissertation in Polish: Rozprawa dotyczy inżynierii półprzewodnikowych fotoanod aktywnych w świetle słonecznym, opartych na nanorurkach ditlenku tytanu (TiO_2-NTs), oraz ich modyfikacji prowadzących do poprawy właściwości elektro- i fotoelektrochemicznych podczas utleniania wody (OER). Opracowano i porównano cztery ścieżki modyfikacji: (i) obróbkę hydrotermalną (HA), wpływającą na morfologię, czystość powierzchni, położenie krawędzi pasm energetycznych, fotoprądy pod symulowanym światłem słonecznym i nadpotencjał OER; (ii) domieszkowanie kobaltem TiO_2-NTs, skutkujące obniżeniem nadpotencjału OER i 2.6-krotnym wzrostem fotoprądów; (iii) elektrochemiczne osadzanie warstw Co_3O_4 oraz warstw CoOOH jako kokatalizatorów OER, co istotnie obniżyło nadpotencjał OER (o 0.6 V) oraz zwiększyło aktywność elektro-, foto- i fotoelektrokataliczną; oraz (iv) zastosowanie wolnych od metali kokatalizatorów na bazie azotków węgla (melem, melam, g-C_3N_4) oraz ich modyfikacji kwasem siarkowym, prowadzących do powstania aktywnych materiałów sprzyjających efektywniejszej konwersji energii słonecznej. Zaproponowano modele mechanizmów transportu elektronów na granicy faz elektroda/elektrolit. Praca porządkuje zależności „modyfikacja-struktura-właściwości-wydajność" dla TiO_2-NTs i wyznacza kierunki dalszych badań nad trwałymi fotoanodami do wydajnego rozkładu wody.

Summary of PhD dissertation in English: This dissertation concerns the engineering of semiconductor photoanodes active under solar illumination, based on titanium dioxide nanotubes (TiO_2-NTs), and their modification to enhance electrochemical and photoelectrochemical performance for the oxygen evolution reaction (OER). Four modification routes were investigated and compared: (i) hydrothermal annealing (HA), which affects morphology, surface composition, band-edge positions, photocurrent under simulated sunlight, and the OER overpotential; (ii) cobalt doping of TiO_2-NTs, which reduces the OER overpotential and yields an approximately 2.6-fold increase in photocurrent; (iii) electrodeposition of Co_3O_4 and CoOOH layers as OER cocatalysts, which markedly lowered the OER overpotential (by 0.6 V) and increased electro-, photo- and photoelectrocatalytic activity; and (iv) metal-free cocatalysts based on carbon nitrides (melem, melam, g-C_3N_4) and their sulphuric-acid modifications, producing active materials that promote more efficient solar-to-electrical energy conversion. Proposed are models of the electron-transport mechanisms at the electrode-electrolyte interface. The study systematises the 'modification-structure-property-performance' relationships for TiO_2 nanotube arrays and sets out directions for further research towards durable photoanodes for efficient water splitting.

Acknowledgments

I dedicate this thesis to my parents and my sister, whose unwavering support, patience, and belief in me sustained every step of this journey. Without your love and encouragement, none of this would have been possible.

My deepest gratitude goes to my supervisor, Professor Anna Lisowska-Oleksiak, for her unfailig availability, profound expertise, and remarkable effectiveness. Her guidance, clear scientific judgement, and timely advice have shaped both this work and my development as a researcher.

I also wish to thank Zuzanna (Zuzia) Zarach for insightful discussions, thoughtful comments, and generous help with the literature. I am equally grateful to Asst. Prof. Mariusz Szkoda, Assoc. Prof. Andrzej Nowak, and Dr Konrad Trzciński for their scientific support and constructive criticism, and for fostering a positive, collaborative atmosphere at work. My warm thanks also go to Mateusz Malus for the years we shared in the student dormitory and the academic life we built together, and to Daria Roda for steadfast support through many challenges.

I am grateful to all colleagues in our research group and to collaborators from other institutions for their support, shared experience, and the collegial environment that has enabled this research to flourish.

Finally, to my friends - thank you for your day-to-day encouragement and understanding. Your kindness made the challenges of the doctoral path lighter and the successes more meaningful.

Acknowledgments

NCBR National Centre for Research and Development

A part of this work was supported by the National Centre for Research and Development (NCBR) under the LIDER project (LIDER/15/0088/L-10/18/NCBR/2019), which funded the purchase of essential reagents and equipment, as well as research on the hydrothermal modification and cobalt doping of TiO_2 nanotubes.

TECHNETIUM TALENT MANAGEMENT GRANTS

Additional support was provided by a Mini-grant for Young Scientists from the Faculty of Chemistry, Gdańsk University of Technology, for research on the hydrothermal modification of TiO_2 nanotubes and the electrochemical deposition of cobalt-based compounds (Co_xO_y and CoOOH).

Konkurs Mini-granty WCh

The last part of this research was enabled by the IDUB “Technetium” grant (17/1/2021/IDUB/III.4c/Tc), which supported the synthesis and modification of metal-free cocatalysts and tantalum anodisation.

Table of Contents

List of important symbols and abbreviations 10
Chapter I Literature Background 11

1. Introduction 13
2. Principles and strategies for solar Photoelectrochemical Cells 15
3. Semiconductor photoanodes 22
3.1. Semiconductor materials 22
3.2. Key features of photoanodes 28

4. Titanium dioxide nanotubes photoanodes 31
4.1. Synthesis methods 33
4.2. Modification strategies 37
4.2.1. Morphological engineering 37
4.2.2. Non-metal and metal doping 41
4.2.3. Cocatalyst deposition 43
4.2.4. Semiconductor/semiconductor junctions 45

5. Applications of TiO_2 nanotubes 45
6. References 47
The aim of the thesis and research objectives 63
Chapter II *Materials characterisation* 67

II.1 Chemicals and reagents 69
II.2 Techiques of characterisations 69
Chapter III Hydrothermal modification of TiO_2 nanotubes in water and alkali metal electrolytes ($LiNO_3$, $NaNO_3$, KNO_3) – Direct evidence for photocatalytic activity enhancement 73

III.1 Methods in Brief and Key Results 75
III.2 Publication 77
III.3 Supplementary Information 92
Chapter IV Hydrothermal cobalt doping of titanium dioxide nanotubes towards photoanode activity enhancement 99

IV.1 Methods in Brief and Key Results 101
IV.2 Publication 102
IV.3 Supplementary Information 120
Chapter V Tailoring TiO_2 nanotubes photoanodes with electrodeposited Co_3O_4 and CoOOH cocatalysts for enhanced electrocatalytic and photoelectrocatalytic oxygen evolution. 121

V.1 Methods in Brief and Key Results 123
V.2 Publication 125
V.3 Supplementary Information 141
Chapter VI Exploring the role of carbon nitrides (melem, melon, g-C_3N_4) in enhancing photoelectrocatalytic properties of TiO_2 nanotubes for water electrooxidation 151

VI.1 Methods in Brief and Key Results 153
VI.2 Publication 156
VI.3 Supplementary Information 174
General Conclusions 185
Scientific achievements 189
Author Contribution Statements 197

List of important symbols and abbreviations

AC – Alternative current
BDD — Boron-doped diamond
CA — Chronoamperometry
CB — Conduction band
CE — Counter electrode
CV — Cyclic voltammetry
TiO_2-NTs – titanium dioxide nanotubes
EIS — Electrochemical impedance spectroscopy
EDX (EDS) — Energy-dispersive X-ray spectroscopy
FTIR — Fourier-transform infrared spectroscopy
FTO — Fluorine-doped tin oxide
g-C_3N_4 — Graphitic carbon nitride
GC — Glassy carbon
HA — Hydrothermal annealing
HER — Hydrogen evolution reaction
LSV — Linear sweep voltammetry
MB — Methylene blue (dye)
NHE — Normal hydrogen electrode
OER — Oxygen evolution reaction
PEC — Photoelectrochemical (cell/system)
REF — Reference electrode
RHE — Reversible hydrogen electrode
SC — Semiconductor
SCE — Saturated calomel electrode
SEM — Scanning electron microscopy
UV — Ultraviolet
VB — Valence band
Vis — Visible
WE — Working electrode
XPS — X-ray photoelectron spectroscopy
XRD — X-ray diffraction
η – overpotential (V),
j_{ph} – current density (mA/cm^2),
R – universal gas constant (8.31 J/molK),
T – temperature (K),
$\mathrm{E_{BG}}$ – bandgap energy (eV)
$\mathrm{E_{FB}}$ – flat-band potential (V)
λ – wavelength (nm)
iR – ohmic drop (Ω)

If a symbol is not included in the above list, its meaning is given in the text of this work.

Chapter I

Literature Background

1. Introduction

“Becquerel’s pioneering photoelectric experiments in 1839 were done with liquid, not solid-state devices - a fact that is often ignored” [1]. Those experiments required advances in instrumentation and the framework of quantum physics to explain their mechanisms, neither of which existed at the time. Consequently, the Industrial Revolution followed the readily available and inexpensive path of coal combustion and steam power. Coal and steam production scaled rapidly, and long-lived carbon dioxide from coal accumulated in the atmosphere, while widespread engine use increased water vapour emissions. In the year 1800, the carbon dioxide concentration in Earth’s atmosphere was about 280 ppm [2]. As technology develops year after year, energy demand increases. Nowadays (October 2025), the indicator shows a global mean near 424.54 ppm [3]. This is roughly 1.5 times higher than it was two centuries ago. Human activity associated with technological development has contributed to exceeding 1.5 °C above the global mean temperature 200 years ago [4].

It is nevertheless important to note that other gases also contribute to climate change. The second most abundant toxic greenhouse gas is methane (CH_4), which is produced primarily from the decomposition of organic matter, notably enteric fermentation in ruminants [5,6]. The effect per molecule is much higher than for CO_2, although its atmospheric concentration is much lower (1.94 ppm) and its average atmospheric lifetime is about 9 years [5,6]. The third major greenhouse gas is nitrous oxide (N_2O), mainly of industrial and agricultural origin. Unfortunately, it is a gas with a very high global-warming potential, but its relatively low atmospheric abundance (0.34 ppm) and its atmospheric average lifetime is 116 years [5,7]. In aggregate, estimates of total greenhouse gas (GHG) emissions from the energy sector typically include CO2, CH4, and N_2O from fuel combustion, as well as fugitive emissions [8]. The resulting changes to the climate affect societies, ecosystems and the long-term habitability of the planet. Addressing these challenges requires alternative, non-toxic energy carriers - ideally clean fuels - and a more rational use of energy in daily life.

Most primary energy still comes from fossil fuels. The International Energy Agency estimates the global share of fossil fuels at about 80% in recent years [9]. In 2023, global GHG emissions from fuel combustion were: 45% from coal,

peat, and oil shale; 33% from oil; and 22% from natural gas [9]. Renewable energy (solar, wind, hydropower, geothermal, and biomass) is expanding, but unevenly. In the European Union (EU), renewables supplied about 24.6% of gross final energy use in 2023 [7]. In Poland, the national statistics office reports a 16.7% share of renewables in gross final energy consumption in 2023 [10], placing Poland 22nd among the 27 EU member countries.

To address both greenhouse gas mitigation and rising energy demand, new strategies are required to produce efficient energy from clean fuels without harmful by-products. Here, hydrogen is widely regarded as a strategic fuel [11]. Hydrogen is commonly classified using a colour-coded scheme based on its production route and environmental impact; for example, green hydrogen is produced via renewable-powered electrolysis, blue hydrogen from fossil fuels with carbon capture, utilisation and storage, and red (or pink) hydrogen using nuclear-derived energy [12]. Practical deployment spans onshore photovoltaic-electrolyser coupling and promising offshore schemes that combine wind turbines with electrolysers on dedicated or repurposed platforms [13]. An alternative that avoids combining such large devices is to employ photoelectrochemical cells (PECs) based on semiconductors, which are still under development [1,14]. The PECs obtain direct hydrogen from solar energy, with the eco-friendly co-product of oxygen. The key element in a PEC system is the photoelectrode. Unfortunately, some disadvantages must be overcome when producing materials for this purpose, such as absorption in a narrow part of the UV–VIS spectrum, fast recombination of electron–hole pairs, and the need to catalyse the oxygen evolution reaction at high overpotential [15,16]. Constant technological progress now allows the production of new electrodes using nanomaterials and their characterisation with advanced spectroscopy and operando techniques with improved resolution.

Within PEC, the photoanode is usually the most important element, analogous to the heart in a human body. Here, stable metal-oxide semiconductors are a favourable choice because they are resistant to various aqueous solutions and offer useful band positions [17]. Titanium dioxide is a well-studied example and provides stable morphologies, especially titanium dioxide nanotubes (TiO_2-NTs),

surface chemistry, and junction designs that can improve photocurrent and reduce overpotential without relying on rare elements [18,19].

PEC could address the above-mentioned problems with greenhouse gases. This is why continued development of PEC systems, especially photoanodes, matters. Researchers worldwide use many methods to increase the catalytic and photoelectrocatalytic efficiency of photoanodes, which is a challenge. This dissertation is devoted to finding enhanced photoanodes, focusing on TiO_2-based electrodes and evaluating performance primarily by photocurrent generation and the overpotential for oxygen evolution at defined benchmarks.

2. Principles and strategies for solar Photoelectrochemical Cells

Photoelectrochemical cells convert light energy into electricity via electrochemical processes [1]. The first demonstration of water splitting on a single-crystal TiO_2 (rutile) wafer using visible light was documented by A. Fujishima and K. Honda in 1972 [20]. Generally, in PEC solar light illumination (photons) generate charge carriers (electrons and holes), see Equation (1) [20,21]. The holes oxidise water to oxygen molecules at the electrolyte/electrode interface, and the electrons reduce protons to hydrogen at a counter electrode [22,23], as shown in Equations (2-3). The proposed schema of the PEC system is depicted in Figure 1.

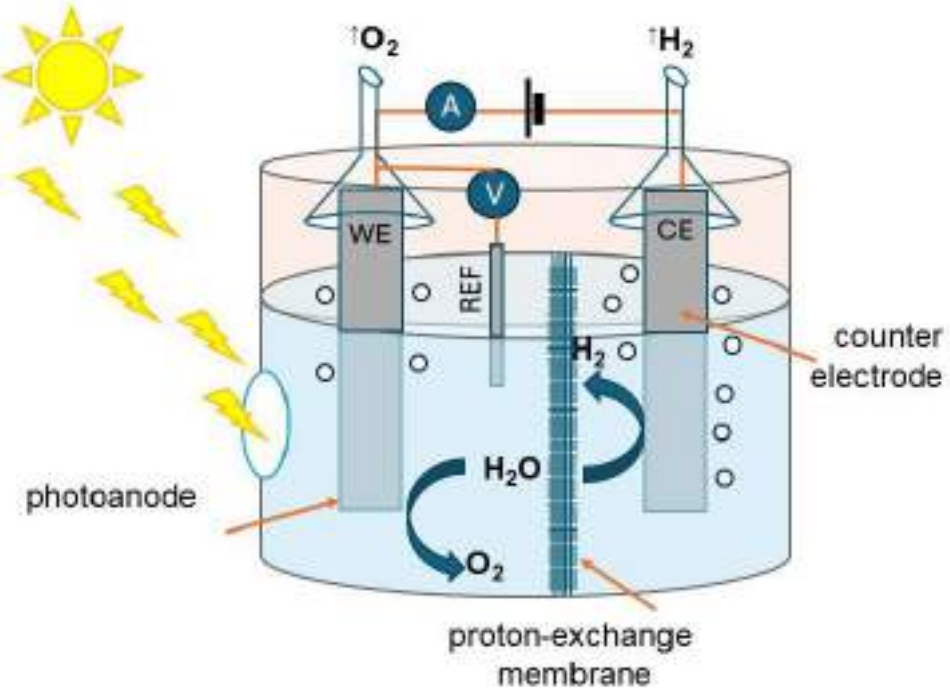

Figure 1. The proposed typical PEC scheme (adapted from [24]*).*

The phenomenon is the production of current and nontoxic gases, such as oxygen and hydrogen, and green fuel of the future, only by photoelectrolysis of water molecules. Equation (4) is known as the water-splitting reaction.

$$4\ h\nu \xrightarrow{\text{photoelectrode}} 4\ \mathrm{h^+} + 4\ \mathrm{e^-} \quad (1)$$

$$4\ \mathrm{h^+} + 2\ \mathrm{H_2O_{(liq)}} \rightarrow \mathrm{O_{2\ (gas)}} + 4\ \mathrm{H^+} \quad (2)$$

$$4\ \mathrm{e^-} + 4\ \mathrm{H^+} \rightarrow 2\ \mathrm{H_{2\ (gas)}} \quad (3)$$

$$2\ \mathrm{H_2O_{(liq)}} + 4\ h\nu \rightarrow \mathrm{O_{2\ (gas)}} + 2\ \mathrm{H_{2\ (gas)}} \quad (4)$$

A typical PEC consists of three electrodes immersed in an aqueous electrolyte solution (e.g., KOH, K_2SO_4) [1]. These are the working electrode (WE) – the photoelectrode, the counter electrode (CE), and the reference electrode (REF) [22,25]. The photoelectrode is most often made of an n- or p-type semiconductor (e.g., a metal oxide or a chalcogenide). The counter electrode is typically a corrosion-resistant metal (e.g., Pt, Au, Ag) to prevent electrolyte contamination, or a GC (Glassy Carbon) or BDD (Boron-Doped Diamond) electrode [26]. In general, three main WE/CE configurations can be distinguished [27]:

- WE: n-type semiconductor (photoanode) and CE: metal or carbon (cathode)
- WE: n-type semiconductor (photoanode) and CE: p-type semiconductor (photocathode)
- WE: p-type semiconductor (photocathode) and CE: metal or carbon (anode)

In a typical PEC design, the photoanode produces oxygen, while hydrogen evolves at the metal cathode. In contrast, when a photocathode is used, H^+ is reduced to hydrogen, and oxygen evolves at the metal anode. In this work, an n-type semiconductor/platinum (SC/Pt) system is employed. The dissertation mainly focuses on the photoelectrode consisting of TiO_2 nanotubes deposited on a titanium substrate, with the counter electrode a high-surface-area platinum mesh immersed in a 0.2 M K_2SO_4 aqueous electrolyte. To illustrate this, Figure 2 shows a simplified diagram of the electrode-electrolyte system used.

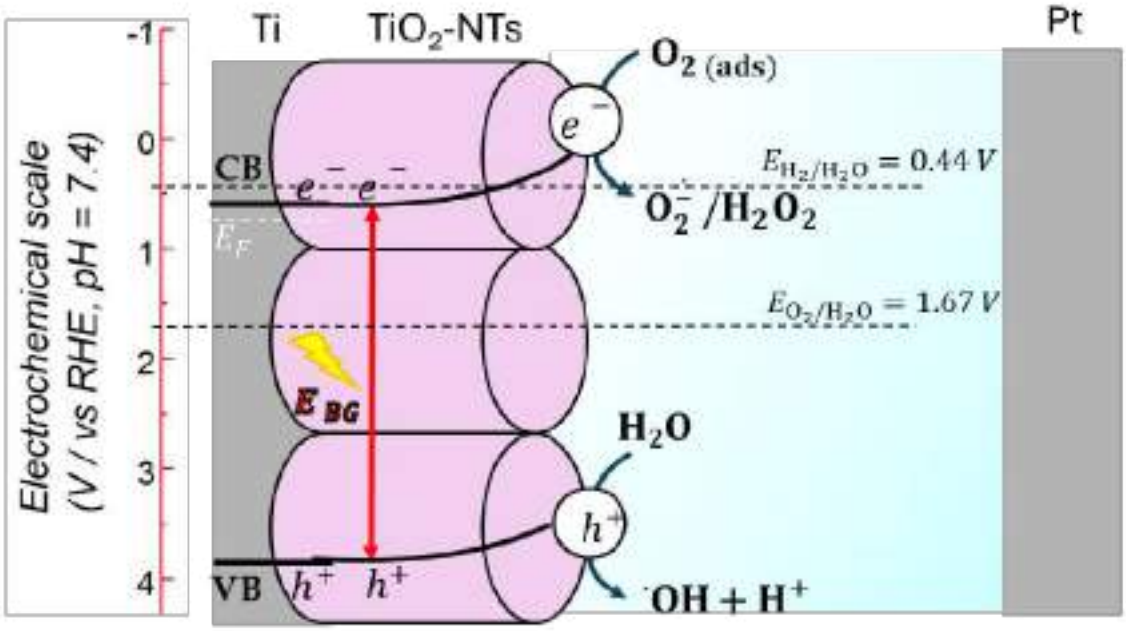

Figure 2. The scheme of the electrode (Ti/TiO_2-NTs) and electrolyte (0.2 M K_2SO_4) PEC system.

Solar radiation reaching the Earth's surface includes 3-5% UV, 42-43% VIS, and 52-55% near infrared light [28]. In the PEC, there is a special quartz window (Figure 1), through which nearly all incident solar light reaches the photoelectrode. When the incident photon energy equals or exceeds the semiconductor bandgap energy, an electron is excited to the conduction band (CB), leaving a hole in the valence band (VB) [22]. The resulting electron-hole pair diffuses through the solid material. If the pair reaches the SC/electrolyte interface, the energy bands bend, creating a space-charge region [29]. This bending generates an internal electric field (the so-called depletion layer) that separates the charge carriers: holes migrate toward the interface, while electrons move along the outer circuit [30].

The degree of band bending depends on the offset between the semiconductor Fermi level and the redox potential of the contacting electrolyte, as well as on the semiconductor's donor density [24]. To determine whether specific electrochemical reactions can occur, two key parameters are typically measured: (i) the flat-band potential E_{FB} and (ii) the optical bandgap energy E_{BG}. These are obtained from two complementary analyses: E_{FB} from Mott–Schottky plots derived via electrochemical impedance spectroscopy (EIS), and E_{BG} from Tauc plots constructed using UV–Vis diffuse-reflectance data. Together, these

parameters allow a practical band alignment to be drawn for PEC operation. Using EIS, it is possible to identify the semiconductor type and to estimate E_{FB}. For that purpose, the dependence of the space-charge capacitance on the applied potential is used as Equation (5) [31]:

$$\frac{1}{{C_{SC}}^2} = \frac{2}{\varepsilon\varepsilon_0|q_e|N_A}\left(E - E_{FB} - \frac{k_B T}{|q_e|}\right) \quad (5)$$

where ε is the relative permittivity of the semiconductor, $\varepsilon_0 = 8.85 \cdot 10^{-12}\,\frac{\mathrm{F}}{\mathrm{m}}$ is the vacuum permittivity, $|q_e| = 1.6 \cdot 10^{-19}\,\mathrm{C}$ is the elementary charge, N_A is the acceptor density, or it can be replaced by N_D as the donor density, $k_B = 1.38 \cdot 10^{-23}\,J/K$ is the Boltzmann constant, T is the temperature [32,33].

The sign of the slope $\left[\frac{\Delta C_{SC}^{-2}}{\Delta E}\right]$ indicates the semiconductor type. A negative slope is characteristic of p-type SC, whereas a positive slope indicates n-type material. For HA TiO_2-NTs, $E_{FB} = -0.01\,V$ vs. Ag/AgCl/3 M KCl, as estimated in Figure 3A. The second parameter, E_{BG}, helps estimate the band edges by providing the optical gap [34]. It is obtained from UV–Vis diffuse reflectance measurements of the electrode material. The measured reflectance, $R(\lambda)$, is transformed using the Kubelka–Munk function, as given in Equation (6) [35]:

$$F(R) = \frac{(1-R)^2}{2R} \quad (6)$$

which is proportional to the absorption coefficient for optically thick, diffusely scattering samples. A Tauc plot is then constructed by plotting $[F(R)hv]^n$ against hv, where the exponent n depends on the nature of the electronic transition [34]. The value of n indicates the type of transition as follows:

- $n = 3$ corresponds to an indirect forbidden electronic transition,
- $n = 2$ corresponds to a direct allowed electronic transition,
- $n = 3/2$ corresponds to a direct forbidden electronic transition,
- $n = 1/2$ corresponds to an indirect allowed electronic transition.

In the literature, reported bandgap values for modified semiconductors often differ. To obtain a physically meaningful E_{BG}, Tauc analysis should be applied to the semiconductor's intrinsic absorption edge rather than to regions dominated

by Urbach tail or background absorption [35]. In practice, a tangent to the linear band-to-band segment of the Tauc plot is drawn and extrapolated to the energy axis to obtain the optical gap (Figure 3B). This procedure minimises the influence of dopants, defects or auxiliary layers, and ensures consistent comparisons between materials or processing conditions. For HA TiO_2-NTs, $E_{BG} = 3.2\ eV$ for $n = 1/2$, see Figure 3B. Combining E_{BG} with E_{FB} allows us to estimate the CB and VB edge positions. These band edge positions can then be illustrated in a band-edge diagram relative to the relevant redox potentials presented in Figure 3C.

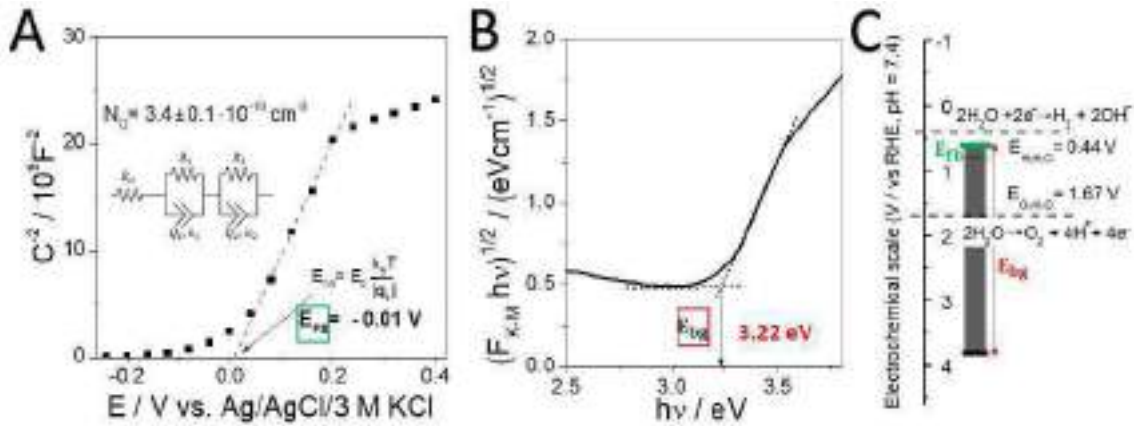

Figure 3. (A) Mott–Schottky plot obtained from EIS, measured in frequency range from 20 kHz to 1 Hz, (B) Tauc plot, and (C) band edge positions of CB and VB obtained for HA TiO_2-NTs.

As mentioned above, photogenerated excitons in photoanodes are separated, and holes oxidise water to form oxygen (Equation 2). The reaction is called the oxygen evolution reaction (OER) [36]. Protons then migrate through the electrolyte while electrons flow through the external circuit to the cathode, where hydrogen ions are reduced to hydrogen (Equation 3) [37]. This is called the hydrogen evolution reaction (HER) [2]. In most PEC cells, OER at the photoanode is kinetically slower than HER at the cathode. The rate of OER is limited by the required transfer of 4 electrons and 4 protons to yield the two bond-making steps (π+σ of O_2) [38], whereas HER is a 2-electron, 2-proton step that proceeds readily on good metals such as Pt. For the successful splitting of a water molecule, a Gibbs free energy of at least 237 kJ/mol is required [39]. Unfortunately, after reaching the threshold potential of 1.23 V vs RHE, an additional driving force is often required at the anode to overcome interfacial charge-transfer barriers, as observed in the OER overpotential, η. The slow

transfer of holes and surface states on oxide photoanodes further promotes unfavourable charge-carrier recombination [29]. Linear sweep voltammetry (LSV) is used to monitor changes in the onset potential and overpotential for anodic water oxidation (Figure 4A).

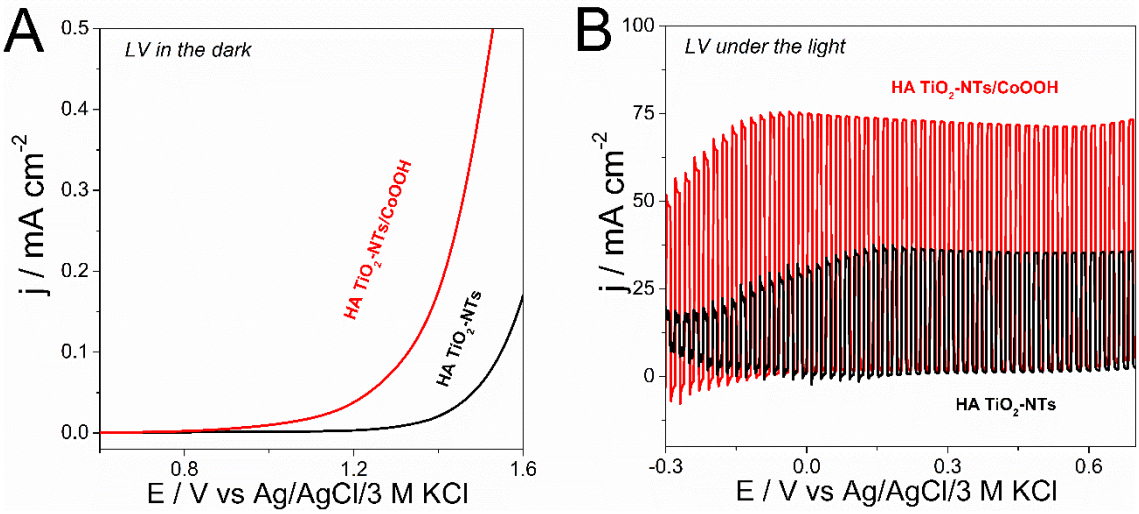

Figure 4. Linear sweep voltammetry curve (A) in the dark at a sweep rate of v=10 mV/s and (B) under illumination (v=20 mV/s) obtained for HA TiO_2-NTs electrode and HA TiO_2-NTs decorated with CoOOH cocatalysts, measured in 0.2 M K_2SO_4 electrolyte (adapted from [40]*).*

However, during the measurement, the electrode is polarised at a defined scan rate, which at high current values (i) may distort the curve shape. Between the working electrode and the reference electrode, there is an electrolyte solution with its own resistance (R), set by the electrolyte type and concentration and by the cell geometry (inter-electrode distance), which strongly influences the measured current [41]. In the analysis, iR compensation should be applied to correct the voltage loss (iR drop) [42]. For photoanodes modified with an additional catalyst (for example, TiO_2-NTs decorated with CoOOH), the iR compensation should also account for contact and catalyst resistance in addition to the solution resistance, and that R is given in Equation (7) [43]:

$$R = R_{solution} + R_{catalyst} + R_{contact} \quad (7)$$

This aspect is often omitted in literature on photoanodes. Correctly processed LSV data allow estimation of the overpotential with appropriate accuracy (Figure

4A). iR compensation also affects another kinetic parameter in water-electrocatalysis – the Tafel slope – as given in Equation (8) [44]:

$$b = \frac{\partial \eta}{\partial \log(i)} = \frac{2.303 R_{gas} T}{\alpha n F} \quad (8)$$

where R_{gas} –is the universal gas constant, T – temperature, α – electron transfer coefficient (0.5), F – Faraday constant. Proper consideration of the Tafel slope provides information on charge transfer. It can help identify the rate-determining step (RDS), which correlates with the number of electrons involved in the electrode process and supports discussion of mechanisms at the electrode/electrolyte interface [45].

The most desirable PEC outcome is a high and stable photocurrent. Using LSV under dark and solar-light illumination, the dark current and the illuminated current can be determined, and their difference is the photocurrent (Equation 9).

$$i_{photocurrent} = i_{light} - i_{dark} \quad (9)$$

Generally, because the tested electrodes have different surface morphologies, current is reported as current density normalised to a geometric area of 1 cm^2. An example of LSV under light and in the dark for HA TiO_2-NTs and HA TiO_2-NTs/CoOOH is presented in Figure 4B. Its stability depends on several linked factors. First, photons must have sufficient energy to be absorbed by the semiconductor [46]. Many oxides respond mainly in the near-UV (about 5% of terrestrial sunlight), so additional modification is often needed to extend absorption to lower-energy light. Second, the resulting electron-hole pairs must be separated by the space-charge field or internal junctions [24]. Third, carriers must reach the relevant interfaces without recombining [39]. Losses at any of these steps reduce the net photocurrent.

Reliable photoelectrocatalytic data also depend on careful test practice. To obtain reproducible and meaningful values, it is essential to control cell geometry, the cleanliness of glassware and substrates, electrode dimensions, lamp power and spectral calibration, temperature, and the dissolved-gas content of the electrolyte (for example, argon purging to remove oxygen). Electrical contacts must be low-

resistance, non-active areas must be well insulated, the cell must be sealed, and the electrolyte should be fresh and of known purity. These practical aspects are essential to materials engineering and strongly influence the final PEC performance. In summary, the key descriptors for PEC systems - optical bandgap, flat-band potential, OER overpotential, Tafel slope, and the magnitude and stability of the photocurrent - jointly provide the energetic and kinetic framework needed to interpret performance, and they will be applied consistently in the sections that follow.

3. Semiconductor photoanodes

3.1. Semiconductor materials

Presently, the best photoanode materials are metal oxides such as $BiVO_4$, α-Fe_2O_3, WO_3, ZnO [47–51] and the first reported over 50 years ago – titanium dioxide [20]. To demonstrate the substantial academic interest in photoanodes, Scopus (an interdisciplinary database indexing approximately 23,000 peer-reviewed journals) was queried for bibliometric statistics. In the “Article title, Abstract, Keywords” search field, the following terms were entered: “photoanode”, “TiO_2 photoanode”, “$BiVO_4$ photoanode”, “Fe_2O_3 photoanode” and “ZnO photoanode”. Based on the retrieved counts, a bar chart for the years 2001-2025 is presented in Figure 5.

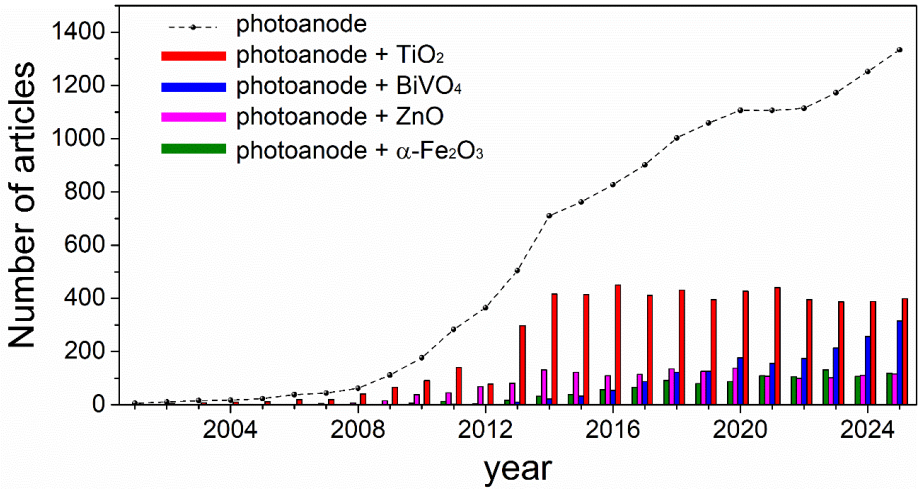

Figure 5. Annual publication counts in Scopus for 2001-2025. The line plot reports results for the query "photoanode". The grouped bar charts report "TiO_2 photoanode", "$BiVO_4$ photoanode", "Fe_2O_3 photoanode", and "ZnO photoanode". Queries were entered in the Article title, Abstract, Keywords field. Data were retrieved on 31.12.2025 and exported by year. No smoothing or normalisation was applied.

Over the last 25 years, more than 14,000 articles related to the term "photoanode" have been published. The number of publications containing this term has increased year by year, with a particularly marked rise over the past five years (a total of ~6,000 new articles, representing approximately 43% of all articles published in the XXI century). Moreover, TiO_2-based semiconductors appear to attract the greatest interest: since 2014, on average at least one new article has been published daily. It can therefore be inferred that the development of PEC photoanodes is most frequently explored using TiO_2-based materials. Nevertheless, interest in $BiVO_4$-based photoanodes has also grown in recent years. In general, semiconductor photoanode materials can be divided into the following groups:

- **metal oxides (Me_xO_y)** e.g.: TiO_2 [52], $BiVO_4$ [53], α-Fe_2O_3 [50], WO_3 [54], ZnO [55].
- **metal nitrides (Me_xN_y)** e.g.: Ta_3N_5 [56], GaN [57], InGaN [58].
- **metal oxynitrides (Me–O–N)** e.g.: $LaTiO_2N$ [59], TaON [60], $SrTaO_2N$ [61], $CaNbO_2N$ [62], $BaTaO_2N$ [63].
- **metal oxyhalides (Me–O–X)** e.g.: BiOCl [64], BiOBr [65], BiOI [66].
- **metal chalcogenides, besides oxides (Me_xS_y / Me_xSe_y / Me_xTe_y)** e.g.: SnS_2 [67], In_2S_3 [68], CdSe [69], Bi_2Te_3 [70].
- **perovskites and layered perovskite-type oxides** e.g.: $SrTiO_3$ [71], $LaFeO_3$ [72], $BiFeO_3$ [73], $NaTaO_3$ [74], Bi_2WO_6 [75].
- **spinel ferrites (AFe_2O_4)** — e.g.: $ZnFe_2O_4$ [76], $CoFe_2O_4$ [77], $NiFe_2O_4$ [78], $CuFe_2O_4$ [79], $MgFe_2O_4$ [80].
- **carbon-based materials** e.g.: graphitic carbon nitride (g-C_3N_4), melem, melam [81], covalent triazine frameworks (CTFs) [82], covalent organic frameworks (COFs) [83], metallic organic frameworks (MOFs) [84], graphdiyne [85].

Metal oxide semiconductors remain the most widely studied photoanodes (about ¾ of the relevant articles indexed in the Scopus database). In PEC cells, materials with the same nominal stoichiometry do not necessarily yield the same

photocurrent because performance depends on crystal structure, defect density, and morphology. For example, TiO_2 occurs as anatase, rutile, and brookite, which differ in band structure, carrier lifetimes, and surface energetics [86,87]. The synthesis pathway governs the formation and distribution of point defects (for example, oxygen or metal vacancies that create donor or acceptor states), impurity incorporation at the surface or in the bulk, crystallographic ordering (space group and octahedral connectivity), and the metal-to-oxygen ratio; together these factors set carrier density and mobility, band bending, trap-assisted recombination rates, minority-carrier diffusion length and, ultimately, the photocurrent [88]. Morphology likewise matters: powders, layered films, nanotubes, or nanowires present different optical paths, depletion widths, and surface areas that modulate light absorption, minority-carrier diffusion, and OER kinetics [89]. Equally critical is a rigorous definition of the illumination and electrochemical protocol. Reports of unusually high photocurrents often omit key parameters, such as irradiance at the electrode plane (typically 100 mW/cm^2), spectral filtering (e.g., a UV cutoff), or the solar simulator standard (AM 1.5G). Without these, results are not directly comparable.

In my PhD thesis, changing a single factor increased the photocurrent by threefold for nominally identical TiO_2 nanotube electrodes: the titanium substrate purity during anodisation (from 99.5% to 99.99%), with all other preparation and measurement conditions held constant. It's worth noting that the price of a 100x2000 mm titanium foil with a 99.5% metal basis is PLN 3029 (thickness 0.25 mm), while a 100x100 mm foil with a 99.99% metal basis costs PLN 3078. The price of a purer Ti sheet was 20 times higher per unit area (purchased by Alfa Aesar, Kandel, Germany). A comparison of materials such as TiO_2 nanotubes (anatase), $BiVO_4$ layers, WO_3 powder, ZnO nanowire, or Fe_2O_3 nanorods in terms of photocurrent is provided in Table 1.

Table 1. Bandgap energy and performance comparison of different semiconductor photoanodes for PEC.

Semicondutor material	Synthesis method	Bandgap (eV)	ELECTROLYTE	Light source	Photocurrent density (mA/cm^2)	Stability of photocurre	Ref
TiO_2 nanotubes (anatase)	Anodisation	3.0	0.5 M K_2SO_4	150 W Xenon lamp (AM 1.5 G) 100 mW/cm^2	0.03 (at 0.5 V vs. Ag/AgCl/0.1 M KCl)	95% after |5 min	[90]
$BiVO_4$ layers	Plasma Layer Deposition	2.5	0.5 M K_2SO_4+ 0.01 M hydroquinone	150 W Xenon lamp (AM 1.5 G) 100 mW/cm^2	0.17 (at 0.5 V vs. Ag/AgCl/0.1 M KCl)	60% after 3 min	234
$BaTiO_3$ nanorods	Hydrothermal method	3.2	0.1 M Na_2SO_4 + 0.1 M KH_2PO_4	300 W Xenon lamp (AM 1.5 G)	0.17 (at 1.23V vs. RHE)	99% after 5 min	[91]
WO_3 powder	Thermal decomposition	2.6	Buffer solution (pH=3.8) + 0.1 M KCl	450 W Xenon lamp	0.003 (at 0.5 vs. SCE)	66% after 2.5 min	[92]
ZnO nanowire	Hydrothermal method	3.3	phosphate buffer (pH=7) + 0.5 M $NaClO_4$	1000W Xe-lamp 100 mW/cm^2	0.2 (0.5 V vs. NHE)	80% after 3 min	[93]
$\alpha - Fe_2O_3$ nanorods	Hydrothermal method	2.1	0.5 M Na_2SO_4	Xenon lamp (AM 1.5 G) 100 mW/cm^2	0.09 (at 1.23 V vs. RHE)	75% after 3 hours	[94]
Ta_3N_5 thin films	Physical vapour deposition	2.1	phosphate buf.(pH=12.3) + 0.1 M $K_4Fe(CN)_6$	(AM 1.5 G) 100 mW/cm^2	0.6 (at 1.23 V vs. RHE)	80% after 1 hour	[95]
C_3N_4 materials	Thermal polycondensation	2.8	0.2 M Na_2SO_4	Lamp: LOT LS0500/ 1 (AM 1.5 G) 100 mW/cm^2	0.002 (at 0.5 V vs. Ag/AgCl/3 M KCl)	50% after 2 min	[81]
CdS nanorods	Hydrothermal method	2.1	0.25 M Na_2SO_4 + 0.35 M Na_2S	300 W Xenon lamp	0.62 (at 0.28 V vs. RHE)	95% after 5 min	[96]
PbS thin films	Chemical bath deposition	1.8	0.3 M $Na_2S_2O_3$	400W Xe-lamp	0.16 (at 1.6V vs. RHE)	30% after 5 min	[97]
$ZnIn_2S_4$ layers	Plasma Layer Deposition	2.3	0.5 M NaOH	Lamp: LOT LS0500/ 1 (AM 1.5 G) 100 mW/cm^2	1.13 (at 0.7 V vs. Ag/AgCl/3 M KCl)	95% after 5 min	[98]

Bandgap values vary less than photocurrents but are still sensitive to crystallinity and phase composition. Single crystals generally exhibit slightly larger gaps than polycrystals, and disorder can change the apparent direct or indirect character. For TiO_2, E_{BG} is 3.2 eV for anatase, and E_{BG} is 3.0 eV for rutile [87]. Importantly, difficulties with Mott-Schottky analysis often cause confusion and incorrect assignments of E_{BG} by various researchers. The reported values must be subjected to critical evaluation.

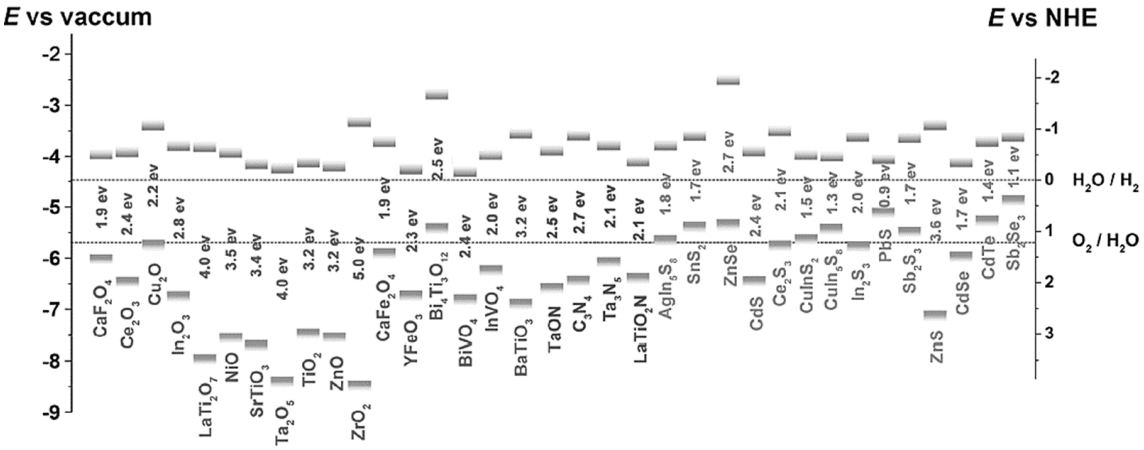

Figure 6. Band edge positions (CB and VB levels) and bandgap energies for different semiconductors (adapted from [99]*)*

Another interesting group of materials is metal nitrides, especially tantalum nitride. In 2002, this compound was reported by Hitoki et al [100]. It is characterised by strong visible-light absorption and a narrow bandgap (2.1 eV), and is expected to be a promising photocatalyst in the future. Over the last 10 years, this material has undergone extensive modifications with great results. Schmuki et al. synthesised Ta_3N_5 open nanotubes [101,102]. They were formed from Ta_2O_5 nanotubes [103] followed by calcination in an NH_3 atmosphere. Moreover, tantalum can be obtained in the form of thin layers [104] or nanorods [105]. It would also be worthwhile to attempt to synthesise a new photoanode, in addition to TiO_2 nanotubes. During my doctoral research, I synthesised anodised tantalum oxide layers using 0.127 mm-thick, 99.9% pure tantalum foil. For context, in November 2022, a 100x100 mm sheet cost PLN 1298. After extensive optimisation of the anodisation electrolyte, electrochemical oxidation of the tantalum substrate was achieved; however, the as-formed amorphous layer did not operate as a proper photoanode. Subsequent thermal treatment of the

anodised sheets at 600–800 °C in oxygen or argon failed to produce photoanodes active under visible light. During calcination, the samples either became brittle and cracked, rendering them non-functional when thermally treated in argon (Figure 7A), or transformed into a pure white powder when heated in air (oxygen) (Figure 7B). In Figure 7C, one of the results obtained from photocurrent generation testing (in the dark and under solar illumination) using the LSV technique (10 mV/s) is shown. The powder was identified as β-Ta_2O_5 [106], as evidenced by the diffraction pattern in Figure 7D. Due to the cost of the raw material and the difficulty of thermal processing, further research on this compound was not continued.

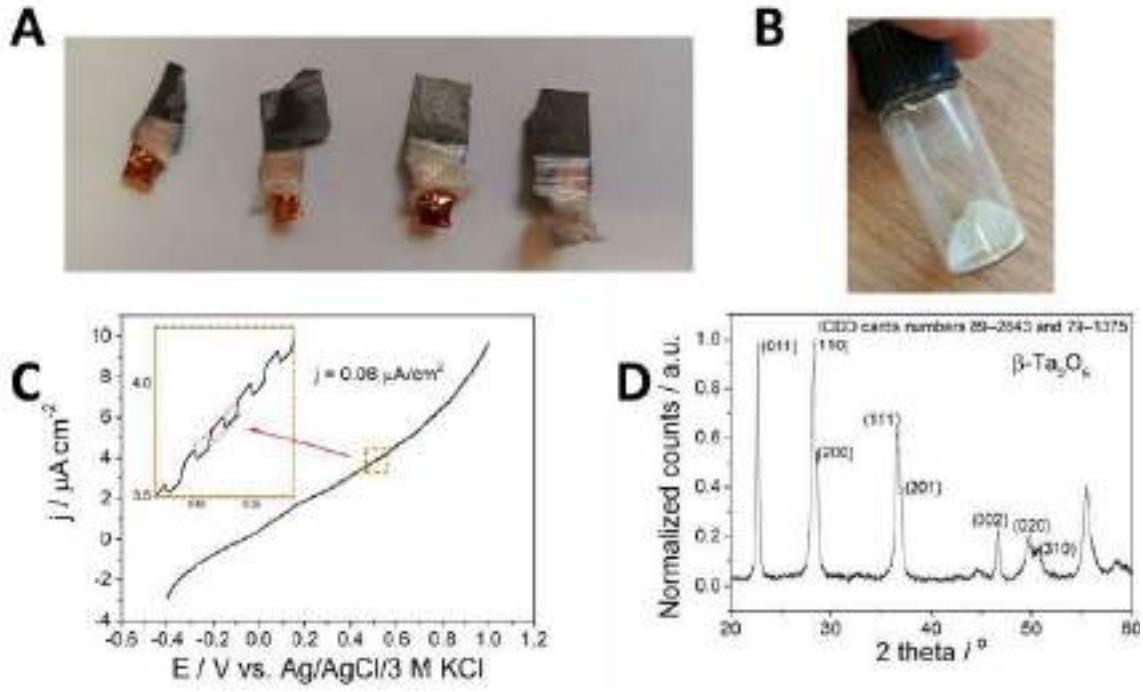

Figure 7. (A) Ta_2O_5 photoanodes obtained by anodisation and thermal heating in Ar atmosphere at 750 °C, (B) Ta_2O_5 powder (oxygen atmosphere), (C) LSV for Ta_2O_5 photoanode in the dark and under solar light illumination with a sweep polarisation of 10mV/s, (D) XRD pattern for Ta_2O_5 powder.

The novel and first research on the use of $CaBi_6O_{10}$ as a photoanode for photoelectrochemical water oxidation was reported by Zhifeng Liu et al. in 2017 [107]. This paper shows that films were successfully fabricated directly on FTO substrates. The bandgap energy was determined to be 2.3 eV, and the photocurrent density was 0.39 mA/cm^2 at 1.23 vs. RHE under simulated sunlight illumination. As the authors showed, obtaining 300 nm thickness of $CaBi_6O_{10}$

nanoplates improves photocatalytic performance towards water splitting, so this material is a promising photoanode. In addition, there are many other materials such as: In_2S_3 nanocubes (0.50 mA/cm^2 at 1.23 V vs. RHE) [108], In_2S_3 nanoplates (0.42 mA/cm^2 at 1.23 V vs. RHE) [108], In_2S_3 nanoflakes (0.31 mA/cm^2 at 1.23 V vs. RHE) [108], g-C_3N_4 film (bandgap energy 2.6 eV, 89 µA/cm^2 at 1.1 V vs. RHE) [109], 1D Fe_2O_3 nanorod arrays (1.64 mA/cm^2 at 1.23 V vs. RHE) [110] etc.

3.2. Key features of photoanodes

Unfortunately, basic semiconductor photanodes are often limited by large bandgaps, weak visible-light absorption, low conductivity, short hole-diffusion lengths and sluggish interfacial kinetics [111]. For this reason, scientists face the challenge of inventing a cheaper, more effective and oxidative stable electrode. The excellent photoanode material must meet the following basic conditions:

1) **Low energy gap value** [112] (difference of energies between the conduction band and the valence band by electronic band structure theory)

   Practical windows frequently quoted for water oxidation are 1.4–3.5 eV, balancing photon harvesting against overpotential requirements; this selection rule is stated explicitly in classic PEC criteria and used in oxide case studies [113]

2) **Strong light absorption in the visible** irradiation spectra [114]

   Absorption can be increased by morphology engineering and optical management (nanorods, nanotubes – reflection effect, porous films, resonant trapping), which lengthen the optical path and raise the effective absorption without sacrificing charge-collection length [115].

3) **Low net carrier recombination rate**, increase carrier lifetimes [116]

   The photocurrent efficiency is closely related to the separation efficiency of charge carriers and the interfacial transfer rate; the short diffusion length of the carriers (2–4 nm) and the low bulk conductivity of the material result in an increased recombination frequency [117].

4) **Band-edge alignment** for spontaneous charge transfer [118]

   The CB must be more negative than H^+/H_2*, and the VB must be more positive than* O_2/H_2O *at the operating pH; the flat-band potential and bandgap together set the driving force* [22]*.*

5) **Long-term stability in aqueous electrolytes** (resistance to corrosion and photo-corrosion) [86]

   Stability is a first-order selection criterion in PEC; oxide families are preferred in part for their chemical robustness and photo-corrosion resistance, as emphasised in the survey of oxide photoanodes [92]*.*

To obtain the best possible photoanode, it is necessary to consider multiple, interconnected modifications while taking into account all of the above aspects. An example of a high-performance photoanode with the highest reported photocurrent density is based on a multilayer TCO/n–p–Si/TCO/Ni architecture, in which a crystalline silicon n–p junction serves as the light absorber, transparent conductive oxide (TCO) layers are deposited as charge-collecting and protective contacts, and a Ni-based oxygen evolution cocatalyst is formed by electrochemical deposition, enabling a saturation photocurrent density of 39.6 mA/cm^2 at 1.23 V vs. RHE under AM 1.5G illumination (100 mW/cm^2), approaching the theoretical maximum photocurrent of silicon (42.7 mA/cm^2) [115]. Based on commonly studied photoanodes, the principal advantages and limitations are juxtaposed below in Table 2.

Table 2. Advantages and Disadvantages for selected photoanodes materials.

SC	Advantages	Disadvantages	Ref.
TiO_2	high surface area; fast electron injection; thermally, chemically, electronically and photo-stable; favorable electrochemical properties; abundant, not expensive; biocompatible and non-toxic;	limited electron mobility; significant trap density and recombination; absorption only in UV spectra;	[119, 120]
ZnO	high surface area; thermally and mechanically stable; high electron mobility and diffusivity; abundant, not expensive; enhanced ability to suppress charge recombination as a result of higher electron mobility and rapid electron diffusion	Lower efficiency compared to TiO_2; Instability under acidic dye conditions; Complexation with dyes; high bandgap energy.	[119, 121]
$BiVO_4$	visible-light absorber; favourable band positions for OER; low onset when integrated in heterostructures; Earth-abundant and relatively low-cost; Good chemical stability under neutral conditions	short hole-diffusion length; low carrier mobility and poor bulk conductivity; strong surface and interfacial recombination; stability can be electrolyte-dependent;	[122, 123]
WO_3	visible absorption (2.6–3.0 eV); valence band strongly oxidizing, well-suited for OER; good electron mobility; can be prepared by multiple scalable thin-film routes;	positive E_{FB} cannot drive H_2 evolution on its own; electrolyte-dependent photocorrosion; limited solar absorption	[124, 125]
$SrTiO_3$	high chemical and photochemical stability; conduction pathways can be engineered by doping	Wide bandgap - only UV absorption; fast charge recombination;	[126, 127]
Zn_2SnO_4	electron mobility higher than TiO_2; aiding fast electron diffusion; chemically robust oxide;	UV-dominated absorption; performance often limited by interfacial recombination;	[128, 129]

In my doctoral dissertation, a TiO_2-based semiconductor was chosen as the photoanode material. Below, I explain in detail why I chose this material:

- Robustness, abundance, low cost and mature processing. TiO_2 is routinely described as abundant, low cost, non-toxic and photochemically robust; it is a stable n-type oxide that likes long illumination without severe photo-corrosion [130].
- Tunable electronic structure and morphology: the flat-band potential and bandgap can be modulated through dopants and structural architectures, enabling optical and interfacial engineering at scale [22].
- Oxygen-vacancy 'self-healing' under operation. OV-engineered oxides tend to re-oxidise during PEC operation; in TiO_2, surface vacancies are refilled by water/oxygen species, tempering initial OV gains but underscoring intrinsic lattice stability under bias and light [131].
- Exceptional chemical and photochemical stability relative to peers. Compared with other common photoanodes, TiO_2 is particularly resistant to chemical and photo-corrosion across a wide pH range, whereas ZnO is unstable in acidic media and prone to dye complexation without passivation; WO_3 often requires bias and can face stability issues in neutral/alkaline electrolytes [88].

4. Titanium dioxide nanotubes photoanodes

TiO_2 occurs in three polymorphs: anatase, rutile and brookite, with distinct crystal symmetries (anatase, tetragonal $I4_1/amd$; rutile, tetragonal $P4_2/mnm$; brookite, orthorhombic Pbca) [132]. The anatase structure is shown in Figure 8A. The electrochemical and photoelectrochemical properties of TiO_2 have been recognised since the report of Fujishima and Honda [20]. Over subsequent decades, the photoelectrochemical behaviour of TiO_2 nanocrystals and their modifications has been investigated extensively. Figure 8B presents a Tauc plot indicating that iodine doping reduced the bandgap from about 3.25 eV to about 2.8 eV, with an associated increase in photoactivity of about 30% in the case of nanopowder [133]. Similar behaviour is observed for titania nanotubes photoanode [134]. Advances in synthesis and processing have also driven the

development of diverse TiO_2 architectures, including nanotubes, nanorods, thin shells, nanospheres and nanoparticles (Figure 8C) [135].

The first solvothermal or hydrothermal synthesis of TiO_2 nanotubes, obtained by treating TiO_2 powders in concentrated NaOH followed by acid washing, was reported by Kasuga and co-workers in 1998 [136]. This route produced free multiwalled nanotubes dispersed in solution, typically tens to hundreds of nanometres in length. Self-organised TiO_2 nanotube layers grown directly on titanium were observed during anodisation in fluoride containing electrolytes by Zwilling et al. in 1999 [137]. They described the formation of ordered porous or tubular oxides in chromic acid with HF. Subsequent work by the groups of Grimes, Schmuki and Macak optimised the anodisation method to obtain highly ordered, long tubes with controllable diameter and length, and near hexagonal ordering [15,138].

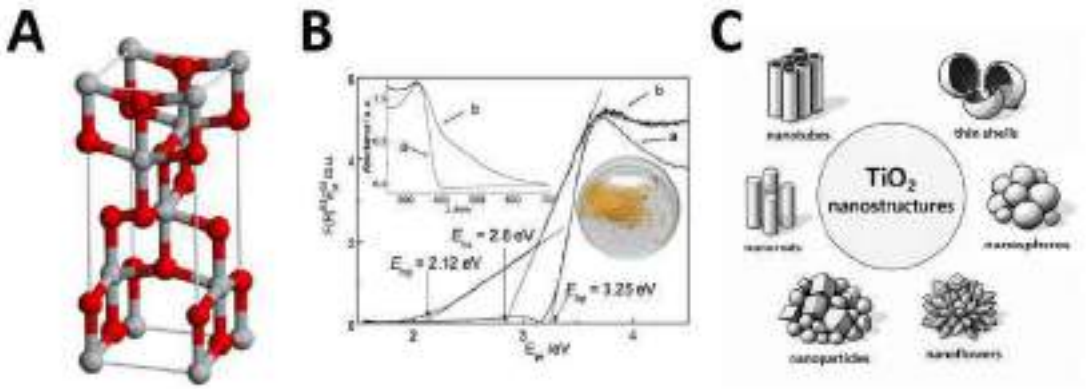

Figure 8. (A) Crystal structure of anatase (TiO_2), (B) Tauc plot for TiO_2 and I-doped TiO_2 nanopowders (adapted from [132]), (C) schematic images of various TiO_2 nanostructures (AI-generated).

Over the last two decades, many other transition metal oxides have been explored for photocatalysis and photoelectrochemistry. Substantial advances in the non-metal doping of TiO_2 photoanodes (nanopowders and nanotubes) have been achieved by the group led by Professor Anna Lisowska-Oleksiak. This body of work underpins the present study: without the positive results, accumulated knowledge and methodological expertise developed by that group, the current project would likely not have appeared. Detailed methods and results are presented in Section 4.2.2. Nevertheless, TiO_2 remains the most widely used and a highly promising platform, with nanotube architectures valued for their

robustness, processability and performance. The following sections describe methods for synthesising and modifying TiO_2 nanotube photoanodes.

4.1. Synthesis methods

There are several methods for obtaining TiO_2 nanotubes. They are shortly presented below.

1. **Hydrothermal method**

   TiO_2 (often anatase powders such as Degussa P25) is dispersed in concentrated NaOH, sealed in an autoclave, and heated at 110-150 °C for several hours to a day; the as-formed sodium titanate product is then proton-exchanged by acid washing (typically 0.1 M HCl), followed by rinsing and optional calcination to convert titanate to TiO_2. Typical conditions are 10 M NaOH, 110-150 °C, 12-24 h, yielding multi-walled nanotubes with tens nm of inner diameter and lengths from tens to hundreds of nanometres. Hydrothermal parameters (precursor phase and size, alkali concentration, temperature–time profile, and the post-wash sequence) control wall layering, diameter and length; formation mechanisms include peeling–scrolling of titanate nanosheets and seed-assisted oriented growth [17].

2. **Template-based method**

   A highly porous carbon nanotubes (CNTs) is first soaked with an ethanolic solution of tetrabutyl titanate, so the precursor permeates the open network. On exposure to water, the precursor hydrolyses and condenses to coat the CNTs strands with an amorphous TiO_2 shell, producing a TiO_2/CNTs core-shell framework. Next calcination at 450 °C for 2 hours removes the carbon scaffold and crystallises the oxide, leaving a macroporous network of hollow TiO_2 tubes [19].

3. **Sol-gel method**

   A sol-gel transcription in self-assembled organogels enables unusual TiO_2 morphologies. $Ti(OiPr)_4$ is introduced into an organic gel (e.g., a crown-appended cholesterol gelator in 1-butanol) and allowed to hydrolyse/condense under ambient humidity, followed by staged calcination

(e.g., 200 °C then 500 °C) to yield TiO_2 helical ribbons and double-layered nanotubes (outer diameters ~500 nm; ~8–9 nm interlayer spacing) [139].

4. **Chemical exfoliation**

This delaminates layered titanates or transforms quasocrystalline TiO_2 into tubular titanates without the mechanical constraints of hard templates. These soft-chemical processes emphasise ion-exchange and sheet scrolling/delamination rather than confinement by a rigid host; they are tunable via alkali type/concentration, washing sequence and calcination [140].

5. **Electrochemical oxidation of titanium (anodisation)**

Finally, the electrochemical route for preparing titania nanotubes is widely regarded as the most suitable option when controlled and reproducible architectures are required [15]. The morphology of TiO_2 nanotubes is closely linked to synthesis parameters such as the electrolyte and its composition, the thickness and purity of the Ti substrate, the set temperature, the anodisation time, the applied potential or current, and the cell geometry, including electrode spacing and area. Parameter optimisation has primarily focused on improving conductivity, extending charge-carrier lifetimes, and narrowing the bandgap of TiO_2 [44]. Moreover, simple anodisation does not obtain a material with a high photocatalytic activity due to the formation of an amorphous oxide. The following heat treatment process is required to crystallize TiO_2 - calcination. In this process, the essential parameters are heating rate, time, temperature and gas atmosphere. According to the literature, electrodes with an anatase phase are the most favourable [141]. There are some papers [142–144] that describe the optimization of parameters for obtaining titanium dioxide nanotubes and morphology control. They mainly concern improving conductivity, charge-carrier lifetimes, and the narrowing of the bandgap energy of TiO_2 [145]. Figure 9 summarises the sequence of steps used to obtain the final TiO_2 nanotube photoanode.

Figure 8 Schematic diagram with pictures showing the steps leading to obtaining crystalline structures of TiO_2 nanotubes (stages: anodization/rinsing/calcination).

In my PhD, the process of obtaining TiO_2-NTs is consisted of following steps:

- Titanium foil (99.5% metals basis, 0.25 mm thickness) is cut into plates of about 2 × 2 cm, flattened if necessary to ensure planarity, then degreased ultrasonically in a 1:1 (v/v) acetone–isopropanol bath for roughly 20 minutes at about 40 °C. The plates are rinsed thoroughly with deionised water and dried in warm air. These preparatory steps improve field uniformity and minimise adventitious contamination prior to anodisation.
- The electrolyte is an ethylene glycol formulation containing ammonium fluoride, water and phosphoric acid. The electrolyte composition consist of 0.27 M NH_4F in ethylene glycol with 5 vol% H_2O and 3.5 vol% H_3PO_4 (95%). The mixture is stirred until optically clear.
- Anodisation is carried out in a two-electrode glass cell with titanium as the anode and a platinum mesh as the cathode. The electrode spacing is set to about 2 cm, and the bath temperature is maintained at 20 ± 1 °C. A constant potential of 40 V is applied for 2 hours to grow the nanotube layer. Immediately after anodisation, the foils are rinsed copiously with water; a brief rinse in a 1:1 acetone–isopropanol bath to remove loosely bound residues, followed by a final water rinse and warm-air drying.

- The amorphous titania nanotubes is crystallised by calcination in air. The electrodes are heated at about 2.5 °C/min to 450 °C, held for 2 hours, then removed fast and cooled to room temperature in air. This treatment yields anatase-dominated, single-wall TiO_2 nanotubes suitable for photoelectrochemical testing.

This phenomenon of tubular shapes is casuing by the action of fluoride ions at the electrolyte exposed top of the growing layer, where continuous contact with the etchant promotes preferential dissolution [146]. Hydrofluoric acid was the first and is still the most frequently used source of fluoride in electrolytes for anodising titanium to produce TiO_2 nanotubes [147], although many other acids and mixed electrolytes have also been employed successfully. In practice, the electrochemical formation of TiO_2 nanotubes relies on the presence of fluoride, which complexes Ti in the (+IV) state and enables the porous, tubular architecture to emerge during anodisation. Below the stages are described, as summarised form based on the literature [15,17,148]:

I. **Barrier layer growth.** A compact TiO_2 film forms on titanium. The cell current falls rapidly as the oxide thickens, according to (10-12):

$$\mathrm{Ti} \rightarrow \mathrm{Ti^{4+}} + 4\,\mathrm{e^-} \quad (10)$$

$$\mathrm{Ti^{4+}} + 2\,\mathrm{H_2O} \rightarrow 4\,\mathrm{H^+} + 2\,\mathrm{TiO_2} \quad (11)$$

$$\mathrm{OVERALL:\ Ti} + 2\,\mathrm{H_2O} \rightarrow 4\,\mathrm{H^+} + 4\,\mathrm{e^-} + 2\,\mathrm{TiO_2} \quad (12)$$

II. **Fluoride activation and pore initiation.** Fluoride begins to dissolve TiO_2 or Ti, generating randomly distributed nanopores while competing with oxide growth. The onset of this dissolution thins the barrier and the current increases. The key reactions are presented below (13,14):

$$\mathrm{TiO_2} + 6\mathrm{F^-} + 4\,\mathrm{H^+} \rightarrow [\mathrm{TiF_6}]^{2-} + 2\,\mathrm{H_2O} \quad (13)$$

$$6\mathrm{F^-} + \mathrm{Ti} \rightarrow [\mathrm{TiF_6}]^{2-} + 4\,\mathrm{e^-} \quad (14)$$

Dissolution of TiO_2 or Ti by fluoride is non faradaic and therefore competes with the faradaic oxide growth.

III. **Pore deepening and onset of ordering.** Thinning occurs at the pore bases, which deepens the features and produces nanodimples. Under conditions where the current is distributed uniformly, the porous layer begins to order and evolves towards an array of nanotubes. A slight decrease in current is often observed in this stage.

IV. **Steady state tube growth.** When the rate of titanium oxidation matches the rate of fluoride assisted dissolution of TiO_2, the nanotubes elongate progressively. The current stabilises at a near constant value and the growth rate gradually declines as anodisation continues.

4.2. Modification strategies

4.2.1. Morphological engineering

Several TiO_2 modification strategies lead to increased visible light photoactivity through morphology-altering treatments. The following can be distinguished:

- creating porous

Porous anodic TiO_2 provides a very large internal surface area and an interconnected pore network, which promotes adsorption, light scattering and mass transport at the solid–liquid interface [149,150].

- double-walled nanotubes

This structural transformation leads to a cleaner tube interior and an enlarged inner diameter, which together improve charge transport and overall electronic quality. As a result, the modified nanotubes exhibit a reduced density of trap states, more efficient carrier separation, and enhanced photoelectrochemical performance, manifested by an increased photoresponse and higher activity in PEC applications [151].

- bamboo structures

Bamboo-type tubes with periodic constrictions increase internal surface and can enhance axial light scattering and local electric fields [150].

- ultra-long with a small diameter

Two-step anodisation tailored for small diameters and great lengths yields tubes that combine a long optical path with short radial diffusion distances to

the walls. In dye-sensitised photoanodes, this geometry improves both light harvesting and electron collection, delivering higher efficiencies [152].

- laser-treated

Ultra-short, local heating crystallises amorphous tubes to anatase or modulates crystallinity in pre-calcined tubes, often producing a thin melted/re-solidified top layer (~300 nm). In contrast, the underlying tube architecture remains intact. The treatment alters band structure (band-gap narrowing), absorption and defect population, which together enhance photoresponse relative to untreated tubes [153].

- hydrothermal annealing (HA) [154]

The first study devoted to the testing effect of HA on the photocatalytic properties of anodized TiO_2 was described by Jiaguo Yu in 2010 [155]. The work shows that amorphous nanotubes hydrothermally treated in autoclaves lead to aggregation of TiO_2 into particles. Subsequent similar works [156–160] show the dissolution and anatase recrystallization of amorphous TiO_2 by water annealing (also known as the water-soaking method). These tests were carried out under atmospheric pressure. The only report that showed the effect of hydrothermal modification in an autoclave on calcined TiO_2-NTs under increased pressure is reported in ref. [161]. However, after annealing titania nanotubes were finally calcined after HA. According to the literature above, no one before focused on the effect of HA on calcined titania nanotubes without subsequent calculations. In 2022, improved photocatalytic activity of TiO_2 nanotubes hydrothermally modified in mild alkali solutions, have been showed by Wtulich et al. [154]. Recently, mechanical property of TiO_2 nanotubes calculated via molecular dynamics simulations [162], or experimental studied when formed on titanium by anodic oxidation [163] or by sonoelechtrochemical anodisation [164] have been investigated. Therefore, achieving simultaneous improvements in both photocatalytic efficiency and mechanical stability is highly desirable. Unfortunately, the mechanical results of the HA study have not been published in any journal. To obtain HA TiO_2-NT electrodes were subjected to hydrothermal annealing in a Teflon-lined stainless steel autoclave (50 mL total volume). Each TiO_2-NT sample was placed in the Teflon vessel and 30 mL of triple-distilled water was added (covering the sample).

The autoclave was sealed and heated in an oven at the desired temperature (in this study: 75, 100, 125, 150, 175, or 200 °C) for 24 h. After the HA step, the autoclave was fast cooled to room temperature, removed and dried. The process with parameters you can see in Figure 10.

Figure 9. Schematic of the synthesis of HA TiO_2-NTs via anodisation, calcination, and hydrothermal annealing.

Figures 11A–H show SEM images of TiO_2-NTs before and after hydrothermal annealing (HA) at various temperatures. The reference TiO_2-NTs sample (after anodisation and calcination only), presented in Figure 11A, consists of vertically and obliquely oriented nanotubes forming small clusters (bundles) on the Ti substrate. These clusters likely result from localised stress or uneven growth during anodisation and calcination, leading to slight agglomeration of neighbouring tubes. After hydrothermal treatment at 75–125 °C for 24 h (Figure 11B–D), the overall nanotubular architecture is preserved; the tubes remain vertically aligned and open at the top. Notably, HA-treated samples exhibit a more homogeneous distribution of nanotubes. Clusters are particularly eliminated after HA at 100 °C, yielding a more evenly spaced array of individual tubes. This suggests that hot-water treatment induces subtle reorganisation or relaxation within the nanotube layer, allowing tightly clustered tubes to separate. The tubes open primarily due to the dissolution of minor contaminants (such as phosphorus and fluorides from the anodisation process) that initially connect the tubes, thus cleaning the structure. At the highest HA temperatures (175 °C and 200 °C), SEM images still reveal intact nanotube arrays but with significant structural deterioration. The nanotubes appear damaged, with a stratified structure and partial detachment from the substrate, leading to overlapping nanotubes. In

particular, apparent detachment of TiO_2 nanotubes from the Ti substrate can be observed in Figure 11H.

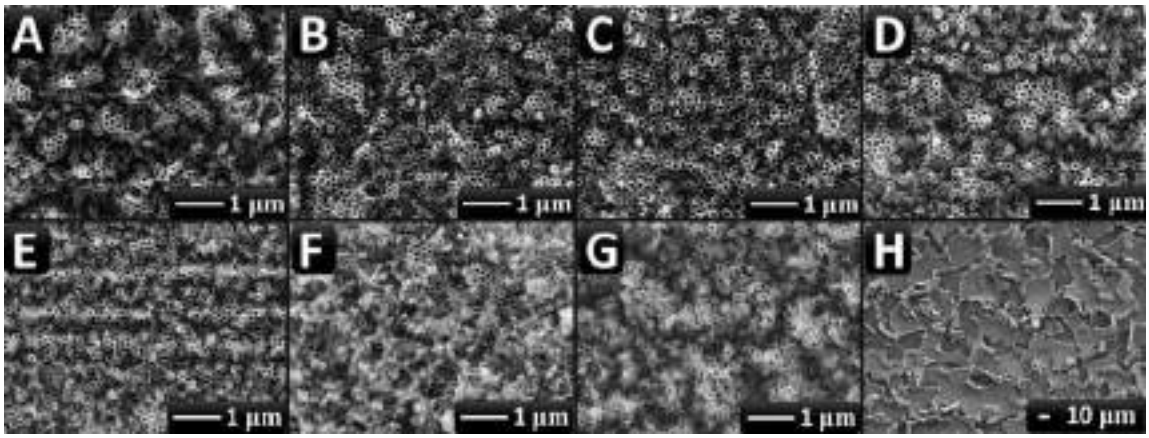

Figure 10. SEM images: (A) pure TiO_2 nanotubes TiO_2-NTs; (B-F) hydrothermally modified in distilled water for 24 hours at 75, 100, 125, 150, 175 and (G-H) 200 ^{O}C.

Detailed results on the correlation between the mechanical and photoelectrochemical properties of the TiO_2 nanotubes are in preparation (Provisional article title: 'Optimizing TiO_2 nanotubes photoanodes activity: Interplay of mechanical and electrochemical properties via hydrothermal annealing'). The work is being prepared in collaboration with Dr. Aleksandra Mirowska and Professor Marek Szkodo from the Faculty of Mechanical Engineering and Ship Technology (Wydział Inżynierii Mechanicznej i Okrętownictwa), Gdańsk University of Technology, who specialise in determining mechanical properties. Preliminary findings were presented as a poster at the 16th Fast Ion Conductors Symposium (Augustów, 2024). X-ray diffraction and Williamson–Hall analysis of my PhD samples, indicate that HA relieves the substantial microstrains (σ ~151 MPa) present in as-formed nanotubes, nearly eliminating residual stress (to zero) at 100 °C, whereas higher HA temperatures introduce slight residual strains. Nanoindentation tests indicated that the HA process does not significantly change the hardness of the nanotube layer (~0.8 GPa), preserving the mechanical integrity of the photoanode. Linear sweep voltammetry and transient photocurrent (at +0.5 V vs. Ag/AgCl/3M KCl) demonstrated enhanced photoelectrocatalytic activity for HA-treated TiO_2-NTs: the photocurrent density increased by ~40% after HA at 100 °C compared to untreated TiO_2-NTs.

4.2.2. Non-metal and metal doping

A modification method to improve photoelectrochemical properties of photoanode materials is doping with a non-metal or a metal element. In 2001, one of the first works on non-metal TiO_2 doping was presented by Asahi et al [165]. The dopant of nitrogen increased the photoactivity of titanium dioxide in the visible range compared to pure TiO_2. The reason for the increased photocatalytic activity was the narrowing bandgap, caused by the mixing of replacing N *2p* orbitals with O *2p* orbitals. In the case of titania nanotubes, non-metal doping can take place by calcination in the atmosphere of a gas which is the source of the doping atoms (e.g. with nitrogen in an NH_3 or N_2 atmosphere) [166,167] or by electrochemical doping in a two-electrode system (e.g. with nitrogen, iodine or boron) [134,168]. In addition, nanotubes were also modified in various ways with dopants of carbon [169,170] or sulphur [171,172]. In Table 3, band-gap energies and photocurrent generation are juxtaposed for selected non-metal dopants, including results from Professor Lisowska-Oleksiak's team.

Table 3. Comparison of energy bandgap and photocurrent density for selected metal-doped TiO_2 (j_{doped}—photocurrent density for doped TiO_2, j_{TiO2}—photocurrent density for pure TiO_2). */Electrode potential E vs. Ag/AgCl/3M KCl.

Electrode Material	**Luminous Intensity ($mW \cdot cm^{-2}$)**	**Energy Bandgap, E_g (eV)**	**Photocurrent Density ($\mu A \cdot cm^{-2}$)/*E(V)**	**Enhancement Factor (j_{doped}/j_{TiO2})**	**Ref.**
I-TiO_2-NTs	100	3.00	155.2 at 0.5 V	6.1	[134]
B-TiO_2-NTs	100	2.91	300.0 at 0.5 V	7.5	[173]
N-TiO_2-NTs	100	2.65	55.8 at 0.5 V	2.8	[174]
P-TiO_2-NTs	100	no data	250.0 at 0.2 V	4.5	[175]
S-TiO_2-NTs	100	3.41	69.5 at 1.0 V	1.2	[176]

Besides this, researchers investigated methods of doping nanotubes with transition metals [177,178]. Metal-doped TiO_2-NTs can be obtained through sol-gel, hydrothermal, electrochemical processes or sputtering in the atmosphere of dopant [179]. As it turns out, only small contents (generally up to a few atomic per cent) allow improving the efficiency of recombination of electron-hole pairs

and increasing absorption into light [180–182]. Table 4 presents selected data from the literature and contains values for photocurrent generation by the metal-doped TiO_2 photoanode.

Table 4. Comparison of energy bandgap and photocurrent density for selected metal-doped TiO_2 (j_{doped}—photocurrent density for doped TiO_2, j_{TiO2}—photocurrent density for pure TiO_2). */Electrode potential E vs. Ag/AgCl/3M KCl.

Electrode Material	Luminous Intensity ($mW \cdot cm^{-2}$)	Energy Bandgap, E_g (eV)	Photocurrent Density ($\mu A \cdot cm^{-2}$)/*E(V)	Enhancement Factor (j_{doped}/j_{TiO2})	Ref.
Ni-TiO_2-NTs	100	3.00	850.0 at 0 V	2.1	[183]
Co-TiO_2-NTs	100	no data	40.0 at 0.4 V	3.0	[184]
Cr-TiO_2-NTs	100	2.82	360.0 at 1.0 V	9.2	[185]
V-TiO_2-NTs	16	no data	5.8 at 0.5 V	4.8	[186]
Ag-TiO_2-NTs	400	3.35	80 at 0.6 V	5.3	[187]
Cu-TiO_2-NTs	400	3.22	100 at 0.6 V	6.7	[187]
Ag-TiO_2 film	4.4	2.50	1.2 at 0.2 V	3.5	[188]
Fe-TiO_2 nanorods	100	3.12	550.0 at 0 V	5.5	[189]
Cu-TiO_2 film	44.42	2.82	18.2 at 0.4 V	1.3	[190]

An interesting metal, from the point of view of physicochemical properties, used in devices such as batteries, sensors, hard disk drives or superalloys is cobalt [191–194]. One of the methods of doping materials with cobalt is two-electrode anodisation process with electrolyte contains cobalt salts [184].

Another promising method of modification TiO_2-NTs is the deposition of noble metal nanoparticles (eg Au, Ag, Pt, Pd) [195–198] on its electrode surface. Many researchers proved, that modification with these metals reduces the efficiency of exciton recombination against to increase the absorption in the Vis range. This is caused by the effect of surface plasmon resonance (SPR) [199,200]. All this leads to an increase in photocatalytic and photoelectrochemical activity [201].

4.2.3. Cocatalyst deposition

A subsequent method of obtaining improved photocatalytic efficiency toward water splitting is the use of titanium oxide nanotube systems decorated with a cocatalyst [111,202]. Table 5 presents the division into different types of cocatalysts with examples and short characteristics. Although the efficiency of water oxidation in the PEC system is much higher than already known modification methods, many of the reasons for this remain unclear (explained in various perspectives). Moreover, there are not many articles on cocatalysts deposited on titania nanotubes. Thus, it is necessary to continue and develop research to improve the modification and clearly explain the photocatalytic cocatalyst mechanisms.

Cobalt oxides (CoO_x) are known to be effective cocatalysts for OER. Catalysis is possible due to the cobalt ion's activity in electron transfer, supported by hydrogen transfer [203]. The redox characterisation of metal oxide clusters can be predicted using DFT calculations [204]. Minimising the particle size of oxide clusters and controlling their oxidation states can significantly affect their redox characteristics and photocatalytic activity [111]. Furthermore, cobalt oxyhydroxide may prove to be a more efficient and promising cocatalyst. As shown in the literature [205–207], the rate-determining step of the oxygen evolution reaction is the release of dioxygen from the superoxide intermediate. An attempt to synthesize these compounds will be interested in the context of new developments and achievements. Taking all factors into account, selecting appropriate deposition parameters for cocatalyst loading on TiO_2-NTs can significantly improve photoanode performance.

Table 5. Types of cocatalysts with selected examples and short characteristics.

No.	Type	Examples	Characteristic
1	Metal Phosphates (M-Pi) / Phosphides (MP)	• cobalt phosphate (Co-Pi) [208] • nickle phosphate (Ni-Pi) [209] • iron phosphate (Fe-Pi) [210] • TiO_2/FeMnP (j_{ph} 1.8 $mAcm^{-2}$ at 1.23 V vs. RHE) [211]	The precursor towards OER in the PEC system (lots of available material on the Earth, easy to synthesize, modify and catalyse over a wide pH range).
2	Metal Oxides (MO_x)	• RuO_x, CoO_x IrO_x, NiO_x [212,213] • Fe_2O_3/IrO_2 (j_{ph} 3 $mAcm^{-2}$ at 1.23 V vs. RHE) [214]	Metal oxides are easy to synthesize and cost-efficient. They have high stability and activity that promotes water oxidation.
3	Metal (oxy)hydroxides ($MO_x(OH)_y$)	• NiO(OH), $Ni(OH)_2$ [215,216] • FeO(OH) [217] • CoO(OH)[218] • LDHs (layered double hydroxides)[219,220] $M_{1-x}^{2+}M_x^{3+}(OH)_2X^+\left[A^{x}/_{n}\right]^{n-} \cdot mH_2O$	Metal oxy(hydroxides) are currently among the most promising cocatalysts for water oxidation in PECs, with outstanding efficiency. Inexpensive, widely available in nature, capable to form multilayers and cause a huge potential drop of the Helmholtz layer at the electrode/electrolyte interface.
4	Metal-based boron compounds (M-Bi)	• cobalt-borate (Co-Bi)[221] • nickel-borate (Ni-Bi)[222]	They are similar (mechanisms of photocatalysis) to M-Pi compounds. Promisingly efficient, new and inspiring (known for about 10 years).
5	Metal-Free cocatalysts	• graphene[223] • reduced graphene oxide (rGO)[224] • graphitic carbon nitride (g-C_3N_4)	Most materials containing metal ions are hazardous to human health; carbon-based materials may be a competitor. The synthesis of such cocatalysts is complex and not cheap, but the yields are comparable.
6	Molecular Cocatalysts	• mesoporous indium-tin oxide (meso-ITO)[225] • Photosystem II /benzoquinone polymer-based[226]	Materials with high porosity and a real surface area. Used in OER in natural photosynthesis, bioelectrochemical devices. Difficult-to-design materials.
7	Dual Cocatalysts	• rGO/Ni:FeOOH[224] • Co_3O_4/Co–Pi[227]	The combination of two different catalysts can improve the photocatalytic water oxidation.

4.2.4. Semiconductor/semiconductor junctions

Another important method of photoanode modification is the construction of heterojunction, the interfacial area between two different semiconductors. A combination of high-gap and low-gap semiconductors is often used here to maximize the absorption range of UV-Vis light [228]. In this case, due to the type of donor (n-type) or acceptor (p-type) admixture of the semiconductor, we can distinguish the following junctions: n-n, p-p or n-p. Examples of n-type semiconductors are: TiO_2, $BiVO_4$, WO_3, Fe_2O_3, SnO_2, $BiVO_4$, $NiTiO_3$ and p-type are: SnS_2, In_2S_3, $ZnIn_2S_4$, Cu_2O, and NiO [229,230]. In addition, there is also a heterojunction with the so-called Z-scheme, due to charge transfer along the Z-shape. These combinations of semiconductors can improve the efficiency of the PEC, but it is not so easy to obtain ideal junctions conducive to the charge carrier transport [228]. There are also ways to combine hybrid semiconductors with organic materials, such as conductive polymers (PEDOT:PSS) [231]. Nevertheless, the construction of heterojunction is widely used among scientists. Examples of such materials are: Cu_2S/Fe_2O_3 (j_{ph} 1.19 mA/cm^2) [232], $NiOOH/FeOOH/Co_3O_4/BiVO_4$ (j_{ph} 6.34 mA/cm^2) [233], $ZnO\text{-}WO_{3-x}$ (j_{ph} 3.38 mA/cm^2) [234] or $BaTiO_3/TiO_2$/graded QDs (j_{ph} 15.3 mA/cm^2) [235]. All the photocurrent densities are relative to the reverse hydrogen electrode (RHE). In fact that, there are many possibilities of heterojunction construction (a wide range of materials with different nanostructures, innovative possibilities of synthesis, manipulation of bandgap energy and increased absorption in VIS light), this modification becomes a very promising method of improving catalytic and photocatalytic

5. Applications of TiO_2 nanotubes

Titanium dioxide nanotubes are used in various fields, including photovoltaics, environmental remediation, photo-optics, self-cleaning coatings, batteries, and biomedicine [236]. Their popularity stems from their chemical resistance, biocompatibility, large specific surface area, and ordered structure that supports rapid charge transport, making them attractive substrates for biosensors [237,238]. In photocatalysis, TiO_2 has gained popularity in the decomposition of water pollutants using semiconductor powders [239]. Under illumination,

photogenerated carriers drive redox processes that mineralize organic compounds via hydroxyl radical pathways or direct surface oxidation [238]. In the case of nanotubes, geometry is crucial: increasing the tube length typically increases activity, while the diameter has a weaker effect-an effect related to surface scaling and carrier lifetime. Compared to nanopowders, nanotubes are ordered and easily recoverable, and their tubular channels reduce recombination losses during photocatalysis [240].

Dye-sensitised and quantum-dot-sensitised architectures are particularly important for solar energy conversion. Dye sensitisation extends absorption beyond the wide bandgap of TiO_2; early nanotube-based cells achieved almost 2.9% power conversion with nanoparticle decoration [241], TiO_2 nanotubes enabled about 6.9%, and their combination (TiO_2 nanotubes with TiO_2 nanoparticles) achieved up to 8% on luminescence [242]. Noble metal modification (like Au, Ag, Pt, Pd) and coupling with semiconductor quantum dots (e.g., CdS, CdSe, CdTe) improve absorption and promote charge separation [243–245]. Together, these strategies highlight how interface engineering and morphology control translate into higher device efficiency. Future progress will likely come from tandem strategies that combine several modifications into a single architecture, even if integrating multiple methods is experimentally challenging. Addressing such challenges is part of our role as researchers in delivering technologies that support a sustainable future.

6. References

[1] M. Grätzel, Photoelectrochemical cells, Nat. 2001 4146861 414 (2001) 338–344. https://doi.org/10.1038/35104607.

[2] C. MacFarling Meure, D. Etheridge, C. Trudinger, P. Steele, R. Langenfelds, T. Van Ommen, A. Smith, J. Elkins, Law Dome CO2, CH4 and N2O ice core records extended to 2000 years BP, Geophys. Res. Lett. 33 (2006). https://doi.org/10.1029/2006GL026152.

[3] Lan, X., Tans, P. and K.W. Thoning: Trends in globally-averaged CO2 determined from NOAA Global Monitoring Laboratory measurements. Version (05.01.2026), (n.d.). https://doi.org/10.15138/9N0H-ZH07 (accessed January 14, 2026).

[4] J. Tollefson, Earth breaches 1.5 °C climate limit for the first time: what does it mean?, Nature 637 (2025) 769–770. https://doi.org/10.1038/D41586-025-00010-9;SUBJMETA.

[5] Lan, X., K.W. Thoning, and E.J. Dlugokencky: Trends in globally-averaged CH4, N2O, and SF6 determined from NOAA Global Monitoring Laboratory measurements. Version (05.01.2026), (n.d.). https://doi.org/10.15138/P8XG-AA10 (accessed January 14, 2026).

[6] I. Heimann, P.T. Griffiths, N.J. Warwick, N.L. Abraham, A.T. Archibald, J.A. Pyle, Methane Emissions in a Chemistry-Climate Model: Feedbacks and Climate Response, J. Adv. Model. Earth Syst. 12 (2020) e2019MS002019. https://doi.org/10.1029/2019MS002019.

[7] M.J. Prather, J. Hsu, N.M. DeLuca, C.H. Jackman, L.D. Oman, A.R. Douglass, E.L. Fleming, S.E. Strahan, S.D. Steenrod, O.A. Søvde, I.S.A. Isaksen, L. Froidevaux, B. Funke, Measuring and modeling the lifetime of nitrous oxide including its variability, J. Geophys. Res. Atmos. 120 (2015) 5693. https://doi.org/10.1002/2015JD023267.

[8] A. Garg, K. Kazunari, T. Pulles, 2006 IPCC Guidelines for National Greenhouse Gas Inventories., Geneva, 2006. https://doi.org/10.1016/S0167-5060(08)70670-8.

[9] Greenhouse Gas Emissions from Energy Data Explorer – Data Tools - IEA, (n.d.). https://www.iea.org/data-and-statistics/data-tools/greenhouse-gas-emissions-from-energy-data-explorer (accessed January 14, 2026).

[10] Eurostat Data Browser, Eurostat. “Share of Energy from Renewable Sources (nrg_ind_ren).,” https://ec.europa.eu/eurostat/databrowser/view/nrg_ind_ren/bookmark/table?lang=en&bookmarkId=d445ebf6-3196-4dd5-9c2c-fe067c1b949f&c=1732143909387 (accessed January 14, 2026).

[11] M. Kwaśniewski, K. Żmuda, Wodór - paliwo przyszłości, Gaz, Woda I Tech. Sanit. 1 (2022) 1–10. https://doi.org/10.15199/17.2022.6.1.

[12] J. Incer-Valverde, A. Korayem, G. Tsatsaronis, T. Morosuk, “Colors” of hydrogen: Definitions and carbon intensity, Energy Convers. Manag. 291 (2023) 117294. https://doi.org/10.1016/J.ENCONMAN.2023.117294.

[13] J. Cihlar, L. Villar, A. Wang, F. Melgar, J. Jens, P. Rio, Hydrogen generation in Europe: Overview of costs and key benefits, Publications Office of the European Union, Luxembourg, 2020. https://op.europa.eu/ga/publication-detail/-/publication/7e4afa7d-d077-11ea-adf7-01aa75ed71a1 (accessed January 14, 2026).

[14] M.R. Nellist, F.A.L. Laskowski, F. Lin, T.J. Mills, S.W. Boettcher, Semiconductor-Electrocatalyst Interfaces: Theory, Experiment, and Applications in Photoelectrochemical Water Splitting, Acc. Chem. Res. 49 (2016) 733–740. https://doi.org/10.1021/acs.accounts.6b00001.

[15] J.M. Macak, H. Tsuchiya, A. Ghicov, K. Yasuda, R. Hahn, S. Bauer, P. Schmuki, TiO2 nanotubes: Self-organized electrochemical formation, properties and applications, Curr. Opin. Solid State Mater. Sci. 11 (2007) 3–18. https://doi.org/10.1016/J.COSSMS.2007.08.004.

[16] R. Fernández, F. Fernández-Climent, S. Giménez, G. Giménez, M. Garcíagarcía-

Tecedor, The role of oxygen vacancies in water splitting photoanodes, Sustain. Energy Fuels 4 (2020) 5916–5926. https://doi.org/10.1039/D0SE01305F.

[17] P. Roy, D. Kim, I. Paramasivam, P. Schmuki, Improved efficiency of TiO2 nanotubes in dye sensitized solar cells by decoration with TiO2 nanoparticles, Electrochem. Commun. 11 (2009) 1001–1004. https://doi.org/10.1016/J.ELECOM.2009.02.049.

[18] G.D. Sulka, Introduction to anodization of metals, Nanostructured Anodic Met. Oxides (2020) 1–34. https://doi.org/10.1016/B978-0-12-816706-9.00001-7.

[19] P. Roy, S. Berger, P. Schmuki, TiO2 nanotubes: Synthesis and applications, Angew. Chemie - Int. Ed. 50 (2011) 2904–2939. https://doi.org/10.1002/ANIE.201001374.

[20] A. Fujishima, K. Honda, Electrochemical photolysis of water at a semiconductor electrode, Nature 238 (1972) 37–38. https://doi.org/10.1038/238037A0.

[21] T.R. Harris-Lee, F. Marken, C.L. Bentley, J. Zhang, A.L. Johnson, A chemist's guide to photoelectrode development for water splitting - the importance of molecular precursor design, EES Catal. 1 (2023) 832–873. https://doi.org/10.1039/d3ey00176h.

[22] M.G. Walter, E.L. Warren, J.R. McKone, S.W. Boettcher, Q. Mi, E.A. Santori, N.S. Lewis, Solar Water Splitting Cells, Chem. Rev. 110 (2010) 6446–6473. https://doi.org/10.1021/CR1002326.

[23] H. Gerischer, The impact of semiconductors on the concepts of electrochemistry, Electrochim. Acta 35 (1990) 1677–1699. https://doi.org/10.1016/0013-4686(90)87067-C.

[24] C.A. Grimes, O.K. Varghese, S. Ranjan, Light, Water, Hydrogen: The Solar Generation of Hydrogen by Water Photoelectrolysis, Springer, 2008. https://doi.org/10.1021/ja803884k.

[25] A. Vilanova, P. Dias, T. Lopes, A. Mendes, The route for commercial photoelectrochemical water splitting: a review of large-area devices and key upscaling challenges, Chem. Soc. Rev. 53 (2024) 2388–2434. https://doi.org/10.1039/D1CS01069G.

[26] A. Currao, A. Currao, Photoelectrochemical Water Splitting, Chimia (Aarau). 61 (2007) 815. https://doi.org/10.2533/chimia.2007.815.

[27] C. Jiang, S.J.A. Moniz, A. Wang, T. Zhang, J. Tang, Photoelectrochemical devices for solar water splitting – materials and challenges, Chem. Soc. Rev. 46 (2017) 4645–4660. https://doi.org/10.1039/C6CS00306K.

[28] L. Wang, J. Yu, Principles of photocatalysis, Interface Sci. Technol. 35 (2023) 1–52. https://doi.org/10.1016/B978-0-443-18786-5.00002-0.

[29] L.M. Peter, K.G. Upul Wijayantha, Photoelectrochemical Water Splitting at Semiconductor Electrodes: Fundamental Problems and New Perspectives, ChemPhysChem 15 (2014) 1983–1995. https://doi.org/10.1002/CPHC.201402024.

[30] A.J.. Bard, L.R. Faulkner, Electrochemical Methods: Fundamentals and Applications, John Wiley and Sons Inc, 2001.

[31] H. Gerischer, Solar photoelectrolysis with semiconductor electrodes, (1979) 115–172. https://doi.org/10.1007/3-540-09224-2_4.

[32] S.M. Sze, K.K. Ng, Physics of Semiconductor Devices, Phys. Semicond. Devices (2006). https://doi.org/10.1002/0470068329.

[33] A. Lasia, Electrochemical impedance spectroscopy and its applications, 2014. https://doi.org/10.1007/978-1-4614-8933-7.

[34] J. Tauc, R. Grigorovici, A. Vancu, Optical Properties and Electronic Structure of Amorphous Germanium, Phys. Status Solidi 15 (1966) 627–637. https://doi.org/10.1002/PSSB.19660150224.

[35] P. Makuła, M. Pacia, W. Macyk, How To Correctly Determine the Band Gap Energy of Modified Semiconductor Photocatalysts Based on UV-Vis Spectra, J. Phys. Chem. Lett. 9 (2018) 6814–6817. https://doi.org/10.1021/acs.jpclett.8b02892.

[36] C.R. Lhermitte, B.M. Bartlett, Advancing the Chemistry of CuWO4 for Photoelectrochemical Water Oxidation, Acc. Chem. Res. 49 (2016) 1121–1129. https://doi.org/10.1021/acs.accounts.6b00045.

[37] K. Maeda, K. Domen, Photocatalytic water splitting: Recent progress and future challenges, J. Phys. Chem. Lett. 1 (2010) 2655–2661. https://doi.org/10.1021/jz1007966.

[38] Y. Surendranath, D.G. Nocera, Progress in inorganic chemistry, Wiley, 2014.

[39] K. Sivula, R. van de Krol, Erratum: Semiconducting materials for photoelectrochemical energy conversion, Nat. Rev. Mater. (2016) 16010-. https://doi.org/10.1038/natrevmats.2015.10.

[40] M. Wtulich, A. Lisowska-Oleksiak, Tailoring TiO2 nanotubes photoanodes with electrodeposited Co3O4 and CoOOH cocatalysts for enhanced electrocatalytic and photoelectrocatalytic oxygen evolution, Appl. Surf. Sci. 714 (2025) 164376. https://doi.org/10.1016/j.apsusc.2025.164376.

[41] W. Zheng, iR Compensation for Electrocatalysis Studies: Considerations and Recommendations, ACS Energy Lett. 8 (2023) 1952–1958. https://doi.org/10.1021/ACSENERGYLETT.3C00366.

[42] D. Britz, iR elimination in electrochemical cells, J. Electroanal. Chem. Interfacial Electrochem. 88 (1978) 309–352. https://doi.org/10.1016/S0022-0728(78)80122-3.

[43] M.S. Burke, S. Zou, L.J. Enman, J.E. Kellon, C.A. Gabor, E. Pledger, S.W. Boettcher, Revised Oxygen Evolution Reaction Activity Trends for First-Row Transition-Metal (Oxy)hydroxides in Alkaline Media, J. Phys. Chem. Lett. 6 (2015) 3737–3742. https://doi.org/10.1021/ACS.JPCLETT.5B01650.

[44] R. Guidelli, R.G. Compton, J.M. Feliu, E. Gileadi, J. Lipkowski, W. Schmickler, S. Trasatti, Definition of the transfer coefficient in electrochemistry (IUPAC Recommendations 2014), Pure Appl. Chem. 86 (2014) 259–262. https://doi.org/10.1515/pac-2014-5025.

[45] N.T. Suen, S.F. Hung, Q. Quan, N. Zhang, Y.J. Xu, H.M. Chen, Electrocatalysis for the oxygen evolution reaction: recent development and future perspectives, Chem. Soc. Rev. 46 (2017) 337–365. https://doi.org/10.1039/C6CS00328A.

[46] T. Hisatomi, J. Kubota, K. Domen, Recent advances in semiconductors for photocatalytic and photoelectrochemical water splitting, Chem. Soc. Rev. 43 (2014) 7520–7535. https://doi.org/10.1039/C3CS60378D.

[47] D. Chen, Z. Xie, Y. Tong, Y. Huang, Review on BiVO4-Based Photoanodes for Photoelectrochemical Water Oxidation: The Main Influencing Factors, Energy & Fuels (2022). https://doi.org/10.1021/ACS.ENERGYFUELS.2C02119.

[48] M.B. Costa, M.A. de Araújo, M. V. de Lima Tinoco, J.F. de Brito, L.H. Mascaro, Current trending and beyond for solar-driven water splitting reaction on WO3 photoanodes, J. Energy Chem. 73 (2022) 88–113. https://doi.org/10.1016/J.JECHEM.2022.06.003.

[49] Y. Lin, S. Liu, Robust ZnO nanowire photoanodes with oxygen vacancies for efficient photoelectrochemical cathodic protection, Appl. Surf. Sci. 566 (2021) 150694. https://doi.org/10.1016/J.APSUSC.2021.150694.

[50] K. Sivula, F. Le Formal, M. Grätzel, Solar water splitting: Progress using hematite (α-Fe 2O3) photoelectrodes, ChemSusChem 4 (2011) 432–449. https://doi.org/10.1002/CSSC.201000416.

[51] M. Skompska, K. Zarębska, Electrodeposition of ZnO nanorod arrays on transparent conducting substrates-a review, Electrochim. Acta 127 (2014) 467–488. https://doi.org/10.1016/j.electacta.2014.02.049.

[52] X. Zhang, S. Zhang, X. Cui, W. Zhou, W. Cao, D. Cheng, Y. Sun, Recent Advances in TiO2-based Photoanodes for Photoelectrochemical Water Splitting, Chem. - An Asian J. 17 (2022) e202200668. https://doi.org/10.1002/ASIA.202200668.

[53] Q. Yi, H. Wang, J.M. Lee, BiVO4-Based Photoelectrochemical Water Splitting,

ChemElectroChem 12 (2025) e202400600. https://doi.org/10.1002/CELC.202400600.

[54] J.A. Seabold, K.S. Choi, Effect of a Cobalt-Based Oxygen Evolution Catalyst on the Stability and the Selectivity of Photo-Oxidation Reactions of a WO3 Photoanode, Chem. Mater. 23 (2011) 1105–1112. https://doi.org/10.1021/CM1019469.

[55] R. Abdullah, A.A. Jalil, M. Asmadi, N.S. Hassan, M.B. Bahari, M. Alhassan, N.M. Izzudin, M.H. Sawal, R. Saravanan, H. Karimi-Maleh, Recent advances in zinc oxide-based photoanodes for photoelectrochemical water splitting, Int. J. Hydrogen Energy 107 (2025) 183–207. https://doi.org/10.1016/J.IJHYDENE.2024.05.461.

[56] J. Fu, Z. Fan, M. Nakabayashi, H. Ju, N. Pastukhova, Y. Xiao, C. Feng, N. Shibata, K. Domen, Y. Li, Interface engineering of Ta3N5 thin film photoanode for highly efficient photoelectrochemical water splitting, Nat. Commun. 2022 131 13 (2022) 729-. https://doi.org/10.1038/s41467-022-28415-4.

[57] S. Han, S. Noh, Y.T. Yu, C.R. Lee, S.K. Lee, J.S. Kim, Highly Efficient Photoelectrochemical Water Splitting Using GaN-Nanowire Photoanode with Tungsten Sulfides, ACS Appl. Mater. Interfaces 12 (2020) 58028–58037. https://doi.org/10.1021/ACSAMI.0C17811.

[58] B. Alotaibi, H.P.T. Nguyen, S. Zhao, M.G. Kibria, S. Fan, Z. Mi, Highly Stable Photoelectrochemical Water Splitting and Hydrogen Generation Using a Double-Band InGaN/GaN Core/Shell Nanowire Photoanode, Nano Lett. 13 (2013) 4356–4361. https://doi.org/10.1021/NL402156E.

[59] J. Feng, W. Luo, T. Fang, H. Lv, Z. Wang, J. Gao, W. Liu, T. Yu, Z. Li, Z. Zou, Highly photo-responsive LaTiO2N photoanodes by improvement of charge carrier transport among film particles, Adv. Funct. Mater. 24 (2014) 3535–3542. https://doi.org/10.1002/ADFM.201304046.

[60] M. Higashi, K. Domen, R. Abe, Highly Stable Water Splitting on Oxynitride TaON Photoanode System under Visible Light Irradiation, J. Am. Chem. Soc. 134 (2012) 6968–6971. https://doi.org/10.1021/JA302059G.

[61] Y. Zhong, Z. Li, X. Zhao, T. Fang, H. Huang, Q. Qian, X. Chang, P. Wang, S. Yan, Z. Yu, Z. Zou, Enhanced Water-Splitting Performance of Perovskite SrTaO2N Photoanode Film through Ameliorating Interparticle Charge Transport, Adv. Funct. Mater. 26 (2016) 7156–7163. https://doi.org/10.1002/ADFM.201603021.

[62] F. Haydous, W. Si, V.A. Guzenko, F. Waag, E. Pomjakushina, M. El Kazzi, L. Sévery, A. Wokaun, D. Pergolesi, T. Lippert, Improved Photoelectrochemical Water Splitting of CaNbO2N Photoanodes by CoPi Photodeposition and Surface Passivation, J. Phys. Chem. C 123 (2018) 1059–1068. https://doi.org/10.1021/ACS.JPCC.8B09629.

[63] M. Higashi, K. Domen, R. Abe, Fabrication of an Efficient BaTaO2N Photoanode Harvesting a Wide Range of Visible Light for Water Splitting, J. Am. Chem. Soc. 135 (2013) 10238–10241. https://doi.org/10.1021/JA404030X.

[64] L. Zhang, C.G. Niu, X.F. Zhao, C. Liang, H. Guo, G.M. Zeng, Ultrathin BiOCl Single-Crystalline Nanosheets with Large Reactive Facets Area and High Electron Mobility Efficiency: A Superior Candidate for High-Performance Dye Self-Photosensitization Photocatalytic Fuel Cell, ACS Appl. Mater. Interfaces 10 (2018) 39723–39734. https://doi.org/10.1021/ACSAMI.8B14227.

[65] S.S. Liu, Q.J. Xing, Y. Chen, M. Zhu, X.H. Jiang, S.H. Wu, W. Dai, J.P. Zou, Photoelectrochemical Degradation of Organic Pollutants Using BiOBr Anode Coupled with Simultaneous CO2 Reduction to Liquid Fuels via CuO Cathode, ACS Sustain. Chem. Eng. 7 (2018) 1250–1259. https://doi.org/10.1021/ACSSUSCHEMENG.8B04917.

[66] Y. Zhang, Q. Pei, J. Liang, T. Feng, X. Zhou, H. Mao, W. Zhang, Y. Hisaeda, X.M. Song, Mesoporous TiO2-Based Photoanode Sensitized by BiOI and Investigation of Its Photovoltaic Behavior, Langmuir 31 (2015) 10279–10284. https://doi.org/10.1021/ACS.LANGMUIR.5B02248.

[67] Y. Zuo, Y. Liu, J. Li, R. Du, X. Yu, C. Xing, T. Zhang, L. Yao, J. Arbiol, J. Llorca, K.

Sivula, N. Guijarro, A. Cabot, Solution-Processed Ultrathin SnS2–Pt Nanoplates for Photoelectrochemical Water Oxidation, ACS Appl. Mater. Interfaces 11 (2019) 6918–6926. https://doi.org/10.1021/ACSAMI.8B17622.

[68] M.D. Sharma, C. Mahala, M. Basu, Photoelectrochemical Water Splitting by In2S3/In2O3 Composite Nanopyramids, ACS Appl. Nano Mater. 3 (2020) 11638–11649. https://doi.org/10.1021/ACSANM.0C02876.

[69] G. Sreedhar, A. Sivanantham, S. Venkateshwaran, S.K. Panda, M. Eashwar, Enhanced photoelectrochemical performance of CdSe quantum dot sensitized SrTiO3, J. Mater. Chem. A 3 (2015) 13476–13482. https://doi.org/10.1039/C5TA00304K.

[70] C. Lu, M. Luo, W. Dong, Y. Ge, T. Han, Y. Liu, X. Xue, N. Ma, Y. Huang, Y. Zhou, X. Xu, Bi2Te3/Bi2Se3/Bi2S3 Cascade Heterostructure for Fast-Response and High-Photoresponsivity Photodetector and High-Efficiency Water Splitting with a Small Bias Voltage, Adv. Sci. 10 (2023) 2205460. https://doi.org/10.1002/ADVS.202205460.

[71] A.N. Pinheiro, E.G.S. Firmiano, A.C. Rabelo, C.J. Dalmaschio, E.R. Leite, Revisiting SrTiO3 as a photoanode for water splitting: development of thin films with enhanced charge separation under standard solar irradiation, RSC Adv. 4 (2013) 2029–2036. https://doi.org/10.1039/C3RA45066J.

[72] Y. Liu, J. Quiñonero, L. Yao, X. Da Costa, M. Mensi, R. Gómez, K. Sivula, N. Guijarro, Defect engineered nanostructured LaFeO3 photoanodes for improved activity in solar water oxidation, J. Mater. Chem. A 9 (2021) 2888–2898. https://doi.org/10.1039/D0TA11541J.

[73] M. Gunawan, O. Bowdler, S. Zhou, X. Fang, Q. Zhang, Y. Sakamoto, K. Sun, D. Gunawan, S.L.Y. Chang, R. Amal, N. Valanoor, J. Scott, J.N. Hart, C.Y. Toe, Ferroelectric Polarization-Induced Performance Enhancements in BiFeO3/BiVO4 Photoanodes for Photoelectrochemical Water Splitting, Adv. Funct. Mater. 35 (2025) 2417651. https://doi.org/10.1002/ADFM.202417651.

[74] L. Polak, J.H. Rector, M.J. Slaman, R.J. Wijngaarden, NaTaO3 Photoanode for Bias-Free Water Splitting: A Photo-Electrochemical and Kelvin Probe Surface Photovoltage Study, J. Phys. Chem. C 120 (2016) 23559–23565. https://doi.org/10.1021/ACS.JPCC.6B07247.

[75] S.Y. Chae, E.S. Lee, H. Jung, Y.J. Hwang, O.S. Joo, Synthesis of Bi2WO6 photoanode on transparent conducting oxide substrate with low onset potential for solar water splitting, RSC Adv. 4 (2014) 24032–24037. https://doi.org/10.1039/C4RA02868F.

[76] N. Cheng, L. Kanzler, Y. Jiang, A.M. Mingers, M. Weiss, C. Scheu, R. Marschall, S. Zhang, Activity and Stability of ZnFe2O4 Photoanodes under Photoelectrochemical Conditions, ACS Catal. 14 (2024) 10789–10795. https://doi.org/10.1021/ACSCATAL.4C02186.

[77] S. Singh, N. Khare, Low field magneto-tunable photocurrent in CoFe2O4 nanostructure films for enhanced photoelectrochemical properties, Sci. Reports 2018 81 8 (2018) 6522-. https://doi.org/10.1038/s41598-018-24947-2.

[78] S.K. Jang, S.H. Jeong, A. Hong, W.Y. Sohn, Mitigation of the Anodic Shift of the Onset Potential in a TiO2/α-Fe2O3 Photoanode by Inserting a Nickel Ferrite (NiFe2O4) Blocking Layer, ACS Omega 10 (2025) 57407–57417. https://doi.org/10.1021/ACSOMEGA.5C07668.

[79] Y. Liu, F. Le Formal, F. Boudoire, L. Yao, K. Sivula, N. Guijarro, Insights into the interfacial carrier behaviour of copper ferrite (CuFe2O4) photoanodes for solar water oxidation, J. Mater. Chem. A 7 (2019) 1669–1677. https://doi.org/10.1039/C8TA11160J.

[80] Y. Hou, F. Zuo, A. Dagg, P. Feng, A three-dimensional branched cobalt-doped α-Fe2O 3 nanorod/MgFe2O4 heterojunction array as a flexible photoanode for efficient photoelectrochemical water oxidation, Angew. Chemie - Int. Ed. 52 (2013) 1248–1252. https://doi.org/10.1002/ANIE.201207578.

[81] M. Wtulich, A. Skwierawska, S. Ibragimov, A. Lisowska–Oleksiak, Exploring the role of

carbon nitrides (melem, melon, g-C3N4) in enhancing photoelectrocatalytic properties of TiO2 nanotubes for water electrooxidation, Appl. Surf. Sci. 685 (2025) 161994. https://doi.org/10.1016/J.APSUSC.2024.161994.

[82] H. Chai, S. Wang, X. Wang, J. Ma, J. Jin, Modulation of the Chemical Microenvironment at the Hematite-Based Photoanode Interface with a Covalent Triazine Framework for Efficient Photoelectrochemical Water Oxidation, ACS Catal. 12 (2022) 3700–3709. https://doi.org/10.1021/ACSCATAL.2C00285.

[83] C. Lin, Z. Shan, C. Dong, Y. Lu, W. Meng, G. Zhang, B. Cai, G. Su, J.H. Park, K. Zhang, Covalent organic frameworks bearing Ni active sites for free radical-mediated photoelectrochemical organic transformations, Sci. Adv. 9 (2023). https://doi.org/10.1126/SCIADV.ADI9442.

[84] W. Ni, S. Zhang, L. Cheng, T. Luo, H. Yang, T. Duan, D. Yan, Construction of MIL-88(Fe) derived MOF/TiO2 photoanode for efficient photoelectrochemical water splitting, J. Environ. Chem. Eng. 12 (2024) 113683. https://doi.org/10.1016/J.JECE.2024.113683.

[85] S. Zhang, C. Yin, Z. Kang, P. Wu, J. Wu, Z. Zhang, Q. Liao, J. Zhang, Y. Zhang, Graphdiyne Nanowall for Enhanced Photoelectrochemical Performance of Si Heterojunction Photoanode, ACS Appl. Mater. Interfaces 11 (2018) 2745–2749. https://doi.org/10.1021/ACSAMI.8B06382.

[86] M. Radecka, M. Rekas, A. Trenczek-Zajac, K. Zakrzewska, Importance of the band gap energy and flat band potential for application of modified TiO2 photoanodes in water photolysis, J. Power Sources 181 (2008) 46–55. https://doi.org/10.1016/j.jpowsour.2007.10.082.

[87] M. Ashrafuzzaman, A. Kalam, A.G. Al-Sehemi, P. Yadav, M. Dubey, A review of photoanode materials, challenges, and outlook of dye-sensitized solar cells, J. Power Sources 638 (2025). https://doi.org/10.1016/j.jpowsour.2025.236636.

[88] U. Diebold, The surface science of titanium dioxide, Surf. Sci. Rep. 48 (2002) 53–229. http://linkinghub.elsevier.com/retrieve/pii/S0167572902001000.

[89] P. Sharma, J.W. Jang, J.S. Lee, Key Strategies to Advance the Photoelectrochemical Water Splitting Performance of α-Fe2O3 Photoanode, ChemCatChem 11 (2019) 157–179. https://doi.org/10.1002/cctc.201801187.

[90] M. Szkoda, A. Lisowska-Oleksiak, K. Siuzdak, Optimization of boron-doping process of titania nanotubes via electrochemical method toward enhanced photoactivity, J. Solid State Electrochem. 2016 206 20 (2016) 1765–1774. https://doi.org/10.1007/S10008-016-3185-8.

[91] S. Zhang, D. Chen, Z. Liu, M. Ruan, Z. Guo, Novel strategy for efficient water splitting through pyro-electric and pyro-photo-electric catalysis of BaTiO3 by using thermal resource and solar energy, Appl. Catal. B Environ. 284 (2021) 119686. https://doi.org/10.1016/J.APCATB.2020.119686.

[92] M. Radecka, P. Sobas, M. Wierzbicka, M. Rekas, Photoelectrochemical properties of undoped and Ti-doped WO3, Phys. B Condens. Matter 364 (2005) 85–92. https://doi.org/10.1016/J.PHYSB.2005.03.039.

[93] X. Yang, A. Wolcott, G. Wang, A. Sobo, R.C. Fitzmorris, F. Qian, J.Z. Zhang, Y. Li, Nitrogen-Doped ZnO Nanowire Arrays for Photoelectrochemical Water Splitting, Nano Lett. 9 (2009) 2331–2336. https://doi.org/10.1021/NL900772Q.

[94] B. Zhang, M. Ruan, C. Wang, Z. Guo, Z. Liu, Enhanced photoelectrochemical performance of α-Fe2O3 photoanode modified with NiCo layered double hydroxide, J. Electroanal. Chem. 936 (2023) 117388. https://doi.org/10.1016/J.JELECHEM.2023.117388.

[95] L.M. Wolz, G. Grötzner, T. Rieth, L.I. Wagner, M. Kuhl, J. Dittloff, G. Zhou, S. Santra, V. Streibel, F. Munnik, I.D. Sharp, J. Eichhorn, Impact of Defects and Disorder on the Stability of Ta3N5 Photoanodes, Adv. Funct. Mater. 34 (2024) 2405532. https://doi.org/10.1002/ADFM.202405532.

[96] M. Ruan, X. Cai, Y. Lan, H. Xing, Hexagonal CdS photoanode modified with Pt and cobalt phosphate cocatalyst for efficient photoelectrochemical performance, Mater. Lett. 260 (2020) 126947. https://doi.org/10.1016/J.MATLET.2019.126947.

[97] M. Ibrahim, M. Zayed, A.M. Ahmed, M.A. Ghanem, M. Shaban, S. Abd Elkhalik, F. Mohamed, Synthesis and characterization of Mo-doped PbS thin films for enhancing the photocatalytic hydrogen production, Mater. Chem. Phys. 315 (2024) 128962. https://doi.org/10.1016/J.MATCHEMPHYS.2024.128962.

[98] D. Roda, K. Trzciński, M. Sawczak, A. Ilnicka, M. Łapiński, M. Szkoda, A.P. Nowak, ZnIn2S4 thin films grown by pulsed laser deposition: Effect of electrolyte and illumination conditions on photoanode performance, Appl. Surf. Sci. 708 (2025) 163694. https://doi.org/10.1016/J.APSUSC.2025.163694.

[99] Q. Lu, Y. Yu, Q. Ma, B. Chen, H. Zhang, 2D Transition-Metal-Dichalcogenide-Nanosheet-Based Composites for Photocatalytic and Electrocatalytic Hydrogen Evolution Reactions, Adv. Mater. 28 (2016) 1917–1933. https://doi.org/10.1002/adma.201503270.

[100] G. Hitoki, A. Ishikawa, T. Takata, J.N. Kondo, M. Hara, K. Domen, Ta3N5 as a Novel Visible Light-Driven Photocatalyst (λ<600 nm), Http://Dx.Doi.Org/10.1246/Cl.2002.736 (2002) 736–737. https://doi.org/10.1246/CL.2002.736.

[101] Z. Su, L. Wang, S. Grigorescu, K. Lee, P. Schmuki, Hydrothermal growth of highly oriented single crystalline Ta2O5 nanorod arrays and their conversion to Ta3N5 for efficient solar driven water splitting, Chem. Commun. 50 (2014) 15561–15564. https://doi.org/10.1039/C4CC05673F.

[102] S. Grigorescu, S. So, J.E. Yoo, A. Mazare, R. Hahn, P. Schmuki, Open top anodic Ta3N5 nanotubes for higher solar water splitting efficiency, Electrochim. Acta 182 (2015) 803–808. https://doi.org/10.1016/J.ELECTACTA.2015.09.159.

[103] W. Wei, J.M. Macak, P. Schmuki, High aspect ratio ordered nanoporous Ta2O5 films by anodization of Ta, Electrochem. Commun. 10 (2008) 428–432. https://doi.org/10.1016/J.ELECOM.2008.01.004.

[104] D. Yokoyama, H. Hashiguchi, K. Maeda, T. Minegishi, T. Takata, R. Abe, J. Kubota, K. Domen, Ta3N5 photoanodes for water splitting prepared by sputtering, Thin Solid Films 519 (2011) 2087–2092. https://doi.org/10.1016/J.TSF.2010.10.055.

[105] V. Nandal, Y. Pihosh, T. Higashi, T. Minegishi, T. Yamada, K. Seki, M. Sugiyama, K. Domen, Probing fundamental losses in nanostructured Ta3N5photoanodes: Design principles for efficient water oxidation, Energy Environ. Sci. 14 (2021) 4038–4047. https://doi.org/10.1039/D1EE01004B.

[106] K. Lehovec, Lattice structure of β-Ta2O5, J. Less Common Met. 7 (1964) 397–410. https://doi.org/10.1016/0022-5088(64)90036-0.

[107] Z. Liu, X. Wang, Q. Cai, C. Ma, Z. Tong, CaBi6O10: a novel promising photoanode for photoelectrochemical water oxidation, J. Mater. Chem. A 5 (2017) 8545–8554. https://doi.org/10.1039/C7TA01875D.

[108] D. Chen, Z. Liu, Efficient Indium Sulfide Photoelectrode with Crystal Phase and Morphology Control for High-Performance Photoelectrochemical Water Splitting, ACS Sustain. Chem. Eng. 6 (2018) 12328–12336. https://doi.org/doi.org/10.1021/acssuschemeng.8b02801.

[109] X. Lu, Z. Liu, J. Li, J. Zhang, Z. Guo, Novel framework g-C3N4 film as efficient photoanode for photoelectrochemical water splitting, Appl. Catal. B Environ. 209 (2017) 657–662. https://doi.org/10.1016/J.APCATB.2017.03.030.

[110] D. Chen, Z. Liu, Dual-Axial Gradient Doping (Zr and Sn) on Hematite for Promoting Charge Separation in Photoelectrochemical Water Splitting, ChemSusChem 11 (2018) 3438–3448. https://doi.org/10.1002/CSSC.201801614.

[111] X.-T. Xu, L. Pan, X. Zhang, L. Wang, J.-J. Zou, X. Xu, L. Pan, X. Zhang, L. Wang, J. Zou, Rational Design and Construction of Cocatalysts for Semiconductor-Based Photo-

Electrochemical Oxygen Evolution: A Comprehensive Review, Adv. Sci. 6 (2019) 1801505. https://doi.org/10.1002/ADVS.201801505.

[112] P.A. Cox, The electronic structure and chemistry of solids, (1987) 259. https://global.oup.com/academic/product/the-electronic-structure-and-chemistry-of-solids-9780198552048 (accessed August 28, 2022).

[113] K.T. Fountaine, H.J. Lewerenz, H.A. Atwater, Efficiency limits for photoelectrochemical water-splitting, Nat. Commun. 2016 71 7 (2016) 13706-. https://doi.org/10.1038/ncomms13706.

[114] A. Tofanello, S. Shen, F.L. De Souza, L. Vayssieres, Strategies to improve the photoelectrochemical performance of hematite nanorod-based photoanodes, APL Mater. 8 (2020) 040905. https://doi.org/10.1063/5.0003146.

[115] S. Peng, D. Liu, Z. Ying, K. An, C. Liu, W.F. Ip, K.H. Lo, H. Pan, Bridge Layer–Enabled Silicon-Based Photoanode With High Photocurrent Density for Efficient and Stable Water Splitting, Carbon Energy 7 (2025) n/a-n/a. https://doi.org/10.1002/CEY2.70052.

[116] M.L. Inche Ibrahim, A.A. Zakhidov, An improved model for describing the net carrier recombination rate in semiconductor devices, Appl. Phys. A Mater. Sci. Process. 128 (2022) 1–11. https://doi.org/10.1007/S00339-021-05104-5/FIGURES/4.

[117] S. Corby, R.R. Rao, L. Steier, J.R. Durrant, The kinetics of metal oxide photoanodes from charge generation to catalysis, Nat. Rev. Mater. 2021 612 6 (2021) 1136–1155. https://doi.org/10.1038/s41578-021-00343-7.

[118] Y. Matsumoto, Energy Positions of Oxide Semiconductors and Photocatalysis with Iron Complex Oxides, J. Solid State Chem. 126 (1996) 227–234. https://doi.org/10.1006/JSSC.1996.0333.

[119] X.-X. Xue, H. Meng, Z. Huang, al -, J.O. Majasan, J.B. Robinson, R.E. Owen, Y. Liu, J. Zhang, N. Bodappa, S. Bera, D. Sengupta, S. Roy, K. Mukherjee, Research into dye-sensitized solar cells: a review highlighting progress in India, J. Phys. Energy 3 (2021) 032013. https://doi.org/10.1088/2515-7655/ABFF6C.

[120] L.O.A. Salim, M.Z. Muzakkar, A. Zaeni, M. Maulidiyah, M. Nurdin, S.N. Sadikin, J. Ridwan, A.A. Umar, Improved photoactivity of TiO2 photoanode of dye-sensitized solar cells by sulfur doping, J. Phys. Chem. Solids 175 (2023) 111224. https://doi.org/10.1016/J.JPCS.2023.111224.

[121] K. Magiswaran, M.N. Norizan, I.S. Mohamad, N. Mahmed, S.N. Idris, S.A. Sobri, Charge Recombination in Zinc Oxide-Based Dye-Sensitized Solar Cell: A Mini Review, Int. J. Nanoelectron. Mater. 14 (2021) 59–66. https://www.scopus.com/pages/publications/85126083395 (accessed January 18, 2026).

[122] Q. Yi, H. Wang, J.M. Lee, BiVO4-Based Photoelectrochemical Water Splitting, ChemElectroChem 12 (2025) e202400600. https://doi.org/10.1002/CELC.202400600;WGROUP:STRING:PUBLICATION.

[123] K.H. Ye, H. Li, D. Huang, S. Xiao, W. Qiu, M. Li, Y. Hu, W. Mai, H. Ji, S. Yang, Enhancing photoelectrochemical water splitting by combining work function tuning and heterojunction engineering, Nat. Commun. 2019 101 10 (2019) 3687-. https://doi.org/10.1038/s41467-019-11586-y.

[124] S.M. Yong, T. Nikolay, B.T. Ahn, D.K. Kim, One-dimensional WO3 nanorods as photoelectrodes for dye-sensitized solar cells, J. Alloys Compd. 547 (2013) 113–117. https://doi.org/10.1016/J.JALLCOM.2012.08.124.

[125] K. Hara, Z.G. Zhao, Y. Cui, M. Miyauchi, M. Miyashita, S. Mori, Nanocrystalline Electrodes Based on Nanoporous-Walled WO3 Nanotubes for Organic-Dye-Sensitized Solar Cells, Langmuir 27 (2011) 12730–12736. https://doi.org/10.1021/LA201639F.

[126] P. Jayabal, V. Sasirekha, J. Mayandi, K. Jeganathan, V. Ramakrishnan, A facile hydrothermal synthesis of SrTiO3 for dye sensitized solar cell application, J. Alloys Compd. 586 (2014) 456–461. https://doi.org/10.1016/J.JALLCOM.2013.10.012.

[127] S. Gholamrezaei, M. Salavati Niasari, M. Dadkhah, B. Sarkhosh, New modified sol–gel method for preparation SrTiO3 nanostructures and their application in dye-sensitized solar cells, J. Mater. Sci. Mater. Electron. 2015 271 27 (2015) 118–125. https://doi.org/10.1007/S10854-015-3726-4.

[128] X. Wang, Y.F. Wang, Q.P. Luo, J.H. Ren, D.J. Li, X.F. Li, Highly uniform hierarchical Zn2SnO4 microspheres for the construction of high performance dye-sensitized solar cells, RSC Adv. 7 (2017) 43403–43409. https://doi.org/10.1039/C7RA06906E.

[129] M.M. Jaculine, C.J. Raj, H.J. Kim, A.J. Rajendran, S.J. Das, Zinc stannate nanoflower (Zn2SnO4) photoanodes for efficient dye sensitized solar cells, Mater. Sci. Semicond. Process. 25 (2014) 52–58. https://doi.org/10.1016/J.MSSP.2013.11.003.

[130] J.M. Macak, H. Tsuchiya, L. Taveira, S. Aldabergerova, P. Schmuki, S. Aldabergerova, P. Schmuki,] We, A. Friedrich, H. Hildebrand, Smooth Anodic TiO2 Nanotubes, Angew. Chemie Int. Ed. 44 (2005) 7463–7465. https://doi.org/10.1002/ANIE.200502781.

[131] X. Zheng, Y. Yang, C. Fang, X. Liu, Stability of oxygen vacancies at metal/oxide interfaces, Phys. Chem. Chem. Phys. 25 (2023) 19970–19975. https://doi.org/10.1039/D3CP00765K.

[132] U. Diebold, The surface science of titanium dioxide, Surf. Sci. Rep. 48 (2003) 53–229. https://doi.org/10.1016/S0167-5729(02)00100-0.

[133] A. Lisowska-Oleksiak, K. Szybowska, V. Jasulaitiené, Preparation and characterisation of visible light responsive iodine doped TiO2 electrodes, Electrochim. Acta 55 (2010) 5881–5885. https://doi.org/10.1016/J.ELECTACTA.2010.05.039.

[134] K. Siuzdak, M. Szkoda, M. Sawczak, A. Lisowska-Oleksiak, J. Karczewski, J. Ryl, Enhanced photoelectrochemical and photocatalytic performance of iodine-doped titania nanotube arrays, RSC Adv. 5 (2015) 50379–50391. https://doi.org/10.1039/C5RA08407E.

[135] D. Nunes, E. Fortunato, R. Martins, Flexible nanostructured TiO2-based gas and UV sensors: a review, Discov. Mater. 2022 21 2 (2022) 2-. https://doi.org/10.1007/S43939-022-00023-5.

[136] T. Kasuga, M. Hiramatsu, A. Hoson, T. Sekino, K. Niihara, Formation of Titanium Oxide Nanotube, Langmuir 14 (1998) 3160–3163. https://doi.org/10.1021/LA9713816.

[137] V. Zwilling, M. Aucouturier, E. Darque-Ceretti, Anodic oxidation of titanium and TA6V alloy in chromic media. An electrochemical approach, Electrochim. Acta 45 (1999) p.921-929. https://doi.org/10.1016/S0013-4686(99)00283-2.

[138] D. Gong, C.A. Grimes, O.K. Varghese, W. Hu, R.S. Singh, Z. Chen, E.C. Dickey, Titanium oxide nanotube arrays prepared by anodic oxidation, J. Mater. Res. 2001 1612 16 (2011) 3331–3334. https://doi.org/10.1557/JMR.2001.0457.

[139] J.H. Jung, H. Kobayashi, K.J.C. Van Bommel, S. Shinkai, T. Shimizu, Creation of Novel Helical Ribbon and Double-Layered Nanotube TiO2 Structures Using an Organogel Template, Chem. Mater. 14 (2002) 1445–1447. https://doi.org/10.1021/CM011625E.

[140] V. Madurai Ramakrishnan, M. N., B. P., S. Pitchaiya, D. Velauthapillai, A. Pugazhendhi, Transformation of TiO2 nanoparticles to nanotubes by simple solvothermal route and its performance as dye-sensitized solar cell (DSSC) photoanode, Int. J. Hydrogen Energy 45 (2020) 15441–15452. https://doi.org/10.1016/J.IJHYDENE.2020.04.021.

[141] T. Luttrell, S. Halpegamage, J. Tao, A. Kramer, E. Sutter, M. Batzill, Why is anatase a better photocatalyst than rutile? - Model studies on epitaxial TiO2 films, Sci. Reports 2014 41 4 (2014) 1–8. https://doi.org/10.1038/srep04043.

[142] M.Á. López Zavala, S.A. Lozano Morales, M. Ávila-Santos, Synthesis of stable TiO2 nanotubes: effect of hydrothermal treatment, acid washing and annealing temperature, Heliyon 3 (2017) e00456. https://doi.org/10.1016/J.HELIYON.2017.E00456.

[143] A. Tighineanu, T. Ruff, S. Albu, R. Hahn, P. Schmuki, Conductivity of TiO2 nanotubes: Influence of annealing time and temperature, Chem. Phys. Lett. 494 (2010) 260–263.

https://doi.org/10.1016/J.CPLETT.2010.06.022.

[144] S.P. Albu, H. Tsuchiya, S. Fujimoto, P. Schmuki, TiO2 Nanotubes – Annealing Effects on Detailed Morphology and Structure, Eur. J. Inorg. Chem. 2010 (2010) 4351–4356. https://doi.org/10.1002/EJIC.201000608.

[145] A. El Ruby Mohamed, S. Rohani, Modified TiO2 nanotube arrays (TNTAs): progressive strategies towards visible light responsive photoanode, a review, Energy Environ. Sci. 4 (2011) 1065–1086. https://doi.org/10.1039/C0EE00488J.

[146] A. El Ruby Mohamed, S. Rohani, Modified TiO2 nanotube arrays (TNTAs): progressive strategies towards visible light responsive photoanode, a review, Energy Environ. Sci. 4 (2011) 1065–1086. https://doi.org/10.1039/C0EE00488J.

[147] G.K. Mor, O.K. Varghese, M. Paulose, N. Mukherjee, C.A. Grimes, Fabrication of tapered, conical-shaped titania nanotubes, J. Mater. Res. 2003 1811 18 (2003) 2588–2593. https://doi.org/10.1557/JMR.2003.0362.

[148] D. Kowalski, D. Kim, P. Schmuki, TiO2 nanotubes, nanochannels and mesosponge: Self-organized formation and applications, Nano Today 8 (2013) 235–264. https://doi.org/10.1016/J.NANTOD.2013.04.010.

[149] M. Jarosz, A. Pawlik, M. Szuwarzyński, M. Jaskuła, G.D. Sulka, Nanoporous anodic titanium dioxide layers as potential drug delivery systems: Drug release kinetics and mechanism, Colloids Surfaces B Biointerfaces 143 (2016) 447–454. https://doi.org/10.1016/J.COLSURFB.2016.03.073.

[150] M.B. Hanif, M. Sihor, V. Liapun, H. Makarov, O. Monfort, M. Motola, Porous vs. Nanotubular Anodic TiO2: Does the Morphology Really Matters for the Photodegradation of Caffeine?, Coatings 2022, Vol. 12, Page 1002 12 (2022) 1002. https://doi.org/10.3390/COATINGS12071002.

[151] F. Riboni, N.T. Nguyen, S. So, P. Schmuki, Aligned metal oxide nanotube arrays: key-aspects of anodic TiO2 nanotube formation and properties, Nanoscale Horizons 1 (2016) 445–466. https://doi.org/10.1039/C6NH00054A.

[152] X. Wang, L. Sun, S. Zhang, X. Wang, Ultralong, Small-Diameter TiO2 Nanotubes Achieved by an Optimized Two-Step Anodization for Efficient Dye-Sensitized Solar Cells, ACS Appl. Mater. Interfaces 6 (2014) 1361–1365. https://doi.org/10.1021/AM404966E.

[153] Ł. Haryński, K. Grochowska, J. Karczewski, J. Ryl, K. Siuzdak, Scalable Route toward Superior Photoresponse of UV-Laser-Treated TiO2 Nanotubes, ACS Appl. Mater. Interfaces 12 (2020) 3225–3235. https://doi.org/10.1021/acsami.9b19206.

[154] M. Wtulich, M. Szkoda, G. Gajowiec, K. Jurak, G. Trykowski, A. Lisowska-Oleksiak, Hydrothermal modification of TiO2 nanotubes in water and alkali metal electrolytes (LiNO3, NaNO3, KNO3) – Direct evidence for photocatalytic activity enhancement, Electrochim. Acta 426 (2022). https://doi.org/10.1016/j.electacta.2022.140802.

[155] J. Yu, G. Dai, B. Cheng, Effect of crystallization methods on morphology and photocatalytic activity of anodized TiO2 nanotube array films, J. Phys. Chem. C 114 (2010) 19378–19385. https://doi.org/10.1021/jp106324x.

[156] D. Wang, L. Liu, F. Zhang, K. Tao, E. Pippel, K. Domen, Spontaneous phase and morphology transformations of anodized titania nanotubes induced by water at room temperature, Nano Lett. 11 (2011) 3649–3655. https://doi.org/10.1021/NL2015262.

[157] C. Cao, J. Yan, Y. Zhang, L. Zhao, Stability of titania nanotube arrays in aqueous environment and the related factors, Sci. Reports 2016 61 6 (2016) 1–8. https://doi.org/10.1038/srep23065.

[158] S. Ng, H. Sopha, R. Zazpe, Z. Spotz, V. Bijalwan, F. Dvorak, L. Hromadko, J. Prikryl, J.M. Macak, TiO2 ALD coating of amorphous TiO2 nanotube layers: Inhibition of the structural and morphological changes due to water annealing, Front. Chem. 7 (2019) 38. https://doi.org/10.3389/FCHEM.2019.00038.

[159] A.B. Tesler, M. Altomare, P. Schmuki, Morphology and Optical Properties of Highly Ordered TiO2Nanotubes Grown in NH4F/ o-H3PO4Electrolytes in View of Light-Harvesting and Catalytic Applications, ACS Appl. Nano Mater. 3 (2020) 10646–10658. https://doi.org/10.1021/ACSANM.0C01859.

[160] F. Fu, G. Cha, N. Denisov, Y. Chen, Y. Zhang, P. Schmuki, Water Annealing of TiO2 Nanotubes for Photocatalysis Revisited, ChemElectroChem 7 (2020) 2792–2796. https://doi.org/10.1002/CELC.202000622.

[161] N. Liu, S.P. Albu, K. Lee, S. So, P. Schmuki, Water annealing and other low temperature treatments of anodic TiO2 nanotubes: A comparison of properties and efficiencies in dye sensitized solar cells and for water splitting, Electrochim. Acta 82 (2012) 98–102. https://doi.org/10.1016/J.ELECTACTA.2012.06.006.

[162] Y. Xu, M. Wang, N. Hu, J. Bell, C. Yan, Atomistic investigation into the mechanical behaviour of crystalline and amorphous TiO2 nanotubes, RSC Adv. 6 (2016) 28121–28129. https://doi.org/10.1039/C5RA27268H.

[163] S. Durdu, G. Cihan, E. Yalcin, A. Altinkok, Characterization and mechanical properties of TiO2 nanotubes formed on titanium by anodic oxidation, Ceram. Int. 47 (2021) 10972–10979. https://doi.org/10.1016/J.CERAMINT.2020.12.218.

[164] K. Arkusz, A. Jędrzejewska, P. Siwak, M. Jurczyk, Electrochemical and Mechanical Properties of Hexagonal Titanium Dioxide Nanotubes Formed by Sonoelectrochemical Anodization, Mater. 2024, Vol. 17, Page 2138 17 (2024) 2138. https://doi.org/10.3390/MA17092138.

[165] R. Asahi, T. Morikawa, T. Ohwaki, K. Aoki, Y. Taga, Visible-Light Photocatalysis in Nitrogen-Doped Titanium Oxides, Science (80-.). 293 (2001) 269–271. https://doi.org/10.1126/SCIENCE.1061051.

[166] Q. Wang, Y.Z. Pan, S.S. Huang, S.T. Ren, P. Li, J.J. Li, Resistive and capacitive response of nitrogen-dopedTiO2 nanotubes film humidity sensor, Nanotechnology 22 (2010) 025501. https://doi.org/10.1088/0957-4484/22/2/025501.

[167] G. Liu, F. Li, D.W. Wang, D.M. Tang, C. Liu, X. Ma, G.Q. Lu, H.M. Cheng, Electron field emission of a nitrogen-dopedTiO2 nanotube array, Nanotechnology 19 (2007) 025606. https://doi.org/10.1088/0957-4484/19/02/025606.

[168] M. Szkoda, A. Lisowska-Oleksiak, K. Siuzdak, Optimization of boron-doping process of titania nanotubes via electrochemical method toward enhanced photoactivity, J Solid State Electrochem 20 (2016) 1765–1774.

[169] X. Peng, J. Fu, X. Zhang, Y. Li, M. Huang, K. Huo, P.K. Chu, Carbon-doped tio2 nanotube array platform for visible photocatalysis, Nanosci. Nanotechnol. Lett. 5 (2013) 1251–1257. https://doi.org/10.1166/NNL.2013.1681.

[170] J.H. Park, S. Kim, A.J. Bard, Novel carbon-doped TiO 2 nanotube arrays with high aspect ratios for efficient solar water splitting, Nano Lett. 6 (2006) 24–28. https://doi.org/10.1021/NL051807Y.

[171] C. Yang, S. Shang, X. yan Li, Fabrication of sulfur-doped TiO2 nanotube array as a conductive interlayer of PbO2 anode for efficient electrochemical oxidation of organic pollutants, Sep. Purif. Technol. 258 (2021) 118035. https://doi.org/10.1016/J.SEPPUR.2020.118035.

[172] D. Sabaghi, M. Madian, A. Omar, S. Oswald, M. Uhlemann, M. Maghrebi, M. Baniadam, D. Mikhailova, Directly Anodized Sulfur-Doped TiO2 Nanotubes as Improved Anodes for Li-ion Batteries, Batter. 2020, Vol. 6, Page 51 6 (2020) 51. https://doi.org/10.3390/BATTERIES6040051.

[173] M. Szkoda, K. Siuzdak, A. Lisowska-Oleksiak, J. Karczewski, J. Ryl, Facile preparation of extremely photoactive boron-doped TiO2 nanotubes arrays, Electrochem. Commun. 60 (2015) 212–215. https://doi.org/10.1016/J.ELECOM.2015.09.013.

[174] K. Siuzdak, M. Szkoda, M. Sawczak, A. Lisowska-Oleksiak, Novel nitrogen precursors for electrochemically driven doping of titania nanotubes exhibiting enhanced

photoactivity, New J. Chem. 39 (2015) 2741–2751. https://doi.org/10.1039/C5NJ00127G.

[175] D.D. Qin, Q.H. Wang, J. Chen, C.H. He, Y. Li, C.H. Wang, J.J. Quan, C.L. Tao, X.Q. Lu, Phosphorus-doped TiO2 nanotube arrays for visible-light-driven photoelectrochemical water oxidation, Sustain. Energy Fuels 1 (2017) 248–253. https://doi.org/10.1039/C6SE00045B.

[176] M.A. Mutalib, N.A. Ludin, M.S. Su'ait, M. Davies, S. Sepeai, M.A.M. Teridi, M.F.M. Noh, M.A. Ibrahim, Performance-Enhancing Sulfur-Doped TiO2 Photoanodes for Perovskite Solar Cells, Appl. Sci. 2022, Vol. 12, Page 429 12 (2022) 429. https://doi.org/10.3390/APP12010429.

[177] D. Zhang, J. Chen, Q. Xiang, Y. Li, M. Liu, Y. Liao, Transition-Metal-Ion (Fe, Co, Cr, Mn, Etc.) Doping of TiO2 Nanotubes: A General Approach, Inorg. Chem. 58 (2019) 12511–12515. https://doi.org/10.1021/acs.inorgchem.9b01889.

[178] N. V. Lebukhova, N.F. Karpovich, S.A. Pyachin, E.A. Kirichenko, K.S. Makarevich, M.A. Pugachevskii, Synthesis and optic properties of titanium dioxide nanostructures doped with alkali metals, Theor. Found. Chem. Eng. 51 (2017) 820–824. https://doi.org/10.1134/S0040579517050141.

[179] Y.C. Nah, I. Paramasivam, P. Schmuki, Doped TiO2 and TiO2 nanotubes: Synthesis and applications, ChemPhysChem 11 (2010) 2698–2713. https://doi.org/10.1002/CPHC.201000276.

[180] P. Jiang, W. Xiang, J. Kuang, W. Liu, W. Cao, Effect of cobalt doping on the electronic, optical and photocatalytic properties of TiO2, Solid State Sci. 46 (2015) 27–32. https://doi.org/10.1016/J.SOLIDSTATESCIENCES.2015.05.007.

[181] T. Mishra, L. Wang, R. Hahn, P. Schmuki, In-situ Cr doped anodized TiO2 nanotubes with increased photocurrent response, Electrochim. Acta 132 (2014) 410–415. https://doi.org/10.1016/j.electacta.2014.03.101.

[182] M.M. Fadlallah, U. Eckern, Electronic and optical properties of metal-doped TiO2nanotubes: Spintronic and photocatalytic applications, New J. Phys. 22 (2020). https://doi.org/10.1088/1367-2630/abae87.

[183] Z. Dong, D. Ding, T. Li, C. Ning, Ni-doped TiO2 nanotubes photoanode for enhanced photoelectrochemical water splitting, Appl. Surf. Sci. 443 (2018) 321–328. https://doi.org/10.1016/J.APSUSC.2018.03.031.

[184] W.C. Guaglianoni, C.L. Florence, F. Bonatto, J. Venturini, S. Arcaro, A.K. Alves, C.P. Bergmann, Novel nanoarchitectured cobalt-doped TiO2 and carbon nanotube arrays: Synthesis and photocurrent performance, Ceram. Int. 45 (2019) 2439–2445. https://doi.org/10.1016/J.CERAMINT.2018.10.169.

[185] M.M. Momeni, Y. Ghayeb, Photoelectrochemical water splitting on chromium-doped titanium dioxide nanotube photoanodes prepared by single-step anodizing, J. Alloys Compd. 637 (2015) 393–400. https://doi.org/10.1016/J.JALLCOM.2015.02.137.

[186] M. Zhang, D. Lu, Z. Zhang, J. Yang, Enhancement of Visible-Light-Induced Photocurrent and Photocatalytic Activity of V and N Codoped TiO 2 Nanotube Array Films , J. Electrochem. Soc. 161 (2014) H416–H421. https://doi.org/10.1149/2.119406JES.

[187] M.M. Momeni, P. Zeinali, Photochemical Deposition of Ag, Cu, Cu@Ag, and Ag@Cu on TiO2 Nanotubes and their Optical Properties and Photoelectrochemical Activity, J. Electron. Mater. 50 (2021) 5810–5818. https://doi.org/10.1007/S11664-021-09090-5/TABLES/1.

[188] D. Gogoi, A. Namdeo, A.K. Golder, N.R. Peela, Ag-doped TiO2 photocatalysts with effective charge transfer for highly efficient hydrogen production through water splitting, Int. J. Hydrogen Energy 45 (2020) 2729–2744. https://doi.org/10.1016/J.IJHYDENE.2019.11.127.

[189] W. Chakhari, J. Ben Naceur, S. Ben Taieb, I. Ben Assaker, R. Chtourou, Fe-doped TiO2

nanorods with enhanced electrochemical properties as efficient photoanode materials, J. Alloys Compd. 708 (2017) 862–870. https://doi.org/10.1016/J.JALLCOM.2016.12.181.

[190] I. Ganesh, P.P. Kumar, I. Annapoorna, J.M. Sumliner, M. Ramakrishna, N.Y. Hebalkar, G. Padmanabham, G. Sundararajan, Preparation and characterization of Cu-doped TiO2 materials for electrochemical, photoelectrochemical, and photocatalytic applications, Appl. Surf. Sci. 293 (2014) 229–247. https://doi.org/10.1016/J.APSUSC.2013.12.140.

[191] M. Hawkins, Why we need cobalt, Http://Dx.Doi.Org/10.1179/Aes.2001.110.2.66 110 (2013). https://doi.org/10.1179/AES.2001.110.2.66.

[192] K.B. Shedd, A. Hwang, Mineral Industry Surveys, (2022). https://www.usgs.gov/centers/national-minerals-information-center/mineral-industry-surveys (accessed August 28, 2022).

[193] S. Delpeux, K. Szostak, E. Frackowiak, S. Bonnamy, F. Béguin, High Yield of Pure MuItiwalled Carbon Nanotubes from the Catalytic Decomposition of Acetylene on in-Situ Formed Cobalt Nanoparticles, J. Nanosci. Nanotechnol. 2 (2002) 481–484. https://doi.org/10.1166/JNN.2002.139.

[194] J. Molenda, A. Stokłosa, T. Bąk, Modification in the electronic structure of cobalt bronze LixCoO2 and the resulting electrochemical properties, Solid State Ionics 36 (1989) 53–58. https://doi.org/10.1016/0167-2738(89)90058-1.

[195] Y. Zhang, H. Hu, M. Chang, D. Chen, M. Zhang, L. Wu, X. Li, Non-uniform doping outperforms uniform doping for enhancing the photocatalytic efficiency of Au-doped TiO2 nanotubes in organic dye degradation, Ceram. Int. 43 (2017) 9053–9059. https://doi.org/10.1016/J.CERAMINT.2017.04.050.

[196] M.T. Aytekin Aydın, H.L. Hoşgün, A. Dede, K. Güven, Synthesis, characterization and antibacterial activity of silver-doped TiO2 nanotubes, Spectrochim. Acta Part A Mol. Biomol. Spectrosc. 205 (2018) 503–507. https://doi.org/10.1016/J.SAA.2018.07.063.

[197] Y. Su, Y. Deng, Effect of structure on the photocatalytic activity of Pt-doped TiO2 nanotubes, Appl. Surf. Sci. 257 (2011) 9791–9795. https://doi.org/10.1016/J.APSUSC.2011.05.133.

[198] C. Xiang, Z. She, Y. Zou, J. Cheng, H. Chu, S. Qiu, H. Zhang, L. Sun, F. Xu, A room-temperature hydrogen sensor based on Pd nanoparticles doped TiO2 nanotubes, Ceram. Int. 40 (2014) 16343–16348. https://doi.org/10.1016/J.CERAMINT.2014.07.073.

[199] J. Low, S. Qiu, D. Xu, C. Jiang, B. Cheng, Direct evidence and enhancement of surface plasmon resonance effect on Ag-loaded TiO2 nanotube arrays for photocatalytic CO2 reduction, Appl. Surf. Sci. 434 (2018) 423–432. https://doi.org/10.1016/J.APSUSC.2017.10.194.

[200] Z. Lian, W. Wang, S. Xiao, X. Li, Y. Cui, D. Zhang, G. Li, H. Li, Plasmonic silver quantum dots coupled with hierarchical TiO2 nanotube arrays photoelectrodes for efficient visible-light photoelectrocatalytic hydrogen evolution, Sci. Reports 2015 51 5 (2015) 1–10. https://doi.org/10.1038/srep10461.

[201] L. Wu, F. Li, Y. Xu, J.W. Zhang, D. Zhang, G. Li, H. Li, Plasmon-induced photoelectrocatalytic activity of Au nanoparticles enhanced TiO2 nanotube arrays electrodes for environmental remediation, Appl. Catal. B Environ. 164 (2015) 217–224. https://doi.org/10.1016/J.APCATB.2014.09.029.

[202] S.Y. Xiao, Y. Liu, X.F. Wu, L.T. Gan, H.Y. Lin, L.R. Zheng, S. Dai, P.F. Liu, H.G. Yang, A low-valent cobalt oxide co-catalyst to boost photocatalytic water oxidation via enhanced hole-capturing ability, J. Mater. Chem. A 9 (2021) 14786–14792. https://doi.org/10.1039/D1TA01858B.

[203] Z. Wang, Q. Wang, Y. Han, Y. Ma, H. Zhao, A. Nowak, J. Li, Deep learning for ultra-fast and high precision screening of energy materials, Energy Storage Mater. 39 (2021) 45–53. https://doi.org/10.1016/j.ensm.2021.04.006.

[204] A.K. Sieradzan, C. Czaplewski, A. Bielicka-Gieldon, M. Bobrowski, A. Gieldon, Theoretical investigation of the structural insights of the interactions of γ-Fe2O3

nanoparticle with (EMIM TFSI) ionic liquid, J. Mol. Liq. 340 (2021) 117198. https://doi.org/10.1016/J.MOLLIQ.2021.117198.

[205] J.T. Mefford, A.R. Akbashev, L. Zhang, W.C. Chueh, Electrochemical Reactivity of Faceted β-Co(OH)2 Single Crystal Platelet Particles in Alkaline Electrolytes, J. Phys. Chem. C 123 (2019) 18783–18794. https://doi.org/10.1021/ACS.JPCC.9B03589.

[206] M. Suksomboon, K. Kongsawatvoragul, S. Duangdangchote, M. Sawangphruk, Reducing the Energy Band Gap of Cobalt Hydroxide Nanosheets with Silver Atoms and Enhancing Their Electrical Conductivity with Silver Nanoparticles, ACS Omega 6 (2021) 20804–20811. https://doi.org/10.1021/ACSOMEGA.1C01908/ASSET/IMAGES/LARGE/AO1C01908_0006.JPEG.

[207] J.B. Gerken, J.G. McAlpin, J.Y.C. Chen, M.L. Rigsby, W.H. Casey, R.D. Britt, S.S. Stahl, Electrochemical water oxidation with cobalt-based electrocatalysts from pH 0-14: The thermodynamic basis for catalyst structure, stability, and activity, J. Am. Chem. Soc. 133 (2011) 14431–14442. https://doi.org/10.1021/JA205647M.

[208] M.W. Kanan, D.G. Nocera, In situ formation of an oxygen-evolving catalyst in neutral water containing phosphate and Co2+, Science 321 (2008) 1072–1075. https://doi.org/10.1126/SCIENCE.1162018.

[209] G. Liu, Y. Zhao, K. Wang, D. He, R. Yao, J. Li, Ultrasmall NiFe-Phosphate Nanoparticles Incorporated α-Fe2O3 Nanoarrays Photoanode Realizing High Efficient Solar Water Splitting, ACS Sustain. Chem. Eng. 6 (2018) 2353–2361. https://doi.org/10.1021/ACSSUSCHEMENG.7B03804.

[210] J.F. Callejas, C.G. Read, C.W. Roske, N.S. Lewis, R.E. Schaak, Synthesis, Characterization, and Properties of Metal Phosphide Catalysts for the Hydrogen-Evolution Reaction, Chem. Mater. 28 (2016) 6017–6044. https://doi.org/10.1021/ACS.CHEMMATER.6B02148.

[211] D.E. Schipper, Z. Zhao, A.P. Leitner, L. Xie, F. Qin, M.K. Alam, S. Chen, D. Wang, Z. Ren, Z. Wang, J. Bao, K.H. Whitmire, A TiO2/FeMnP Core/Shell Nanorod Array Photoanode for Efficient Photoelectrochemical Oxygen Evolution, ACS Nano 11 (2017) 4051–4059. https://doi.org/10.1021/ACSNANO.7B00704.

[212] E. Fabbri, A. Habereder, K. Waltar, R. Kötz, T.J. Schmidt, Developments and perspectives of oxide-based catalysts for the oxygen evolution reaction, Catal. Sci. Technol. 4 (2014) 3800–3821. https://doi.org/10.1039/C4CY00669K.

[213] K. Sun, N. Park, Z. Sun, J. Zhou, J. Wang, X. Pang, S. Shen, S.Y. Noh, Y. Jing, S. Jin, P.K.L. Yu, D. Wang, Nickel oxide functionalized silicon for efficient photo-oxidation of water, Energy Environ. Sci. 5 (2012) 7872–7877. https://doi.org/10.1039/C2EE21708B.

[214] S.D. Tilley, M. Cornuz, K. Sivula, M. Grätzel, Light-Induced Water Splitting with Hematite: Improved Nanostructure and Iridium Oxide Catalysis, Angew. Chemie Int. Ed. 49 (2010) 6405–6408. https://doi.org/10.1002/ANIE.201003110.

[215] G. Wang, Y. Ling, X. Lu, T. Zhai, F. Qian, Y. Tong, Y. Li, A mechanistic study into the catalytic effect of Ni(OH)2 on hematite for photoelectrochemical water oxidation, Nanoscale 5 (2013) 4129–4133. https://doi.org/10.1039/C3NR00569K.

[216] A.G. Tamirat, W.N. Su, A.A. Dubale, H.M. Chen, B.J. Hwang, Photoelectrochemical water splitting at low applied potential using a NiOOH coated codoped (Sn, Zr) α-Fe2O3 photoanode, J. Mater. Chem. A 3 (2015) 5949–5961. https://doi.org/10.1039/C4TA06915C.

[217] A. Jia, M. Kan, J. Jia, Y. Zhao, A. Jia, M. Kan, J. Jia, Y. Zhao, Photodeposited FeOOH vs electrodeposited Co-Pi to enhance nanoporous $BiVO_4$ for photoelectrochemical water splitting, J. Semicond. 2017, Vol. 38, Issue 5, Pages 053004-053004-6 38 (2017) 053004-053004–6. https://doi.org/10.1088/1674-4926/38/5/053004.

[218] L. Wang, D. Mitoraj, S. Turner, O. V. Khavryuchenko, T. Jacob, R.K. Hocking, R. Beranek, Ultrasmall CoO(OH)x Nanoparticles As a Highly Efficient “True” Cocatalyst in

Porous Photoanodes for Water Splitting, ACS Catal. 7 (2017) 4759–4767. https://doi.org/10.1021/ACSCATAL.7B01466.

[219] P.J. Sideris, U.G. Nielsen, Z. Gan, C.P. Grey, Mg/Al ordering in layered double hydroxides revealed by multinuclear NMR spectroscopy, Science (80-.). 321 (2008) 113–117. https://doi.org/10.1126/SCIENCE.1157581.

[220] Z. Yu, Q. Huang, X. Jiang, X. Lv, X. Xiao, M. Wang, Y. Shen, G. Wittstock, Effect of a Cocatalyst on a Photoanode in Water Splitting: A Study of Scanning Electrochemical Microscopy, Anal. Chem. 93 (2021) 12221–12229. https://doi.org/10.1021/ACS.ANALCHEM.1C01235.

[221] C.L. Farrow, D.K. Bediako, Y. Surendranath, D.G. Nocera, S.J.L. Billinge, Intermediate-range structure of self-assembled cobalt-based oxygen-evolving catalyst, J. Am. Chem. Soc. 135 (2013) 6403–6406. https://doi.org/10.1021/JA401276F/SUPPL_FILE/JA401276F_SI_001.PDF.

[222] K. Dang, T. Wang, C. Li, J. Zhang, S. Liu, J. Gong, Improved Oxygen Evolution Kinetics and Surface States Passivation of Ni-Bi Co-Catalyst for a Hematite Photoanode, Engineering 3 (2017) 285–289. https://doi.org/10.1016/J.ENG.2017.03.005.

[223] A. Raza, X. Zhang, S. Ali, C. Cao, A.A. Rafi, G. Li, Photoelectrochemical Energy Conversion over 2D Materials, Photochem 2 (2022) 272–298. https://doi.org/10.3390/photochem2020020.

[224] X. Zhang, B. Zhang, S. Liu, H. Kang, W. Kong, S. Zhang, Y. Shen, B. Yang, RGO modified Ni doped FeOOH for enhanced electrochemical and photoelectrochemical water oxidation, Appl. Surf. Sci. 436 (2018) 974–980. https://doi.org/10.1016/J.APSUSC.2017.12.078.

[225] C. Feng, Z. Wang, Y. Ma, Y. Zhang, L. Wang, Y. Bi, Ultrathin graphitic C3N4 nanosheets as highly efficient metal-free cocatalyst for water oxidation, Appl. Catal. B Environ. 205 (2017) 19–23. https://doi.org/10.1016/J.APCATB.2016.12.014.

[226] O. Yehezkeli, R. Tel-Vered, J. Wasserman, A. Trifonov, D. Michaeli, R. Nechushtai, I. Willner, Integrated photosystem II-based photo-bioelectrochemical cells, Nat. Commun. 2012 31 3 (2012) 1–7. https://doi.org/10.1038/ncomms1741.

[227] B. Liu, H.Q. Peng, C.N. Ho, H. Xue, S. Wu, T.W. Ng, C.S. Lee, W. Zhang, Mesoporous Nanosheet Networked Hybrids of Cobalt Oxide and Cobalt Phosphate for Efficient Electrochemical and Photoelectrochemical Oxygen Evolution, Small 13 (2017) 1701875. https://doi.org/10.1002/SMLL.201701875.

[228] S. Li, W. Xu, L. Meng, W. Tian, L. Li, Recent Progress on Semiconductor Heterojunction-Based Photoanodes for Photoelectrochemical Water Splitting, Small Sci. 2 (2022) 2100112. https://doi.org/10.1002/SMSC.202100112.

[229] P. Salvador, C. Gutierrez, J.B. Goodenough, Photoresponse of n-type semiconductor NiTiO3, Appl. Phys. Lett. 40 (1998) 188. https://doi.org/10.1063/1.93003.

[230] W. Xu, W. Tian, L. Li, Two-Dimentional Nanostructured Metal Oxide/Sulfide–Based Photoanode for Photoelectrochemical Water Splitting, Sol. RRL 5 (2021) 2000412. https://doi.org/10.1002/SOLR.202000412.

[231] K. Trzciński, M. Szkoda, K. Siuzdak, M. Sawczak, A. Lisowska-Oleksiak, Enhanced photoelectrochemical performance of inorganic–organic hybrid consisting of BiVO 4 and PEDOT:PSS, Appl. Surf. Sci. 388 (2016) 753–761. https://doi.org/10.1016/j.apsusc.2016.02.143.

[232] Y. Zhang, Y. Huang, S.S. Zhu, Y.Y. Liu, X. Zhang, J.J. Wang, A. Braun, Covalent S-O Bonding Enables Enhanced Photoelectrochemical Performance of Cu2S/Fe2O3 Heterojunction for Water Splitting, Small 17 (2021). https://doi.org/10.1002/SMLL.202100320.

[233] B. He, S. Jia, M. Zhao, Y. Wang, T. Chen, S. Zhao, Z. Li, Z. Lin, Y. Zhao, X. Liu, General and Robust Photothermal-Heating-Enabled High-Efficiency Photoelectrochemical Water Splitting, Adv. Mater. 33 (2021) 2004406. https://doi.org/10.1002/ADMA.202004406.

[234] Y. Chen, L. Wang, R. Gao, Y.C. Zhang, L. Pan, C. Huang, K. Liu, X.Y. Chang, X. Zhang, J.J. Zou, Polarization-Enhanced direct Z-scheme ZnO-WO3-x nanorod arrays for efficient piezoelectric-photoelectrochemical Water splitting, Appl. Catal. B Environ. 259 (2019). https://doi.org/10.1016/J.APCATB.2019.118079.

[235] M. Zhang, F. Li, D. Benetti, R. Nechache, Q. Wei, X. Qi, F. Rosei, Ferroelectric polarization-enhanced charge separation in quantum dots sensitized semiconductor hybrid for photoelectrochemical hydrogen production, Nano Energy 81 (2021) 105626. https://doi.org/10.1016/J.NANOEN.2020.105626.

[236] P. Roy, S. Berger, P. Schmuki, TiO2 nanotubes: Synthesis and applications, Angew. Chemie - Int. Ed. 50 (2011) 2904–2939. https://doi.org/10.1002/anie.201001374.

[237] J. Sengupta, C.M. Hussain, TiO2 Nanotube-Enabled Glucose Biosensing: Transformative Insights from 2009 to 2024, Micromachines 2025, Vol. 16, Page 1235 16 (2025) 1235. https://doi.org/10.3390/MI16111235.

[238] K. Nakata, A. Fujishima, TiO2 photocatalysis: Design and applications, J. Photochem. Photobiol. C Photochem. Rev. 13 (2012) 169–189. https://doi.org/10.1016/J.JPHOTOCHEMREV.2012.06.001.

[239] M. Kowalkińska, S. Dudziak, J. Karczewski, J. Ryl, G. Trykowski, A. Zielińska-Jurek, Facet effect of TiO2 nanostructures from TiOF2 and their photocatalytic activity, Chem. Eng. J. 404 (2021) 126493. https://doi.org/10.1016/J.CEJ.2020.126493.

[240] C.B.D. Marien, T. Cottineau, D. Robert, P. Drogui, TiO_2 Nanotube arrays: Influence of tube length on the photocatalytic degradation of Paraquat., Appl. Catal. B Environ. 194 (2016) 1–6. https://doi.org/10.1016/J.APCATB.2016.04.040.

[241] G.K. Mor, K. Shankar, M. Paulose, O.K. Varghese, C.A. Grimes, Use of highly-ordered TiO(2) nanotube arrays in dye-sensitized solar cells, Nano Lett. 6 (2006) 215–218. https://doi.org/10.1021/NL052099J.

[242] S. So, I. Hwang, P. Schmuki, Hierarchical DSSC structures based on “single walled” TiO2 nanotube arrays reach a back-side illumination solar light conversion efficiency of 8%, Energy Environ. Sci. 8 (2015) 849–854. https://doi.org/10.1039/C4EE03729D.

[243] Y.C. Liang, C.C. Wang, C.C. Kei, Y.C. Hsueh, W.H. Cho, T.P. Perng, Photocatalysis of Ag-Loaded TiO2 Nanotube Arrays Formed by Atomic Layer Deposition, J. Phys. Chem. C 115 (2011) 9498–9502. https://doi.org/10.1021/JP202111P.

[244] W.T. Sun, A. Yu, H.Y. Pan, X.F. Gao, Q. Chen, L.M. Peng, CdS Quantum Dots Sensitized TiO2 Nanotube-Array Photoelectrodes, J. Am. Chem. Soc. 130 (2008) 1124–1125. https://doi.org/10.1021/JA0777741.

[245] X.F. Gao, H.B. Li, W.T. Sun, Q. Chen, F.Q. Tang, L.M. Peng, CdTe Quantum Dots-Sensitized TiO2 Nanotube Array Photoelectrodes, J. Phys. Chem. C 113 (2009) 7531–7535. https://doi.org/10.1021/JP810727N.

The aim of the thesis and research objectives

This dissertation aims to develop semiconductor photoanodes for solar supported water splitting, with an emphasis on titanium dioxide nanotube arrays (TiO_2-NTs) as a durable, stable substrate for oxygen evolution under solar illumination. The work combines experimental investigations with a critical review of the literature to link structure, surface chemistry and interface engineering to electrochemical and photoelectrochemical properties. The main performance parameters are photocurrent generation under simulated solar illumination and the overpotential required for the oxygen evolution reaction under specific conditions.

The primary research objectives are:

I. **Hydrothermal annealing (HA) of TiO_2-NTs**. To examine how hydrothermal treatment in controlled media (water and neutral aqueous solutions) reorganises tube morphology, affects the electrode surface, and how these changes influence charge separation, OER kinetics and photocurrent generation.

II. **Metal doping at low levels**. To introduce a small amount of cobalt into TiO_2-NTs by the hydrothermal process and find the influence of semiconductor energy bands and charge-carrier recombination.

III. **Surface modification with metal-based cocatalysts**. To precisely deposit cobalt nanoparticles (size control and distribution) onto TiO_2-NTs and oxidise them to CoOOH or Co_3O_4. Further, to test electrocatalytic activity for the OER and to understand the mechanism of photoelectrochemical water oxidation.

IV. **Surface modification with metal-free cocatalysts**. To synthesise 6 metal-free carbon nitride photoanode cocatalyst materials: three yellow (melem, melon, g-C3N4) and three white (melem, melon, g-C3N4 modified with sulfuric acid). To evaluate and compare them in the context of Z-scheme junctions and to test their permeability to the electrolyte under the influence of polarisation and illumination.

This research centres on n-type titanium dioxide nanotube photoanodes grown on titanium and evaluated in aqueous electrolytes under simulated solar

illumination. The processing route comprises anodisation, calcination, hydrothermal annealing, targeted morphology control, low-level cobalt doping and cocatalyst deposition. The materials are characterised by SEM for morphology, XRD and Raman Spectroscopy for crystal structure, XPS and FTIR for surface chemistry, and UV-Vis spectroscopy for optical response. Electrochemical and photoelectrochemical behaviour is assessed by cyclic and linear sweep voltammetry, chronoamperometry and electrochemical impedance spectroscopy, recorded in the dark and under illumination. Performance is judged by the photocurrent density under simulated sunlight at defined potentials and by the overpotential required for the oxygen evolution reaction (OER) under specified conditions.

Chapter I. It outlines the fundamentals of photoelectrochemical water splitting, the role of photoanodes, synthesis of TiO_2 nanotubes, and key modification strategies (thermal treatment, morphology control, metal and non-metal doping, cocatalysts and semiconductor–semiconductor junctions). It also surveys applications and summarises the methods used throughout the thesis. The subsequent experimental chapters (Chapters III–VI) provide an integrated commentary on the collection of publications that constitutes the core of this doctoral thesis.

Chapter II. It summarises the materials and methods used throughout the thesis. It lists key reagents and sample preparation routes, and outlines the core optical (like microscopy, diffraction, spectroscopy), electrochemical and photoelectrochemical characterisation employed to evaluate TiO_2 nanotube photoanodes and their modifications.

Chapter III. Hydrothermal modification of TiO_2 nanotubes in water and alkali metal electrolytes ($LiNO_3$, $NaNO_3$, KNO_3) – Direct evidence for photocatalytic activity enhancement. Here, the focus is on post-synthetic hydrothermal treatments, linking changes in morphology and surface chemistry to operational descriptors. This is one of the simplest methods for heat- and water-based modification. No toxic elements are introduced, and the process is inexpensive and safe. The chapter includes the publication and its supplementary information.

Chapter IV. Hydrothermal Cobalt Doping of Titanium Dioxide Nanotubes towards Photoanode Activity Enhancement. This chapter describes the introduction of cobalt via a hydrothermal route, the resulting structural and surface changes, and the shared testing framework, followed by the publication and its supplementary information.

Chapter V. Tailoring TiO_2 nanotube photoanodes with electrodeposited Co_3O_4 and CoOOH cocatalysts for enhanced electrocatalytic and photoelectrocatalytic oxygen evolution. The third modification method is to reuse cobalt, but in different oxide forms. It details electrodeposition and phase conversion of cobalt species and compares their roles as OER cocatalysts on hydrothermally treated TiO_2-NTs, followed by the publication and supplementary information.

Chapter VI. Exploring the role of carbon nitrides (melem, melon, g-C_3N_4) in enhancing photoelectrocatalytic properties of TiO_2 nanotubes for water electro-oxidation. The last modification method is to use cobalt-free catalysts, in line with trends in environmental ecology, especially new carbon-based catalysts. The application of a metal-free cocatalyst makes it possible to avoid limitations related to mineral resources, especially the critical cobalt mineral resources. This chapter covers the preparation of metal-free interlayers, junction formation and assessment within the common protocol, together with the publication and supplementary information.

The thesis closes with an integrated discussion of how processing choices shape structure and surface states, how these control photocurrents and OER overpotentials, and where future work should concentrate.

Chapter II

Materials characterisation

II.1 Chemicals and reagents

All reagents used were of analytical grade. We purchased ammonium fluoride (NH_4F) and ethylene glycol from Chempur (Piekary Śląskie, Poland), whilst orthophosphoric acid (H_3PO_4), sodium nitrate ($NaNO_3$) and potassium nitrate (KNO_3) were obtained from POCH Gliwice (Gliwice, Poland). Lithium nitrate ($LiNO_3$), potassium sulphate (K_2SO_4) and methylene blue were supplied by Sigma-Aldrich (St. Louis, USA). Titanium foil (99.5% metals basis, annealed, thickness 0.25 mm) was obtained from Alfa Aesar (Kandel, Germany). Triple-distilled water was used for all preparations and measurements. For experiments involving cobalt modification by hydrothermal insertion or electrochemical deposition, cobalt(II) chloride (POCH Gliwice, Poland; $CoCl_2$ or $CoCl_2 \cdot 6H_2O$, analytical grade) was used as the cobalt source. Trisodium citrate ($Na_3C_6H_5O_7$) and methylene blue were purchased from Sigma-Aldrich (St. Louis, USA), while sodium hydroxide (NaOH), ethylene glycol and orthophosphoric acid were from POCH Gliwice (Gliwice, Poland). Distilled water with an electrical conductivity of 0.1 µS/cm was used for these cobalt-deposition studies unless otherwise indicated. For carbon nitride modification, melamine (Thermo Scientific Chemicals, 99% purity) served as the precursor. Nafion - perfluorinated resin solution (5 wt% in lower alcohols/water) was purchased from Sigma-Aldrich. Sodium sulphate (Na_2SO_4), sulphuric acid (H_2SO_4, 95%) and orthophosphoric acid (H_3PO_4, 85%) were analytical grade, and ethylene glycol was sourced from Chempur (Piekary Śląskie, Poland).

II.2 Techiques of characterisations

All electrode morphologies and synthesised materials were characterised using a field-emission scanning electron microscope (JSM-7800F, JEOL, Tokyo, Japan). Microscopic studies were carried out at an accelerating voltage of 5 kV. The images revealed changes in nanotube dimensions and ordering. They also showed the size and spatial distribution of cocatalyst deposits. Elemental composition and/or mapping were obtained with an energy-dispersive X-ray detector (Octane Elite, EDAX, Mahwah, NJ, USA). X-ray diffraction patterns were collected using Rigaku MiniFlex 600 (Rigaku, Tokyo, Japan) or X'Pert PRO-MPD

(Philips, Amsterdam, The Netherlands) diffractometers with Cu Kα radiation (λ = 1.5406 Å). Diffractograms were used to confirm the anatase structure and detect changes in the modified materials. Raman spectra were recorded using an InVia Raman microscope (Renishaw, Wotton-under-Edge, UK) with 514 nm argon-ion excitation. Spectra confirmed the crystal structures of the materials. Shifts and broadening of the spectra of modified materials were used to investigate structural changes or to verify the deposited compounds on TiO_2. X-ray photoelectron spectroscopy employed monochromatic Al Kα radiation on PHI VersaProbe II (ULVAC-PHI, Chanhassen, MN, USA) or Escalab 250Xi (Thermo Fisher Scientific, Waltham, MA, USA). Binding energies were calibrated to adventitious carbon C 1s at 285.0 eV. Survey and high-resolution spectra were collected with appropriate pass energies. High-resolution Ti 2p, O 1s, C 1s, and Co 2p or impurity (phosphorus, sulphur, etc.) envelopes were deconvoluted using mixed Gaussian–Lorentzian line shapes (Avantage/MultiPak) to quantify oxidation states and surface composition. ATR-FTIR spectra were obtained on a Nicolet iS10 spectrometer (Thermo Fisher Scientific, Waltham, MA, USA). Thirty-two scans at 4/cm resolution were averaged to improve the signal-to-noise ratio. Characteristic bands of carbon nitride and cobalt species were assigned to verify the XPS findings.

Diffuse reflectance spectra were recorded using an Evolution 220 (Thermo Fisher Scientific) or a Lambda 35 (PerkinElmer, Waltham, MA, USA) spectrophotometer with dual Si photodiode detectors. Using $BaSO_4$ as a blank, spectra were measured over 200–800 nm. Subsequently, optical bandgaps were estimated from Kubelka–Munk-transformed data using Tauc plots (indirect allowed). The interference (electronic transitions) in the visible range for TiO_2 nanotubes was further discussed using absorbance spectra.

Cyclic voltammetry, linear sweep voltammetry, and chronoamperometry were performed using a PGSTAT 30 (Eco Chemie/Metrohm Autolab, Utrecht, Netherlands). Figure 11A shows the potentiostat-galvanostat. Experiments used a three-electrode cell with TiO_2 nanotube working electrodes, a platinum mesh counter electrode, and an Ag/AgCl/3 M KCl reference. Electrolytes were 0.2 M Na_2SO_4 for TiO_2-NTs/CxNy, and 0.1 or 0.2 M K_2SO_4 for unmodified and cobalt-modified TiO_2 nanotubes. All electrolytes were purged with argon for 30 minutes.

A Julabo F-12 thermostat maintained the temperature. For PEC measurements, a 150 W xenon lamp (Osram XBO 150, Quantum Design, Darmstadt, Germany) with an AM 1.5 filter and a quartz window provided illumination. The lamp's shutter operated in 5-second cycles. Figure 11B shows a schematic of the electrochemical/photoelectrochemical cell.

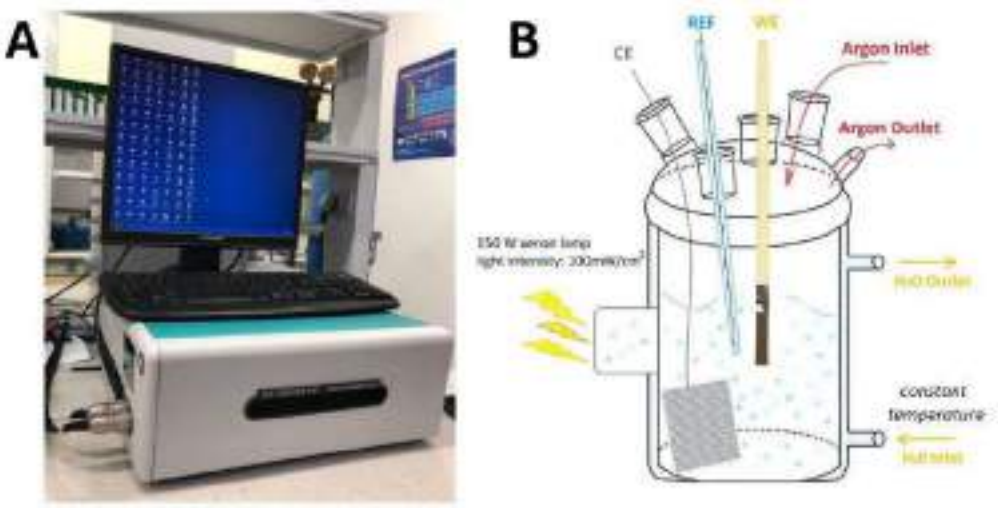

Figure 11. (A) The image of potentiostat-galvanostat PGSTAT 30, (B) photoelectrochemical cell

Electrochemical impedance spectroscopy was acquired on an Autolab PGStat10 with an FRA module from Eco Chemie B.V. Measurements were provided in the range of 20 kHz–0.1 Hz with an amplitude of 10 mV point–to–point in the AC signal. Capacitances were obtained from measured 1000 Hz point or obtained from equivalent-circuit fits (Brug approach). These values were needed to estimate flat-band potentials from Mott–Schottky plots.

Photocatalytic methylene-blue decolourisation was measured in a black glass reactor stirred at 150 rpm under the same xenon lamp. Each experiment used 10 μM MB in a 50 ml flask, followed by 20 min of 'dark' adsorption and 2 h of illumination. Photodegradation was examined by analysing UV-Vis spectra (UV5100, METASH, Shanghai, China), with parallel blank controls. For UV-Vis tests, 0.75 mL of solution was withdrawn every 20 min.

Chapter III

Hydrothermal modification of TiO_2 nanotubes in water and alkali metal electrolytes ($LiNO_3$, $NaNO_3$, KNO_3) – Direct evidence for photocatalytic activity enhancement

III.1 Methods in Brief and Key Results

This paper examines how hydrothermal annealing of calcined titanium dioxide nanotubes in water or aqueous solutions of alkali metal nitrates (Li, Na, K) can provide reproducible improvements in photocatalytic and photoelectrochemical performance. Attention was focused on the correlation of morphology, surface chemistry (hydroxyl, phosphate, and carbon-containing groups), and light absorption with OER activity. This assumption was confirmed: the introduction of Li^+, Na^+, or K^+ did not result in a photoactivity increase comparable to that observed when water was used as the processing medium. After HA modification, the samples showed reduced surface concentrations of fluorine, phosphorus, and carbon compounds. The duration of hydrothermal annealing strongly influenced the nanotube architecture, removing agglomerates and changing the nanotube inclination, wall thickness, and spacing between adjacent tubes due to HA time (SEM images in the publication clearly demonstrate this). The idea is presented in Figure 12.

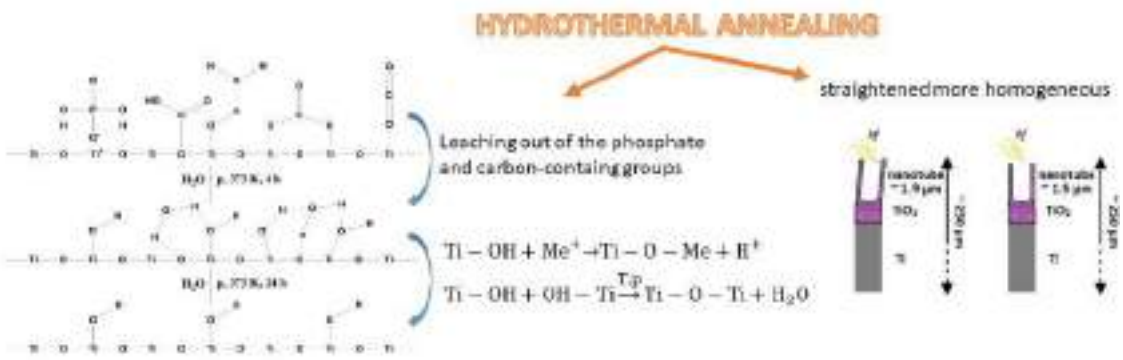

Figure 12. Graphical abstract.

Interestingly, these changes correlated with color-interference effects, as evidenced by shifts in the absorption maximum in the UV-visible spectra. Among the tested conditions, hydrothermal treatment in water produced the most photoactive and photoelectroactive material, resulting in only minor changes in the bandgap and flat-band potential. In contrast, electrodes treated with alkali metal electrolytes exhibited a reduced bandgap (down to 2.72 eV) and an anodic shift in the flat-band potential (up to 0.25 V). The HA TiO_2-NTs electrode, modified in H_2O for 24 hours at 100°C, achieved almost twice the photocurrent efficiency (from 20.7 µA/cm² to 39.5 µA/cm²). This minor treatment effectively enhanced

both photoelectrocatalysis and photocatalysis (as evidenced by higher absorption in methylene blue decolorization), achieving a higher absorption than in samples modified with electrolytes. Prolonged hydrothermal exposure in both water and electrolyte also reduced the initial potentials required for the oxygen evolution reaction. Overall, these results demonstrate that hydrothermal treatment is an effective method for improving the photocatalytic properties of TiO_2 nanotubes, while indicating that the inclusion of alkali metals is detrimental to maintaining high photocatalytic performance.

III.2 Publication

Electrochimica Acta 426 (2022) 140802

Contents lists available at ScienceDirect

Electrochimica Acta

journal homepage: www.journals.elsevier.com/electrochimica-acta

Hydrothermal modification of TiO_2 nanotubes in water and alkali metal electrolytes ($LiNO_3$, $NaNO_3$, KNO_3) – Direct evidence for photocatalytic activity enhancement

Mariusz Wrzesiak [a,*], Mariusz Szkoda [b], Grzegorz Gajowiec [b], Kacper Jurak [c], Grzegorz Trykowski [d], Anna Lisowska-Oleksiak [b,*]

[a] Department of Chemistry and Technology of Functional Materials, Faculty of Chemistry, Gdańsk University of Technology, Gdańsk 80-233, Poland
[b] Institute of Marine Technology and Materials, Faculty of Mechanical Engineering and Ship Technology, Gdańsk University of Technology, Gdańsk 80-233, Poland
[c] Department of Electrochemistry, Corrosion and Materials Engineering, Faculty of Chemistry, Gdańsk University of Technology, Gdańsk 80-233, Poland
[d] Department of Materials Chemistry, Adsorption and Catalysis, Faculty of Chemistry, Nicolaus Copernicus University in Toruń, Toruń 87-100, Poland

ARTICLE INFO

Keywords:
TiO_2 nanotubes
Hydrothermal annealing
Modified Vis absorbance
Interfaces

ABSTRACT

The influence of hydrothermal annealing (HA) of TiO_2 nanotubes (TiO_2 NTs) in various baths (H_2O, $LiNO_3$, $NaNO_3$, KNO_3, performed for 1 h, 24 h, 48 h), on their photocatalytic and photoelectrocatalytic properties, was studied. The use of electrolytes was to enable the monitoring of photoactivity changes as a result of the expected impact on the population of hydroxyl groups on the surface. The assumption turned out to be correct and it was proved that the presence of Li^+, Na^+ or K^+ does not allow achieving the same increment in photoactivity as observed for water. Modified samples exhibit significantly decreased F, P and carbon containing species. The length of the HA annealing time considerably affected the geometry of the nanotubes: diminished diameter, changing the tilting angle of nanotubes, the wall thickness and inter-nanotube distance. Morphology changes due to HA treatment were associated with the interference phenomenon recorded as oscillations in the Vis range. HA treatment in water brings about the more photoactive and photoelectroactive material characterized with minor modifications in the optical bandgap and position of the flat band potential. The optical energy bandgap values for electrodes containing alkali metals were reduced (up to 2.72 eV) and flat band potential was shifted towards the anodic direction (up to 0.26 V disparity). However, increased activity in photocatalysis in the methylene blue degradation process and higher photocurrent generation was achieved for samples after modification in distilled water than in electrolytes, but these parameters are still better in comparison to unmodified titania nanotubes. Long-term treatment in water and electrolytes reduced threshold potentials for oxygen evolution reaction. The studies confirmed the effectiveness of the hydrothermal method for obtaining better photocatalytic parameters of TiO_2 NTs and indicate that the presence of alkali metals is not favourable for maintaining high photocatalytic parameters.

1. Introduction

In recent decades, much work has been done on methods of controlling the morphology of TiO_2 nanotubes (TiO_2 NTs). One of the first reports, in 2001, on titanic nanotubes arrays obtained by anodizing titanium foil under properly maintained conditions was published by Grimes et al. [1]. The formation of an anodically grown TiO_2 tubular structure is described in detail in Ref. [2]. It has been indicated many times that the following parameters have an enormous influence on the morphology of nanotubes in the anodization process: electrolyte composition (content of water, NH_4F, H_3PO_4 or pH) [3–5], processing time, temperature [6] and anodization potential [7,8]. Furthermore, researchers demonstrate their results on the modification of nanotubes in various ways, such as: doping with non-metals [9–11], metal doping [12–14] and building multi-component electrodes towards cascade or 2-scheme photocatalytic system [15–18] or changing morphology (single or double-wall nanotubes) [19,20]. One can find applications of different types of titanium dioxide compounds in catalysis, self-cleaning, wetting, gas sensing, interference coating, optical devices, biomedical materials (the release of drugs, implants), Li-ion batteries or

* Corresponding authors.
E-mail addresses: mariusz.wrzesiak@pg.edu.pl (M. Wrzesiak), alisow@pg.edu.pl (A. Lisowska-Oleksiak).

https://doi.org/10.1016/j.electacta.2022.140802
Received 20 April 2022; Received in revised form 1 July 2022; Accepted 3 July 2022
Available online 8 July 2022

supercapacitors [3,24–25]. Moreover, there is an increasing importance of nanomaterials in the design of solar cells and photocatalytic devices for environmental protection. This applies to both the production of so-called solar fuels and the removal of organic pollutants from water and air. All applications related to photocatalysis and photoelectrocatalysis focus on geometric [26,27], optical [20,28] and electrochemical properties [29] in conjunction with the morphology and electronic structure of TiO_2 nanotubes.

A little known method of modifying produced nanotubes is their modification using hydrothermal annealing (HA). The first study devoted to the tuning effect of HA on the photocatalytic properties of anodized TiO_2 was described by Yu et al. [21]. The work shows that amorphous nanotubes hydrothermally treated in autoclaves lead to aggregation of TiO_2 into particles. Subsequent similar works [30–34] show the dissolution and anatase recrystallization of amorphous TiO_2 by water annealing (also known as the water-soaking method). These tests were carried out under atmospheric pressure.

The only report that showed the effect of hydrothermal modification in an autoclave on calcined TiO_2-NTs under increased pressure is reported in Ref. [35]. However, after annealing titania nanotubes were finally calcined after HA. To our knowledge, no one focused on the effect of HA on calcined titania nanotubes without subsequent calcinations.

Therefore, in this study, the influence of hydrothermal annealing process time and the bath composition (H_2O, $LiNO_3$, $NaNO_3$, KNO_3) for HA modification of TiO_2 nanotubes on the morphology, elemental composition, photoelectrocatalytic activity towards water oxidation and the photocatalytic degradation of methylene blue (MB) were tested. Tests in the presence of alkali metal cations were undertaken as cations may modify -OH groups' surface population and have an impact on photocatalytic activity of hydrothermally modified anodized titania nanotubes.

Here changes in optical, electrochemical, photoelectrochemical and photocatalytic properties are evaluated to hydrothermal procedure conditions. Samples have been characterized using scanning electron microscopy (SEM), X-ray photoelectron spectroscopy (XPS), X-ray powder diffraction (XRD) and UV-Vis spectroscopy. All electrodes were tested using cyclic voltammetry (CV), linear sweep voltammetry (LSV), electrochemical impedance spectroscopy (EIS) in the dark and chronoamperometry (CA) under solar light illumination.

2. Experimental

2.1. Materials

Chemical reagents used in the anodization process, HA modification, electrochemical and photocatalytic process were of analytical grade: MILLI, ethylene glycol were purchased from Chempur (Piekary Śląskie, Poland); H_3PO_4, $NaNO_3$, KNO_3 were purchased from POCH Gliwice (Gliwice, Poland); $LiNO_3$, K_2SO_4 and methylene blue were purchased from Sigma-Aldrich (St. Louis, USA). Alfa Aesar (Kandel, Germany) provided titanium foil (99.8% metals basis, annealed, thickness 0.25 mm). In all studies, triple distilled water was used. The electrical conductivity of triple distilled water is $1.5 \cdot 10^{-6}$ S cm^{-1}.

2.2. Preparation of the electrode materials

The titanium foil was cut into thin 2 × 2 cm^2 squares and subjected to pressing with a force of 2 tons. Samples were degreased in an ultrasonic bath in a 1:1 solution of acetone and isopropyl alcohol for 20 min at 40°C, then dried in warm. Next, both metal plates were placed for anodization in a two-electrode glassy cell keeping the 2 cm distance between the anode and cathode plates. One compartment, thermostated cell was filled with the 100 ml solution of an ethylene glycol electrolyte containing 1 g NH_4F, 5 ml H_2O and 3.5 ml H_3PO_4 [12] to obtain titania nanotubes. TiO_2-NTs were synthesized at the constant voltage of 40 V for 3 h, keeping the temperature at 20 ± 1°C. Beyond thoroughly rinsing, the samples were calcined in a furnace at 450°C (the rate of heating – 2.0 °C/min) with airflow and cooled down in air at room temperature after 2 h of heating. The final step was to transfer electrodes to an autoclave equipped with a PTFE-lined stainless steel chamber for further HA at 100° C (30 ml electrolyte per 50 ml total chamber volume). This modification was performed at different times (4, 24 and 64 h) and various solutions (a triple distilled water, non-aqueous electrolyte of 0.15 M $LiNO_3$, 0.15 M KNO_3, 0.15 M KNO_3).

2.3. Materials characterization

The electrode morphologies were characterized by JSM-7800 F (JEOL, Tokyo, Japan) field emission scanning electron microscope. The microscopic studies were analyzed using a beam accelerating voltage at 5 kV. Energy-dispersive X-ray spectroscopy (EDX) was used to identify chemical elements by a silicon nitride window's detector (OCTANE ELITE model, EDAX company, New Jersey, USA). The technique for measuring the intensity of diffuse wavelengths in the range 200 ÷ 800 nm was provided by UV-Vis spectroscopy, using the Perkin Elmer UV-Vis spectrometer (Lambda 35, Perkin Elmer, Waltham, MA, USA) equipped with the integrating sphere module to estimate the reflection of the measurements. X-ray powder diffraction was used to determine the crystal structure of the obtained TiO_2 samples. Measurements were made using a diffractometer (Xpert PRO-MPD, Philips, Amsterdam, Netherlands). X-ray photoelectron spectroscopy measurements were performed on the Escalab 250Xi device (Thermo Fisher Scientific, Waltham, Massachusetts, USA) with Al Kα radiation and pass energy. The analysis and deconvolution of the spectrum of the elements were described using a Gaussian-Lorentzian sum envelope with an asymmetry coil supported by commercial Avantage version 5.973 spectrometer software [36]. All of the binding energies obtained in the XPS were calibrated by the C1s line at 284.8 eV. The spot width with a diameter of 650 μm was used. The electrochemical and photoelectrochemical measurements of titania nanotubes were carried out with a potentiostat-galvanostat (Autolab PGSTAT 30, Metrohm Autolab B.V. and AutolabPGStat10 with an FRA module, Eco Chemie B.V. both from Utrecht, Netherlands) in a three-electrode cell: TiO_2-NTs (active surface area of 0.2 ± 0.1 cm^2) as the working electrode (WE), a platinum mesh as the counter electrode (CE) and Ag/AgCl/0.1 M KCl as the reference electrode (RE). Linear sweep voltammetry, cyclic voltammetry, chronoamperometry and electrochemical impedance spectroscopy were conducted in water-based solution electrolyte (0.1 M K_2SO_4) purged with argon (Ar gas high purity, O_2<0.2 ppm) for half an hour before measurements. The temperature was kept constant (20 ± 1°C) with a thermostat (Julabo F-12, Seelbach, Germany) in all measurements. The flat band (E_{fb}) potentials were determined using EIS. Frequencies were measured from 20 kHz to 1 Hz for 10 points per decade with low amplitude (10 mV point-to-point) of the AC signal. Photoelectrochemical studies were conducted in a three-electrode glassy cell with a quartz window. The tested electrodes remained in the same electrolyte and under the conditions described above. Solar lighting was a xenon lamp (Osram XBO 150, Quantum Design, Darmstadt, Germany), which generates light with an intensity of up to 100 mW/cm^2, equipped with an air mass 1.5 filter and an automatic shutter that opens/closes every 5 s. The studies on the influence of TiO_2-NTs on the degradation of methylene blue were carried out in a dark glass reactor, isolated from external light. The photocatalytic reactions were conducted in a 50 ml water-based solution of 10^{-5} M methylene blue (MB) under illumination using the lamp described above. The decomposition of the MB was recorded every 30 min using the UV-vis spectrophotometer (model UV5100, METASH). The current MB concentration was registered to an absorbance measurement at λ = 665 nm. For reference, a blank test was performed under the same conditions but without TiO_2-NTs.

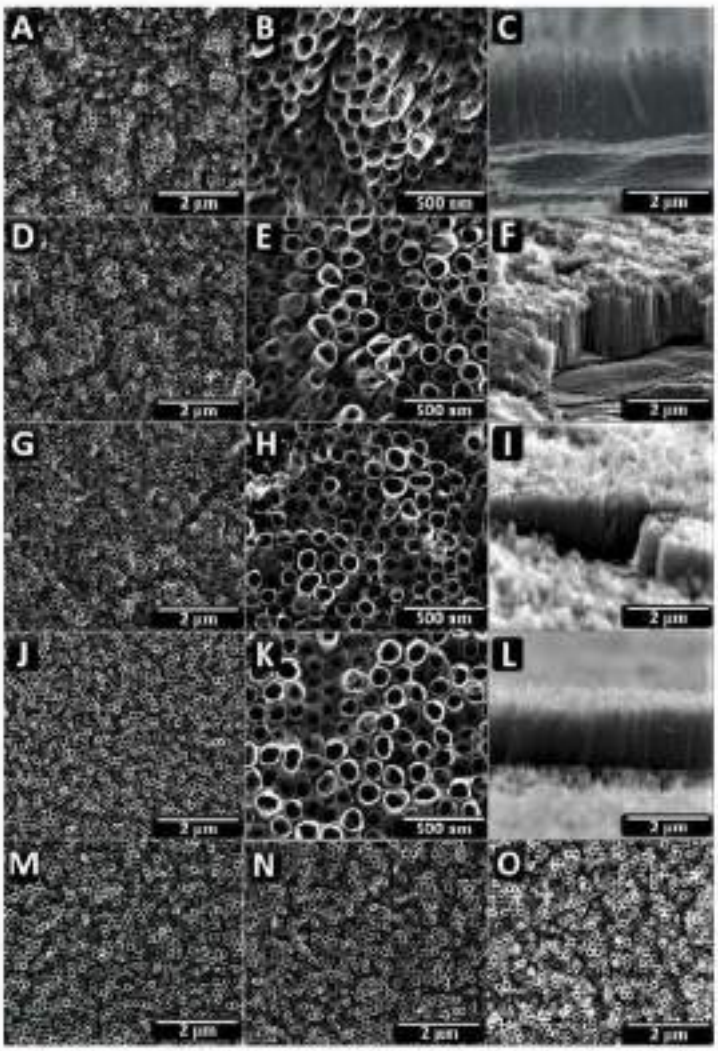

Fig. 1. Top-view SEM images at 10k, 100k magnification and cross-section images at 10k magnification respectively for: (A-C) annealed TiO_2-NTs; HA TiO_2-NTs in water for (D-F) 4 h, (G-I) 24 h, (J-L) 64 h and top-view SEM images at 10k magnification for HA TiO_2-NTs in an electrolyte of 0.15 M (M) $LiNO_3$, (N) $NaNO_3$, (O) KNO_3 for 64 h.

3. Results and discussion

3.1. Morphology and composition of the samples

3.1.1. Scanning electron microscope imaging

Fig. 1 A-O show SEM images of the top-view and cross-sectional images of the: (1A-C) TiO_2-NTs - calcined, (1D-F) TiO_2-NTs after hydrothermal annealing in water for 4 h, (1G-I) for 24 h and (1J-L) for 64 h and TiO_2 NTs after HA in an aqueous solution of 0.15 M (1M) $LiNO_3$, (1N) $NaNO_3$, (1O) KNO_3 for 64 h. All obtained nanotubes have a single-wall structure. As shown in Fig. 1A, the electrode surface consists of titania nanotubes agglomerated into small local clusters. At higher magnification (Fig. 1B), it can be seen that each one cluster is created of a dozen interconnected nanotubes by their walls. Some upper parts edges of the nanotubes touch each other and look like to be stratified, jagged and inhomogeneous. The average inner nanotubes diameter is 99

Table 1
Data obtained from geometrical analysis of SEM images (Fig. 1), where h – the length of the nanotube, R_1 – a the internal radius, R_2 – a distance between the nanotube center and the center of the nanotube wall, y – a distance between neighbouring nanotubes, w – a thickness of nanotube, S – a total developed surface.

Sample	h (nm)	$2R_1$ (nm)	R_2 (nm)	y (nm)	w (nm)	S_r (cm^2)
TiO_2-NTs	1481 ± 50	99 ± 9	58 ± 5	19 ± 4	10 ± 3	368 ± 17
in H_2O, 4 h	1556 ± 93	103 ± 11	60 ± 5	20 ± 3	17 ± 4	386 ± 165
in H_2O, 24 h	1556 ± 94	103 ± 9	56 ± 6	20 ± 5	14 ± 3	386 ± 80
in H_2O, 64 h	1552 ± 82	107 ± 12	60 ± 5	21 ± 4	10 ± 6	385 ± 93

± 9 nm and the length is 1552 ± 82 nm estimated from 15 counts from Fig. 1B and C). In Fig. 1D, one can still see cluster of nanotubes. However, when enlarged (Fig. 1E), it can be seen that nanotubes have been separated, they do not touch their walls. The significant change is the diminution of the thickness of the nanotube layer to 1556 ± 93 nm (Fig. 1D). It is well known that nanotubes are etched [39]. The diminution in length is very likely to be caused by the etching of parts of the nanotubes at the thinnest or unratified places. During HA in water, molecules of H_2O and residual fluoride anions [40], can etch the TiO_2-NTs via $[TiF_6]^{2-}$ soluble complex formation. The view of the more homogeneous nanotubes than unratified TiO_2-NTs is depicted in Fig. 1G and J. Titania nanotubes were separated and no clusters are present. The enlarged shows that the nanotubes do not touch each other edges of the neighbouring walls (Fig. 1H and K) as well as TiO_2-NTs HA in water (4 h). Additionally, they were straightened after the hydrothermal annealing for a longer time (24 h, 64 h). This suggests that possibly the long term HA decreased residual stresses and complete relaxation occurring during this process, as can be seen on the XRD diffractogram, see paragraph 3.1.2 The inner diameter and the length of these TiO_2-NTs are similar and collected in Table 1. The top view images of TiO_2-NTs HA in electrolyte (Fig. 1M–O) show that the morphology of the electrodes is very similar in comparison to titania nanotubes hydrothermally annealed in water for 64 h.

Table 1 shows the geometric parameters (symbols are the same as given in Ref. [41]) that are important to optimize the TiO_2-NTs morphology, thanks to which the electrode material shows better photoactivity. Although the TiO_2-NTs calcined layer (before HA) was thicker, the morphology was heterogeneous (inclined, stratified nanotubes preventing light from propagating deep into), which may result in lower photocurrent being generated [42].

As shown in the literature [43], the efficiency of a solar cell strongly depends on its morphology. The open tube tops have a significant advantage in this system. The condition of the surface for any catalytic processes is of great importance [44]. Therefore, not only in the morphological changes, the cause of the increase in photoactivity should be sought, but also in the chemical state of the surface, so it is presented below.

Table 2
Elemental content (at. %) of TiO_2-NTs before and after hydrothermal annealing were detected by EDS.

Sample	TiO_2-NTs	in H_2O			in $LiNO_3$			in $NaNO_3$			in KNO_3		
		4 h	24 h	64 h	4 h	24 h	64 h	4 h	24 h	64 h	4 h	24 h	64 h
Ti (at. %)	31.50	42.33	43.86	46.26	44.08	42.32	42.50	48.67	41.24	41.54	37.35	42.37	45.98
O (at. %)	68.03	56.72	54.69	53.36	54.48	56.66	56.45	50.68	54.76	57.43	60.97	54.28	52.57
F (at. %)	0.46	0.55	0.56	0.54	1.39	0.57	0.57	0.46	0.91	0.63	0.68	0.65	0.39
P (at. %)	0.01	0.39	0.29	0.14	0.24	0.45	0.49	0.19	0.09	0.40	0.29	0.30	0.36

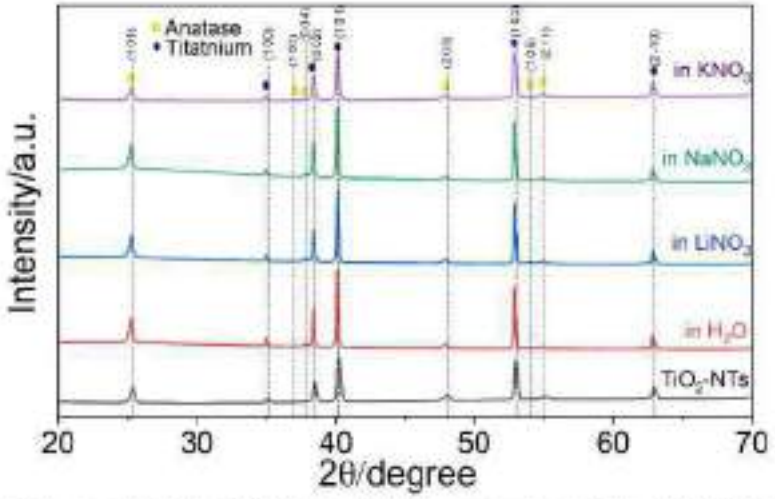

Fig. 2. Comparison of XRD patterns of TiO_2-NTs before and after hydrothermal annealing in water ($LiNO_3$, $NaNO_3$, KNO_3 (64h)).

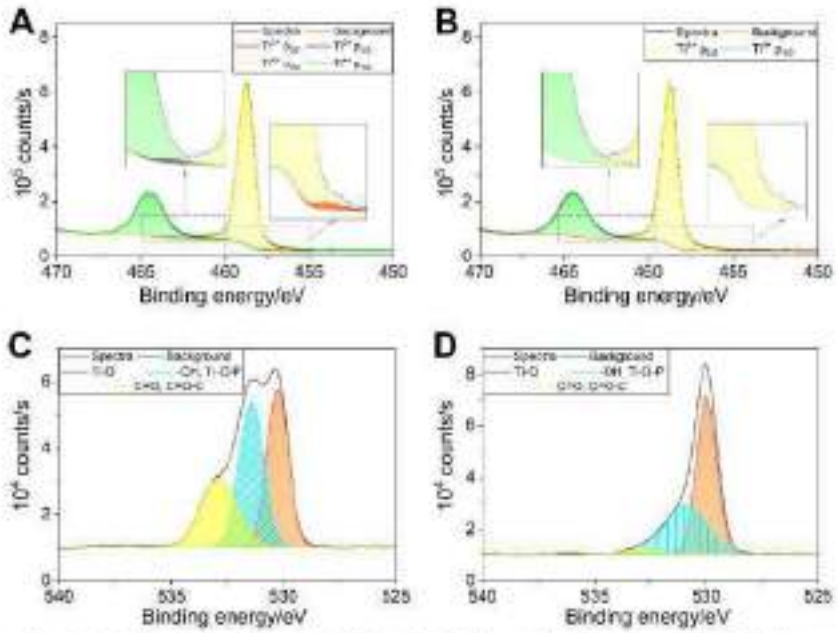

Fig. 8. Deconvolution of titanium 2p peak in the XPS spectra of TiO_2 NTs after HA for 24 h in water in the (A) presence of Ti^{4+} and Ti^{3+} (B) presence only Ti^{4+}; and oxygen 1 s peak for TiO_2-NTs (C) before and (D) after treatment (H_2O, 24 h).

3.1.2. Energy dispersive X-ray analysis

EDX measurements were performed to determine the atomic percentages of the elements: titanium, oxygen, as well as the contamination of fluorine and phosphorus, obtained by the modification of Ti foil as described earlier [33]. It is known that the calcination of the as-formed nanotubes removes the fluorine ions due to the evaporation of gases such as F_2 and HF [45]. However, a small residual content of fluoride ions, less than 1 at. %, remains in the structure of the calcined TiO_2 nanotubes. Table 3 shows that the sample after the HA in water contains a significantly lower amount of F (almost twice) and P (fourfold). Moreover, the content of phosphorus in the samples subjected to HA in all electrolytes was reduced at least 2.5 times. Except for the sample modified in an aqueous electrolyte $NaNO_3$, a tendency was noticed that the HA eliminates the residual elements after anodization. It can be concluded that the HA method reduces the content of impurities in the form of fluoride and phosphorous. As the authors write in Ref. [36], for the sample subjected to a 3-day water annealing at 70 °C, the content of the elements is: 51.79% for O, 46.09% for Ti and 0.09% for F, which is comparable with the result obtained for TiO_2 NTs in H_2O 64 h from this work. In particular, they show that fluoride residues are removed by a longer water annealing time of the nanotubes by leaching out. However, water soaking requires a longer time to achieve the same results as HA in our work.

3.1.3. XRD

Crystallinity and phase composition of TiO_2-NTs unmodified, hydrothermally annealed in water, and 0.15 M aqueous solution of $LiNO_3$, $NaNO_3$, KNO_3 for 64 h was assessed by XRD. Fig. 9 shows the registered diffraction at 25.2°, 36.9°, 37.8°, 38.6°, 47.9°, 53.6°, 54.9° which correspond to the (1 0 1), (1 0 3), (0 0 4), (2 0 0), (1 0 5), (2 1 1) planes, respectively [46]. All electrodes are composed of the anatase phase. No reflections referring to rutile or brookite were recognized. The observed signal at 35.0°, 38.3°, 40.1°, 52.9°, 53.9° correlates to Miller indices (1 0 1), (0 0 2), (1 1 1), (1 0 2), (2 −1 0) of HCP crystal structure of titanium [47]. The highest intensity reflections correspond to Ti planes because it is the main electrode material. No additional differences were detected in the changes in the XRD pattern for the tested samples. However, for HA of TiO_2-NTs, a slight shift and less broadening of the peaks with reflections corresponding to the anatase phase are observed. This may mean that the quantitative residual stresses (microstrains) and the size of the crystallites have decreased compared to the pure titania nanotubes [48–50]. One could expect traces of rutile at the bottom of the tubes [51], but in our case, XRD patterns show only the anatase phase in all cases, which is consistent with XRD data of TiO_2 NTs calcined at 450 °C [52].

3.1.4. X-ray photoelectron spectroscopy

The Ti2p spectra are very similar for all samples, regardless of the electrolyte used in HA, composition and the annealing time. Minor discrepancies at the level of 0.1–0.2 eV are due to the accuracy of the measuring device and the accuracy of the calibration based on C1s. The observation of all XPS spectra for the HA modified (12 pieces) and the unmodified samples allows distinguishing qualitative differences (insignificant) in the course of the curves, see Fig. 5L. A slight broadening is observed at the base of the Ti (IV) peak at about 460 eV. The observed broadening disappears for all the modified electrodes. This change occurs regardless of the type of hydrothermal bath. Moreover, all modified samples are characterized by a narrower XPS spectrum at maximum ($Ti^{4+}p_{3/2}$) compared to the original, unmodified TiO_2 NTs. This widening at the bottom, which disappears with all other HA

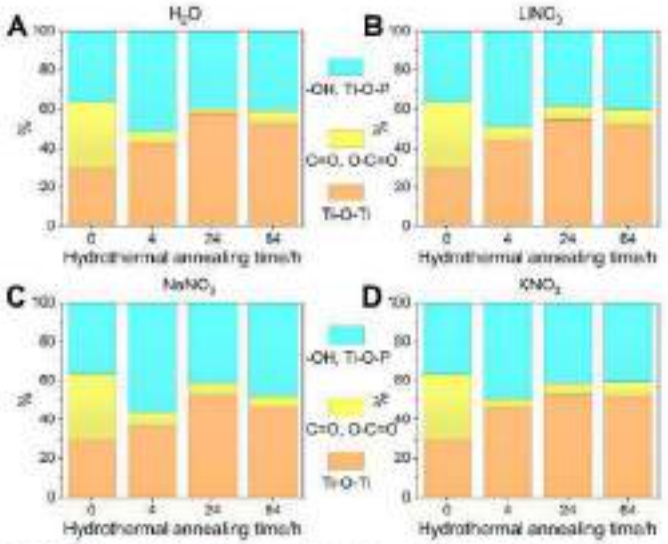

Fig. 4. XPS spectra of O 1s for TiO_2 NTs before and after hydrothermal annealing in (A) water, (B) 0.15 M $LiNO_3$, (C) 0.15 M $NaNO_3$, (D) 0.15 M KNO_3. Spectra are narrowing with Hs.

modified samples, may indicate that the surrounding area of the Ti (IV) ion is altered as a result of the hydrothermal process. A model for the Ti2p analysis was proposed, taking into account the simultaneous occurrence of Ti^{4+} and Ti^{3+}. After analysing all spectra, the Ti^{3+} content was estimated at 0.5–2.5% (Fig. 5A). There was no dependence of the percentage of this form of titanium on the electrolyte composition or the length of the annealing. Since the presumed Ti^{3+} content is very low, a model with Ti^{4+} only was proposed (Fig. 5B). Powell fitting algorithm and Gaussian-Lorentzian Convolution were used. In both models, the Ti^{4+} $2p_{3/2}$ peak appears at BE around 458.8 eV and the Ti^{4+} $2p_{1/2}$ peak at BE around 464.5 eV. The splitting between these peaks equals 5.7 eV which is consistent with the literature [53] and corresponds to TiO_2 lattice structure (O^{2-} is coordinated Ti^{4+} in the tetragonal phase of anatase) [54]. Ti^{3+} shows the best match for BE at around 457 eV, which is also in line with the literature. Normalised Chi Sqr for the model without Ti^{3+} was 7.1148 with 3 iterations, and for the model with two forms of titanium was 4.1314 with 6 iterations. Detecting a negligible amount of Ti^{3+} on a Ti^{4+} background is not easy and the measurement

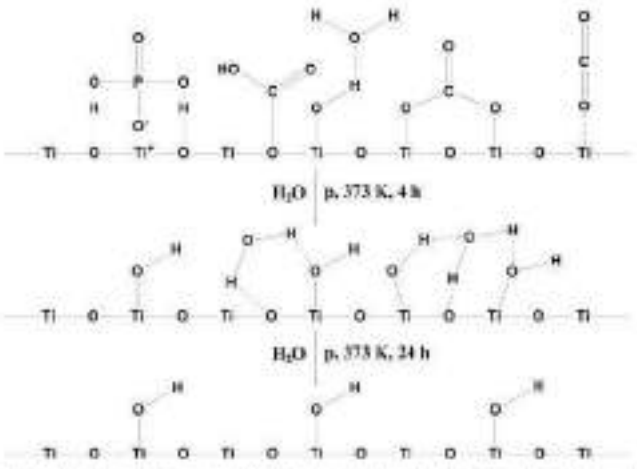

Fig. 6. Possible surface structures on the TiO_2 NTs surface for calcined and hydrothermal annealed samples.

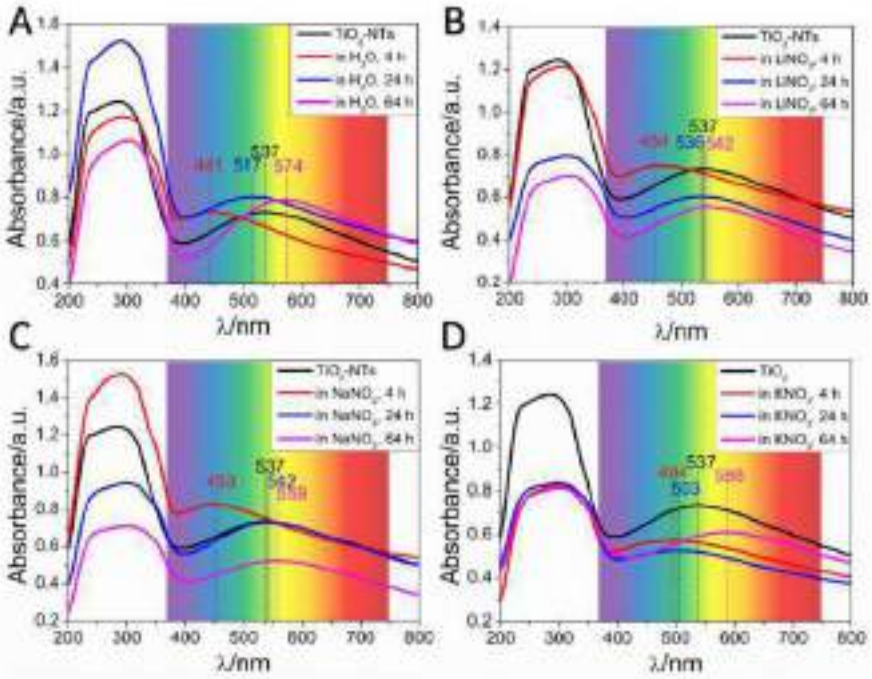

Fig. 6. Absorbance spectra for TiO_2-NTs after hydrothermal annealing in: (A) water, (B) in 0.10 M $LiNO_3$, (C) in 0.10 M $NaNO_3$, (D) in 0.10 M KNO_3.

capabilities of the device are limited. When analysing such small contents, high measurement accuracy is needed, hence the models assuming the presence of Ti^{3+} and its absence match at a similar level and in assessing the presence of titanium forms, additional measurement methods should be used.

Fig. 5C shows the deconvolution of the XPS spectrum in the O 1s peak, with the resolution of three main signals for TiO_2-NTs electrode. The first peak is localized at 530.2 eV and is attributed to the oxygen state of the TiO_2 lattice (octahedral TiO_6 formed by anions O^{2-}-Ti^{4+}) [31,58]. The second peak at 531.4 eV has the biggest share in the distribution of the oxygen spectrum (36.57%) and can be assigned to the surface -OH and TiO_x species [56] or the oxygen atoms in the phosphonate group (Ti-O-P, O=P) [54,57]. The last signal localized at a binding energy of 532.8 eV corresponds to carbon-containing groups (O=C-O, C=O) [59], physically absorbed H_2O [31] on the near-surface area or C-OH [59], P-OH [57] bonds.

For all XPS spectra of O 1s for TiO_2-NTs after HA in H_2O, $LiNO_3$, $NaNO_3$ and KNO_3 see Fig. S2. Fig. 7D depicts the deconvolution of the oxygen of TiO_2-NTs HA in water for 24 h. It can be seen that the peak (O1) at 530.0 eV attributed to Ti-O-Ti bond is more intense. The signal O 1s at 532.3 eV is significantly lower than for the electrode before HA. The third O1s signal from carboxylate is detectable in the range of error. The detailed distributions of oxygen towards the HA time for all electrodes are shown in Fig. 4. Regardless of the choice of water or electrolyte for hydrothermal modification, after 4 h of HA, a significant drop in the peak contribution O 1s at the highest 532.8 eV binding energy can be seen, in Fig. 5 and Fig. 4. The reason for this is most likely the fact that carbon-containing groups (firstly present due to anodization in glycol electrolyte) are leached out during HA.

Fig. S8 shows all XPS spectra of C 1s. For each electrode subjected to hydrothermal modification in water and electrolytes, spectra showing decreased intensities were recorded (lower carbon content) for modified samples, which is generally in accordance with changes of oxygen content. Fig. 6A shows the deconvolution of carbon 1s peak for TiO_2-NTs HA in water. It can be seen that HA leads to leach out the C=O and O=C-OH groups attributed at binding energies of 287.6 eV and 289.2 eV, respectively [58]. After 24 h, these signals disappear and a new one appears at the energy of 288.6 eV, which is assigned to the HCO_3 group [60]. This change may be attributed to the surface chemical reaction between carbon near-surface species and water resulting in HCO_3 formation, see a green hump in Fig. S4. These changes of carbon species content are consistent with those observed for the XPS spectra of O 1s in Figs. S2 and 4.

Nonetheless, at higher temperatures and under increased pressure, various changes in surface chemistry are expected to occur. Fig. 5 shows possible changes in the TiO_2-NTs surface during HA. The remaining adsorbed water could have undergone various surface adsorption processes. With increasing time of treatment, different species on TiO_2-NTs surface stabilize by the hydrogen bonds with adjacent anions, which are described in more detail in Ref. [61]. We see this as the highest proportion of oxygen (over 50%) for the peak at the binding energy of 530.0 ± 0.1 eV. Moreover, it differs from the O 1s from an unmodified sample by as much as 0.5 ± 0.1 eV. This can be explained by the removal of the phosphate groups during HA, as shown in Figs. S2 and S6.

Hydrothermal annealing caused the oxygen content to dropout the O 1s 530.0 ± 0.1 eV (Ti-OH) peak and increase at O 1s 529.9 ± 0.1 eV (Ti-O-Ti). This was probably due to the chemical reaction taking place on

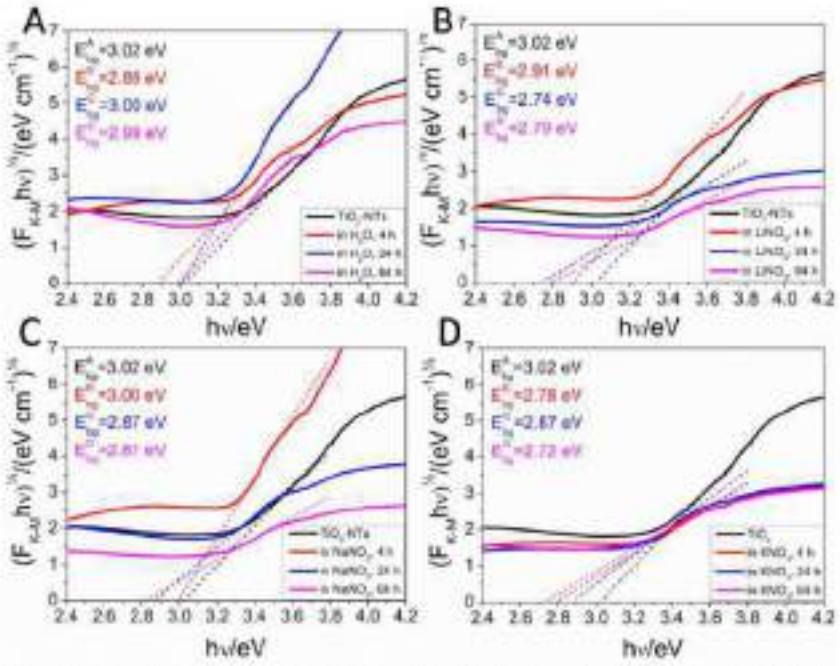

Fig. 7. Tauc plot for TiO_2 NTs after hydrothermal annealing in: (A) water, (B) in 0.15 M $LiNO_3$, (C) in 0.15 M $NaNO_3$, (D) in 0.15 M KNO_3.

the TiO_2 NTs surface during the hydrothermal process, given by the equation below [62]:

$$Ti-OH + OH-Ti \xrightarrow{T,t} Ti-O-Ti + H_2O \quad (1)$$

The content of hydroxyl groups is crucial in the context of photocatalytic properties [62,63]. The following hours of HA do not show a significant change in the content of individual bonds with oxygen. However, it can be assumed that titanates of the Ti-O-Me structure (where Me is: Li, Na or K) may be formed [64,65], within the measurement error influencing the surface hydrogen groups population.

$$Ti-OH + Me^+ \rightarrow Ti-O-Me + H^+ \quad (2)$$

Besides, as shown in Fig. S7, small amounts of potassium or sodium, but not light lithium, were detected on the TiO_2 NTs nanosurface. All of the above elements were in small amounts (up to ca. 1.5%). No fluoride was detected on the surface of any samples measured by XPS. On the other hand, according to EDX studies, which reveal a low content of fluorine in the electrode (per volume), probably most of the fluoride accumulates within the bulk of the nanotubes (more at the bottom – F-rich layer) [43]. According to reaction (1), hydrothermally treated TiO_2 surface can adsorb H_2O molecule effectively on Ti centre. Subsequent hydrogen bonding with O centre may result in H_2O dissociation – influencing the catalytic activity of the oxide surface [44]. Thus, samples with higher content of oxygen from Ti-O-Ti are expected to present higher catalytic activity as observed.

3.2. UV-vis spectroscopy

It is known from the literature that spectra in the UV-vis range for titanium dioxide nanotubes usually have two well-formed, wide absorption maxima, one in the UV range and the other in the Vis range. Fig. 6A–D shows the UV-vis spectra, illustrating the absorbance curves for TiO_2 NTs before and after HA. The highest absorbance maxima, typical for TiO_2 in the crystal structure of anatase and determining bandgap energy E_g, are in the range of ultraviolet. The absorption spectra were used to determine the E_g value (see the next paragraph). Hydrothermal modification leads to an increase in absorption under optimal conditions for each system. And so, for the electrode modified in water, the highest values were obtained after 24 h of HA (Fig. S3A). The factors influencing the change in absorption in the UV region are the changes in the geometry of the TiO_2 NT layer and the removal of surface-containing groups such as C=O, C-O=C, F, O-P, see XPS data, Figs. 5, S3 and S6. The influences of these factors are opposite. Observed changes in geometry over time lower the absorption, while the removal of pollutants influences its growth. Moreover, the share of alkali metal cations tends rather lower the absorption of UV light due to alkali metal cations' insertion into the near-surface area, probably in a form of titanates.

The analysis of the absorbance spectrum in the Vis range shows a certain trend in the position of the maximum related to treatment time. In the first period of HA (up to 4 h), the maximum shifts towards higher energies, an blueshift is observed. Regardless of the medium contained in the hydrothermal bath, the maximum absorbance values of TiO_2 NTs are in the region of blue light. Further extending the modification time results in a shift of the peak in the visible range into the area of lower energy, so we observed a redshift. For samples after 24 and 64 h of treatment, the maximum is in the range of green and yellow light, respectively. This trend is notably visible in Fig. 6A. The reason for these changes in the position of the wide maximum in the Vis range can be

Table 3
Flat band potentials estimated from impedance fraction measured at 1000 Hz vs Ag/AgCl 0.1 KCl reference electrode.

Sample	TiO_2 NTs	In H_2O			In $LiNO_3$			In $NaNO_3$			In KNO_3		
		4 h	24 h	64 h	4 h	24 h	64 h	4 h	24 h	64 h	4 h	24 h	64 h
E_{fb} (V)	-0.25	-0.18	-0.08	-0.19	-0.21	-0.17	-0.05	-0.06	-0.03	-0.07	-0.16	-0.20	-0.00

found in two zones, namely: (a) in changes in the electronic properties of the area near the surface and (b) in changes resulting from the geometry of the sample and in the interference phenomenon due to thin-film optical properties.

The first reason is that changes in such a spectrum may correspond to self-trapped excitons, oxygen vacancies (OVs) and surface states [66]. According to the literature, the most intense signal of unmodified TiO_2 is associated with the presence of fluorine and phosphorus [67]. Diminishing the atomic content of F and P can change the energy of the electron transitions and the self-trapped excitons, resulting in the higher absorption of shorter wavelength light, which is seen as a blueshift for all samples after 4 h of HA [68,69]. However, the major factor responsible for redshift may be the oxygen vacancy occupied by one or two electrons [70]. Moreover, as reported in the literature [71], higher Ti^{3+} content causes the absorbance curve to shift towards longer wavelengths in the Vis range. As shown in Fig. 3A, the presented model of the deconvolution of the XPS spectrum shows a low presence of Ti^{3+}. For this reason, it cannot be excluded that the presence of Ti^{3+} is responsible for the peak in the Vis region. Slight differences in the maximum absorbance shift may result from the insertion of alkali metal ion to the TiO_2-NTs surface area as proven by XPS.

The second reason, but the most prominent, explaining the change in the absorbed wavelength of light in Vis region, is based on the theory of interference phenomenon (Fabry–Pérot interference) [72]. As reported in the works [73,74], the local minimum value of the Vis spectrum depends on the thickness of the obtained TiO_2 layer, which corresponds to a specific colour. As it turns out, for all TiO_2 NTs (calcined and HA), the key role in the absorbance measurement in Vis region is their geometry, especially: diameter, thickness and length of the nanotube, internube distance and wall structure [65,72]. Moreover, the higher the tilting angle of titania nanotubes to the surface, the local minimum shifts towards the UV range, as shown by the numerical calculations [66]. Our work shows that HA causes an increase in the wall thickness of TiO_2 NTs and reduces the angle of inclination of TiO_2 NTs to titanium substrate and the length of nanotubes, see SEM images (Fig. 1). According to the conditions of wave interference and the results discussed above, it could be confirmed that the trend in the position of maximum in Vis region spectrum is caused by changes in morphology.

Considering the above, we show that the change in the local maximum absorbance of titania nanotubes in visible light has two kinds of grounds – electronic states and geometry of TiO_2 NTs able to produce interferential colours [35].

Using the absorbance spectra and the Kubelka-Munk function, the values of bandgap energy (E_{bg}) were determined for all obtained materials based on the Tauc plot, which is presented in Fig. 7A–D. Hydrothermal modification of titania nanotubes in water did not change the E_{bg} value, except for negligible change for sample TiO_2-NTs in H_2O (4h). The samples hydrothermally annealed with alkali metal electrolytes exhibited lower values of the bandgap energy. As noted above, TiO_2-NTs in KNO_3 (64h) exhibits the smallest value of E_{bg} and equal 2.72 eV.

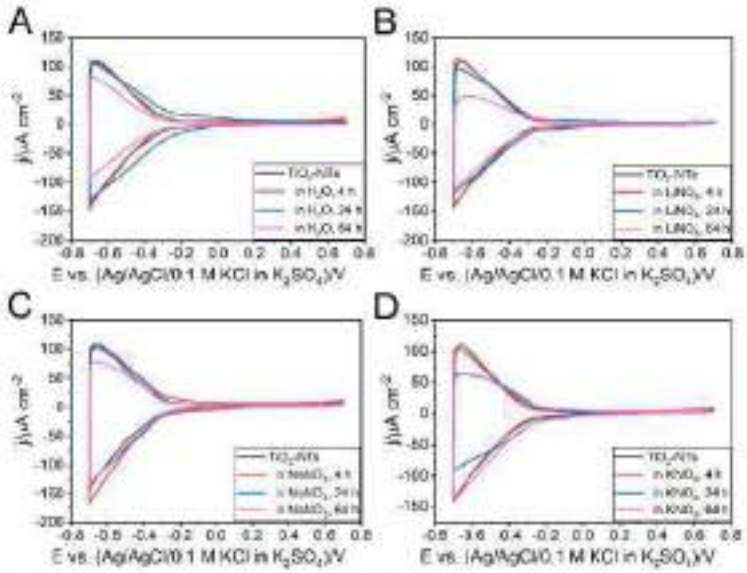

Fig. 8. Cyclic voltammetry curves obtained for samples without and after hydrothermal annealing, with a sweep rate of 50 mV/s.

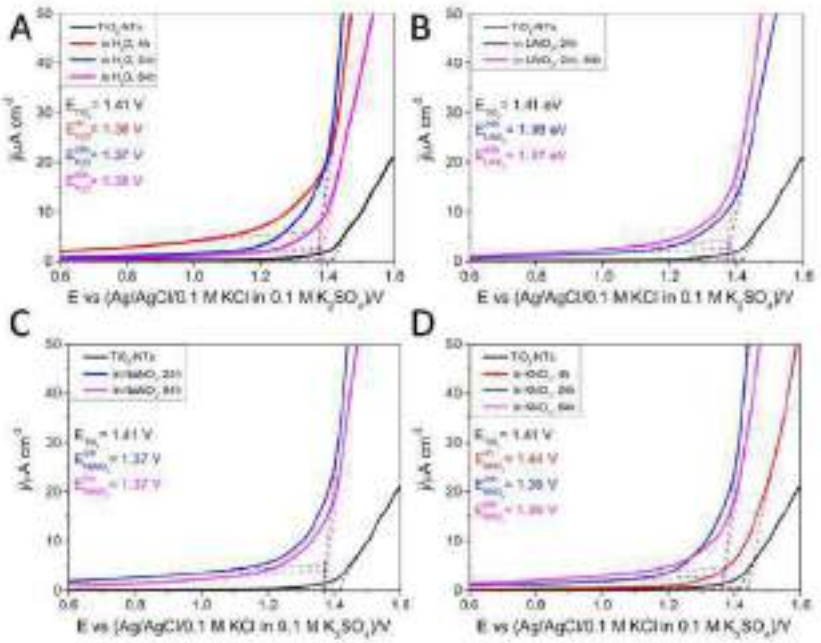

Fig. 9. Linear sweep voltammetry curves obtained for samples without and after hydrothermal annealing, used for the evaluation of the water oxidation threshold potential with a sweep rate of 20 mV/s.

3.3. Electrochemical and photoelectrochemical properties

3.3.1. Electrochemical impedance spectroscopy in the dark

Electrochemical impedance spectroscopy was used to measure the impedance of polarized samples under stationary conditions in the frequency range from 20 kHz to 1 Hz (AC signal amplitude 10 mV). Figs. S9-S12 show the typical capacitive character of the electrode/electrolyte interface, as the almost vertical spike of impedance function is recorded. According to the Mott-Schottky function, the values of the flat band potential (E_{fb}) obtained based on EIS measurements were determined. Obtained results show that HA changes the effective flat band potential. The evaluated means E_{fb} of the obtained electrodes are juxtaposed in Table 3. The samples after HA in water (24 h) and aqueous electrolytes of 0.15 M KNO_3 (64 h) exhibit changed E_{fb} values compared to TiO_2-NTs before hydrothermal treatment (0.2 V and 0.25 differences toward anodic direction, respectively). These changes significantly affect the availability of electrons in the conduction band and the course of the electrode reaction. Furthermore, for the sample hydrothermally annealed in water for 24 h, the number of donors (N_D) was estimated. Constant values, like the static dielectric constant for anatase nanotubes $\varepsilon = 38$, used for calculations of N_D were taken from [18,76]. The average value of N_D is $3.62 \cdot 10^{17}$ cm^{-3} (calculated from impedance function measured at 1 kHz). Estimated values of N_D are in agreement with previous reports on titania nanotubes [77,78].

3.3.2. Cyclic voltammetry in the dark

Obtained electrode materials were subjected to electrochemical studies in the dark using cyclic voltammetry measurements in 0.1 M K_2SO_4 in the three-electrode cell. Recorded current can indicate changes in electroactivity caused under hydrothermal treatment [120]. Fig. S13A-D show typical CV curves for all titania nanotube electrodes elicited in this work. For all samples hydrothermally annealed for 4 h, the curves overlap with the CV plot for unmodified TiO_2-NTs. Thus one may conclude no significant changes influence surface species reduction. However long-term hydrothermal modification brings about diminishing electroactivity in comparison with the activity of not modified TiO_2. Every obtained electrode subjected to the 64-h treatment achieved reduced current densities in the potential range −0.1 to −0.7 V. Such observation may indicate geometric changes of studied electrodes caused during long-term HA both in water and in alkali metal electrolytes. Fig. 9A–C show that the samples, modified in H_2O and electrolytes $LiNO_3$, $NaNO_3$ up to 24 h behave similarly with minor trends in diminishing current density. Fig. 9D gives proof that a drop in current density for a sample modified in KNO_3 is recorded for the sample treated shorter in a hydrothermal autoclave – 24h. Current holds the same value in progressive treatment for 64h in KNO_3. Polarization limited to −0.6 V does not allow the appearance of complete reduction of H_2O with hydrogen generation. Thus in this narrow potential range one may test electroactive surface area without changes in the bulk TiO_2.

3.3.3. Linear sweep voltammetry in the dark

LSV curves are presented in Fig. 9A–D. Polarization towards high anode potentials for water thermal annealed samples shows slight differences in the threshold potentials (E_{th}) for oxygen evolution reaction (OER). In the case of thermally modified samples in water (Fig. 9A), an increase in electroactivity towards water oxidation in the dark (up to 40 mV compared to calcined TiO_2-NTs) was observed. The largest slope of the tangent to the LSV curve was obtained for TiO_2-NTs in H_2O (24 h).

Samples treated with 0.15 M $LiNO_3$ and 0.15 M $NaNO_3$ for 4 h show the worst evaluation in threshold potentials (not observed in this range).

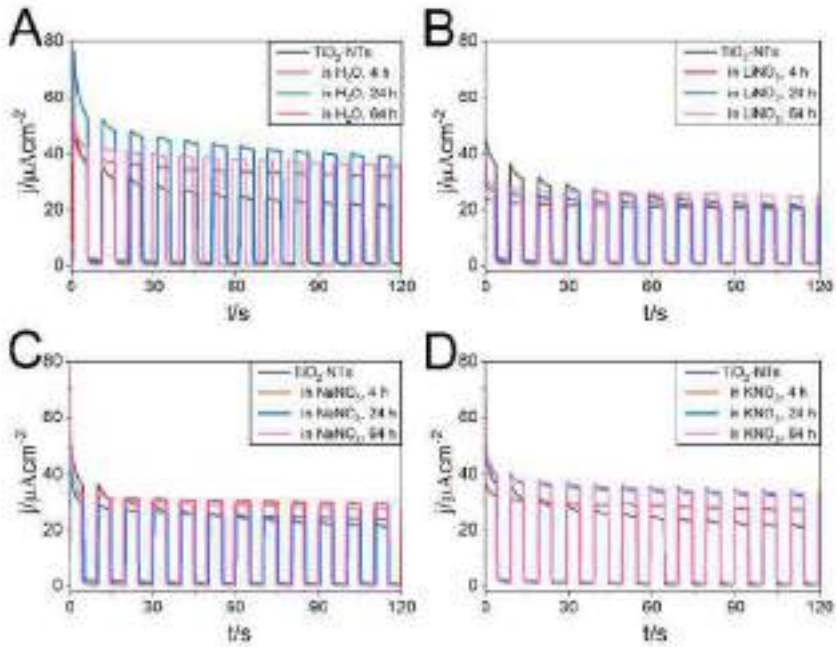

Fig. 10. The chronoamperometry curves, showing the photocurrent density for pure and hydrothermally modified water, $LiNO_3$, $NaNO_3$, KNO_3 titania nanotubes electrodes, at E = + 0.5 V, measured in an aqueous solution of 0.1 M K_2SO_4.

Table 4
Determined differences between the current registered for a sample in the dark and under its illumination (Δj) at E = + 0.5 V for TiO_2-NTs (for t = 120 s) before and after hydrothermal annealing.

Δj (mA cm^{-2}) for TiO_2-NTs	in $LiNO_3$	in $NaNO_3$	in KNO_3	in H_2O
4 h	19.7	20.3	27.2	31.9
24 h	20.6	25.2	30.2	36.5
64 h	24.1	29.1	32.8	38.9

For the other electrodes hydrothermally modified in all electrolytes for 24 and 64 h (Fig. 9B–D), the curves have a very similar course, reaching reduced E_{in}. The drop in the E_{in} for the HA electrodes indicates the efficiency of this process indicating improvement in most cases of electrode kinetics for hydrothermally treated titania nanotubes in water and alkali metals nitrates.

3.3.4. Chronoamperometry under solar light illumination

Fig. 10A-D shows the dependence of the generated photocurrent density with time at a constant potential of 0.5 V versus Ag/AgCl in 0.1 M KCl for titania nanotubes before and after HA. Under simulated sunlight illumination, the highest photocurrent generation exhibit TiO_2-NTs after 24 h of water annealing at 100 °C. It is nearly twofold higher in comparison to titania nanotubes without hydrothermal modification. Table 4 presents a summary of the photocurrent response (difference between the current density under light illumination and the current density in the dark) for all electrodes.

The photocurrent obtained for the unmodified TiO_2 NTs is 20.7 μA cm^{-2} (taken from the chronoamperometry curve). Table 4 shows that for each chosen HA time, electrodes treated in water obtained the highest photocurrent densities. In addition, TiO_2-NTs modified in the electrolytes tend to obtain better photoactivity with a larger alkali metal cation. The exception here is one sample HA in the sodium electrolyte after 4 h. The observed photoactivity is in agreement with the UV absorption data presented above. Recorded differences are also consistent with expected changes in surface –OH groups population in the case of alkali metal cations, see Eq. (2). Formation of –OMe surface groups is expected to cause a diminution in possible dissociative absorption of water molecules during the oxidation process. However, differences between particular cations require further studies. One may expect direct relation between the number of cations present in TiO_2 and titania photoactivity, but the quantitative evaluation is not possible due to the low EDX measurement accuracy. Despite this, the experiment confirms that the absorption of light in the UV range is the key factor considering an increase in photoelectroactivity. The highest photogeneration of the currents (obtained for 24 h of HA) can be explained by the additional absorption of light from the outer walls of the nanotubes (spared TiO_2-NTs) [79].

3.4. Photocatalytic performance

The adsorption and photodegradation activity of the obtained photocatalysts were evaluated through investigating the changes of MB dye concentration in the dark as well as under simulated sunlight illumination (Fig. 11). First, the samples were left without irradiation for 30 min before switching on the light to achieve equilibrium of the adsorption/desorption process. As can be seen, the adsorption of the dye by the materials (within 30 min) is insignificant. Next, for comparison, a blank experiment under sunlight illumination without a photocatalyst

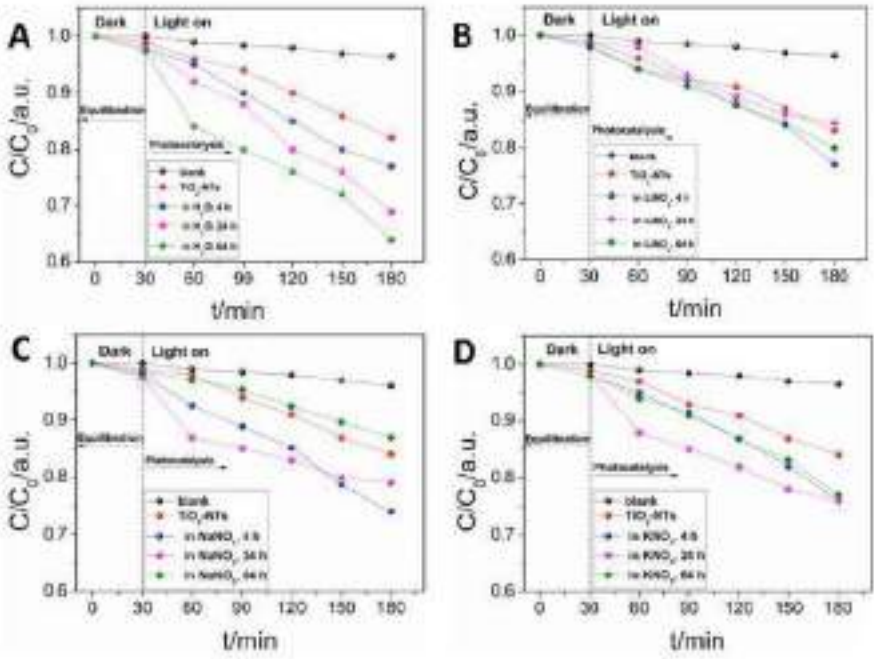

Fig. 11. Methylene Blue degradation for all obtained samples

Table 3
Determined relative percentages of the final concentration of MB obtained after 30 min of photocatalytic degradation for 150 min (preceded by the 30-min adsorption-desorption equilibrium) in the presence of appropriate electrodes.

C/C_0 · 100 (%) for TiO_2-NTs in	$LiNO_3$	$NaNO_3$	KNO_3	H_2O
4 h	29	35	28	35
24 h	16	21	24	31
44 h	20	12	29	36

material was also performed (black line in each chart). A positive effect of hydrothermal annealing on the photocatalytic properties of titanium dioxide nanotubes was observed in almost every case. However, the greatest improvement can be seen for a material that has been modified in water. The highest photocatalytic activities were observed for the samples modified in water, although the narrowing of the energy gap was the smallest here. It can be concluded that E_{bg} narrowing is not essential. The final results of the increments of photodegradation of methylene blue (after 30 min of achieving the adsorption-desorption equilibrium and 150 min of illumination) are presented in Table 3. As observed in the SEM, the material after hydrothermal treatment is characterized by a different, more ordered morphology, nanotubes are opened and the distances between the tubes are greater (spaced NTs). Moreover, the absorption in the UV region for the TiO_2-NTs(HA,24h) is the highest among all samples. Thus, enhanced activity can be attributed to the improved absorbance capability in the UV range. Moreover, heterogeneous photocatalysis is a surface process and catalysts after hydrothermal treatment have different surface characteristics [93]. This causes a difference in the total TiO_2 surface exposed to the light beam and available for contaminant adsorption.

Furthermore, probably the HA led to a change in the surface physicochemical properties of the TiO_2 (hydroxyl groups population increases in comparison with calcined nanotubes, removal of carbon-containing species, as proven by XPS studies, Figs. 4, S3 and S4). It had been proved that the hydroxyl groups have a significant effect on the photocatalytic activity of the photocatalyst [81]. The surface hydroxyls could mediate electron transfer from the TiO_2-NTs surface to electron acceptors [82]. This results in a reduction of electron-hole recombination. Therefore, the enhanced photocatalytic activity may be related to the increasing number of hydroxyl groups on the surface of titania nanotubes. However, the presence of alkali metal ions leads to a reduction in the photocatalytic efficiency of modified nanotubes compared to those modified in water. It is most visible in the case of HA in $LiNO_3$, regardless of the lowest bandwidth.

In general, the qualitative results of the photocatalytic MB decolorization presented in Fig. 11 prove that hydrothermal modification of time to obtain better results (especially those HA in water) compared to TiO_2 nanotubes after simple calcination, as well as it is achieved for photoelectrocatalytic oxidation of water.

4. Conclusions

It has been shown in the work that the hydrothermal annealing of calcined TiO_2-NTs samples is a good tool to increase the photo and photoelectrochemical activity TiO_2-NTs photoanode. The TiO_2-NTs samples obtained in the results of the HA carried out in water show the best photoactivity and photoelectroactivity. Hydrothermally treated samples in electrolytes ($LiNO_3$, $NaNO_3$, KNO_3) exhibit better photoactivity and photoelectroactivity in comparison to not HA modified TiO_2-NTs,

however not as high as there modified in water. The presence of alkali metal cations in the subsurface area lowers photoactivity. All samples show higher photoactivity towards MB degradation, lower threshold potential of the OER process, and slightly higher photoelectroactivity. The main factors that led to such a change were the increase in UV absorbance as a result of morphology alteration and the elimination of F and P elements from TiO_2-NTs material. The optical bandgap narrowed and markedly shifted position of flat-band potential was recorded mostly for samples modified in electrolytes. It was noted that for the hydrothermally treated samples, the XPS Ti (2*p*) p spectra change, proving alternation in the surroundings of the Ti (IV) ion and a decrease in the content of carbon common species (–CO, – C=O). F and P (XPS, EDS) was recorded for each sample. These changes are accompanied by a significant increase in the photoactivity of the modified samples in water. The changes in photoactivity and photoelectroactivity for the modified samples in electrolytes are not so significant, very likely due to cations taking part in building semiconductor near surface space. Their presence is any result in the proportion of surface hydroxyl groups participation in the photocatalytic and photoelectrochemical processes. Conclusions resulting from the observation of changes in the spectrophotometric VIS spectrum allow for the assessment of changes in the geometry/morphology of the sample due to Fabry-Pérot interferometry. The phenomena of interferometry may overlap with the described effects of the absorption of visible light due to the appearance of mid-gap band states and electronic transitions. The evaluation of their quantitative participation is not feasible. As it is expected sample exhibiting the highest absorption maximum, obtained after HA treatment in water for 24 h, is presenting the best photoelectrocatalytical activity.

CRediT authorship contribution statement

Mariusz Wolak: Methodology, Formal analysis, Data curation, Writing – original draft, Visualization, Writing – review & editing. **Mariusz Szkoda:** Writing – review & editing, Data curation. **Grzegorz Gajowiec:** Funding acquisition. **Kacper Juraś:** Funding acquisition, Methodology. **Grzegorz Trykowski:** Funding acquisition, Methodology. **Anna Lisowska-Oleksiak:** Conceptualization, Methodology, Supervision, Writing – review & editing.

Declaration of Competing Interest

The authors declare that we have no known competing financial interests or personal relationships that could have appeared to influence the work reported in this paper.

Data availability

Data will be made available on request.

Acknowledgments

Authors MW and ALO are grateful for financial support from Gdańsk University of Technology Statutory financial support, especially from the mini grant subsidy from the fund supporting the development of young academics in 2021 (grant no. 035138). Authors MSz acknowledges financial support from The National Centre for Research and Development, grant no. LIDER/15/0008/L-10/18/NCBR/2019 (Integrated prototype of a photo-supercapacitor for energy storage obtained as a result of solar radiation conversion). Authors acknowledge Professor Anna Zielińska-Jurek from Gdańsk University of Technology for providing equipment for XRD and UV-Vis spectroscopic measurement.

Supplementary materials

Supplementary material associated with this article can be found, in the online version, at doi:10.1016/j.electacta.2022.140988.

References

[1] D. Gong, C.A. Grimes, O.K. Varghese, W. Hu, R.S. Singh, Z. Chen, E.C. Dickey, Titanium oxide nanotube arrays prepared by anodic oxidation, J. Mater. Res. 16 (2001) 3331–3334, https://doi.org/10.1557/JMR.2001.0457.

[2] J.M. Macak, H. Tsuchiya, A. Ghicov, K. Yasuda, R. Hahn, S. Bauer, P. Schmuki, TiO_2 nanotubes: self-organized electrochemical formation, properties and applications, Curr. Opin. Solid State Mater. Sci. 11 (2007) 3–18, https://doi.org/10.1016/j.cossms.2007.08.004.

[3] S. Berger, J. Kunze, P. Schmuki, A.T. Valota, D.J. LaCflare, P. Skeldon, G. E. Thompson, Influence of water content on the growth of anodic TiO_2 nanotubes in dimethylsulfoxide containing ethylene glycol electrolytes, J. Electrochem. Soc. 157 (2010) C18, https://doi.org/10.1149/1.3253588.

[4] H. Ozkan, S. Dursun, A. Sarf, A.R. Anderson, Influence of anodization parameters on the morphology of TiO_2 nanotube arrays, Superlattices Microstruct. 98 (2016) 24–38, https://doi.org/10.1016/j.spmi.2016.08.026.

[5] S. Sreekantan, Z. Lockman, R. Hazan, M. Tasbihi, A.R. Tseng, A.R. Mohamed, Influence of electrolyte pH on TiO_2 nanotube formation by Ti anodization, J. Alloy. Compd. 485 (2009) 478–483, https://doi.org/10.1016/j.jallcom.2009.05.122.

[6] T. Arnoldi, T. Bharagavendra, I. De Graeve, J. Fransaer, H. Terryn, Influence of the anodizing temperature on surface porosity and the mechanical properties of the porous oxide style film, Surf. Coat. Technol. 201 (2007) 7310–7315, https://doi.org/10.1016/j.surfcoat.2007.01.014.

[7] W. Jun, L. Zhiqiu, Anodic formation of ordered TiO_2 nanotube arrays: effects of electrolyte temperature and anodization potential, J. Phys. Chem. C 113 (2009) 4026–4030, https://doi.org/10.1021/jp811023d.

[8] M. Kulkarni, A. Mazare, P. Schmuki, A. Iglic, Influence of anodization parameters on morphology of TiO_2 nanotube-mediated multicom, Int. Assoc. Adv. Mater. 7 (2016) 33–39, https://doi.org/10.53292/aam.2016.7.4.033.

[9] A. Paszkiewicz, M. Zatoń, R. Szymański, S. Mozia, G.-N. and S-doped TiO_2 photocatalysts: a review, Catalysts 11 (2021) 144, https://doi.org/10.3390/catal11010144.

[10] A. Lisowska-Oleksiak, K. Nadolna, V. Anicai, Preparation and characterization of visible light responsive iodine doped TiO_2 electrodes, Electrochim. Acta 85 (2012) 583–589, https://doi.org/10.1016/j.electacta.2012.08.094.

[11] M. Szkoda, K. Trzciński, A. Lisowska-Oleksiak, Non-metal doped TiO_2 nanotube arrays for high efficiency photocatalytic decomposition of organic species in water, Phys. Status Solidi Rapid Res. Lett. 10 (2016) 151–158, https://doi.org/10.1002/pssr.201510304.

[12] D. Zhang, J. Chen, Q. Xiao, Y. Li, M. Liu, Y. Hou, Transition-metallic (Fe, Co, Ni, Mn, Zn) Doping of TiO_2 nanotubes: a general approach, Inorg. Chem. 59 (2019) 12551–12562, https://doi.org/10.1021/acs.inorgchem.9b01691.

[13] M. Wolak, M. Szkoda, G. Gajowiec, M. Gazda, K. Juraś, M. Szeremeta, A. Lisowska-Oleksiak, Hydrothermal cobalt doping of titanium dioxide nanotubes towards photocurrent activity enhancement, Materials 14 (2021) 2907, https://doi.org/10.3390/ma14112907, 2021, Vol. 14, Page 2907.

[14] S.P. Shirsath, S.M. Jadhav, V.K. Tamboli, V.V. Kane, Ways to improve the efficiency of TiO_2 based photocatalysts (review), Phys. Chem. Solid State 11 (2010) 380–391, https://doi.org/10.15330/PCSS.11.2.380-391.

[15] M.J. Abdi, S. Pourazar, S. Farrokhi, T. Ahmadi, Z. Bagheri, M. Tang, Highly integrated microcomposite of $BiVO_4/TiO_2$ nanotubes for enhanced removal of microbes from water, Environ. Technol. 40 (2019) 2567–2576, https://doi.org/10.1080/09593330.2018.1447021/SUPPL_FILE/TENT_A_1447021_SM4424.DOCX.

[16] A. Gnayfeddi, P. Gnedovets, J. Kaczmarek, J. Ryl, I. Wysocka, E. Stanfak, G. Trykowski, E. Grochowska, A. Zielińska-Jurek, Enhanced photocatalytic activity of nanofilm Cu-layered TiO_2 (MXene) coupled with Fe-modified covalent triazine particles exposing {1 0 1} and {0 0 1} facets, Chem. Eng. J. 426 (2021) 130831, https://doi.org/10.1016/J.CEJ.2021.130831.

[17] M. Sun, X. Shi, K. Chen, Y. Sun, S. Cui, T. Lu, A nanocomposite of cuprous oxide and TiO_2 nanotube arrays enhancing photoelectrochemical and photocatalytic properties, RSC Adv. 4 (2013) 1128–1137, https://doi.org/10.1039/C3RA45470F.

[18] A.S. Arapov, M. Klimkiewicz, T. Łęcki, M. Zarębska, J. Wilczura-Wachnik, M. Szczepanik, Synthesis and application of N-doped TiO_2/GO/poly(1,5-diaminoanthracene) composite for photocatalytic degradation of 4-chlorophenol under visible light, Electrochim. Acta 314 (2019) 79–89, https://doi.org/10.1016/J.ELECTACTA.2019.05.092.

[19] M. Skoda, H. Duda, M. Erkal, L. Hasanlou, Z.O. Tandoğdu, O. Bucak, J. M. Macak, Comparison of photoelectrochemical performance of anodic single- and double-walled TiO_2 nanotube layers, Electrochem. Commun. 97 (2018) 1–5, https://doi.org/10.1016/J.ELECOM.2018.09.018.

[20] M. Skoda, L. Hasanlou, J. Vakili, H. Duda, M. Erkal, J.M. Macak, Intrinsic properties of high-aspect-ratio single- and double-wall anodic TiO_2 nanotube layers annealed at different temperatures, Electrochim. Acta 352 (2020) 136479, https://doi.org/10.1016/J.ELECTACTA.2020.136479.

[21] S. Jafari, R. Mahyad, H. Hadianfard, S. Taghavi, T. Gholikhani, L. Tayebi, Biomedical applications of TiO_2 nanostructures: recent advances, Int. J. Nanomed. 15 (2020) 3447, https://doi.org/10.2147/IJN.S249411.

[22] M. Javed, A. Farid, M. Sivasankaran, M. Jalbani, G.D. Sidhu, Nanoporous anodic titanium dioxide layer as potential drug delivery system: drug release kinetic

M. Wahdi et al. Electrochimica Acta 420 (2022) 140402

and mechanisms, Colloids Surf. B Biointerfaces 140 (2016) 447–454. https://doi.org/10.1016/j.colsurfb.2015.10.053.
[23] D. Martínez-Márquez, E. Odabaş, C.P. Carty, R.A. Stewart, S. Iranzo-Ali, Determining the relative importance of kinetic parameters electrolyte ion and base implant surface performance a quality by design study with a fuzzy approach, Mater. Sci. Eng. C Mater. Biol. Appl. 114 (2020). https://doi.org/10.1016/j.msec.2020.111006.
[24] O. Wittich, P. Meyer, M. Wark, Lifetime insertion ion exited phase thesis nanotubes, Z. Phys. Chem. 231 (2017) 1407–1421. https://doi.org/10.1515/zpch-2016-0917.
[25] P. Roy, S. Berger, P. Schmuki, TiO_2 nanotubes: synthesis and applications, Angew. Chem. Int. Ed. 50 (2011) 2904–2939. https://doi.org/10.1002/anie.201001374.
[26] T. Seesaplasa, J.H. Yun, S.N. Nam, K.D. Suh, P.G. Pinpan, J.-O. Kim, L.R. Chen, The influence of geometrical characteristics on the photocatalytic activity of TiO_2 nanotube arrays for degradation of refractory organic pollutants in wastewater, Water Sci. Technol. 75 (2017) 1304–1309. https://doi.org/10.2166/wst.2016.604.
[27] F. Riboni, H.T. Nguyen, S. So, P. Schmuki, Aligned metal oxide nanotube arrays: key-aspects of anodic TiO_2 nanotube formation and properties, Nanoscale Horizons 1 (2016) 445–466. https://doi.org/10.1039/C6NH00068J.
[28] M. Tomassini, V.A. Bighiardi, D. Pierucci, M.E. Ballard, R. Tremolada, M. Brunori, M. Scarpinelli, T. Ippolito, Optical and electrochemical properties of self-organized TiO_2 nanotube arrays from anodized Ti-6Al-4V alloy, Front. Chem. 7 (2019) 695. https://doi.org/10.3389/fchem.2019.00695.
[29] V. Alwarappan, K. Jayaraman, M. Muthukumar, G. Kumaran, D. Johnstone, A. Bennani, S. Nikolaki, Z.Y. Fan, Optical and electrical properties of TiO_2 nanotubes grown by titanium anodization, MRS Online Proc. Libr. 1170 (2009) 85–90. https://doi.org/10.1557/PROC-1170-A04-07.
[30] L. Ramasubramanian, H. Jia, N. Liu, P. Schmuki, A review of photocatalysis using self-organized TiO_2 nanotubes and other ordered oxide nanostructures, Small 8 (2012) 3071–3109. https://doi.org/10.1002/smll.201200644.
[31] J. Pu, G. Sui, B. Cheng, Effect of crystallization methods on morphology and photocatalytic activity of anodized TiO2 nanotube array films, J. Phys. Chem. C 114 (2010) 19771–19778. https://doi.org/10.1021/jp1064576.
[32] D. Wang, L. Liu, F. Zhang, Z. Yu, R. Pippel, H. Boerner, Spontaneous phase and morphology transformation of anodized TiO_2 nanotubes induced by water at room temperature, Nano Lett. 11 (2011) 3649–3655. https://doi.org/10.1021/nl201945r.
[33] C. Cao, J. Yan, F. Zhang, L. Zhao, Stability of titania nanotube arrays in aqueous environment and the related factors, Sci. Rep. 6 (2016) 1–9. https://doi.org/10.1038/srep32305.
[34] L. Ng, H. Snyder, B. Krupp, J. Speck, V. Rajkovic, P. Strunk, L. Hernandez, J. Pickrell, J.M. Marek, TiO_2 ALD coating of amorphous TiO_2 nanotube layers: inhibition of the structural and morphological changes due to water annealing, Front. Chem. 7 (2019) 50. https://doi.org/10.3389/fchem.2019.00050.
[35] A.E. Tesler, M. Almanza, P. Schmuki, Morphology and optical properties of highly ordered TiO_2 nanotubes grown in NH_4F/o-H_3PO_4 electrolytes in view of light-harvesting and catalytic applications, ACS Appl. Nano Mater. 3 (2020) 10906–10915. https://doi.org/10.1021/acsanm.0c02194.
[36] F. Fu, G. Cha, N. Denisov, Y. Chen, Y. Zhang, P. Schmuki, Water annealing of TiO_2 nanotubes for photocatalysis revisited, ChemElectroChem 7 (2020) 3792–3796. https://doi.org/10.1002/celc.202000622.
[37] N. Liu, G.S. Alberi, E. Lee, S. Ge, P. Schmuki, Water annealing and other low temperature treatments of anodic TiO_2 nanotubes: a comparison of properties and influence on dye sensitized solar cells and for water splitting, Electrochim. Acta 62 (2012) 99–102. https://doi.org/10.1016/j.electacta.2011.06.016.
[38] Anasuya Nair (n.d.). https://www.researchgate.net/profile/Anasuya-Nair-2/publication/321440624_Effect_of_Annealing_Temperature_on_Photocatalytic_Activity_of_TiO2_Nanotube_Arrays/links/5a1f2e0e0f7e9b1b0c5e5e5e/Effect-of-Annealing-Temperature-on-Photocatalytic-Activity-of-TiO2-Nanotube-Arrays.pdf (accessed March 11, 2021).
[39] K. Lopes, M. Sopha, J. Pulpytel, M. Rebl, J. Strnisk, F. Dvorak, L. Hennedbu, J. M. Marek, S. 1D conical nanotubular TiO_2/CdS heterostructure with superior photon-to-electron conversion, Nanoscale 10 (2018) 16801–16812. https://doi.org/10.1039/c8nr05374k.
[40] K. Qian, J. Sun, S.Yi. Kay, J.S. Chen, J. Li, S. Gan, N.S. Godbole, Imaging dynamics on the Fe^{3+}/Fe^{2+} redox potential energy surface from cells to bacteria, Science 365 (2019) 366–369. https://doi.org/10.1126/science.aaw1247.
[41] P. Pu, H. Cachet, E. Sutter, Electrochemical impedance spectroscopy and photoelectrochemical impedance spectroscopy of highly ordered semiconductor TiO_2 nanotube arrays in aqueous electrolyte, J. Solid State Electrochem. 17 (2013) 2709–2717. https://doi.org/10.1007/s10008-013-2169-6.
[42] M. Sahoo, E. Yoshida, A. Lorenzo-Gabriel, E. Emelik, Electrochemical and photoelectrochemical properties of the interface between TiO_2 nanotubes covered by conducting polymer in aqueous by combining polymer in aqueous electrolytes – the effect of various geometry and electrolyte concentration, Appl. Surf. Sci. 440 (2018) 509–519. https://doi.org/10.1016/j.apsusc.2018.01.164.
[43] E. Lee, S. Sloan, P. Schmuki, One-dimensional titanium dioxide nanomaterials: nanotubes, Chem. Rev. 114 (2014) 9385–9454. https://doi.org/10.1021/cr500061m.
[44] D. González, J. Heras-Domingo, T. Plamadeala, A. Rincón, L. Rodríguez-Santiago, X. Solans-Monfort, M. Sodupe, Water adsorption on 001, 101 – Ti, Ru, and Ir surfaces: importance of attractive dispersion and cooperative effects, ACS Omega 4 (2019) 2989–2999. https://doi.org/10.1021/acsomega.8b03149.
[45] J.M. Macak, S. Aldabergerova, A. Ghicov, P. Schmuki, Smooth anodic TiO_2 nanotubes: annealing and structure, Phys. Status Solidi 203 (2006) 967–1004. https://doi.org/10.1002/pssa.200600514.
[46] Anatase R060377 - 88189 Anatase Source, X-ray, Infrared, and ... (n.d.). https://matdata.io/Anatase/R060377 (accessed March 11, 2021).
[47] Crystallography open database information card for entry 9008517. (n.d.). http://www.crystallography.net/cod/9008517.html (accessed March 14, 2021).
[48] P.W. Elfenthaler, T. Ehlenfeld, M. Wenzel, C.P. Liu, M.W. Rudolf, B.-A. Bunea, B. W. Strodthoff, Particle size and grain size of TiO_2 nanoparticles from TEM, Raman spectroscopy and XRD: the crystallinity of the Williamson-Hall plot method, Results Phys. 9 (2018) 835–839. https://doi.org/10.1016/j.rinp.2018.03.068.
[49] N.L. Feighan Cochrane, S. Khamsuwan Ali, M. Magliocchi, The effect of doping concentration of TiO_2 nanotubes on energy levels and its direct correlation with photocatalytic activity, Thin Solid Films 690 (2019). https://doi.org/10.1016/j.tsf.2019.137508.
[50] M. Balakrishnan, P. Marwala, S. Nagarajan, N. Lakshmana, Influence of crystallite size and surface morphology on the mechanical properties of annealed TiO_2 nanotubes, Appl. Surf. Sci. 355 (2015) 1245–1253. https://doi.org/10.1016/j.apsusc.2015.08.015. (accessed February 3, 2022).
[51] K. Gen, E. Ziegler, J. Pelzing, P. Bruder, M. Erbel, H. Snyder, T. Dellmann, J. M. Marek, Influence of annealing temperature on the properties of ion exposed ratio TiO_2 nanotube layers, Electrochim. Acta 313 (2019) 455–468. https://doi.org/10.1016/j.electacta.2019.05.013.
[52] R. Hosein, C. Russell, D.M. Hanna, T.C. Sorrell, Titanium white pigment by melt phase double analysis, J. Mater. Sci. 46 (2011) 4161–4167. https://doi.org/10.1007/s10853-010-5111-0.
[53] SST Kcsp Photoelectrochemistry (3D) Database, 2022. Version 3.0. (n.d.). https://tabletmonster.com/sst/. (accessed March 14).
[54] N. Mahdi, F. Bottari, A. Giovanni, R. Pendolini, S. Shankar, H. Sabirzhan, Robust polymer nanocomposite membranes incorporating discrete TiO_2 nanotubes for water treatment, Nanoscale 9 (2017) 1180. https://doi.org/10.1039/c6nr08881d.
[55] M.V. Kuznetsov, J.F. Zhuravlev, V.A. Gubanov, XPS study of the titanium oxides and oxycarbides of titanium, J. Electron Spectros. Relat. Phenom. 68 (1994) 1–8. https://doi.org/10.1016/0368-2048(94)02012-0.
[56] M. Lübbe, E. Peppel, M. Lerch, I. Mutlu, A. Springer, P. Mazierski, A. Zaleska-Medynska, J. Grzyb, G. Sadowski, Thermal annealing of mixed TiO_2 nanotube arrays with water vapor-mixed synthesis gases under a continuous gas flow for superior photocatalytic performance, Chem. Eng. J. 425 (2021). https://doi.org/10.1016/j.cej.2021.130618.
[57] V. Swaminathan, J. Dawkins, J. Bennett, M. Turner, S. Mango, J.J. Rubin, Self-assembly of poly(ethylene glycol)-poly(alkyl phosphonate) copolymers on titanium oxide surfaces: interface characterization, investigation of oxidation properties, and long-term stability, Langmuir 36 (2018) 74–83. https://doi.org/10.1021/acs.langmuir.9b02130.
[58] R.F. Sun, J.S. Kwon, Y.B. Choi, E.M. Choi, S.N. Han, Cellular attachment and differentiation on titania nanotubes exposed to air- or nitrogen-based post-thermal atmospheric pressure plasma, PLoS ONE 9 (2014), e113477. https://doi.org/10.1371/journal.pone.0113477.
[59] P. Mazierski, M. Mozia, M. Grabowska, W. Lisowski, M. Gazda, M.J. Winiarski, T. Klimczuk, J. Zaleska-Medynska, Photocatalytic activity of nitrogen doped TiO_2 nanotubes prepared by anodic oxidation: the effect of applied voltage, oxidization time and amount of nitrogen dopant, Appl. Catal. B Environ. 198 (2016) 77–86. https://doi.org/10.1016/j.apcatb.2016.05.006.
[60] L. Golicka, K. Bryszak, E. Iwaniec, M. Bacero, C. Escudero, V. Perez-Dieste, J. M. Casavola, D.P. Serrano, J.R. Ramos, V.A. de la Peña O'Shea, Universal log-fit effect of charge dynamics at the photocatalyst-metal/semiconductor interface for CO_2 photoreduction, Nat. Commun. 8 (2017) 1–10. https://doi.org/10.1038/s41467-017-02035-3.
[61] T. Kavinkar, S. Chakkaravarthi, V. Shanmugavelu, J. Kurian, H. Kirsipuu, R. analysis of H-bonded H_2O on the pure TiO_2 surface, J. Mol. Struct. 700 (2004) 175–181. https://doi.org/10.1016/j.molstruc.2003.12.037.
[62] G.E. Park, T.Y. Seo, C.H. Park, J.H. Lim, J. Ave, Effects of calcination temperature on morphology, microstructure, and photocatalytic performance of TiO_2 nanocrystals, Ind. Eng. Chem. Res. 58 (2019) 8238–8248. https://doi.org/10.1021/acs.iecr.9b00307.
[63] N.T. Nolton, D. Marcus, C.F. Kuo, S.L. Lee, M.E.H. Wetsel, Visible light photocrystallization of nanocrystalline rutile TiO_2 nanotubes synthesized via electrochemical oxidation of titanium foil, Nanomater 10 (2020). https://doi.org/10.3390/nano10061118.
[64] S.M. Archontia, T. Sreekanth, M.U. Bernard, D. Lekha, S.S. Nanthkrishna, B. Palanna, Silver modified titanium dioxide thin films for efficient photodegradation of methyl orange, Appl. Catal. B Environ. 43 (2003) 187–201. https://doi.org/10.1016/s0926-3373(02)00313-9.
[65] J.M. Herrmann, J. Disdier, P. Pichat, Photocatalytic deposition of silver on powder titania: consequences for the recovery of silver, J. Catal. 113 (1988) 72–81. https://doi.org/10.1016/0021-9517(88)90258-8.
[66] Y. Jia, L.D. Zhang, G.W. Meng, G.H. Li, X.F. Zhang, C.H. Liang, W. Chen, S. K. Wang, Preparation and photoluminescence of highly ordered TiO_2 nanowire arrays, Appl. Phys. Lett. 78 (2001) 1129. https://doi.org/10.1063/1.1350649.
[67] M. Ewendiksza, S. Dudziak, J. Karczewski, J. Ryl, G. Trykowski, A. Zielińska-Jurek, Role effect of TiO_2 nanostructures from TiNT: and their photocatalytic activity, Chem. Eng. J. 404 (2021), 126496. https://doi.org/10.1016/j.cej.2020.126496.

[68] H. Tang, H. Berger, P.E. Schmid, F. Lévy, G. Burri, Photoluminescence in TiO_2 anatase single crystals, Solid State Commun. 87 (1993) 847–850.

[69] R.T. Wilkins, E.S. Fong, The sulfite radical anion, J. Phys. Chem. Solids 31 (1970) 679–716.

[70] J. Li, H. Fu, Z. Wu, J. Wang, S. He, J. Ji, N. Li, S. Bai, C. Huang, Z. Chen, Y. Chen, C. An, Room temperature synthesis of crystalline anatase TiO_2 on bamboo under ambient and their short-term antifungal capability under natural weather conditions, Colloids Surf. A 543 (2018) 117–125.

[71] L.H.C. Andrade, S.M. Lima, A. Novatski, A.N. Neto, A.C. Bento, M.L. Baesso, F.C.G. Gandra, Y. Guyot, G. Boulon, Spectroscopic assignments of Ti^{3+} and Ti^{4+} in titanium doped-OH- free low silica calcium aluminosilicate glass and role of network defects on the observed long lifetime and high fluorescence of Ti^{3+} ions, Phys. Rev. B 78 (2008) 224202.

[72] J.L. Delplancke, M. Degrez, A. Piscaer, R. Winand, Self-colour anodizing of titanium, Surf. Technol. 16 (1982) 153–162.

[73] G. Archdeacon, F. Gruskiewicz, J. Wiechowski, A new procedure of anodizing of titanium prior films on titanium compositional depth profile analysis, Langmuir 12 (1996) 5009–5010.

[74] A. Wanes, M.F. Garcia-Sanchez, G. Ambrosio, Spectral and physical properties of electrochromically formed colored layers on titanium covered with thin oxides, ACS Appl. Mater. Interfaces 3 (2011) 1195–1203.

[75] A. Al-Hilfeil, Z. Wang, R. Yu, K. Qi, B. Vellaichamy, U. Kumar, T. Liu, Dimensional dependence of the optical absorption band edge of TiO_2 nanotube arrays beyond the quantum effect, J. Phys. Chem. C 119 (2015) 10251–10257.

[76] K. Uddemann, L. Lee, S.Y. Reece, Flat-band potential of a semiconductor: using the Mott-Schottky equation, J. Chem. Educ. 89 (2012) 665–668.

[77] M.C.S. Tellez, E.G. Seebauer, Measurement method for carrier concentration in TiO_2 via the Mott-Schottky approach, Thin Solid Films 519 (2010) 2309–2313.

[78] N. Dreines, N. Dam, H. Gao, P. Schmuki, Photocurrent conversion efficiency of TiO_2 nanotube photoanodes is dependent on illumination intensity, Electrochim. Acta 377 (2021) 137993.

[79] N. Ohtsu, N.T. Nguyen, A. Mazare, P. Schmuki, Optimized spacing between TiO_2 nanotubes for enhanced light harvesting and charge transfer, Chemelectrochem 5 (2018) 3130–3138.

[80] A.L. Rosate, J.M. Archibald, E.S. Tsenkbeis, A.G. Rosate, M.C. Bernard, D. B. Petrakis, P. Falaras, Efficient photocatalysis by hydrothermal treatment of TiO_2, Catal. Today 101 (2005) 255–264.

[81] A. Sclafani, L. Palmisano, M. Schiavello, Influence of the preparation methods of TiO_2 on the photocatalytic degradation of phenol in aqueous dispersion, J. Phys. Chem. 94 (1990) 829–832.

[82] C. Iwakura, F. Salvador, Analysis of the a-TiO_2/electrolyte interface, J. Electroanal. Chem. 530 (2002) 407–413.

III.3 Supplementary Information

Hydrothermal modification of TiO_2 nanotubes in water and alkali metal electrolytes ($LiNO_3$, $NaNO_3$, KNO_3) – direct evidence for photocatalytic activity enhancement

Supplementary

Mariusz Wtulich [1*], Mariusz Szkoda [1], Grzegorz Gajowiec [2], Kacper Jurak [3], Grzegorz Trykowski [4], Anna Lisowska-Oleksiak [1*]

1 Department of Chemistry and Technology of Functional Materials, Faculty of Chemistry, Gdańsk University of Technology, Gdańsk 80-233, Poland;

2 Institute of Machine Technology and Materials, Facuty of Mechanical Engineering and Ship Technology, Gdańsk University of Technology, Gdańsk 80-233, Poland;

3 Department of Electrochemistry, Corrosion and Materials Engineering, Faculty of Chemistry, Gdańsk University of Technology, Gdańsk 80-233, Poland;

4 Department of Materials Chemistry, Adsorption and Catalysis, Faculty of Chemistry, Nicolaus Copernicus University in Toruń, Toruń 87-100, Poland

* Correspondence: mariusz.wtulich@pg.edu.pl; alo@pg.edu.pl

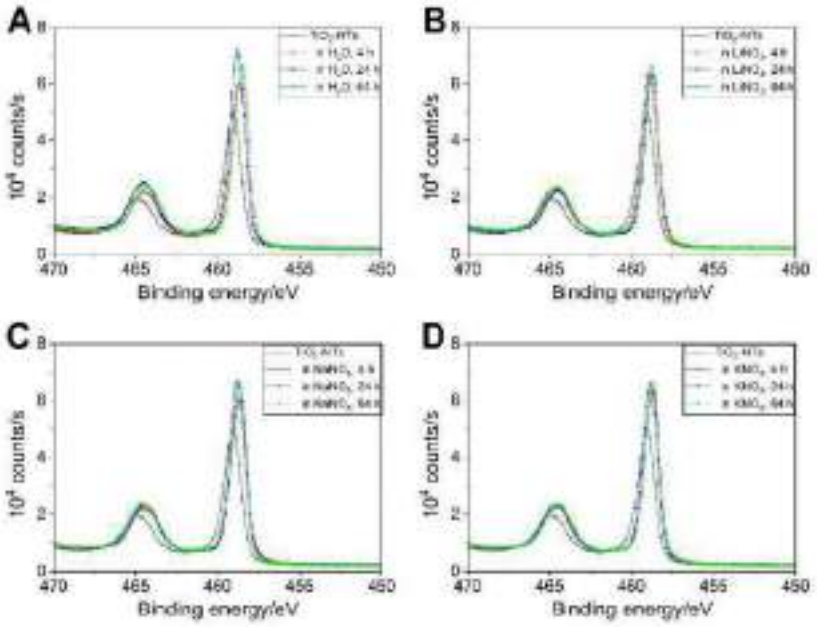

Figure S1. XPS spectra of Ti 2p for TiO_2 NTs before and after hydrothermal annealing in (A) distilled water, (B) 0.15 M $LiNO_3$, (C) 0.15 M $NaNO_3$, (D) 0.15 M KNO_3.

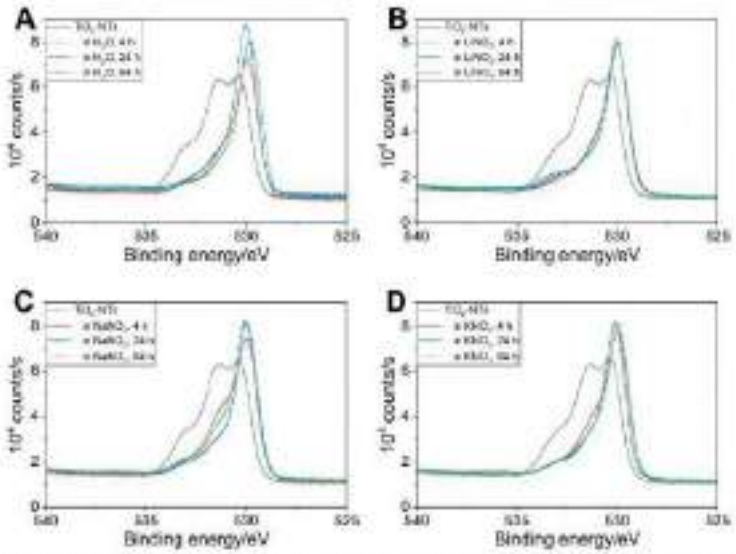

Figure 52. XPS spectra of O 1s for TiO_2-NTs before and after hydrothermal annealing in (A) distilled water, (B) 0.15 M $LiNO_3$, (C) 0.15 M $NaNO_3$, (D) 0.15 M KNO_3. Spectra are narrowing with HA.

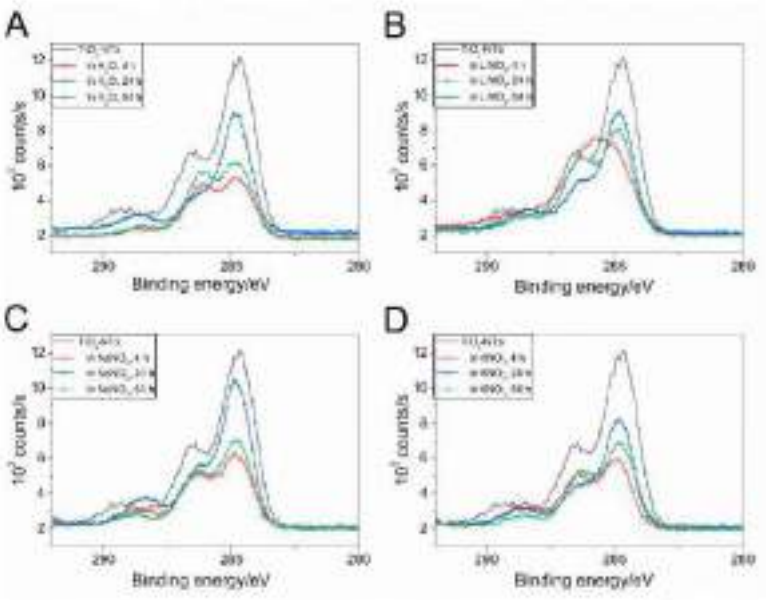

Figure 53. XPS spectra of C 1s for TiO_2-NTs before and after hydrothermal annealing in (A) distilled water, (B) 0.15 M $LiNO_3$, (C) 0.15 M $NaNO_3$, (D) 0.15 M KNO_3.

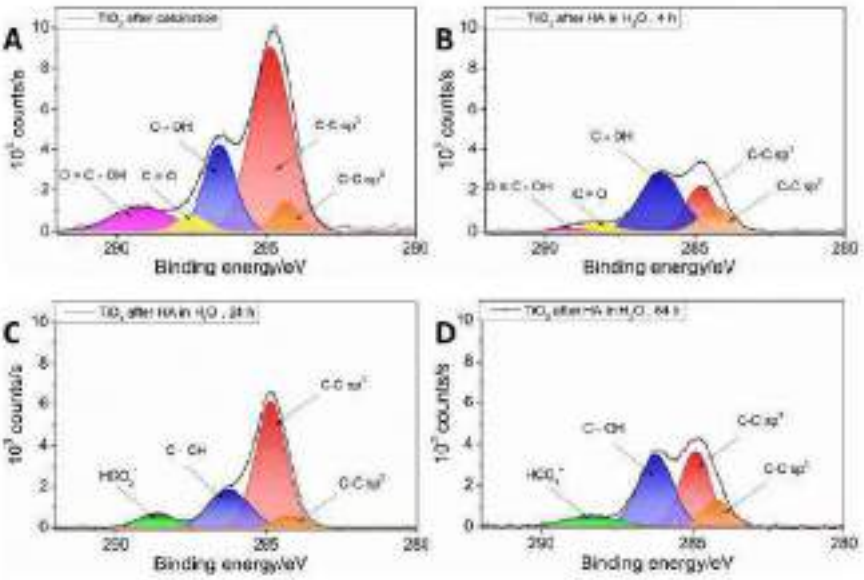

Figure 54. XPS spectra with the fit model including of C 1s for TiO_2-NTs (A) before and after hydrothermal annealing in distilled water for (B) 4 h, (C) 24 h and (D) 64 h.

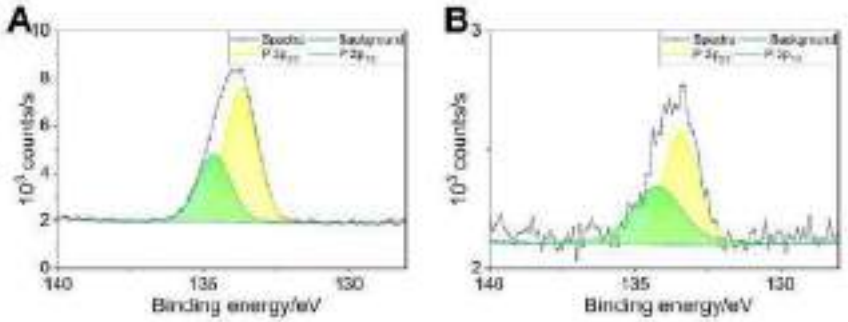

Figure 55. XPS spectra with the fit model including of P 2p for TiO_2-NTs (A) before and (B) after hydrothermal annealing in distilled water for 24 h. Several times lowering the intensity of the peak.

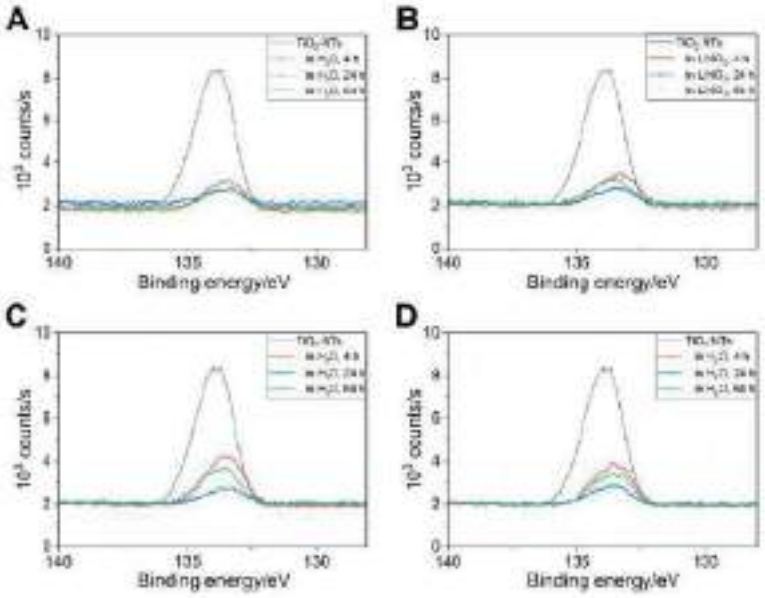

Figure S6. XPS spectra of P 2p for TiO_2-NTs before and after hydrothermal annealing in (A) distilled water, (B) 0.15 M $LiNO_3$, (C) 0.15 M $NaNO_3$, (D) 0.15 M KNO_3.

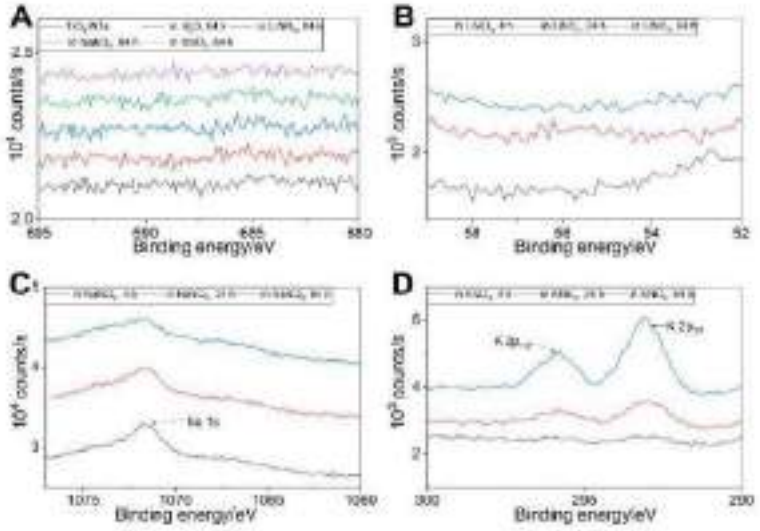

Figure S7. XPS spectra of: (A) fluorine 1s peak, (B) lithium 1s peak, (C) sodium 1s peak and (D) potassium 2p peak for adequate modified TiO_2-NTs.

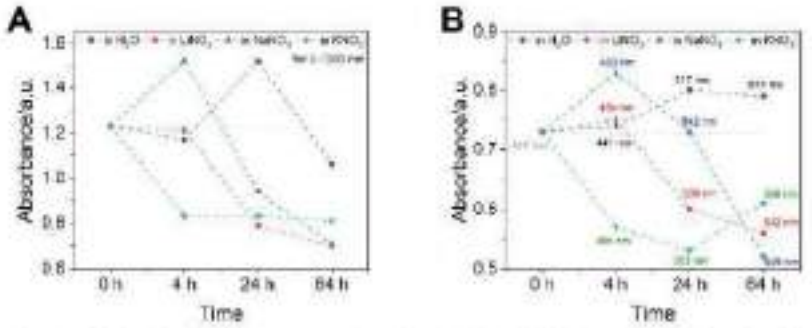

Figure S8. The distribution of the maximum absorption peak for all obtained electrodes in the region of (A) UV (values for all points were selected for λ=300 nm) and (B) Vis light (values for points selected for different wavelengths).

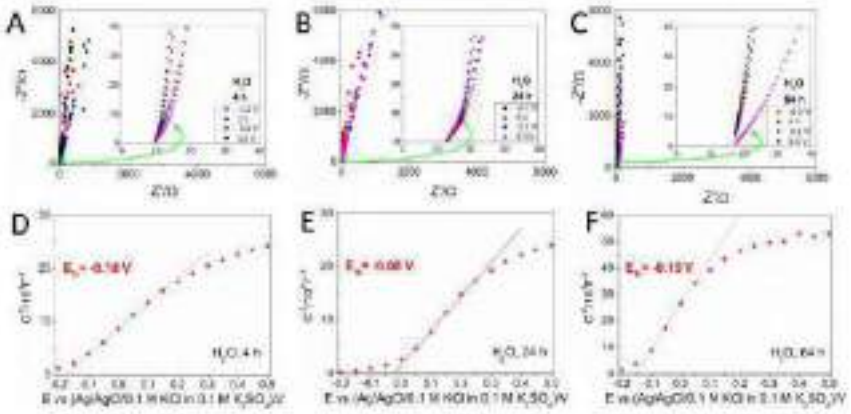

Figure S9. Complex plane impedance and Mott -Schottky plots obtained for TiO_2-NTs HT annealing in: (A-D) H_2O for 4 h, (B) H_2O for 24 h and (C) H_2O for 64 h, frequency range 20 kHz to 1 Hz.

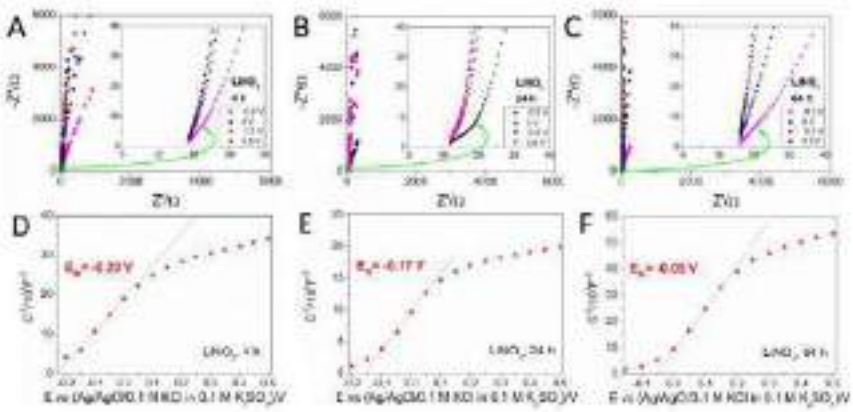

Figure S10. Complex plane impedance and Mott–Schottky plots obtained for TiO_2-NTs HT annealed in: (A-D) $LiNO_3$ for 4 h, (B-E) $LiNO_3$ for 24 h and (C-F) $LiNO_3$ for 64 h, frequency range 20 kHz to 1 Hz.

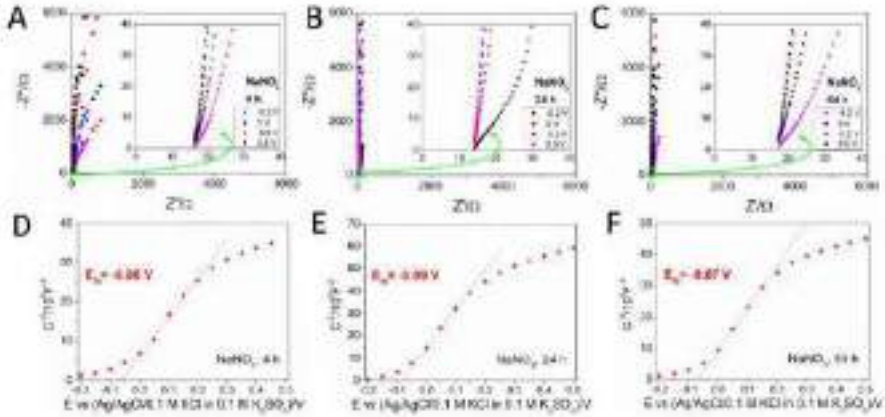

Figure S11. Complex plane impedance plots and Mott–Schottky plots obtained for TiO_2-NTs HT annealed in: (A-D) $NaNO_3$ for 4 h, (B-E) $NaNO_3$ for 24 h and (C-F) $NaNO_3$ for 64 h, frequency range 20 kHz to 1 Hz.

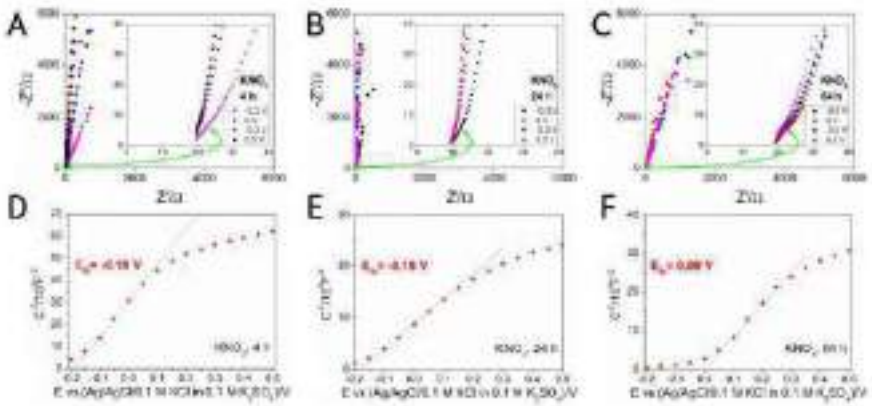

Figure 512. Complex plane impedance and Mott-Schottky plots obtained for TiO_2-NTs HT annealing in: (A-D) KNO_3 for 4 h, (B-E) KNO_3 for 24 h and (C-F) KNO_3 for 64 h. frequency range 20 kHz to 1 Hz.

Chapter IV

Hydrothermal cobalt doping of titanium dioxide nanotubes towards photoanode activity enhancement

IV.1 Methods in Brief and Key Results

This study tests whether trace cobalt, introduced by a hydrothermal process at 100 °C for 24 hours in a bath of $CoCl_2$/$NaNO_3$/HCl. Trace cobalt introduced into the TiO_2 structure alters the electronic structure of anatase TiO_2 nanotubes (XRD, XPS, Raman tests) and enhances their water-oxidation performance. Anodised TiO_2 nanotubes calcined at 450 °C were treated with HA, and a post-calcined treatment provided morphology-loss control. EDX detected ~0.1 at.% Co overall; XPS showed ~0.4 at.% surface Co^{2+}. XRD remained anatase, and Raman Eg(1) broadening/up-shift indicated defect formation. UV–Vis revealed a red shift; Tauc gaps were 2.99 eV (pristine), 2.92 eV (Co–NTs), and 2.85 eV (post-calcined). Despite the narrowest gap, the post-calcined sample was least active. Co–NTs lowered the dark water-oxidation onset by ~100 mV and shifted the flat-band potential anodically by ~0.2 V. Under AM 1.5G, photocurrent at +0.5 V increased from ~13 to ~40 μA/cm², stabilising at ~32 μA/cm². The gains arise from enhanced absorption, increased real surface area, and reduced interfacial charge-transfer resistance. Summary depicted in Figure 13.

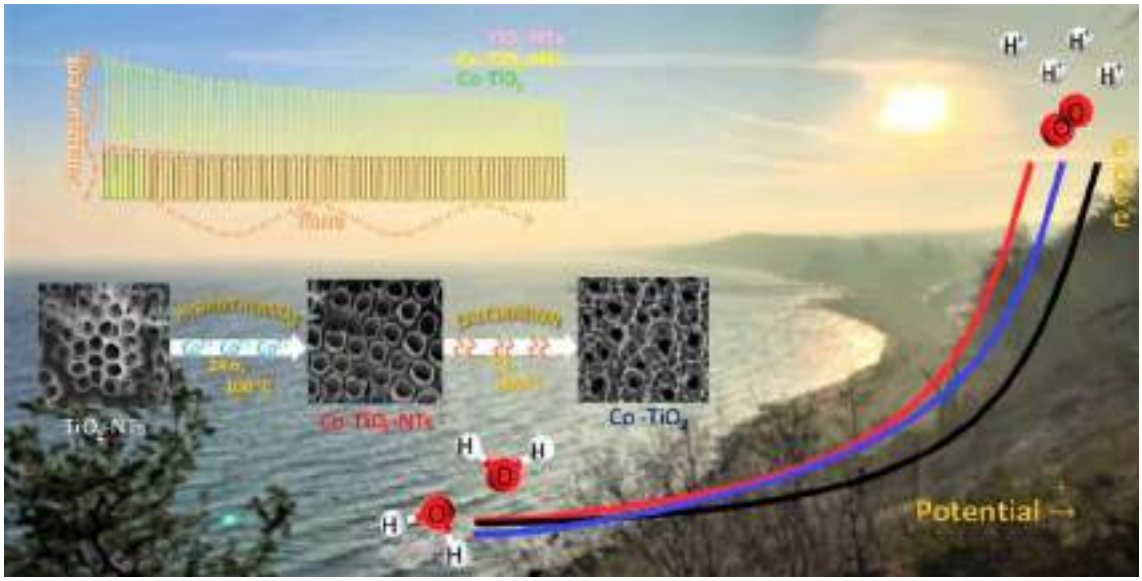

Figure 13. Graphical abstract.

IV.2 Publication

materials

MDPI

Article

Hydrothermal Cobalt Doping of Titanium Dioxide Nanotubes towards Photoanode Activity Enhancement

Mariusz Wtulich [1], Mariusz Szkoda [1], Grzegorz Gajowiec [2], Maria Gazda [3], Kacper Juzak [4], Mirosław Sawczak [5] and Anna Lisowska-Oleksiak [1,*]

[1] Department of Chemistry and Technology of Functional Materials, Chemical Faculty, Gdańsk University of Technology, 80-233 Gdańsk, Poland; wtulgim6@gmail.com (M.W.); mariusz.szkoda26@pg.edu.pl (M.S.)
[2] Faculty of Mechanical Engineering and Ship Technology, Institute of Machine Technology and Materials, Gdańsk University of Technology, 80-233 Gdańsk, Poland; grzegajow@pg.edu.pl
[3] Department of Solid State Physics, Faculty of Applied Physics and Mathematics, Gdańsk University of Technology, 80-233 Gdańsk, Poland; maria.gazda@pg.edu.pl
[4] Department of Electrochemistry, Corrosion and Materials Engineering, Chemical Faculty, Gdańsk University of Technology, 80-233 Gdańsk, Poland; kacper.juzak@pg.edu.pl
[5] The Szewalski Institute of Fluid-Flow Machinery, Polish Academy of Sciences, 80-231 Gdańsk, Poland; msc@imp.gda.pl
* Correspondence: ale@pg.edu.pl

Abstract: Doping and modification of TiO_2 nanotubes were carried out using the hydrothermal method. The introduction of small amounts of cobalt (0.1 at %) into the structure of anatase caused an increase in the absorption of light in the visible spectrum, changes in the position of the flat band potential, a decrease in the threshold potential of water oxidation in the dark, and a significant increase in the anode photocurrent. The material was characterized by the SEM, EDX and XRD methods, Raman spectroscopy, XPS, and UV-Vis reflectance measurements. Electrochemical measurement was used along with a number of electrochemical methods: chronoamperometry, electrochemical impedance spectroscopy, cyclic voltammetry, and linear sweep voltammetry in dark conditions and under solar light illumination. Improved photoelectrocatalytic activity of cobalt-doped TiO_2 nanotubes is achieved mainly due to its regular nanostructure and real surface area increase, as well as improved visible light absorption for an appropriate dopant concentration.

Keywords: titanium dioxide; hydrothermal modification; photoanode; water splitting; Co-doping

check for updates

Citation: Wtulich, M.; Szkoda, M.; Gajowiec, G.; Gazda, M.; Juzak, K.; Sawczak, M.; Lisowska-Oleksiak, A. Hydrothermal Cobalt Doping of Titanium Dioxide Nanotubes towards Photoanode Activity Enhancement. Materials 2021, 14, 1507. https://doi.org/10.3390/ma14061507

Academic Editor: Rosalinda Inguanta

Received: 18 February 2021
Accepted: 15 March 2021
Published: 19 March 2021

1. Introduction

The greatest challenge for the 21st century is without doubt combatting climate change. Globally, we should reduce fossil-originated energy consumption [1]. In response to the requests of society, it is now vital that new, environmentally friendly energy conversion and storage equipment is available; consequently, there has been a colossal development of research in this topic. The performance of energy conversion and storage electrochemical devices depends on the materials they are made of. The innovative solution in material chemistry is very often based on nanotechnology. Nanostructured materials hold the key to the novel generation of supercapacitors, lithium-ion/sodium-ion batteries, thermoelectric cells, and photoelectrochemical cells (PEC) [2–7]. Considering the PEC cell, the heart of the light energy harvesting module is the photoanode [5]. The history of photoanode material development starts half a century ago with the discovery of the photoelectroactivity of the TiO_2 monocrystal electrode under UV electromagnetic wave illumination [8]. Great effort has been undertaken globally to give us novel semiconductor materials with a narrow bandgap, such as $BiVO_4$, Fe_3O_4, WO_3, and their derivatives [9–12], allowing visible light absorption [7–12]. The strategy to increase the photoactivity and electroactivity of TiO_2 focuses on modifying the position of the electron bands of the material by doping with non-metals [13,14], by metal doping [6,7,15], or the application of surface sensitizers [16].

The importance of morphology was demonstrated by studies of TiO_2 nanostructures. Early reports on the possibility of growing titanium dioxide nanotubes come from Asselpour-Dezfuly et al., who managed to obtain them from an acidic electrolyte containing fluoride ions and chromic acid brushes a few hundred nanometers thick [17].

Kasuga et al. produced chemically titania nanotubes (TiNTs) of a diameter below 10 nm [18]. Other chemically synthesized nanotubes are mainly tested in lithium batteries [19]. The earliest fully successful attempt of electrochemical synthesis came from Zwilling et al. in 1999, who reported the first self-organized nanotube coating on a Ti substrate obtained by electrochemical Ti anodization in chromic acid electrolytes containing fluoride ions [20]. Since that point, the interest in the method has increased enormously and the technology of producing nanotubes has developed extensively.

Electrochemical methods were improved significantly in the so-called second generation of titania nanotubes, produced in neutral electrolytes [21]. The most popular method nowadays is growing them from viscous mixed solvent electrolytes based on ethylene glycol (EG), with a complexing agent F^- in the form of HF and NH_4F, often with H_3PO_4 [22–24]. Application of TiNTs grown on the Ti support includes their use in PEC cells, encapsulation of drugs, air purification, water purification, construction of sensors, and use in electrochemical capacitors [25–29]. TiNTs in photoelectrochemical devices act as UV-Vis light absorbing photoanode material. Although the size of the bandgap of nanotubes is reduced compared to pure bulk anatase TiO_2 (3.2 eV), a lot of effort has still been exerted by researchers to obtain higher parameters of photoactivity. The absorption edge of measured spectra for TiO_2 nanotube on Ti substrate is shifted slightly towards the visible range compared to pure bulk anatase TiO_2 powder. This is due to the fact that the barrier layer present at the TiO_2 nanotube—Ti substrate interface has rutile crystallites, and the nanotube walls consist of anatase crystallites. The bandgap of the rutile is lower compared to the anatase. The rutile phase at the barrier layer leads to the shifting of the absorption edge to a higher wavelength [30,31]. The presence of Ti^{3+} in the tubular structure of TiO_2 is also important for the absorption of light. After anodizing, the layers are subjected to a thermal process which causes the formation of oxygen vacancies and reduction of Ti(IV) to Ti(III). This surface-reduced material shows red shift absorption and better electrical conductivity [32]. There are several ways, as with ordinary structures, to increase the photoelectroactivity of nanotubes. Here, we have doping with non-metals [33,34], metal doping [35], and the use of systems with a co-catalyst as reported for Fe_3O_4 and CeO_x decorated titania nanotubes towards water splitting [36,37].

In this study, we focus on transition metal, namely Co, doping of the TiO_2 nanotube structure towards water photoanodic oxidation. Previous reports on photocatalytic organic pollutants degradation show that doping the anatase powder with cobalt leads to the enhancement of photoactivity in the process of phenol disposal from water or dye decoloration [38–40]. Very small amounts of cobalt (0.1–3 at %) introduced into the structure contribute to a significant increase in the photocatalytic organic pollutant decomposition efficiency [38].

Since the photocatalytic activity of Co-doped TiO_2 is documented, one may expect that the material could be in PEC cells as a photoanode. Titania nanotubes, the synthesis of which is easily controlled, were chosen as starting materials. The Co-doping of the TiO_2 structure is performed using a hydrothermal procedure.

The goal of this work is to demonstrate the influence of the hydrothermal process, leading to a slight introduction of cobalt ions into the nanotubes, in the photoanode process of water oxidation. The novel electrode material is characterized using X-ray powder diffraction (XRD) analysis, Raman spectroscopy, UV-Vis spectroscopy, X-ray photoelectron spectrometry (XPS), scanning electron microscopy (SEM), electrochemical methods: electrochemical impedance spectroscopy (EIS), cyclic voltammetry (CV), linear sweep voltammetry (LSV), and chronoamperometry (CA) in the dark and under solar light illumination. We demonstrated that a small amount of Co (~0.1 at %) inserted hydrothermally into the TiO_2 nanotubes causes a threefold increase in the photocurrent under solar light

illumination. The hydrothermal method turned out to be a very effective and cheap way to obtain a material with high photoactivity.

2. Materials and Methods

2.1. Apparatus

The microscopic studies were performed using JSM-7800 F (JEOL, Tokyo, Japan) field emission scanning electron microscope on the surface of pure TiO_2 and with cobalt dopant. The images were analyzed using a beam accelerating voltage at 5 kV. EDX analysis was used for chemical elements detection by a silicon nitride window's detector (OCTANE ELITE model, EDAX company, Mahwah, NJ, USA).

The crystal structure was determined from the XRD pattern using a diffractometer (Xpert PRO-MPD, Philips, Amsterdam, The Netherlands) with CuKα emission (λ = 1.5406 Å). The crystallites sizes were estimated based on the Scherrer formula and were processed using *Fityk* software [41] via fitting to the Gaussian function. UV-Vis spectra were recorded in the from 200 nm to 800 nm by a Perkin Elmer UV-Vis spectrometer (Lambda 35, Perkin Elmer, Waltham, MA, USA) equipped with the integrating sphere module for reflectance measurements. The Raman analysis was performed using a Raman microscope (InVia, Renishaw, Wotton-under-Edge, UK). Spectra were received using an argon-ion laser emitting at 514 nm. The spectrum of every single point at the sample was recorded as an accumulation of three scans.

XPS measurements of the electrode materials were performed on the Escalab 250Xi device (Thermo Fisher Scientific, Waltham, MA, USA). Al Kα radiation was used. The spectra of elements were analyzed and deconvoluted into components described by an envelope of a Gaussian–Lorentzian sum function with an asymmetry tail supported by the spectrometer commercial software Avantage version 5.973 [42]. The binding energies obtained in the XPS analysis are given relative to the C1s line at 284.6 eV. Traces amounts of cobalt were searched for, therefore the largest possible spot width with a diameter of 650 µm was used.

The electrochemical examinations in the dark of TiO_2-NTs, Co-TiO_2-NTs and Co-TiO_2 samples were carried out with a potentiostat–galvanostat (Autolab/PGStat30 with an FRA module, Eco Chemie B.V, Utrecht, The Netherland and Autolab PGSTAT 30, Metrohm Autolab B.V., Utrecht, The Netherlands) in a three-electrode glassy cell with titanium modified foils as the working electrode, Ag/AgCl/0.1 M KCl as the reference electrode, and platinum mesh as the auxiliary electrode. Cyclic voltammetry, linear sweep voltammetry, chronoamperometry and electrochemical impedance spectroscopy were conducted in 0.1 M K_2SO_4, purged with argon gas for 30 min before measurements, and kept at 20 ± 0.1 °C.

The flat band (E_{fb}) potentials were determined for all materials using impedance measurements by EIS at the frequency range from 20 kHz to 1 Hz for 10 points per decade with 10 mV point-to-point amplitude of the AC signal.

Photoelectrochemical measurements were carried out in a three-electrode glassy cell with a high transmittance quartz window. The studied samples, with an active surface area of 0.8 ± 0.1 cm^2, remained in the same electrolyte and under conditions as mentioned above. The light source was a 150 W xenon lamp (Osram XBO 150, Quantum Design, Darmstadt, Germany) equipped with an AM1.5 filter and an automatic shutter that opened every 30 s.

2.2. Chemicals

All reagents used in the electrochemical electrolyte preparation were of analytical grade: $CoCl_2 \cdot 6H_2O$ (POCH, Gliwice, Poland), K_2SO_4, H_3PO_4, $NaNO_3$, ethylene glycol (POCH, Gliwice, Poland), and Ti foils (99.5% metals base, Alfa Aesar, Kandel, Germany). In all experiments, triple distilled water was used.

3. Results

3.1. Preparation of the Electrode Materials

Nanostructures of titanium dioxide were prepared by electrochemical oxidation of the titanium foil (0.25 mm thick, annealed, area 2 × 2 cm^2) in the electrolyte containing 0.27 M NH_4F in a solution containing 5 vol % of water, 3.5 vol % of H_3PO_4 (85%) and 91.5 vol % of EG, at 40 V for 2 h [43]. This process of anodization was performed in a glassy cell with the cooling jacket at 20 ± 0.1 °C, using a thermostat (Julabo F-12, Seelbach, Germany). Afterwards samples were cleaned in an ultrasonic bath in a 1:1 solution of acetone and isopropanol. Samples were then rinsed with triple distilled water and dried using the hot stream of air. The anodized and cleaved TiO_2 films were calcined at 450 °C for 2 h in the air (the heating rate was 2.5 °C/min) and cooled freely. The above-mentioned steps allow to create the titania nanotubes (TiO_2-NTs) on the surface of titanium [43].

Subsequently, the TiO_2-NTs sample was immersed in the 50 cm^3 Teflon chamber with a 30 mL aqueous solution containing: 1.07 g $CoCl_2$ 6 H_2O, 2.56 g $NaNO_3$ and 75 µL (35–38%) HCl. The container was sealed off inside a steel autoclave and placed in an oven at 100 °C for 24 h. After this hydrothermal treatment, the sample was taken out, rinsed several times in a solution of 1:1 acetone/isopropyl alcohol and in distilled water. This process was performed to obtain Co-doped titania nanotubes (Co-TiO_2-NTs). The third sample was prepared by anodization of the Ti plate and hydrothermal modification finally followed by thermal treatment in a tube furnace in contact with air at 450 °C for 2 h. This sample is labeled as Co-TiO_2.

3.2. Morphology and Composition of the Samples

Scanning Electron Microscope and Energy Dispersive X-Ray Analysis

The imaging of the titanium surface covered with nanotubes is most often carried out using scanning electron microscopy. The use of SEM is effective due to the good conductivity of the semiconducting titanium dioxide [44]. Imaging allows for determining the length of nanotubes, their wall thickness, the diameter of pores, and interpose distances [44]. Today, it is widely used to analyze surfaces by means of scanning electron microscopy. In Figure 1 is an image obtained from the scanning electron microscope showing pure TiO_2 nanotubes and modified samples. On the left side, marked as A, is an image of pure TiO_2 nanotubes. The observed neighboring tubes' edges touch each other. The diameters are marked in the picture and do not exceed 120 nm (117, 87, 102 nm). The tubular shapes are slightly irregular. They probably reflect the arrangement of the rolled plate substrate. This sample was next hydrothermally modified. The image of the modified sample is shown in picture 1B. As can be seen, the material marked as Co-TiO_2-NTs is different from the unmodified sample 1A. We have separate tubular shapes with slightly greater diameters. Tubes do not touch their edges. Such an electrode material should have a higher real surface area, and therefore higher currents. Now let us look at what happens to the electrode material if we thermally modify (450 °C, 2 h) the sample Co-TiO_2-NTs (Figure 1B) to obtain sample Co-TiO_2 (Figure 1C). The change is drastic. The nanotubes cease to exist and are sealed together—we observe an intricate lace, but not nanotubes any more. Figure 1D shows the length of the Co-TiO_2-NTs nanotubes. Their length does not exceed 215 µm.

The chemical composition of the sample was estimated by the EDX method. Titanium plates covered with oxide layers were analyzed thoroughly. Two samples showed the presence of small amounts of cobalt. EDX examination of the sample after hydrothermal modification Co-TiO_2-NTs showed the presence of ~0.1 at % of Co. Sample Co-TiO_2 contained also ~0.1 at % of Co. The distribution of elements is presented in Supplementary Materials (Figure S1). Due to the low content of Co, scanning by EDX does not allow for a reliable measurement of this dopant distribution. As is shown below, both electrodes with traces of cobalt have catalytic and photoelectrocatalytic enhanced activity towards water oxidation in comparison with pure TiO_2 nanotubes.

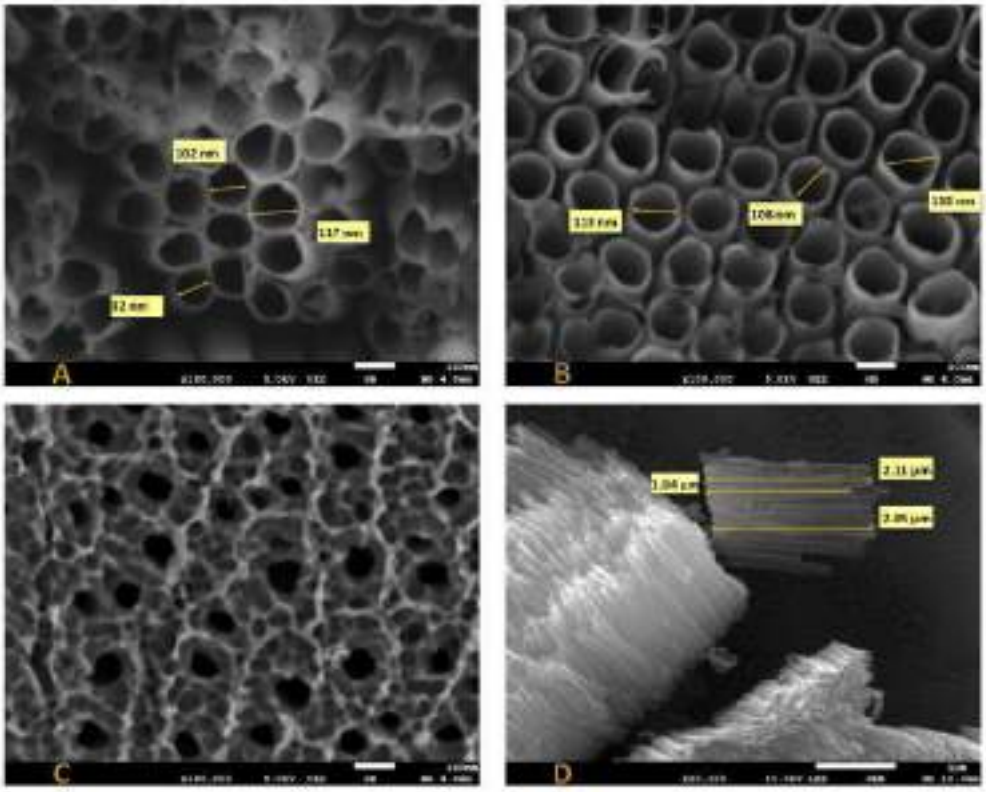

Figure 1. SEM images: (**A**) pure TiO_2 nanotubes TiO_2-NTs; (**B**) sample hydrothermally modified Co-TiO_2-NTs; (**C**) sample Co-TiO_2 after final thermal treatment (450 °C, 2 h); and (**D**) length of nanotubes for Co-TiO_2-NTs.

3.3. Structure

3.3.1. X-Ray Powder Diffraction

XRD analysis was performed to determine the phase composition, crystallinity, and crystallite size of the prepared samples. The results are shown in Figure 2. The diffraction reflections at 35°, 40.1°, and 53° correlate to the (100), (101), and (102) planes of the hexagonal closest packed titanium [45], respectively. All obtained TiO_2 nanostructures consisted of the pure anatase phase without the brookite or rutile phase. This is confirmed by the observed at 25.3°, 37.9°, 38.4°, 48°, 54°, and 55° corresponding to Miller indices (101), (004), (112), (200), (105), and (211), respectively [46].

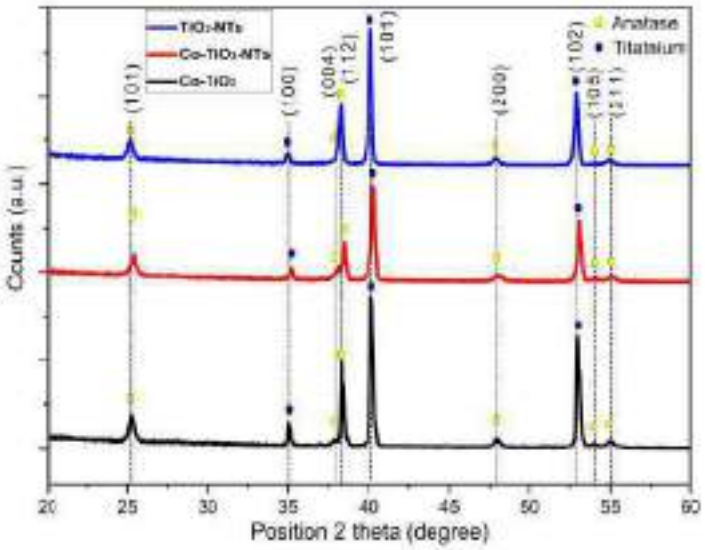

Figure 2. Comparison of XRD patterns of titanium samples covered with TiO_2 nanotubes pure and with cobalt doping.

Based on the Scherrer formula, defined by the equation:

$$D_{hkl} = \frac{K\lambda}{B_h \cos\theta} \quad (1)$$

where K is a dimensionless shape factor ($K = 0.9$), λ is the CuKα radiation X-ray wavelength, B_h is the line broadening at half the maximum intensity (FWHM) [47], mean crystallite sizes for selected crystallographic planes were determined, and are summarized in Table 1.

There are no reflections that identify cobalt compound or Co metal. According to Peng Jiang et al. [38], no changes in XRD analysis were observed for low atomic cobalt contents. All prepared samples receive nanometer sizes. However, for the Co-doped TiO_2, a slight increase in crystallite size in the direction perpendicular to the (112) plane was observed. This phenomenon may affect the frequency shifting and broadening of Raman peaks due to the phonon confinement [48]. It cannot be excluded that small quantities of cobalt had built into the nanostructure of TiO_2.

Table 1. Mean crystallite sizes calculated from the Scherrer's equation based on achieved XRD patterns for TiO_2-NTs, Co-TiO_2-NTs and Co-TiO_2.

Sample	D_{101} (nm)	D_{112} (nm)	D_{200} (nm)	D_{211} (nm)
TiO_2-NTs	18.2	28.2	16.5	25.5
Co-TiO_2-NTs	15.3	41.1	14.6	17.5
Co-TiO_2	19.7	34.6	15.0	13.3

3.3.2. Raman Spectroscopy

Raman spectra of TiO_2-NTs, Co-TiO_2-NTs, and Co-TiO_2 samples recorded in the spectral range of 100–1200 cm^{-1} are presented in Figure 3. The Raman bands centered at 144, 197, 392, 515, and 633 cm^{-1} corresponds to E_g (1), E_g (2), B_{1g}, A_{1g}, and E_g (3) modes of the anatase phase, respectively. The origin of the E_g bands can be attributed to the sym-

metric stretching vibration of O–Ti–O, while the B_{1g} band corresponding to the symmetric bending vibration of O–Ti–O and A_{1g} mode can be assigned to the antisymmetric bending vibration of Ti–O–Ti in the anatase phase. The intense sharp band centered near 144 cm^{-1} corresponds to an external symmetric vibration and confirms the formation of long-range order anatase phase [48,49]. The position of this band correlates to the nanocrystalline grain size and the up-shift of its position can be observed with decreasing of the grain size [50,51]. The broadening and up-shifted position of the E_g (1) mode observed for Co-TiO_2-NTs and Co-TiO_2 samples may be assigned to structural defects resulting from the doping of TiO_2 with Co ions.

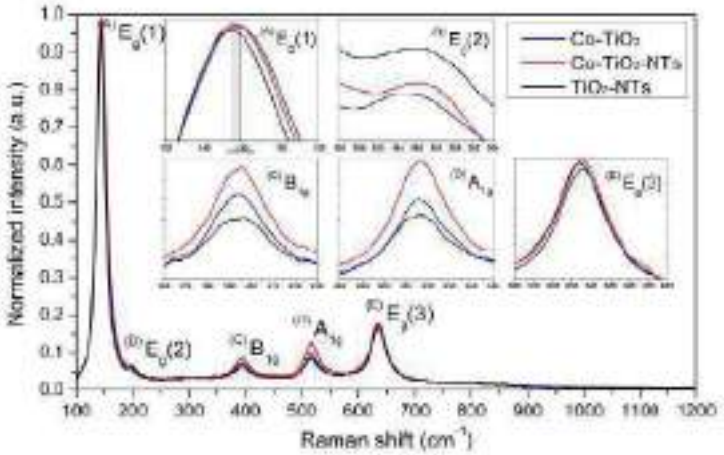

Figure 3. Raman spectra of pure titania nanotubes and Co-doped TiO_2 samples. (A–E) typical modes of the anatase phase.

3.3.3. X-ray Photoelectron Spectroscopy

Helpful information about the chemical structure of modified titania is available from XPS studies. The TiO_2-NTs and Co-TiO_2-NTs samples were examined and compared. The third sample, Co-TiO_2, was not photoactive, and thus was not included in XPS tests. The survey spectra from 0 eV to 1350 eV showed the presence of titanium, carbon, oxygen, and nitrogen for both samples, and additionally cobalt for the Co-TiO_2-NTs sample. The survey spectra made with the 150 eV transition energy showed the difference between the TiO_2-NTs and Co-TiO_2-NTs samples (Figure 4). On the latter, the Co2p peaks and the Auger Co LMM peak (713 eV) are noticeable, which proves the presence of cobalt. Both samples contain titanium, carbon, oxygen, and nitrogen. High-resolution scans were performed in the range of Ti2p, C1s, O1s, N1s, and Co2p. A pass energy of 35 eV and 50 repetitions were used. The carbon came from impurities (adventitious carbon) and was used to calibrate the measurement. A small amount of nitrogen may be from the substrates used to produce the samples and is observed in similar measurements [38].

Titanium appears as a doublet of the $Ti2p_{1/2}$ (464.6 eV) and $Ti2p_{3/2}$ (458.9 eV) peaks. These energies testify to the presence of titanium in the +4 oxidation state in titania [52]. The titanium peaks are identical for the TiO_2-NTs and Co-TiO_2-NTs samples, not shown.

The amount of cobalt is low compared to the rest of the elements, but it is detectable and analyzable. The measurement clearly shows the Co2p5 and Co2p3 doublet and the so-called shake up peaks just after the main peaks [53]. The energy difference between the doublet peaks for Co is 15.4 eV and is consistent with the XPS databases [54,55].

Measurement for $Co2p_{3/2}$ in cobalt oxide is 780.4 eV, which is in agreement with the binding energy of cobalt. The presence of shake up peaks is confirmed in the literature

and proves the existence of Co^{2+} [38,39]. The estimated cobalt atomic percentage from the XPS measurements was ~0.4 at % at 780.4 eV corresponding to $Co2p_{3/2}$, whereas EDX measurements show ~0.1 at %. Higher values of Co content from XPS measurements may suggest that cobalt is accumulated mostly in the near-surface area. It was thus confirmed by XPS that the Co-TiO_2-NTs sample contained cobalt in the +2 valence state, and although there was relatively little of it, it was detectable.

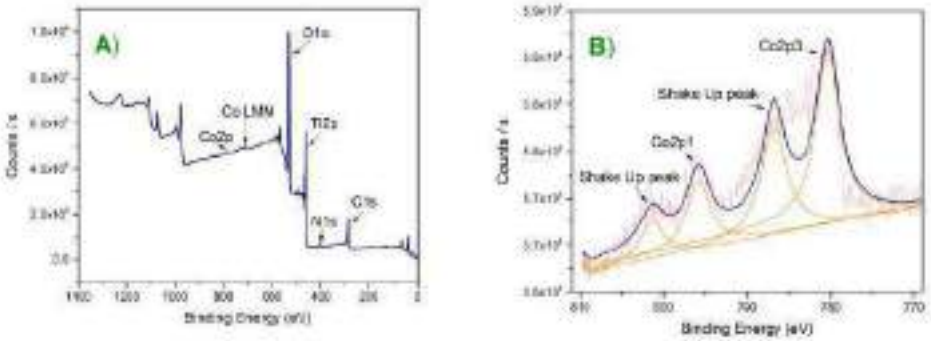

Figure 4. (**A**) Survey spectrum. It is almost identical for both samples. The Co-TiO_2-NTs sample additionally reveals cobalt in the form of Co2p and Co LMM peaks; (**B**) detailed cobalt spectrum for Co-TiO_2-NTs.

Our results are consistent with reported data on powder titania modified during the hydrothermal procedure by a small amount of Co [38]. The authors presented a DFT theory-based calculated electronic structure of Co-doped TiO_2 and indicated that impurity states are introduced into the forbidden band due to the low concentration cobalt doping. They documented that these impurity states are beneficial to the enhancement of visible light absorption and the improvement of photocatalysis efficiency of powder Co-modified titania as experienced with our titania nanotubes.

3.4. Reflectance UV-Vis Spectroscopy

In Figure 5A–C, the absorbance, reflectance, and Tauc plot are given for the obtained materials, respectively. As can be seen, obtained electrodes in the ultraviolet region have the highest absorbance, which is typical for TiO_2 materials. Moreover, the wide absorption band with the maximum at 550 nm could originate from the presence of sub-bandgap states caused by the structure of the titania nanotube that can trap radiation inside the tube [57]. In the case of the Co-TiO_2 sample, the absorbance in the visible range (450–700 nm) is characterized by a lower intensity in comparison with the bare TiO_2 and Co-TiO_2-NTs. This means that absorption in this range of visible light, as clearly seen, is more intense for the samples with the nanotubular structure. The TiO_2 material characterized by a non-tubular structure does not exhibit this feature. In the case of Co-TiO_2-NTs, the redshift of the absorption edge is observed, which is advantageous for the materials expected to be photoactive under visible light illumination. The dopant presence is responsible for changes, very likely due to impurities formed in between the forbidden energy bandgap [38]. On the other hand, physicochemically bond water is also supposed to cause red shift [58]. Taking into account the fact that Co-TiO_2-NTs were not subjected to a thermal process after hydrothermal treatment, the second argument seems to be very likely prevailing.

Based on the Tauc plot, the bandgap energy values were determined and are 2.85 eV, 2.92 eV, and 2.99 eV for Co-TiO_2, Co-TiO_2-NTs, and pure TiO_2, respectively. Therefore, both modified materials were characterized by a slightly narrower bandgap energy in comparison with pure titania nanotubes. Although Co-TiO_2 has the smallest energy bandgap, it has the worst photoelectrochemical activity compared to the other materials. The reason for this is very likely the lack of a tubular structure and low absorption in the visible light range as recorded on UV-Vis spectra (see Figure 5A).

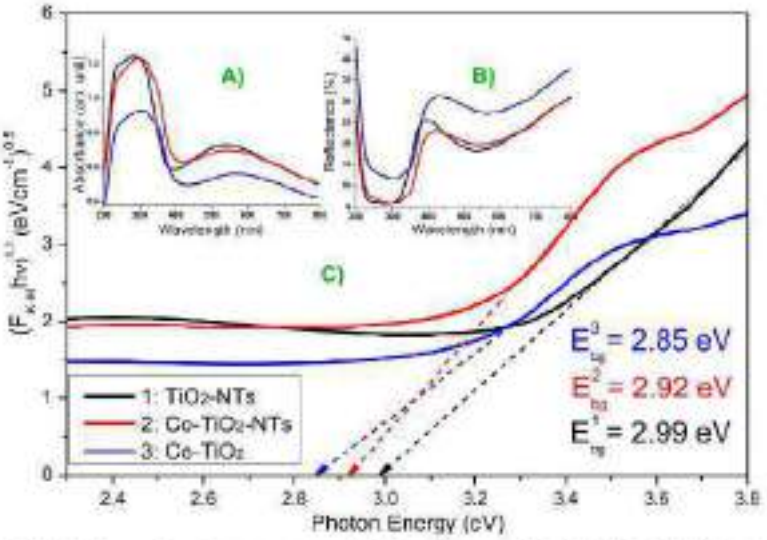

Figure 5. (A) Absorbance, (B) reflectance spectra, and (C) Tauc plot for samples TiO_2-NTs, Co-TiO_2-NTs, Co-TiO_2.

3.5. Electrochemical and Photoelectrochemical Properties

The electrode materials TiO_2-NTs, Co-TiO_2-NTs, and Co-TiO_2 were subjected to electrochemical studies in the dark in the potential range from −0.7 V to 1.3 V versus Ag/AgCl/0.1 M KCl in 0.1 M K_2SO_4. Polarization towards high anode potentials shows whether there are differences in the threshold potentials for oxidation of the water molecule. As you can see, the course of the linear sweep voltammetry curves differs (Figure 6). The threshold potentials E_{th} have been determined and their values increase for the electrodes in the order Co-TiO_2-NTs < Co-TiO_2 < TiO_2-NTs with 100 mV lowering of the E_{th} value for Co-doped nanotubes.

As can be seen, the introduction of cobalt ions into the structure of titanium dioxide, as well as morphological changes after modification by the hydrothermal method, definitely affect the electrochemical properties of the new systems. The environment of cobalt ions in the structure is to some extent similar to that of ordinary cobalt oxide compounds. Such compounds belong to a group known for their catalytic properties in relation to the oxidation of water molecules [99]. Undoubtedly, both electrodes containing a small amount of cobalt catalyze the oxidation of water to molecular oxygen. The decrease in the water oxidation threshold potential E_{th} for the modified electrode indicates the effectiveness of the hydrothermal process.

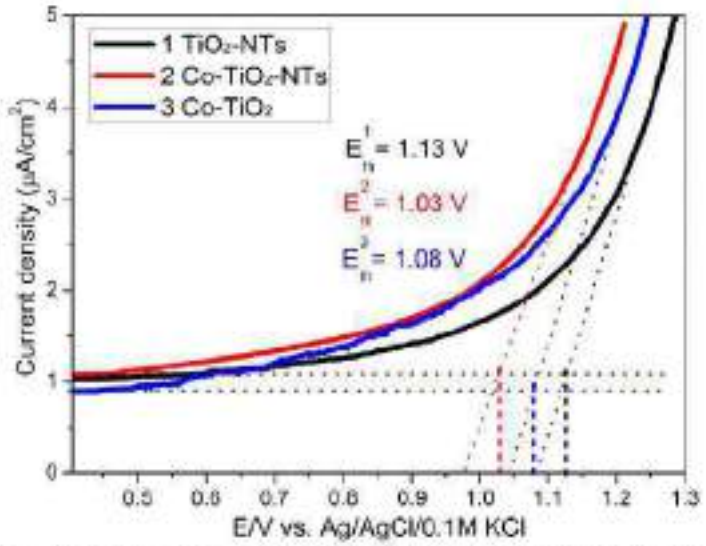

Figure 6. Linear sweep voltammetry (LSV) curves obtained for samples TiO_2-NTs, Co-TiO_2-NTs, and Co-TiO_2, used for the evaluation of the water oxidation threshold potential E_{in}, sweep rate 50 mV s^{-1}.

TiO_2 nanotubes are known for their cathode potential activity. Their typical course of CV curves obtained for pure and modified titania are shown in Figure 7A–C. The CV curves obtained for different sweep rates of polarization allow the diagnosis of the reaction mechanism. Linear regression for changes in current with the square root of the polarization sweep rate indicates diffusive process control. When current intensity changes linearly with the polarization rate v, one deals with kinetic process control, and the charge transfer reaction is surface limited (see Figure 7D–F). However, the most important outcome from these simple polarization measurements is the possibility of comparing the effective current densities. These values are calculated in relation to the geometric surface area. At the same chosen potential (−0.5 V), the highest cathode currents were recorded for the Co-TiO_2-NTs electrode, and the lowest were recorded for the Co-TiO_2 electrode. Considering the microscopic morphology studies showing that each nanotube has a free surface along its entire length, and direct contact between the tubes is almost absent for the Co-TiO_2-NTs material, this condition compared to the pure TiO_2-NTs and calcined Co-TiO_2 represents an increased real surface area. Hence, the recorded current for Co-TiO_2-NTs is the highest. The lowest current densities are recorded for electrodes after final calcination following hydrothermal modification. This material is devoid of a nanotubular structure—it is the result of calcination. The Co-TiO_2 sample has an undeveloped specific surface area, and thus the current density related to the geometric surface area is lower. Thus, the research on polarization in terms of cathode potentials confirmed the typical activity of TiO_2 nanotubes, as was reported in Ref. [60]. Moreover, it allowed us to assess the state of surface development for a hydrothermally modified electrode. The modification was considered to increase the real surface area due to hydrothermal treatment.

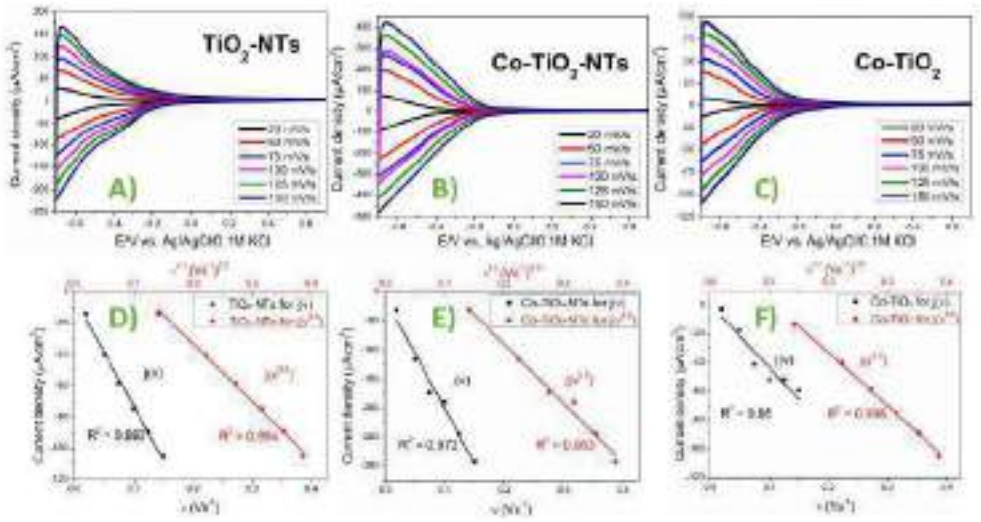

Figure 7. Cyclic voltammetry (CV) curves obtained at varied sweep rates and analysis (A,D) TiO_2-NTs (B,E) Co-TiO_2-NTs (C,F) Co-TiO_2.

Titanium dioxide belongs to the n-type semiconductors. Any changes in structure—doping, the presence of surface modifying substances—will influence the position of the measured value of the flat band potential, the most important value characteristic for the semiconductor electrode [61].

The flat band potential E_{fb} was determined for three electrodes: TiO_2-NTs, Co-TiO_2-NTs, and Co-TiO_2 materials. Electrochemical impedance spectroscopy was used to measure the impedance of the polarized samples under stationary conditions at a frequency range from 20 kHz to 1 Hz, and AC signal amplitude 10mV. Examples are gathered in Figure 8A–C. The impedance functions presented in the figures are of a typical capacitive character, the course of the function is an almost vertical line, slightly rotated, in line with the presence of *CPE* (constant phase element), which is neglected here. The capacitance *C* values were calculated for frequencies: 1 Hz, 100 Hz, and 1000 Hz using the simple relation: $-Z'' = (\omega C)^{-1}$, where *C* is the capacitance, Z'' is the imaginary part of the impedance function, ω is the angular frequency, $j = \sqrt{-1}$.

The E_{fb} values were determined in accordance with the Mott–Schottky function, using *C* values extracted from the impedance measurements. The results are presented in Figure 8D–F. Table 2 gathers evaluated flat band potential for different materials. As can be seen, doping nanotubes with cobalt by hydrothermal treatment changes the effective flat band potential significantly—the difference is about 200 mV towards anodic values. This change will be important for the course of the electrode reactions and the availability of the electrons in the conduction band.

Table 2. Flat band potential values for selected frequency for pure and Co-doped TiO_2 samples.

Sample	E_{fb} (V) for 1 Hz	E_{fb} (V) for 100 Hz	E_{fb} (V) for 1000 Hz
TiO_2-NTs	−0.21 ± 0.02	−0.22 ± 0.02	−0.25 ± 0.02
Co-TiO_2-NTs	−0.02 ± 0.02	0.00 ± 0.02	0.00 ± 0.02
Co-TiO_2	0.15 ± 0.02	0.06 ± 0.02	0.02 ± 0.02

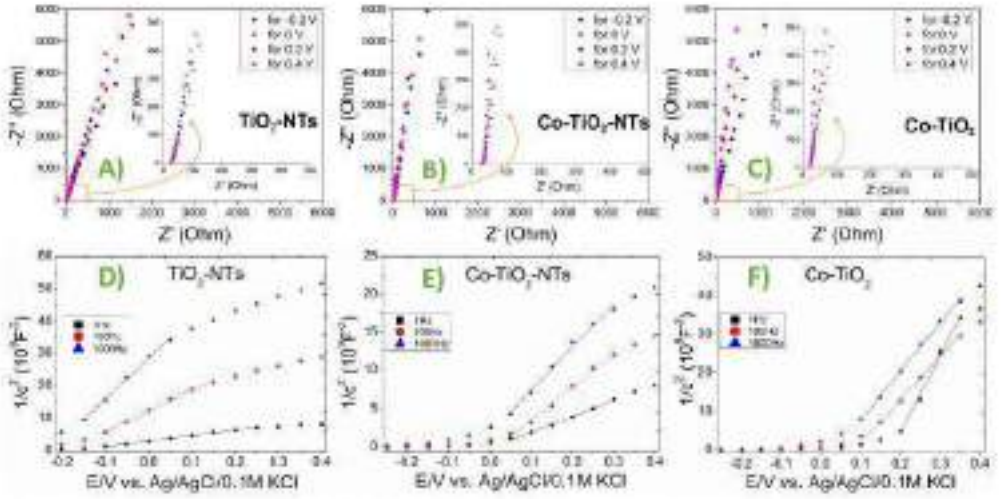

Figure 8. Complex plane impedance plots obtained for: (**A**) TiO_2-NTs, (**B**) $CoTiO_2$ and (**C**) Co-TiO_2, frequency range 20 kHz to 1 Hz. Mott–Schottky plots for: (**D**) TiO_2-NTs, (**E**) $CoTiO_2$, (**F**) Co-TiO_2.

According to the aim of our study, the photoelectroactivity of the material in the field of photoanode operation has been investigated. As mentioned and proved above, oxidation of water in dark conditions occurs more easily for the doped electrode, and the E_{th} potential is lowered for the Co-TiO_2-NTs material. Polarization under solar light illumination was carried out to show how the electrode material behaves as a photoanode.

In Figure 9, the photocurrent generation recorded at a constant potential of 0.5 V vs. Ag/AgCl/0.1 M KCl is given for the pure TiO_2 nanotubes and the Co-modified electrodes. Of all the samples, the material labeled as Co-TiO_2 generates the lowest photocurrent. Such weak photoactivity for modified titania prepared by the hydrothermal method and finished by extra is caused by the non-tubular morphology characterized by lower electron lifetimes than the ordered layer, and does not provide good pathways for electron transport [62,63]. Additionally, Co-TiO_2 has the lowest absorbance intensity compared to other samples in the VIS region, which is considered a very important factor, influencing photoconversion efficiency. The highest photocurrent was observed for Co-TiO_2-NTs reaching about 40 $\mu A \cdot cm^{-2}$ stabilized at 32 $\mu A \cdot cm^{-2}$ under sunlight illumination.

The difference between the current registered for a sample in the dark and under its illumination (Δj) are listed in Table 3 together with the ratio between the current registered for a sample in the dark and under its illumination (j_l/j_d) and the ratio between photocurrent and light source optical power (photoresponsivity).

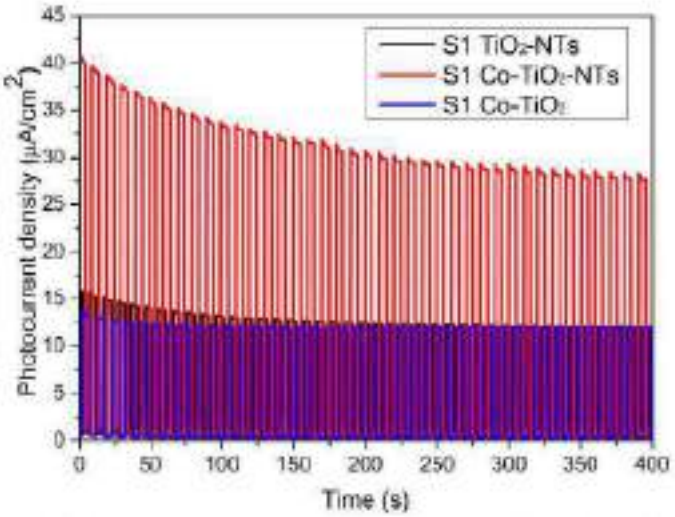

Figure 9. The chronoamperometry curve, showing the photocurrent density registered for modified and pure titania electrodes at E = + 0.5V. Source of light: 150 W xenon lamp equipped with an AM1.5 filter, light intensity: 100 mW·cm^{-2}.

Table 3. Determined photoresponsivity values from Figure 9, where: Δj is the difference between the current registered for a sample in the dark and under its illumination, j_l/j_d is the ratio between the current registered for a sample in the dark and under its illumination, and $\Delta j/P$ (photoresponsivity) is the ratio between photocurrent and light source optical power.

Sample	Δj (μA·cm^{-2})	j_l/j_d	$\Delta j/P$ (μA·W^{-1})
TiO_2-NTs	12.51	33.08	12.5
Co-TiO_2-NTs	32.71	137.29	32.7
Co-TiO_2	11.68	33.44	11.7

LSV measurements were presented also to compare photoactivity of the obtained electrodes. The obtained results are presented in Figure 10. In the early stages, the photocurrent densities in all examined samples increased with increasing potential applied to the photoanode and then stabilized at a potential of around 0 V vs. Ag/AgCl/0.1 M KCl. The highest photocurrent generation value was obtained for Co-TiO_2-NTs. At a potential equal to +0.2 V, the value of the current density is more than two times higher than the current registered for pure TiO_2 nanotubes and sintered Co-TiO_2. Therefore, the Co species on and in the tubular matrix play an important role in the enhanced photocurrent generation (therefore in the case of non-tubular morphology we do not see an improvement in the photocurrent). Thus, the increase in the charge generation is influenced by the presence of Co and this can be caused by the enhanced light absorption in the visible range, as well as the decrease in the recombination rate and the charge transfer resistance.

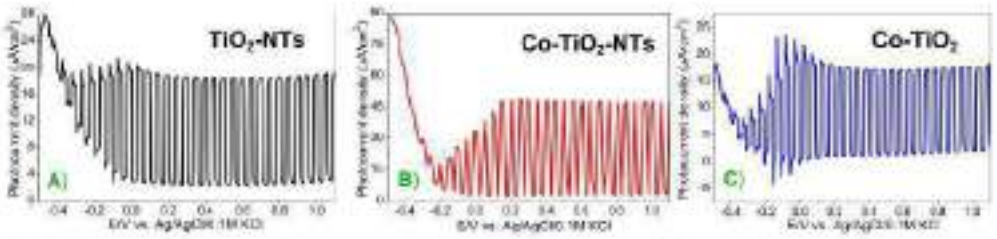

Figure 10. The linear sweep voltammetry curves obtained at a sweep rate 50 mV·s^{-1} for samples (**A**) TiO_2-*NTs* (black line), (**B**) Co-TiO_2-NTs (red line), (**C**) Co-TiO_2 (blue line) in the 0.1 M K_2SO_4 aqueous electrolyte. Source of light: 150 W xenon lamp equipped with an AM1.5 filter, light intensity: 100 mW cm^2.

The low energy bandgap and photocurrent enhancement are the most important parameters to describe novel photoactive materials. Table 4 shows a comparison of selected doped TiO_2 materials obtained with different synthesis methods. Due to the various modifications of nanostructure, there are large discrepancies in photocurrent values. However, as the authors mentioned [64–66], introducing low amounts of chemical elements into the anatase structure promotes increasing the photoresponse. Too high doping level of TiO_2 causes a decrease in photocurrent density. The photocurrent for Co-TiO_2-NTs obtained in this work is similar to the value in article [67]. The energies bandgap for doped titania nanotubes are in the range from 2.82 eV to 3.09 eV [64,68,69]. Thin films of TiO_2 with Ag or Cu dopant achieve lower Eg values, but they also have worse photoelectroactivity.

Table 4. Comparison of energy bandgap and photocurrent density for selected metal-doped TiO_2 (j_{doped}—photocurrent density for doped TiO_2, j_{TiO2}—photocurrent density for pure TiO_2).

Electrode Material	Luminous Intensity (mW·cm^{-2})	Energy Bandgap, E_g (eV)	Photocurrent Density (μA·cm^{-2})/E * (V)	Enhancement Factor (j_{doped}/j_{TiO2})	Ref.
TiO_2-NTs	100	2.99	12.9 at 0.5 V	1	This work
Co-TiO_2		2.85	12.0 at 0.5 V	0.9	
Co-TiO_2-NTs		2.92	70.3 at 0.5 V	2.6	
Co-TiO_2-NTs	100	3.09	95.0 at 0.5 V	1.5	[68]
Co-TiO_2-NTs	100	no data	40.0 at 0.4 V	3.0	[67]
Cr-TiO_2-NTs	100	2.82	360.0 at 1.0 V	9.2	[64]
B-TiO_2-NTs	100	2.91	311.0 at 0.5 V	7.4	[69]
V-TiO_2-NTs	16	no data	5.8 at 0.5 V	4.8	[70]
Ag-TiO_2 film	44	2.5	1.2 at 0.2 V	3.5	[71]
Fe-TiO_2 nanorods	100	3.12	550.0 at 0 V	5.5	[65]
Cu-TiO_2 film	44.42	2.82	18.2 at 0.4 V	1.3	[66]

* Electrode potential E vs. Ag/AgCl.

As shown above, the cobalt doping of TiO_2 nanotubes has an effect on both the reduction in the overpotential of water oxidation under dark conditions and the photooxidation process. This increase in photoactivity is the result of amplified absorption of visible light, a narrowing of the bandgap, and effective increase in the real surface area, all as a result of hydrothermal treatment in $CoCl_2$ electrolyte.

4. Conclusions

A small amount of cobalt 0.1 at % has been successfully doped into TiO_2 nanotubes using the hydrothermal method. Comprehensive characterization (XPS, XRD, EDX, Raman) confirms the introduction of Co^{2+} into the anatase crystal structure. Hydrothermal treatment of TiO_2-NTs in $CoCl_2$ electrolyte leads to an increase in the real surface area of the

tubular structure. Titania is modified considering its morphology and electronic structure. Development of the real surface area and presence of Co-dopant are responsible for the significant rise in UV-Vis light absorption. Novel electrode material exhibits increased electroactivity towards water oxidation in the dark as an anodic threshold potential E_{th} is 100 mV lower in comparison with E_{th} for pure nanotubes. Moreover, the photoelectrocatalytic activity towards water oxidation is significantly enhanced, as a photocurrent of the modified sample Co-TiO_2-NTs is almost threefold higher in comparison to the photocurrent of pure nanotubes. The photoelectrocatalytic and electrocatalytic activity of cobalt-doped TiO_2 nanotubes is attributed to their real surface increase and improved visible light absorption and, above all, their appropriate doped concentration. The presence of Co is necessary to reduce water oxidation potential in the dark and contributes to the growth of photocurrent.

Although we are aware that EDX elemental analysis of the samples combing both Ti support and the thin film only shows estimated values of Co-dopant, it is evident that hydrothermal low-temperature procedure leads to the formation of better photoanodic material. The further thermal treatment causes destruction of the tubular structure and leads to a hefty reduction in photocurrents while maintaining the catalytic properties for OER reactions in the dark. Our results are consistent with previously published data on photocatalytic activity of Co-doped titania [38,72].

Supplementary Materials: The following are available online at https://www.mdpi.com/1996-1944/14/6/1307/s1, Figure S1: EDX maps of the O, Ti and Co distributions.

Author Contributions: Conceptualization, A.L.-O.; resources, M.W., M.S. (Mirosław Sawczak), K.J., M.G., G.G.; data curation, M.W., M.G., M.S. (Mirosław Sawczak), M.S. (Mariusz Szkoda), K.J., G.G.; A.L-O.; writing—original draft preparation, A.L.-O., M.S.(Mariusz Szkoda), M.W.; writing—review and editing, A.L.-O., M.W., M.S.(Mariusz Szkoda); visualization, M.W., K.J., M.S. (Mirosław Sawczak); M.G., G.G., supervision, A.L.-O.; project administration, A.L.-O.; funding acquisition, M.S. (Mariusz Szkoda). All authors have read and agreed to the published version of the manuscript.

Funding: Authors A.L.-O. and M.W are grateful for financial support from Gdańsk University of Technology Statutory financial support. M.S. (Mirosław Sawczak) and M.W are grateful for financial support from The National Centre for Research and Development, grant no. LIDER/15/0088/L-10/18/NCBR/2019 (Integrated prototype of a photo-supercapacitor for energy storage obtained as a result of solar radiation conversion).

Institutional Review Board Statement: Not applicable.

Informed Consent Statement: Not applicable.

Data Availability Statement: Data is contained within the article or supplementary material.

Conflicts of Interest: The authors declare no conflict of interest. The funders had no role in the design of the study; in the collection, analyses, or interpretation of data; in the writing of the manuscript, or in the decision to publish the results.

References

1. Chu, S.; Majumdar, A. Opportunities and challenges for a sustainable energy future. *Nature* **2012**, *488*, 294–303. [CrossRef] [PubMed]
2. Pang, H.; Cao, X.; Zhu, L.; Zheng, M. *Synthesis of Functional Nanomaterials for Electrochemical Energy Storage*; Springer: Singapore, 2020.
3. Li-Oakey, K.D. *Nanoporous Materials for Molecular Separation and Conversion*; Elsevier: Amsterdam, The Netherlands, 2020; pp. 351–386.
4. Hi-Gang, C.; Guang, H.; Lei, Y.; Lina, C.; Jin, Z. Nanostructured thermoelectric materials: Current research and future challenge. *Prog. Nat. Sci. Mater. Int.* **2012**, *22*, 535–549.
5. Graetzel, M. Photoelectrochemical cells. *Nature* **2001**, *44*, 339–344. [CrossRef] [PubMed]
6. Opra, D.P.; Gnedenkov, S.V.; Sokolov, A.A.; Podgorbunsky, A.B.; Ustinov, A.Y.; Mayorov, V.Y.; Kuryavyi, V.G.; Sinebryukhov, S.L. Vanadium-doped TiO_2-B/anatase mesoporous nanotubes with improved rate and cycle performance for rechargeable lithium and sodium batteries. *J. Mater. Sci. Technol.* **2020**, *54*, 181–189. [CrossRef]

7. Ogea, D.P.; Gordienko, S.V.; Sinebryukhov, S.L.; Podgorbunsky, A.B.; Sokolov, A.A.; Ustinov, A.Y.; Kurjavyi, V.G.; Mayorov, V.Y.; Zheleznov, V.V. Doping of titania with manganese for improving cycling and rate performances in lithium-ion batteries. *Chem. Phys.* **2020**, *536*, 110864. [CrossRef]
8. Fujishima, A.; Honda, K. Electrochemical Photolysis of Water at a Semiconductor Electrode. *Nature* **1972**, *238*, 37–38. [CrossRef] [PubMed]
9. Tan, H.L.; Amal, R.; Ng, Y.H. Alternative strategies in improving the photocatalytic and photoelectrochemical activities of visible light-driven $BiVO_4$. *J. Mater. Chem. A* **2017**, *5*, 16498–16521. [CrossRef]
10. Cao, S.; Zhou, P.; Yu, J. Recent advances in visible light Bi-based photocatalysis. *Chin. J. Catal.* **2014**, *35*, 989–1007.
11. Mehraj, O.; Pirzada, B.M.; Mir, N.A.; Khan, M.Z.; Sabir, S. A highly efficient visible-light-driven novel pn junction Fe_2O_3/BiOI photocatalyst: Surface decoration of BiOI nanosheets with Fe_2O_3 nanoparticles. *Appl. Surf. Sci.* **2016**, *387*, 642–651. [CrossRef]
12. Li, D.; Shi, W. Recent developments in visible-light photocatalytic degradation of antibiotics. *Chin. J. Catal.* **2016**, *37*, 792–799. [CrossRef]
13. Lisowska-Oleksiak, A.; Szyborowska, K.; Janulaitiene, V. Preparation and characterisation of visible light responsive iodine doped TiO2 electrodes. *Electrochim. Acta* **2010**, *55*, 5981–5985. [CrossRef]
14. Bakar S.A.; Ribeiro, C. Nitrogen-doped titanium dioxide: An overview of material design and dimensionality effect over modern applications. *J. Photochem. Photobiol. C Photochem. Rev.* **2016**, *27*, 1–29. [CrossRef]
15. Wysocka, I.; Kowalska, E.; Ryl, J.; Nowaczyk, G.; Zielińska, A. Morphology, Photocatalytic and Antimicrobial Properties of TiO_2 Modified with Mono- and Bimetallic Copper, Platinum and Silver Nanoparticles. *Nanomaterials* **2019**, *9*, 1120. [CrossRef] [PubMed]
16. Macyk, W.; Szaciłowski, K.; Stochel, G.; Buchalska, M.; Kuncewicz, J.; Łabuz, P. Titanium (IV) complexes as direct TiO_2 photosensitizers. *Coord. Chem. Rev.* **2010**, *254*, 687–2701. [CrossRef]
17. Assefpour-Dezfuly, M.; Vlachos, C.; Andrews, E.H. Oxide morphology and adhesive bonding on titanium surfaces. *J. Mater. Sci.* **1984**, *19*, 3626–3639. [CrossRef]
18. Kasuga, T.; Hiramatsu, M.; Hoson, A.; Sekino, T.; Niihara, K. Formation of Titanium Oxide Nanotube. *Langmuir* **1998**, *14*, 3160–3163. [CrossRef]
19. Armstrong, A.R.; Canales, J.; Garcia, R.; Bruce, P.G. Lithium-ion intercalation into TiO_2-B Nanowires. *Adv. Mater.* **2005**, *17*, 862–865. [CrossRef]
20. Zwilling, V.; Aucouturier, M.; Darque-Ceretti, E. Anodic oxidation of titanium and TA6V alloy in chromic media. An electrochemical approach. *Electrochim. Acta* **1999**, *45*, 921–929. [CrossRef]
21. Macák, M.; Tsuchiya, H.; Schmuki, P. High-Aspect-Ratio TiO_2 Nanotubes by Anodization of Titanium. *Angew. Chem. Int. Ed.* **2005**, *44*, 2100–2102. [CrossRef]
22. Albu, S.P.; Ghicov, A.; Macak, J.M.; Schmuki, P. 250 μm long anodic TiO_2 nanotubes with hexagonal self-ordering. *Phys. Status Solidi Rapid Res. Lett.* **2007**, *1*, 65–67. [CrossRef]
23. Fu, Y.; Mo, A. A review on the electrochemically self-organized titania nanotube arrays: Synthesis, modifications, and biomedical applications. *Nanoscale Res. Lett.* **2018**, *13*, 1–21. [CrossRef] [PubMed]
24. Yoo, J.E.; Schmuki, P. Critical factors in the anodic formation of extremely ordered titania nanocavities. *J. Electrochem. Soc.* **2019**, *166*, C3389–C3398. [CrossRef]
25. Qi, K.; Cheng, B.; Yu, J.; Ho, W. A review on TiO_2-based Z-scheme photocatalysts. *Chin. J. Catal.* **2017**, *38*, 1936–1955. [CrossRef]
26. Jarosz, M.; Grudzień, J.; Kapusta-Kołodziej, J.; Chudecka, A.; Sołtys, M.; Sulka, G.D. Anodization of titanium alloys for biomedical applications. In *Nanostructured Anodic Metal Oxides: Synthesis and Applications*; Elsevier: Amsterdam, The Netherlands, 2020; p. 211.
27. Li, H.H.; Wu, X.Y.; Yin, S.; Katsumata, K.; Wang, Y.H. Effect of rutile TiO_2 on the photocatalytic performance of g-C_3N_4/brookite-TiO_2-N_y photocatalyst for NO decomposition. *Appl. Surf. Sci.* **2017**, *392*, 531–539. [CrossRef]
28. Sakoda, M.; Trzciński, K.; Nowak, A.P.; Coy, E.; Wicikowski, L.; Łapiński, M.; Stuczak, K.; Lisowska-Oleksiak, A. Titania nanotubes modified by a pyrolyzed metal-organic framework with zero valent iron centers as a photoanode with enhanced photoelectrochemical, photocatalytical activity and high capacitance. *Electrochim. Acta* **2018**, *278*, 13–24. [CrossRef]
29. Paulose, M.; Mor, G.K.; Varghese, O.K.; Shankar, K.; Grimes, C.A. Visible light photoelectrochemical and water-photoelectrolysis properties of titania nanotube arrays. *J. Photochem. Photobiol. A Chem.* **2006**, *178*, 8–15. [CrossRef]
30. Schulte, K.L.; DeSario, P.A.; Gray, K.A. Effect of crystal phase composition on the reductive and oxidative abilities of TiO_2 nanotubes under UV and visible light. *Appl. Catal. B Environ.* **2010**, *97*, 354–360. [CrossRef]
31. Varghese, O.K.; Paulose, M.; Shankar, K.; Mor, G.K.; Grimes, C.A. Water-Photolysis Properties of Micron-Length Highly-Ordered Titania Nanotube-Arrays. *J. Nanosci. Nanotechnol.* **2006**, *5*, 1158–1165. [CrossRef]
32. Nah, Y.-C.; Paramasivam, I.; Schmuki, P. Doped TiO_2 and TiO_2 Nanotubes: Synthesis and Applications. *ChemPhysChem* **2010**, *11*, 2698–2713. [CrossRef]
33. Sakoda, M.; Stuczak, K.; Lisowska-Oleksiak, A.; Kamczewski, J.; Ryl, J. Facile preparation of extremely photoactive boron-doped TiO_2 nanotubes arrays. *Electrochim. Commun.* **2016**, *80*, 212–215. [CrossRef]
34. Piątkowska, A.; Janus, M.; Szymański, K.; Mozia, S. C-, N- and S-Doped TiO_2 Photocatalysts: A Review. *Catalysts* **2021**, *11*, 144. [CrossRef]

35. Sekino, T.; Okamoto, T.; Kasuga, T.; Kusunose, T.; Nakayama, T.; Niihara, K. Synthesis and Properties of Titania Nanotube Doped with Small Amount of Cations. *KEM* **2006**, *317–318*, 251–254. [CrossRef]
36. Sołtys-Mróz, M.; Syrek, K.; Pierzchała, J.; Wierzgroch, E.; Makek, K.; Sulka, G.D. Band gap engineering of nanotubular Fe_2O_3-TiO_2 photoanodes by wet impregnation. *Appl. Surf. Sci.* **2020**, *517*, 146195. [CrossRef]
37. Qarechalloo, S.; Naseri, N.; Salehi, F.; Moshfegh, A.Z. Simply tuned and sustainable cobalt oxide decorated titania nanotubes for photoelectrochemical water splitting. *Appl. Surf. Sci.* **2019**, *464*, 68–77. [CrossRef]
38. Jiang, P.; Xiang, W.; Kuang, J.; Liu, W.; Cao, W. Effect of cobalt doping on the electronic, optical and photocatalytic properties of TiO_2. *Solid State Sci.* **2015**, *46*, 27–32. [CrossRef]
39. Monazzam, P.; Kiasmi, B.F. Co/TiO_2 nanoparticles: Preparation, characterization and its application for photocatalytic degradation of methylene blue. *Desalination Water Treat.* **2017**, *63*, 283–292.
40. Preethi, T.; Abirosa, B.; Vidhya, K.N.; Rajarajeswari, G.R. Sol–gel derived cobalt doped nano-titania photocatalytic system for solar light induced degradation of crystal violet. *Ceram. Int.* **2014**, *40*, 13159–13167. [CrossRef]
41. Wojdyr, M. Fityk: A general-purpose peak fitting program. *J. Appl. Cryst.* **2010**, *43*, 1126–1128. [CrossRef]
42. Available online: https://www.fluorotubes.com/order/catalog/product/1QEAADGACKFAGRMAVI (accessed on 16 March 2021).
43. Sakoda, M.; Siuzdak, K.; Lisowska-Oleksiak, A. Optimization of electrochemical doping approach resulting in highly photoactive iodine-doped titania nanotubes. *J. Sol. State Electrochem.* **2016**, *20*, 563–569. [CrossRef]
44. Sulka, G.D.; Kapusta-Kołodziej, J.; Brzózka, A.; Jaskuła, M. Fabrication of nanoporous TiO_2 by electrochemical anodization. *Electrochim. Acta* **2010**, *55*, 4359–4367. [CrossRef]
45. Zemann, J. Crystal structures. *Acta Cryst.* **1968**, *16*, 139. [CrossRef]
46. Spiridonova, J.; Katerski, A.; Danilson, M.; Krichevskaya, M.; Krunks, M.; Acik, I.O. Effect of the Titanium Isopropoxide Acetylacetone Molar Ratio on the Photocatalytic Activity of TiO_2 Thin Films. *Molecules* **2019**, *24*, 4326. [CrossRef]
47. Patterson, A.L. The scherrer formula for X-ray particle size determination. *Phys. Rev.* **1939**, *56*, 978–982. [CrossRef]
48. Chanda, A.; Rout, K.; Vasundhara, M.; Joshi, S.R.; Singh, J. Structural and magnetic study of undoped and cobalt doped TiO_2 nanoparticles. *RSC Adv.* **2018**, *8*, 10939–10947. [CrossRef]
49. Tian, F.; Zhang, Y.; Zhang, J.; Pan, C. Raman spectroscopy: A new approach to measure the percentage of anatase TiO_2 exposed (001) facets. *J. Phys. Chem. C* **2012**, *116*, 7515–7519. [CrossRef]
50. Ohsaka, T.; Izumi, F.; Fujiki, Y. Raman spectrum of anatase, TiO_2. *J. Raman Spectrosc.* **1978**, *7*, 321–324. [CrossRef]
51. Swamy, S.; Muddle, B.C.; Dai, Q. Size-dependent modifications of the Raman spectrum of rutile TiO_2. *Appl. Phys. Lett.* **2006**, *89*, 163118. [CrossRef]
52. Bassi, A.L.; Cattaneo, D.; Russo, V.; Bottani, C.E.; Barborini, E.; Mazza, T.; Piseri, P.; Milani, P.; Ernst, F.O.; Wegner, K.; et al. Raman spectroscopy characterization of Titania nanoparticles produced by flame pyrolysis: The influence of size and stoichiometry. *J. Appl. Phys.* **2005**, *98*, 074305. [CrossRef]
53. Wani, T.H.M.; Smith, M.F.; Chanlek, N.; Chen, F.; Songsasiritthigul, P. Physical origin of diminishing photocatalytic efficiency for recycled TiO_2 nanotubes and Ag-loaded TiO_2 nanotubes in organic aqueous solutions. *Catalysts* **2020**, *10*, 737. [CrossRef]
54. Cabrera-German, D.; Gomez-Sosa, G.; Herrera-Gome, A. Accurate peak fitting and subsequent quantitative composition analysis of the spectrum of Co 2p obtained with Al Kα radiation: I. Cobalt spinel. *Surf. Interface Anal.* **2016**, *48*, 252–256. [CrossRef]
55. Chaudhury, B.; Choudhury, A.; Islam, A.M.; Alagarsamy, P.; Mukherjee, M. Effect of oxygen vacancy and dopant concentration on the magnetic properties of high spin Co2p doped TiO_2 nanoparticles. *J. Magn. Magn. Mater.* **2011**, *323*, 440–446. [CrossRef]
56. Liu, Y.B.; Yang, Y.M.; Zhuang, B.; Huang, S.L.; Wu, L.P.; Huang, Z.G.; Zhang, F.M.; Du, Y.W. Ferromagnetism of Co-doped TiO_2 films prepared by plasma enhanced chemical vapour deposition (PECVD) method. *J. Phys. D Appl. Phys.* **2008**, *41*, 195007. [CrossRef]
57. Li, J.G.; Ikeda, R.; Ishe, M.; Mori, T.; Ishigaki, T. Cobalt-doped TiO2 nanocrystallites: Radio-frequency thermal plasma processing, phase structure, and magnetic properties. *J. Phys. Chem. C* **2009**, *113*, 8009–8015. [CrossRef]
58. Antonio, J.T.; Cortés-Jácome, M.; Orozco-Cerros, S.; Palacios, E.M.; Suárez-Parra, R.; Angeles-Chávez, C.; Navarrete, J.; López-Salinas, E. Assessing optimal photoactivity on titania nanotubes using different annealing temperatures. *Appl. Catal. B Environ.* **2010**, *100*, 47–54. [CrossRef]
59. Mizukoshi, Y.; Ohtsu, N.; Masahashi, N. Structural and characteristic variation of anodic oxide on pure Ti with anodization duration. *Appl. Surf. Sci.* **2013**, *283*, 1018–1023. [CrossRef]
60. Deng, G.; Hu, H.; Huang, X.; Zhang, Y.; Bi, Y. Rapid activation of Co_3O_4 cocatalysts with oxygen vacancies on TiO_2 photoanodes for efficient water splitting. *J. Mater. Chem. A* **2018**, *6*, 21003–21009. [CrossRef]
61. Sakoda, M.; Siuzdak, K.; Lisowska-Oleksiak, A. Non-metal doped TiO_2 nanotube arrays for high efficiency photocatalytic decomposition of organic species in water. *Phys. E Low-Dimens. Syst. Nanostruct.* **2016**, *84*, 141–145. [CrossRef]
62. Bard, A.J.; Faulkner, L.R.; Wang, J. Electrochemical Methods: Fundamentals and Applications. *J. Chem. Educ.* **1983**, *60*, A25.
63. Sakoda, M.; Trzciński, K.; Lisowska-Oleksiak, A.; Siuzdak, K. Electrochemical and photoelectrochemical properties of the interface between titania nanotubes covered by conducting polymer in aqueous—The effect of various geometry and electrolyte concentration. *Appl. Surf. Sci.* **2018**, *445*, 309–319. [CrossRef]
64. Momeni, M.M.; Ghayeb, Y. Photoelectrochemical water splitting on chromium-doped titanium dioxide nanotube photoanodes prepared by single-step anodizing. *J. Alloys Compd.* **2015**, *637*, 393–400. [CrossRef]

65. Chakhari, W.; Naceur, J.B.; Taieb, S.B.; Amaker, I.B.; Chtourou, R. Fe-doped TiO_2 nanorods with enhanced electrochemical properties as efficient photoanode materials. *J. Alloys Compd.* **2017**, *708*, 862–870. [CrossRef]
66. Ganesh, I.; Kumar, P.P.; Annapoorna, I.; Sumliner, J.M.; Ramakrishna, M.; Hebalkar, N.Y.; Padmanabham, G. Applied Surface Science Preparation and characterization of Cu-doped TiO_2 materials for electrochemical, photoelectrochemical, and photocatalytic applications. *Appl. Surf. Sci.* **2014**, *293*, 229–247. [CrossRef]
67. Guaglianoni, W.C.; Florence, C.L.; Bonatto, F.; Venturini, J.; Arcaro, S.; Alves, A.K.; Bergmann, C.P. Novel nanoarchitectured cobalt-doped TiO_2 and carbon nanotube arrays: Synthesis and photocurrent performance. *Ceram. Int.* **2019**, *45*, 2439–2445. [CrossRef]
68. Venturini, J.; Bonatto, F.; Guaglianoni, W.C.; Lemes, T.; Arcaro, S.; Alves, A.K.; Bergmann, C.P. Applied Surface Science Cobalt-doped titanium oxide nanotubes grown via one-step anodization for water splitting applications. *Appl. Surf. Sci.* **2019**, *464*, 351–359. [CrossRef]
69. Sakeda, M.; Lisowska-Oleksiak, A.; Smedak, K. Optimization of boron-doping process of titania nanotubes via electrochemical method toward enhanced photoactivity. *J. Solid State Electrochem.* **2016**, *20*, 1765–1774. [CrossRef]
70. Zhang, M.; Lu, D.; Zhang, Z.; Yang, J. Enhancement of visible-light-induced photocurrent and photocatalytic activity of V and N co-doped TiO_2 nanotube array films. *J. Electrochem. Soc.* **2014**, *161*, H416–H421. [CrossRef]
71. Gogoi, D.; Namdeo, A.; Kumar, A. ScienceDirect Ag-doped TiO_2 photocatalysts with effective charge transfer for highly efficient hydrogen production through water splitting. *Int. J. Hydrog. Energy* **2019**, *45*, 2729–2744. [CrossRef]
72. Kongkanand, A.; Tvrdy, K.; Takechi, K.; Kuno, M.; Kamat, P.V. Quantum dot solar cells. Tuning photoresponse through size and shape control of CdSe—TiO_2 architecture. *J. Am. Chem. Soc.* **2008**, *130*, 4007–4015. [CrossRef]

IV.3 Supplementary Information

materials

MDPI

Supplementary

Hydrothermal Cobalt Doping of Titanium Dioxide Nanotubes towards Photoanode Activity Enhancement

Mariusz Wtulich [1], Mariusz Szkoda [1], Grzegorz Gajowiec [2], Maria Gazda [3], Kacper Jurak [4], Mirosław Sawczak [5] and Anna Lisowska-Oleksiak [1,*]

[1] Department of Chemistry and Technology of Functional Materials, Chemical Faculty, Gdańsk University of Technology, Gdańsk 80-233, Poland; wtulichd@gmail.com (M.W.); mariusz.szkoda1@pg.edu.pl (M.Sz.)
[2] Institute of Machine Technology and Materials, Faculty of Mechanical Engineering and Ship Technology, Gdańsk University of Technology, Gdańsk 80-233, Poland; grzgajowi@pg.edu.pl
[3] Department of Solid State Physics, Faculty of Applied Physics and Mathematics, Gdańsk University of Technology, Gdańsk 80-233, Poland; maria.gazda@pg.edu.pl
[4] Department of Electrochemistry, Corrosion and Materials Engineering, Chemical Faculty, Gdańsk University of Technology, Gdańsk 80-233, Poland; kacper.jurak@pg.edu.pl
[5] The Szewalski Institute of Fluid-Flow Machinery, Polish Academy of Sciences, Gdańsk 80-231, Poland; msawczak@imp.gda.pl
* Correspondence: alo@pg.edu.pl

Figure S1. EDX maps of the O, Ti and Co distributions.

Citation: Wtulich, M.; Szkoda, M.; Gajowiec, G.; Gazda, M.; Jurak, K.; Sawczak, M.; Lisowska-Oleksiak, A. Hydrothermal Cobalt Doping of Titanium Dioxide Nanotubes towards Photoanode Activity Enhancement. *Materials* **2021**, *14*, 1907. https://doi.org/10.3390/ma14081907

Academic Editor: Rosalinda Inguanta

Received: 10 February 2021
Accepted: 15 March 2021
Published: 19 March 2021

Chapter V

Tailoring TiO_2 nanotubes photoanodes with electrodeposited Co_3O_4 and CoOOH cocatalysts for enhanced electrocatalytic and photoelectrocatalytic oxygen evolution.

V.1 Methods in Brief and Key Results

This study explores the controlled electrodeposition of cobalt onto HA TiO_2 nanotubes to synthesise two different cocatalyst structures, Co_3O_4 and CoOOH, and whether these structures exhibit different OER activity in the dark and under simulated sunlight. In this work, the mechanism by which CoOOH boosts the oxidation of water is explained.

Electrochemical deposition is an effective, controlled process for forming cobalt species on electrode surfaces. At a constant temperature in a buffered solution, metallic cobalt with dimensions of 100 nm x 100 nm was successfully deposited. The deposited charge was precisely controlled within a range from 20 to 100 mC/cm². The TiO_2 electrodes with the deposited cobalt were then subjected to two modifications: 1) calcination in a furnace to obtain Co_3O_4; 2) the appropriate pH and potential range were selected according to the Pourbaix diagram, at which the deposited cobalt was cycled until the cobalt was fully oxidized to form CoOOH. The layers were comprehensively characterized using XPS, FTIR, XRD, and Raman spectroscopy, confirming the stoichiometry of the compounds.

Electrochemical studies in 0.2 M Na_2SO_4 solution revealed a clear difference in the electro-, photo-, and photoelectrocatalytic properties. In the dark, the CoOOH cocatalyst significantly reduced the oxygen evolution overpotential from approximately 1.41 V for the pure nanotubes to approximately 0.80 V at a charge of 100 mC/cm². However, no significant change was observed for Co_3O_4. In measurements using simulated sunlight, the photocurrent almost doubled (from 36 µA/cm² at 0.4 V vs. Ag/AgCl/3M KCl to 70 mC/cm²) for CoOOH at 40 mC/cm², while at 100 mC/cm², a lower efficiency (21 mC/cm²) was observed compared to the pure nanotubes. A similar trend occurs for Co_3O_4; however, the values are lower (maximum 40 µA/cm² at 40 mC/cm²).

Studies were also performed with and without light in the presence of a scavenger (hydroquinone). These studies suggested that CoOOH promotes rapid and reversible cycling between cobalt's valence states, allowing it to consume photogenerated holes from TiO_2 and mediate proton-coupled electron transfer, which is involved in oxygen-oxygen bond formation. Second, CoOOH is permeable to the electrolyte (Co_3O_4 is dense), allowing ions to move more readily

through the cocatalyst layer. Third, the transient cathodic currents that appear after the light is turned off are attributed to the reduction of Co^{4+} and the contribution of superoxides generated from adsorbed oxygen. The introduction of a hole scavenger suppresses these transient states, reduces charge carrier recombination, and increases photocurrent stability, directly confirming the role of cobalt sites in hole storage and transfer. Summary depicted in Figure 14.

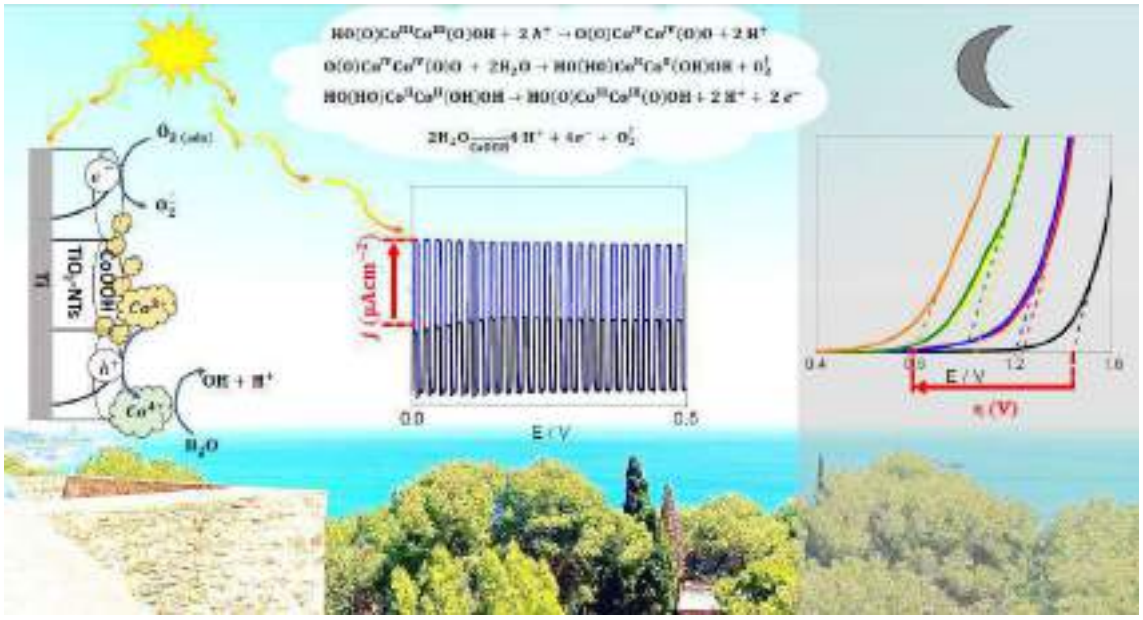

Figure 14. Graphical abstract.

Additionally, photocatalytic studies were conducted to decolorize an aqueous solution with methylene blue. Oxidation of cobalt to (4+) is thought to produce superoxide species with photodegrading properties, leading to decomposition to leuco-methylene blue (LMB) and other products. In summary, this study demonstrates that CoOOH is the preferred cocatalyst for TiO_2 photoanodes because it combines favorable electro/photo/photoelectrochemical reduction properties with electrolyte permeability, providing lower overpotentials, higher and more stable photocurrents, and improved catalytic performance.

V.2 Publication

Applied Surface Science 714 (2025) 164376

Contents lists available at ScienceDirect

Applied Surface Science

journal homepage: www.elsevier.com/locate/apsusc

Full Length Article

Tailoring TiO_2 nanotubes photoanodes with electrodeposited Co_3O_4 and CoOOH cocatalysts for enhanced electrocatalytic and photoelectrocatalytic oxygen evolution

Mariusz Wrzich, Anna Lisowska-Oleksiak *

Department of Chemistry and Technology of Functional Materials, Faculty of Chemistry, Gdańsk University of Technology, Gdańsk 80-233, Poland

ARTICLE INFO

Keywords:
TiO_2 nanotubes
Water splitting
Photoelectrocatalysis
Cobalt oxyhydroxide
OER

ABSTRACT

In this work, titanium dioxide nanotubes (TiO_2-NTs) were functionalized with cobalt-based cocatalysts — Co_3O_4 and CoOOH — via controlled electrodeposition to improve their performance in electrocatalytic and photoelectrocatalytic oxygen evolution reaction (OER). TiO_2-NTs, prepared by anodization and hydrothermal annealing, provided a stable and photoactive platform. Structural and chemical characterization (SEM, EDX, XRD, ATR-FTIR, XPS) confirmed successful deposition of the cocatalyst layers. Electrochemical measurements revealed a markedly superior performance of CoOOH-modified electrodes, which exhibited a significantly reduced OER onset potential (0.60 V vs. Ag/AgCl) compared to pristine TiO_2-NTs and TiO_2-NTs/Co_3O_4. Under illumination, TiO_2-NTs/CoOOH generated up to twice the photocurrent of their Co_3O_4-modified counterparts. Mechanistic analysis attributed this enhancement to the proton-coupled electron transfer capability of CoOOH. Additionally, photocatalytic degradation of methylene blue confirmed that the presence of CoOOH enhances the catalytic performance of TiO_2, indicating improved overall activity of the composite material. These findings highlight CoOOH as a more effective cocatalyst than Co_3O_4 for enhancing TiO_2 NTs-based systems in solar-assisted water splitting and pollutant degradation applications.

1. Introduction

Despite the challenging geopolitical context, researchers should provide society with solutions that, even if only slightly, can help mitigate the effects of global warming. Scientists' efforts to obtain hydrogen from water through aqueous electrolysis remain steadfast. One of the primary challenges in identifying a stable anode for water electrolysis or a reliable photoanode for solar-assisted electrolysis. Among the most stable anodes, which fall under the category of dimensionally stable anodes (DSA), is titanium dioxide (TiO_2). TiO_2, in the form of nanomaterials, warrants special attention, as those produced on conductive substrates through the anodization process offer a viable solution for photoanodic activity when grown on solid Ti substrate conductors.

Titanium dioxide nanotubes have been extensively investigated due to their excellent chemical stability, favourable bandgap, and high specific surface area, which enables efficient absorption of solar radiation across both the visible and ultraviolet regions [1,2]. Their unique tubular structure enhances light harvesting, making them an ideal platform for various photocatalytic applications, particularly as photoanodes in photoelectrochemical (PEC) cells [3]. Despite these advantages, the intrinsic properties of pristine TiO_2-NTs are limited by the rapid recombination of photogenerated charge carriers, necessitating further modifications to improve their overall efficiency [4]. To overcome these challenges, a variety of strategies have been explored, including non-metal doping to narrow the bandgap (e.g., nitrogen [5], carbon [6,7], sulphur [8,9]); incorporation of metal elements into the crystal structure to modify the electronic properties of the semiconductor (e.g., nickel [10], chromium [11], cobalt [12,13]); deposition of noble metal nanoparticles to induce the plasmon effect (e.g., Au [14], Pt [15], Pd [16]); formation of a cocatalyst layer to enhance the oxygen evolution reaction (e.g., metal oxides [17,18], oxyhydroxides [19–21] or phosphates [22]); morphological engineering (e.g., creating porous [23,24], double-walled [25], bamboo structures [26], ultra-long with a small diameter [26], laser-treated [27], or hydrothermal annealed [28] nanotubes); and multi-component electrode construction to develop Z-scheme or staircase photocatalytic systems for improved charge transfer [29–31]. Among these approaches, integrating metal oxide nano-

* Corresponding author.
E-mail address: anna.lisowska-oleksiak@pg.edu.pl (A. Lisowska-Oleksiak).

https://doi.org/10.1016/j.apsusc.2025.164376
Received 24 May 2025; Received in revised form 4 August 2025; Accepted 13 August 2025
Available online 18 August 2025

additives appears to be highly effective in enhancing photoanode performance [34]. In particular, cobalt oxide (Co_3O_4) exhibits favourable characteristics as a constituent in the oxygen evolution reaction [10,24]. The catalytic enhancement is primarily attributed to cobalt ion centres facilitating electron transfer via proton-assisted electron transfer (PAET) [35]. Density functional theory (DFT) calculations further show that reducing the particle size of Co oxide clusters and tuning their oxidation state can modestly improve their redox properties and photocatalytic activity [36]. Therefore, electrodeposition can be used to achieve controlled growth of such nano-additives with desired density and orientation [37]. Numerous studies identified cobalt oxyhydroxide (CoOOH) as a promising cocatalyst that enhances the separation and transport of photogenerated holes while reducing charge recombination [38,39]. Its catalytic activity is based on fast cobalt valency reverse transformation from Co(II) and Co(III) to Co(IV) under high anodic potential and oxidation via holes [39], enabling proton uptake, which accelerates O–O bond formation and oxygen evolution [41,42]. Consequently, CoOOH offers a high density of active sites and facilitates the dynamic regeneration of its catalytic centres through interactions with water molecules. Additionally, its unique structure enhances the storage of photogenerated holes, thereby boosting overall OER efficiency [43,44].

Furthermore, the newest studies on Co_3O_4 and CoOOH coated $BiVO_4$ photoanodes have shown that cocatalyst morphology significantly impacts photoanode performance [45]. In particular, CoOOH show especially activity due to its enhanced electrolyte permeability and improved hole transport properties, which facilitate the efficient accumulation and transfer of photogenerated holes [46,47]. Crucial studies using ultramicroelectrodes indicate that proton-assisted electron transfer (PAET) is a key mechanism underlying the electrocatalytic behaviour of CoOOH [35]. The impact of Co_3O_4 vs CoOOH on TiO_2-NTs photoanode performance can also depend on the nanotubes' morphology, and electrolyte permeability remains a crucial factor. An innovative, cost-effective, hydrothermal annealing (HA) method was developed to modify the titanium plate, producing homogeneous Titania nanotubes with a significant reduction in impurities (e.g., fluorine, phosphorous). This treatment significantly lowers the OER overpotential and enhances photocurrent generation [30].

Here, we report the formation of cocatalysts, namely Co_3O_4 and CoOOH, via a cobalt electrodeposition process onto HA TiO_2 NTs, using chronoamperometry to control nucleation and growth. Here, we compare two distinct cobalt species used for TiO_2 modification towards water photoelectrooxidation: dense Co_3O_4 and the electrolyte-permeable CoOOH. The combined TiO_2/cobalt species junction is investigated concerning its electrochemical properties under dark conditions focusing on recombination processes and OER and its response under solar illumination (photocurrent generation). Additionally, the photocatalytic activity is evaluated by monitoring the degradation of methylene blue. This study compares the effects of Co_3O_4 and CoOOH on hydrothermally annealed TiO_2-NTs used as anode and photoanode active in OER in neutral electrolytes.

2. Experimental section

2.1. Materials

Ammonium fluoride (NH_4F), potassium sulphate (K_2SO_4), sodium citrate ($Na_3C_6H_5O_7$) and methylene blue ($C_{16}H_{18}ClN_3S$) were obtained from Sigma-Aldrich (St. Louis, USA. Cobalt chloride 98 % ($CoCl_2$), sodium hydroxide (NaOH), ethylene glycol ($C_2H_6O_2$) and orthophosphoric acid (H_3PO_4) were purchased from POCH (Gliwice, Poland). Alfa Aesar (Kandel, Germany) provided titanium foil (min. 99.5 % metals basis, annealed, thickness 0.25 mm) and fluorine-doped tin oxide glass (FTO). The water used in the study was distilled and possessed an electrical conductivity of 0.1 μS cm^{-1}.

2.2. Preparation of the HA TiO_2-NTs electrode

For the electrode preparation, the titanium foil underwent cutting into square pieces with a side of 2 cm, followed by pressing with a force of 2 tons. The samples were then subjected to degreasing in an ultrasonic bath for 20 min at 40 °C, where a solution of acetone and isopropyl alcohol in a 1:1 ratio was used. Subsequently, the samples were rinsed with distilled water.

For the anodization process, both metal plates were positioned in a two-electrode glassy cell, ensuring a 2 cm gap between them. The glassy cell was filled with 50 ml of an aqueous electrolyte solution containing ethylene glycol, NH_4F (0.5 g), H_2O (2.5 ml), and H_3PO_4 (1.75 ml) [13]. This setup facilitated the synthesis of Titania nanotubes by applying a constant voltage of 40 V for 2 h while maintaining a temperature of 20 ± 1 °C.

Following the anodization process, thorough rinsing of the samples was carried out, after which they underwent calcination in a furnace at 450 °C. The heating rate was set at 2.5 °C/min, and airflow was maintained throughout the process. Finally, the samples were cooled in ambient air to room temperature after 2 h of calcination, during which the formation of TiO_2-NTs occurred.

The subsequent procedure involved transferring the electrodes to an autoclave with a stainless steel chamber lined with PTFE (30 ml of water per 50 ml of total chamber volume). The electrodes underwent further hydrothermal annealing at a temperature of 100 °C for 24 h. After this process and drying in warm air, HA TiO_2-NTs were obtained.

2.3. Preparation of the HA TiO_2-NTs/Co_3O_4 electrode

First, cobalt was electrochemically deposited on the nanotubes in a three-electrode cell one-compartment configuration with the working electrode (WE) being TiO_2-NTs, counter electrode (CE) as Pt mesh, and reference electrode (REF) as Ag/AgCl/3 M KCl. This process was carried out in an aqueous solution consisting of 0.15 M $CoCl_2$, 0.15 M sodium citrate, and 0.05 M NaCl, with an applied potential of −1.05 V vs. Ag/AgCl (3 M KCl). The electrolyte was maintained at a constant temperature (10 °C) and purged with argon for 1 h. Then, the electrode was subjected to a furnace in the air at 400 °C with a heating rate of 2 °C/min for 2 h. During the calcination process, cobalt is oxidized to cobalt oxide, and HA TiO_2-NTs/Co_3O_4 is obtained.

2.4. Preparation of the HA TiO_2-NTs/CoOOH electrode

To obtain a high-activity TiO_2-NTs/CoOOH electrode with co-catalysts, a two-step process is required. First, cobalt is electrodeposited onto titania nanotubes (as described above). Second, the electrode is fully oxidized via potentiodynamic cycling in the buffered NaOH solution (pH 10) to stabilise the CV curves. This involves 100 cycles at a scan rate of 10 mV/s^{-1}, conducted at a constant temperature of 20 °C. The potential range for the potentiodynamic polarization should be maintained between −0.1 and 0.7 V vs. Ag/AgCl (3 M KCl). Two different cobalt deposition charges were applied: 20 mC/cm^2, 40 mC/cm^2, 60 mC/cm^2, 80 mC/cm^2, and 100 mC/cm^2. The CV curves recorded during the formation of TiO_2-NTs/CoOOH are shown in Fig. S1.

2.5. Materials characterization

The JSM-7900F (JEOL, Tokyo, Japan) field emission scanning electron microscope (SEM), with a beam acceleration voltage of 5 kV, was used to characterize the electrode morphologies. The identification of chemical elements was conducted using energy-dispersive X-ray spectroscopy (EDX), employing a detector with a silicon nitride window (OCTANE ELITE model by EDAX company, New Jersey, USA). The crystal structure and phase composition of the synthesized photocatalysts were determined using X-ray powder diffraction, using a Rigaku MiniFlex 600 X-ray diffractometer with Cuka emission. The

optical characteristics were investigated with the aid of a UV–Vis spectrophotometer (Thermo Fisher Scientific Evolution 220). Barium sulphate served as a reference standard (blank probe). The X-ray photoelectron spectroscopy (XPS) measurements were performed using Omicron NanoScience equipment, including an Argus hemispherical analyser. The analysis and deconvolution of the elemental spectrum were conducted by employing a Pseudo/Voigt sum envelope with an asymmetric tail and applying the Shirley background subtraction technique using Fityk software [48]. All binding energies obtained in the XPS analysis were referenced to the C1s line at 285.0 eV. The Attenuated Total Reflectance Fourier Transformation of Infrared Radiation (ATR-FTIR) analysis in the region of 4000–400 cm^{-1} was carried out using a Nicolet iS10 apparatus (Thermo Fisher Scientific, Waltham, MA, USA). The measurement was averaged from 32 scans with a resolution of 4 cm^{-1}. The electrochemical and photoelectrochemical studies were carried out with a potentiostat–galvanostat system, consisting of an Autolab PGSTat30 with an FRA module from Eco Chemie B.V. and Autolab POSTAT 30 from Metrohm Autolab B.V., both purchased from Utrecht, Netherlands. The measurements were conducted within a three-electrode cell, where TiO_2-NTs served as the working electrode (WE), a platinum mesh functioned as the counter electrode (CE), and an Ag/AgCl/0.1 M KCl electrode acted as the reference electrode (RE). The linear sweep voltammetry (LSV), cyclic voltammetry (CV), chronoamperometry (CA), and electrochemical impedance spectroscopy (EIS), were performed in 0.2 M K_2SO_4 electrolyte that had been purged with high-purity argon gas (Ar gas with O_2 content < 0.2 ppm) for 30 min before the experiment. The temperature was controlled at 20 ± 1 °C using a Julabo F-12 thermostat from Seelbach, Germany, for all measurements. The EIS measurements were performed with frequencies ranging from 20 kHz to 0.1 Hz with ten points per decade and an amplitude of 10 mV peak-to-peak in the AC signal. In the photoelectrochemical measurements, electrodes were maintained in the same electrolyte (0.2 M K_2SO_4) and under the conditions described above. Illumination for these studies was provided by a xenon lamp, specifically the Osram XBO 150 from Quantum Design in Darmstadt, Germany, generating light with an intensity of up to 100 mW/cm^2. The lamp was equipped with an air mass 1.5 filter and an automatic shutter that operated in a 5-second cycle, opening and closing. The investigation regarding the influence of TiO_2-NTs with and without cocatalysts on the degradation of methylene blue (MB) was carried out in a dark glass reactor, insulated from external light. The photocatalytic reactions were conducted in a 50 ml water-based solution containing 10 μM MB, and illumination was provided by the lamp described above. The concentration of the MB solution was registered at 20-minute intervals using a UV–vis spectrophotometer (model UV5100, METASH).

3. Results and discussion

The silent galvanostatic deposition of cobalt metal from a citrate bath was employed to obtain and control the size of Co nanoparticles on hydrothermally annealed TiO_2 nanotubes. According to the literature, when conducted on a glassy carbon electrode, this process is governed by charge transfer kinetics and mass transport [49].

The electrodeposition of cobalt metal onto TiO_2-NTs is illustrated by the CV curve presented in Fig. 1A. As the electrode potential shifts toward the cathodic region, a distinct current increase is observed on the CV curve, indicating cobalt electrodeposition, with a threshold potential of −1.05 V (see Fig. 1A). During the reverse scan toward the anodic region, two peaks are recorded. The first peak, at E_1 = −0.85 V, likely corresponds to the stripping of a hydrogen-rich metallic phase with an hcp cobalt crystalline structure (α-Co), while the second peak, at E_2 = −0.15 V, corresponds to the stripping of a pure fcc cobalt phase (β-Co) [50].

According to the theory of electrocrystallization [51,52], the cobalt nucleation and crystal growth mechanism can be observed by analysing the chronoamperometric (CA) curve recorded at a low overpotential, before (side) overlap occurs, as shown in Fig. 1B. CA curve marked green. In the initial part of the CA curve, the nucleation time reaches 2.0 s at an electrode potential of E = −1.05V vs. Ag/AgCl/3M KCl. The type of crystal growth and nucleation can be determined from the increasing part of the cathodic current, assuming that during the early part of the current transients, any effects from charge transfer and diffusional control are negligible, Fig. 1B. The cathodic current variation with time, resulting from changes in the active surface area of the outer electrode, follows a power-law function $j \sim f(t^n)$ with exponent 'n' representing the electrocrystallization mechanism. This relationship can be quantified using a logarithmic fitting approach, as represented by Eq. (1) [51,53].

$$\frac{d\log j_{ext}}{d\log t} = n \quad (1)$$

Analysis of the run of the chronoamperometric curves depicted in Fig. 1C shows that the exponent n equals 2.03 ± 0.06 (Fig. 1C). The electrocrystallization theory allows us to assume that the nucleation

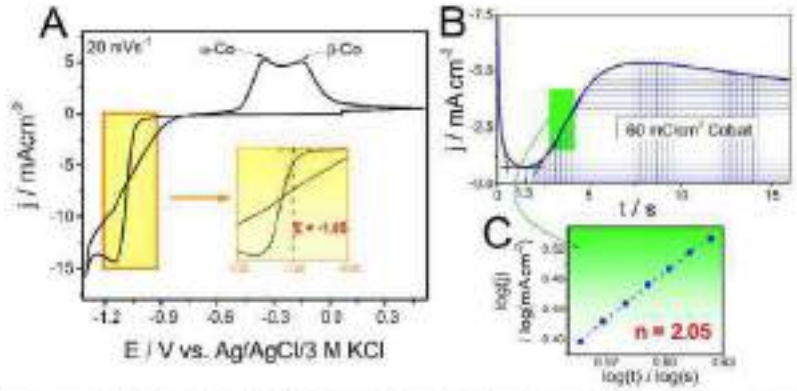

Fig. 1. A) Cyclic voltammetry for 8h TiO_2-NTs in cobalt bath with the determination of electrodeposition potential, B) current-time curve for nucleation measured at −1.05 V, C) fitted plot of determining exponent n for nucleation type.

type is progressive with 2D crystal growth [54]. Thus, chronoamperometric measurements can provide information about the shape of the crystal nuclei and the type of their growth before macroscopic analysis. The SEM morphological analysis confirms the findings from the chronoamperometric data.

A further stage of the photoanode preparation relies on the oxidation of metallic deposits. Cobalt deposit was turned into two types of Cobalt species used as catalysts. The first is cobalt oxyhydroxide, and the second is cobalt oxide. The preparation of the first catalyst was based on electrochemical methods. During the electrochemical procedure, dissolution of Co metal to Co^{2+} and further oxidation of Co^{2+} to Co^{3+} bring about a dispersed amount of CoOOH on the TiO_2 NTs surface. Cobalt metallic deposit was oxidized into cobalt nanoparticle of CoOOH in an alkaline solution (pH = 10) [55]. The obtained material shows activity typical for the redox Co^{II}/Co^{III} couple at $E_{1/2} = 0.45$ V and activity of Co^{III}/Co^{IV} above +0.75 V, depicted in Fig. S1, as expected [56,57]. This whole procedure was also performed on fluorine-doped tin oxide (FTO) glass (Fig. S2). The Co crystal nuclei growth and nucleation type remain the same regardless of the substrate used for cobalt electrodeposition. However, the activity of redox pairs is more pronounced when utilizing the FTO glass; see Fig. S2B. Notably, the redox activity Co^{II}/Co^{III} couple is observed at 0.2 V.

The second co-catalyst, Co_3O_4, was obtained on an HA-TiO_2 substrate with electrodeposited cobalt in a similar way described above. Based on the available literature, researchers subjected cobalt metal nanoparticles to further thermal treatment, such as annealing at 500 °C for 3 h in an Ar atmosphere [58], or at 400 °C for 2 h in the presence of argon [59], or for 2 h at 250 °C [60]. In our work, the electrode calcination was performed for 2 h at 410 °C in a quartz tube furnace open to the ambient air, which provides stable and understanding conditions, avoiding excessive transformation to rutile polymorph [61].

The SEM images reveal the morphology of the obtained HA-TiO_2-NTs without (Fig. 3A) and with (Fig. 3B) metallic cobalt species. The initial image showcases clear nanotubes free from surface contamination. However, the subsequent image highlights notable changes. It is evident that cobalt nanoparticles, adopting various shapes such as nano-cubes and nano-spheres, have formed on the surfaces of the TiO_2 nanotubes (with 40 mC/cm^2 cobalt loading), as observed at higher magnification in Fig. 3. The diameters of these nanoparticles range from 50 to 60 nm. Generally, the nanostructured cobalt particles are predominantly situated at the edges of the nanotubes. At 100 mC/cm^2, some nanoparticles are also observed along the sidewalls and inside the nanotubes (Fig. S4, Fig. 3 and Fig. 4). Although no specific pattern in particle distribution is discernible, their sizes remain relatively uniform. As shown in Fig. 4 and Fig. S4, this suggests that nucleation is progressive—that is, nuclei continue to form throughout the electrodeposition process while simultaneously increasing in size. Such crystal growth can be classified as two-dimensional (2D) with progressive nucleation [62].

In Fig. 3C and 3D, the electrode TiO_2-NTs/Co_3O_4 with previously

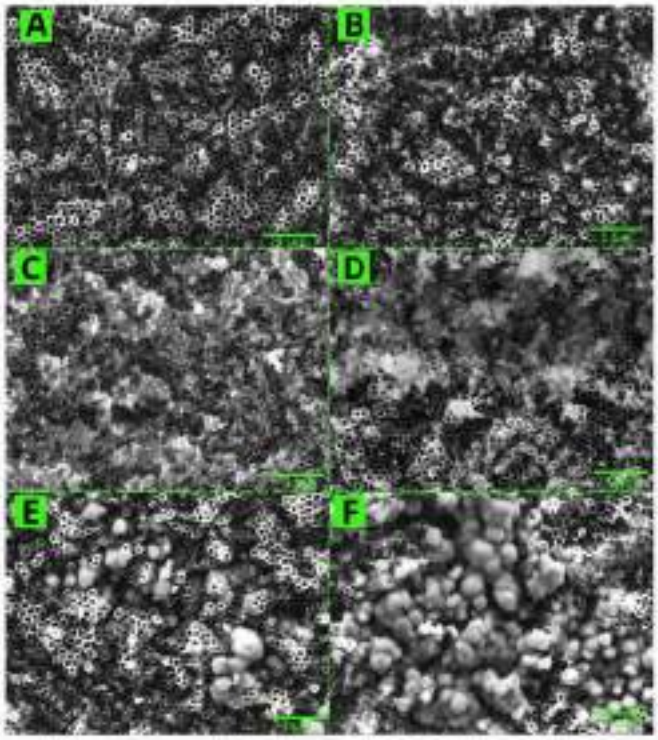

Fig. 3. Top-view SEM images at x30 000 magnification respectively for: (A) unmodified HA-TiO_2-NTs; (B) modified HA-TiO_2-NTs by cobalt electrodeposition electrode HA-TiO_2-NTs/Co_3O_4; (C) with 40 mC/cm^2 and (D) with 100 mC/cm^2 electrodes HA-TiO_2-NTs/CoOOH: (E) with 40 mC/cm^2 and (F) with 100 mC/cm^2

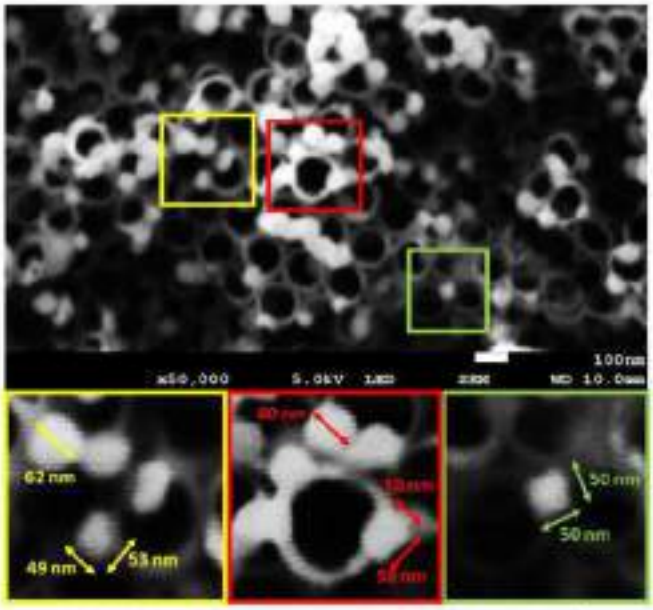

Fig. 3. Cobalt deposits onto HA TiO_2 NTs at higher magnification, charge 40 mC/cm^2.

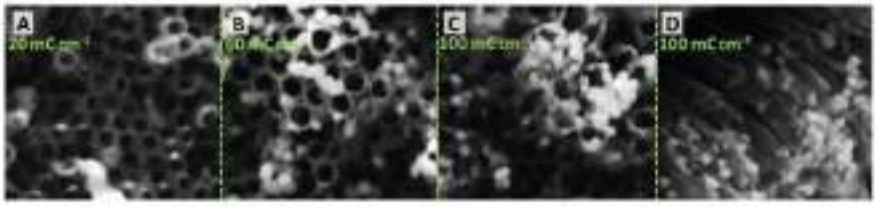

Fig. 4. Cobalt deposits onto HA TiO_2 NTs with different amounts: A) 20 mC cm^{-2}, B) 40 mC cm^{-2}, C) and D) 100 mC cm^{-2}.

deposited cobalt in amounts of 40 mC/cm^2 and 100 mC/cm^2, respectively, is presented. Evident are irregular electrolyst structures on the surface—bushy layers with traces of nanosheet stratification. Such similarities were observed in previous works [30,40,43,44]. These structures significantly obstruct the nanotubes' surface, which may limit light penetration. Fig. 3E and 3F show SEM images obtained for samples TiO_2 NTs/CoOOH with 40 mC/cm^2 and 100 mC/cm^2 of cobalt deposits. Spherical nanoparticles of the electrolyst precursor are visible on the surface, with dimensions on the order of hundreds of nanometers. With a higher amount of deposited cobalt, nanoparticles of the Co species tend to agglomerate, forming multilayer-like deposits.

EDX analyses were conducted to determine the atomic content of titanium, oxygen, cobalt, and phosphorus after the modification [29]. The chemical composition is presented in Table 1. The results confirm the presence of cobalt in the examined samples. HA TiO_2 NTs electrodes containing CoO and CoOOH deposits exhibit a trend in which the cobalt deposition of 40 mC/cm^2, the atomic content of cobalt is 1.5 % lower than in electrodes with 100 mC/cm^2 of deposited cobalt. Furthermore, the oxygen content is also higher in samples with the CoOOH catalyst, as expected. It should be noted that EDX analysis provide averaged

Table 1
The atomic percentage of elements (titanium, oxygen, cobalt, phosphorus) in HA TiO_2 nanotubes with and without cobalt deposits were determined by EDX measurements.

	HA TiO_2 NTs	HA TiO_2/NTs/Co	HA TiO_2/NTs/Co_3O_4 40mC	HA TiO_2/NTs/Co_3O_4 100mC	HA TiO_2 NTs/CoOOH 40mC	HA TiO_2 NTs/CoOOH 100mC
Ti (at. %)	43.1	40.0	41.8	39.0	39.9	35.6
O (at. %)	56.1	55.9	54.8	57.6	57.6	60.5
Co (at. %)	–	3.0	1.9	3.4	2.3	3.0
P (at. %)	0.8	0.9	1.5	0.2	0.2	0.2

elemental composition over a specific surface area and specific depth of sample penetration. Consequently, the slightly overvalued atomic content of titanium is a response from the substrate (due to the titanium foil).

The crystallinity and phase composition of samples were assessed through XRD for HA TiO_2-NTs, HA TiO_2-NTs/Co_3O_4 (40 mC/cm^2 and 100 mC/cm^2) and HA TiO_2-NTs/ CoOOH (40 mC/cm^2 and 100 mC/cm^2). In Fig. 6A, the recorded diffraction peaks at 25.3°, 48.0°, 54.8°, and 55.1° correspond to the (101), (200), (105), and (211) planes of TiO_2 – anatase, respectively [60]. This structure is characteristic of the anatase crystal, confirming the pure anatase phase in the produced TiO_2 nanotubes [61]. The registered maximum signals at 35.1°, 38.5°, 40.2° and 53.0° correlate to the Miller indices (100), (002), (101) and (102) of the structure of titanium, which crystallizes in the hexagonal $P6_3/mmc$ space group [62]. The most intense signals are associated with titanium planes, indicating it is the substrate electrode material. None of the collected diffractograms revealed any signals originating from the lattice planes of the Co_3O_4 or CoOOH species. The absence of these peaks in the XRD pattern suggests that the material under examination may be amorphous or present in an amount too small to be detected under the applied XRD measurement conditions. Additionally, low-angle X-ray diffraction patterns were collected without any signals from cobalt species.

In Fig. 6 B, the ATR-FTIR spectra of the same samples examined in the XRD measurements are presented. The reference curve, labelled as HA TiO_2-NTs, is shown in black. The observed nanotube-wavenumber relationship aligns with findings reported by other authors [63]. Detailed information on signal maxima and their corresponding vibrational modes is summarised in Table S1. For electrodes containing Co_3O_4 or CoOOH species, changes in the IR spectrum were observed. FTIR wavenumbers 2963, 2875 and 2926, 2854 cm^{-1}, vibrations of stretching asymmetrical/symmetrical methyl and methylene groups signals were registered, mainly originating from contaminants associated with drones used in the cobalt electrochemical deposition process. In the near-IR range, especially for TiO_2-NTs/CoOOH, characteristic signal maxima were observed at points 1735, 1583, 1418, 1372, 1282, and 1040 cm^{-1}, corresponding to citrate. However, according to research reports, the peak at 1583 cm^{-1} is attributed to the vibration of the Co-O double bond [59], while vibrations at 1070 and 983 cm^{-1} are related to stretching and bending modes of Co-OH groups, respectively [64,71]. Additionally, a weak but characteristic band at a frequency of 830 cm^{-1} is observed, corresponding to the stretching vibration (O-OH) of an end-on bound hydroperoxide group in transition metal complexes, such as CoOOH [72–74]. Hence, we can confirm that the obtained electrolyst has the cobalt oxyhydroxide structure. As for the cobalt oxide modification during thermal oxidation of Co deposit Co_3O_4, the infrared spectrum particularly revealed bonds at points 662 and 554 cm^{-1} [61], which are assigned to optical phonons (transverse) of tetrahedral (Co^{2+}-O_4) and octahedral (Co^{3+}-O_6) cobalt centres in the typical spinel type lattice [75]. Unfortunately, the signals of these vibrations are not visible for TiO_2-NTs/Co_3O_4 40 mC/cm^2, primarily due to the small amount of material on the surface. The thin layer was further examined using XPS measurements.

Raman spectra were collected for TiO_2-NTs, TiO_2-NTs/Co_3O_4, and TiO_2-NTs/CoOOH to evaluate the phase composition of the surface modifications (Fig. 6C). The HA TiO_2-NTs sample displays characteristic

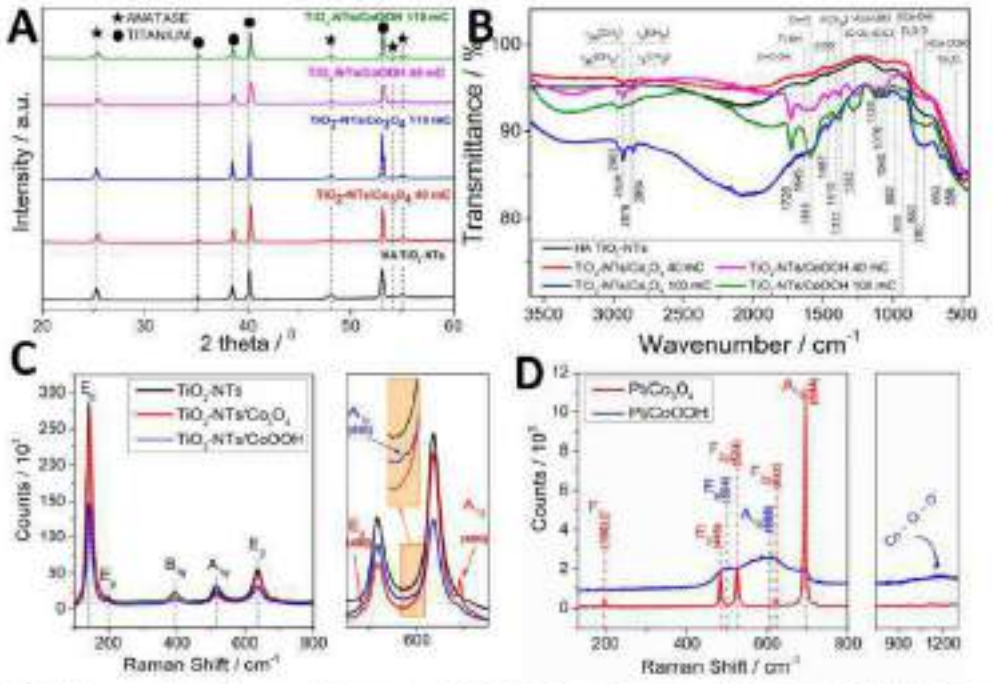

Fig. 6. (A) XRD patterns, (B) ATR-FTIR spectra and (C) Raman spectra of HA TiO_2-NTs with and without electrolyst based on Co_3O_4 and CoOOH and (D) Raman spectra of Pt/Co_3O_4 and CoOOH.

narrow bands at 144 cm^{-1} (E_g), 197 cm^{-1} (E_g), 202 cm^{-1} (B_{1g}), 515 cm^{-1} (A_{1g}), and 640 cm^{-1} (E_g) which correspond to symmetric and asymmetric bending and stretching vibrations of the O-Ti-O bonds in the TiO_2 lattice [73,74]. Fig. 5D shows the Raman spectra of Pt/Co_3O_4, where distinct bands are observed at 196 cm^{-1} (F_{2g}), 485 cm^{-1} (E_g), 524 cm^{-1} (B_{2g}), 622 cm^{-1} (F_{2g}), and 694 cm^{-1} (A_{1g}), consistent with literature reports [77,78]. After Co_3O_4 deposition onto TiO_2 (Fig. 5C), two new peaks emerge at 480 cm^{-1} (E_g), related to symmetric stretching of Co^{2+}–O in tetrahedral coordination, and 600 cm^{-1} (A_{1g}), attributed to symmetric stretching of Co^{3+}–O in octahedral sites [77,79]. In contrast, the Pt/CoOOH spectrum (Fig. 5D) displays broadened bands centred at ~ 504 cm^{-1} (Eg) and ~ 688 cm^{-1} (Ag), associated with Co–O–H and Co–O–O bending and stretching vibrations [79,80] typically found in cobalt oxyhydroxides formed during electrochemical oxidation. The TiO_2-NTs/CoOOH sample also shows a weak, broad peak at ~ 590 cm^{-1}, supporting the presence of CoOOH. Additionally, a broad Raman signal centred around 1100 cm^{-1} was observed (Fig. 5D), which is commonly attributed to surface O–O ("active oxygen") species such as superoxo or peroxo intermediates forming during the OER, as described by Rong et al. [79]. The CoOOH phase in our case is more likely amorphous or nanocrystalline. Nonetheless, the presence of characteristic Raman bands confirms the formation of CoOOH.

Deconvolution of the XPS spectra for (A1-A2) HA TiO_2-NTs, (B1-B2) HA TiO_2-NTs/Co, (C1-C2) HA TiO_2-NTs/Co_3O_4 40 mC/cm^2, (D1-D2) HA TiO_2-NTs/Co_3O_4 100 mC/cm^2, (E1-E2) HA TiO_2-NTs/CoOOH 40 mC/cm^2, (F1-F2) HA TiO_2-NTs/CoOOH 100 mC/cm^2 are depicted in Fig. 6. Spectra of O 1 s are labelled as number 1, while for Co 2p it is marked as number 2. For unmodified Titania nanotubes, there is no signal from the binding energy of the cobalt atom. In measured HA TiO_2 NTs with only electrochemically deposited cobalt, observed signals at 777.3 eV and 792.2 eV correspond to Co^0 $2p_{3/2}$ and Co^0 $2p_{1/2}$ [75], which is in agreement with the spin–orbit splitting ΔE = 15 eV [81], seen in

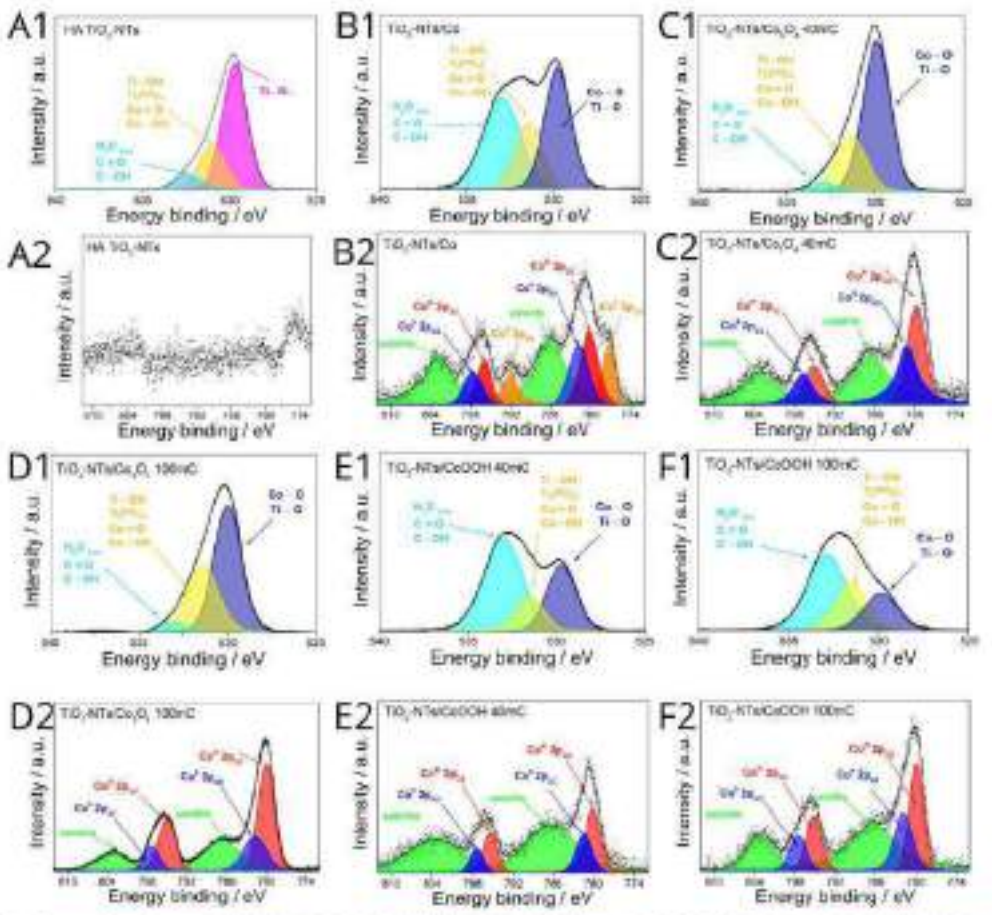

Fig. 6. Deconvolution of oxygen 1 s (1 ordering) and cobalt 2p (2 ordering) peaks in the XPS spectra of HA TiO_2-NTs without cobalt species (A), with electrodeposited cobalt (B), with 40 mC/cm^2 of Co_3O_4 (C), with 100 mC/cm^2 of Co_3O_4 (D), with 40 mC/cm^2 of CoOOH (E) and with 100 mC/cm^2 of CoOOH (F).

Fig. 6B2. The XPS results of TiO_2-NTs/Co reveal the presence of both metallic cobalt and cobalt in oxidised states, attributed to sample exposure to air before the measurements [82,83]. The spectra also show cobalt in +2 and +3 oxidation states, due to the cobalt-oxygen bonding form on the TiO_2-NTs surface (Fig. 6B1). Nevertheless, the cobalt electrodeposition method was successfully confirmed.

The Co 2p spectra of HA TiO_2-NTs decorated with Co_3O_4 or CoOOH cocatalysts are shown in Fig. 6 (G2, D2, E2, F2). The peak values are collected in Table S2. The observed atomic ni binding energy values of 709.9 eV and 795.5 eV correspond to the Co^{+3} $2p_{3/2}$ and Co^{+3} $2p_{1/2}$ peaks, respectively, whereas 795.2 eV and 797.3 eV are assigned as Co^{+2} $2p_{3/2}$ and Co^{+2} $2p_{1/2}$. The broad satellite at 786.6 eV and 803.3 eV is related to $Co\ 2p_{3/2}$ and $Co\ 2p_{1/2}$. The signals identified in the literature are indicative of CoOOH [84,85] material and spinel structures of Co_3O_4 [84,86]. These signals cannot be assigned to CoO or $Co(OH)_2$ compounds due to the observed low binding energy in the spectrum [80,78]. Given the similar location of cobalt peaks [87], distinguishing cobalt oxide species relies on the deconvolution of the oxygen spectrum [87].

The O 1 s spectra are shown in Fig. 6 (C1, D1, E1, F1). The spectra are decomposed into three parts: with maximum position at I) 529.9 eV, II) 531.7 eV, III) 533.0 eV, which are attributed to the oxygen ions in I) lattice oxygen in metal (cobalt, titanium)–oxygen bonds; II) hydroxyl groups bonded with metal centre, phosphonate group, and/or oxygen double bonded with cobalt; III) physically adsorbed water and/or carbon-containing groups, especially –OOH groups. [80,88]. High metal/oxygen content and low hydroxyl groups/oxygen content within the area of the deconvoluted oxygen spectrum are typical for Co_3O_4 material [89,90]. In the case of CoOOH cocatalysts, the oxygen content at 531.7 eV and 533 eV is significantly higher compared to Co_3O_4. Especially for the sample HA TiO_2-NTs/CoOOH 100 mC/cm^2, one can observe an increased area of binding energy related to the cobalt centre in the neighbourhood of oxygen and hydroxyl groups CoOOH. This spectrum is characteristic of cobalt oxyhydroxide [88].

The electrode materials were characterised by UV–Vis spectroscopy. Fig. S5A shows the absorbance spectra, and Fig. S5B shows Tauc plots obtained from the Kubelka-Munk function for electrodes with and without cocatalysts. Titania nanotubes with deposited 100 mC/cm^2 of Co_3O_4 obtained the highest UV-Vis absorption in the whole range. This electrode was the darkest one. The bandgap energy of HA TiO_2-NTs was determined to be 3.2 eV. Titania nanotubes are recognized as an indirect n-type semiconductor [91]. The situation is more complicated for TiO_2-NTs with cocatalysts. In the Tauc plots, the curve tends to flatten (i.e., the slope decreases), making it difficult to accurately determine the bandgap energy from the intersection of the linear fit with the baseline [92]. To improve clarity, an optical measurement was performed on Co_3O_4 electrodeposited onto a platinum substrate. The results revealed two characteristic bandgaps: 1.61 eV and 2.67 eV (Fig. S6A). For the electronic bands alignment construction, the lower-energy transition (~1.6 eV) was selected (Fig. S7).

Based on the KS data, flat band potentials E_{fb} for TiO_2 with and without cocatalysts were evaluated. All impedance function presented in Nyquist plots shown a similar run (Fig. S8A–C). Flat band potential values (E_{fb}) for the obtained materials were determined from the Mott-Schottky plot (Fig. S8D–I) and are as follows: E_{fb} = −0.09 ± 0.02 V (for HA TiO_2-NTs), E_{fb} = 0.03 ± 0.01 V (HA TiO_2-NTs/Co_3O_4), and E_{fb} = 0.17 ± 0.01 V (HA TiO_2-NTs/CoOOH) [93]. The average estimated values of the number of donors (N_D) are equal to $N_{D,A}$ = 4.9 ± 0.9 ·10^{19} cm^{-3}, $N_{D,B}$ = 5.4 ± 0.5 ·10^{19} cm^{-3}, $N_{D,C}$ = 5.8 ± 0.2 ·10^{19} cm^{-3}. The donor concentration for electrodes containing a catalyst is lower than in the case of HA TiO_2 NTs. It is well known that various hydroxyl groups or oxygen vacancies can appear on the semiconductor's surface [28,94]. Depositing a catalyst based on cobalt oxides on the surface may lead to the formation of a junction able to capture electrons from bulk TiO_2. This is possible because cobalt oxide is known to be a p-type semiconductor [95,96]. To verify this, we tested the Pt/Co_3O_4 system using EIS measurements. The Mott–Schottky plot obtained for Pt/Co_3O_4 shows that the flat band potential E_{fb} is located at +0.16 V vs. Ag/AgCl(3 M KCl), as depicted at 1000 Hz, see Fig. S9B. The position of E_{fb} is close to the VB of the p-type semiconductor Co_3O_4. Thus, one may expect a lowering in N_D number for HA TiO_2-NTs/CoOOH and HA TiO_2-NTs/Co_3O_4 in comparison with pure n-type semiconductor HA TiO_2-NTs without surface modification.

Fig. 7A-B illustrates linear sweep voltammetry (LSV) for HA TiO_2-NTs decorated with cobalt species. In the presence of a Co_3O_4 cocatalyst, the OER activity is lower compared to HA TiO_2-NTs without this cocatalyst, as can be seen in decreasing current density. However, they exhibit higher activity relative to TiO_2-NTs without the hydrothermal annealing process. This decrease may be explained by the influence of an additional (second) calcination at 400 °C, resulting in diminished morphological homogeneity and in electronic properties [12]. For the second reason, during additional oxidation (first, due to the crystallization of amorphous TiO_2 into the anatase form, and second, due to the oxidation of cobalt (metal deposits), the nanotubes lose their tubular morphology [1,26], and an oxide layer forms between the titanium substrate and the cocatalyst, leading to decreased of efficiency in water oxidation. In the case HA TiO_2-NTs/CoOOH system, LSV shows higher activity with increasing amounts of cocatalyst. It is known that cobalt oxyhydroxide has good electrocatalytic properties in the dark [10]. One can observe a significant diminishing of OER overpotential.

The threshold potential is changed from 1.41 V for HA TiO_2-NTs to 0.80 V for HA TiO_2-NTs/CoOOH 100 mC/cm^2. In case of producing gas bubbles, the surface of the catalyst can be blocked. At high current, one has to take into account the iR drop to determine the value of the Tafel slope. As observed, Tafel slope corrections with iR drop are not substantial at low current densities, as recorded for the modified TiO_2-NTs (Table 2). However, iR corrections become increasingly significant at higher current levels [97]. The Tafel plots with and without iR correction are presented in Fig. 9B. In Table 2, the Tafel slope values of the anodes with and without the iR correction are compared. According to literature on the electrocatalysis of OER, if the Tafel slope value (b) equals 120 mV/dec, one electron reaction is considered to take place as the rate-determining step (RDS) [98]. It suggests that the RDS is controlled by the single-electron transfer. The Tafel slope is determined by Eq. (2), where η is the value of overpotential, j – current density, R – is the universal gas constant, T – temperature, α – electron transfer coefficient (0.5), F – Faraday constant.

$$b = \frac{\partial \eta}{\partial \log(j)} = \frac{2.303RT}{\alpha F} \quad (2)$$

The lowest Tafel slope value of 157 mV/dec was observed for the HA TiO_2-NTs/CoOOH electrode with a cobalt loading of 100 mC/cm^2. This enhanced performance is likely attributed to the optimal amount and distribution of cobalt species on the surface, acting as active cocatalytic sites. In contrast, samples with lower cobalt loadings or without cobalt exhibit significantly higher Tafel slopes, reaching up to 300 mV/dec. This behaviour may be attributed to the sluggish deprotonation of adsorbed hydroxyl groups on the TiO_2 surface, as reported [99]. The process is kinetically unfavourable, resulting in a higher Tafel slope. It cannot be excluded that the oxygen evolution reaction (OER) proceeds via a single-electron transfer mechanism. The proposed mechanism of cobalt centre activity during electrooxidation in the dark is illustrated in Eq. (3) [99]. Cobalt oxidation appears to proceed via a proton-assisted electron transfer step. In the subsequent reaction, Co^{4+} species interact with water to form molecular oxygen, as described in Eq. (4) [28]. This step leads to the reduction of Co^{4+} to Co^{3+}, which re-enters the catalytic cycle. As the applied potential remains above 0.45 V, Co^{3+} is readily oxidised to Co^{4+}, thereby sustaining the turnover of the catalytic process [28].

$$HO\text{-}O\text{-}Co^{III}\text{-}Co^{III}\text{-}O\text{-}O\text{-}OH \rightarrow O\text{-}O\text{-}Co^{IV}\text{-}Co^{IV}\text{-}O\text{-}O + 2H^+ + 2e^- \quad (3)$$

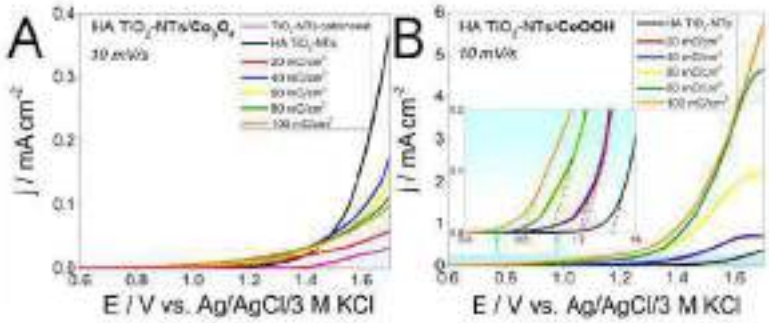

Fig. 7. Linear sweep voltammetry curve with a sweep rate of 10 mV/s and cyclic voltammetry curves (50 mV/s) in the dark obtained for HA TiO_2-NTs electrodes decorated by (A, C) Co_3O_4 and (B, D) CoOOH cocatalysts, measured in 0.2 M K_2SO_4 electrolyte.

Table 2
Values of Tafel slopes with and without iR correction for HA TiO_2-NTs without and with CoOOH cocatalyst.

Tafel Slope (mV/dec)	HA TiO_2-NTs	HA TiO_2-NTs/CoOOH 20 mC	HA TiO_2-NTs /CoOOH 40 mC	HA TiO_2-NTs /CoOOH 60 mC	HA TiO_2-NTs /CoOOH 80 mC	HA TiO_2-NTs /CoOOH 100 mC
without iR correction	384	323	317	323	329	323
with iR correction	277	262	234	262	214	257

$$O_2Co^{III}Co^{III}O_2 + 2H_2O \rightarrow H_2O_2Co^{II}Co^{II}O_2H_2 + O_2\uparrow \quad (4)$$

Fig. 8A-B depicts LSV under UV–Vis light irradiation on covered hydrothermally annealed Titania nanotubes with different amounts of Co_3O_4 and CoOOH nanolayers. For HA TiO_2-NTs, the photocurrent reaches 36 μA/cm² at 0.4 V. The only one photoanode decorated by Co_3O_4 (40 mC/cm²) showed higher photocatalytic activity, and it is equal to 40 μA/cm².

In the case of cobalt oxyhydroxides, for samples with Co deposition equal to 20, 40 and 60 mC/cm², an increase in photocurrents was observed. The best photoelectroactivity was obtained for a sample with 40 mC/cm² of CoOOH (70 μA/cm²). For the rest photoelectrodes, similar or lower photocurrent values were registered. As CoOOH co-catalyst demonstrated significantly better photoelectrocatalytic parameters, further investigations on photoelectrocatalytic activity were conducted. Recent studies have shown that CoOOH generates a higher photocurrent than Co_3O_4 when used as a cocatalyst on a BiVO₄ semiconductor [48]. In the scheme presenting the TiO_2 NTs/ Co_3O_4 junction presented in Fig. 8.7, the redox potentials of CoOOH are more favourably aligned than the valence and conduction band edges of Co_3O_4. Under illumination, photogenerated holes in TiO_2 can therefore be efficiently transferred to Co^{3+} species in CoOOH, promoting their oxidation to Co^{4+}, which subsequently facilitates water oxidation.

The chronoamperometry curves illustrating the variation in a 5-second light/5-second dark cycle at a constant potential of −0.4 V vs. Ag/AgCl/3 M KCl are shown in Fig. 9. The observed activities of photogenerated charge carriers for HA TiO_2-NTs/CoOOH electrodes indicate a trend of decreasing photocurrent over time for all samples with cocatalyst CoOOH besides pure TiO_2-NTs. The appearance of a current signal in the cathodic direction was observed after some time (120 s) for samples with a cocatalyst under dark conditions. However, no cathodic current activity was observed for pure HA TiO_2-NTs. Interestingly, the curve recorded cathodic current (negative values) when the light was turned off, suggesting a reversal in the direction of electron flow.

A similar behaviour involving the modification of TiO_2 nanotubes with CoOOH was observed in a previous study [49]. The proposed mechanism for the photoelectrooxidation reaction is given below in Eqs (5)–(9).

$$2\,h\nu \xrightarrow[h\nu \geq 3.1\,eV]{} 2h^+ + 2e^- \quad (5)$$

$$HO(O)Co^{III}Co^{III}(O)OH + 5h^+ \rightarrow O(O)Co^{IV}Co^{IV}(O)O + 2H^+ \quad (6)$$

$$O(O)Co^{IV}Co^{IV}(O)O + 2H_2O \rightarrow HO(HO)Co^{V}Co^{V}(OH)OH + O_2\uparrow \quad (7)$$

$$HO(HO)Co^{V}Co^{V}(OH)OH \rightarrow HO(O)Co^{III}Co^{III}(O)OH + 2H^+ + 2e^- \quad (8)$$

$$2H_2O \xrightarrow[CoOOH]{} 4H^+ + 4e^- + O_2\uparrow \quad (9)$$

During solar light illumination, electron-hole ($e^- - h^+$) charge carriers are generated in the Titania nanotubes (Eq. (5)) [50]. At the TiO_2-NTs/COOH interface, hole TiO_2 oxidizes Co(III) to Co(IV) (Eq. (6)). The Co(IV) serves as water-oxidizing centres producing molecular oxygen (Eq. (7)) [51]. During CA measurements with a constant potential at +0.4 V, oxidation of Co(II) to Co(III) can occur, see in Eq. (8). The overall reaction using CoOOH as a catalyst for water oxidation requires two molecules of water and produces one molecule of oxygen (Eq. (9)). As can be seen on Fig. 9, the CA curve shows sharper peaks namely more pronounced drop of photocurrent, with the next exposure time of the sample to light. This behaviour may be due to the increased recombination of electrons from CB (e_{CB}^-) and holes from VB (h^+) or to the surface recombination process involving the cocatalyst [52,53]. According to Li et al. [45], the electrodeposited CoOOH cocatalyst is permeable to the electrolyte and thus cannot achieve true electronic passivation of the semiconductor's surface states. In contrast, a dense Co_3O_4 overlayer effectively seals the interface and passivates surface traps, forming a buried p-n junction (Schottky-like contact) with the n-type photoanode [30,31]. CoOOH (as redox-active [32]), it typically exhibits reversible Co^{II}/Co^{III} redox peaks during operation, indicating that ionic charge penetrates the catalyst film and that oxidation state changes occur throughout its bulk. This electrolyte-permeable behaviour leads to the formation of an "adaptive junction" at the HA TiO_2- NTs/CoOOH interface, wherein band bending and charge separation adjust dynamically as the catalyst charges or discharges, rather than being fixed by a rigid

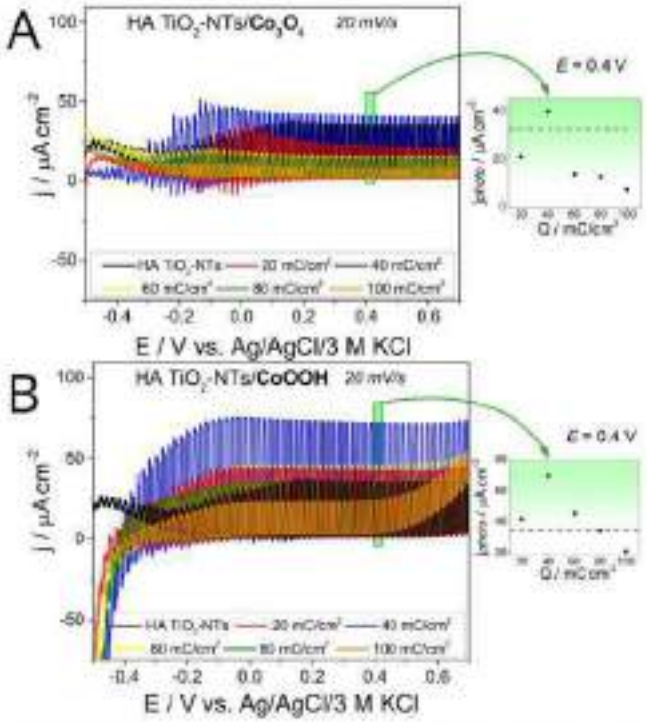

Fig. 8. Linear sweep voltammetry curves under solar light illumination obtained for HA TiO_2-NTs electrodes decorated by (A) Co_3O_4 and (B) CoOOH nanocatalysts, with a sweep rate of 20 mV/s, measured in 0.2 M K_2SO_4 electrolyte.

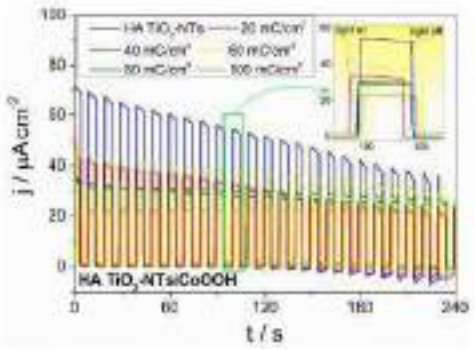

Fig. 9. Chronoamperometry curves under solar light illumination obtained for HA TiO_2-NTs electrodes decorated by CoOOH nanocatalyst, measured at constant potential E = 0.5 V vs Ag/AgCl (3 M KCl), in 0.2 M K_2SO_4 electrolyte.

heterojunction [42]. Nellist et al. [38], describe that such adaptive semiconductor/catalyst interfaces – common when catalysts are deposited by "soft chemistry" methods – can mitigate surface state recombination and Fermi-level pinning, yielding higher photovoltage, whereas dense impermeable catalysts create static junctions that do passivate defects but at the cost of lower attainable photovoltage. Consistent with these insights, the CoOOH-decorated photoanodes study exhibited superior water-oxidation performance compared to their Co_3O_4 counterparts, despite the lack of true surface states passivation by the CoOOH layer. However, cathodic current activity remains noticeable even after illumination is switched off, see Fig. 9 (t > 150s). It cannot be over looked that oxygen adsorption on the photoelectrode surface might block charge carrier activity. As pointed out in Ref. [103], adsorbed oxygen can capture electrons from the conduction band, produced during the electron-hole pair generation, forming superoxide anions (O_2^-) [104]. Photo-assisted electron transfer could accelerate oxygen evolution, as protons are readily available within the bulk structure due to hydroxyl groups. Moreover, a substantial amount of Co(IV) species may persist after the light source is turned off. Therefore, it is presumed that the observed cathodic current also originates from the reduction of cobalt in the Co^{3+}/Co^{4+} species [105,106]. Both of these factors contribute to the appearance of cathodic current in the reverse direction.

To understand the mechanism of the photocatalyst activity, further tests without and with hydroquinone (HQ) as a hole scavenger are depicted in Fig. 10. At first, the electrode activity in the dark was

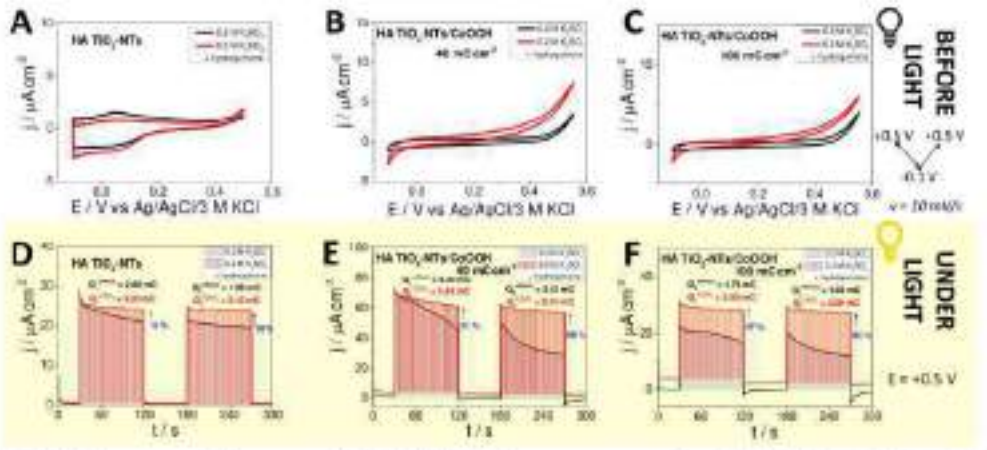

Fig. 10. Cyclic voltammetry curve (with a sweep rate of 50 mV/s) in the dark and chronoamperometry curves under light illumination (at 0.5 V vs Ag/AgCl (3 M KCl)), obtained for (A, D) HA TiO_2 NTs, (B, E) HA TiO_2-NTs/CoOOH 40 mC cm^{-2}, and (C, F) HA TiO_2 NTs/CoOOH 100 mC cm^{-2} measured in 0.2 M K_2SO_4 electrolyte without and with 0.01 M hydroquinone.

examined (Fig. 10 A-C). A platinum disk electrode was used as the working electrode in the detection of the hydroquinone-benzoquinone (HQ/BQ) redox reaction. In Fig. S10, the cyclic voltammetry curve in 0.2 M K_2SO_4 with 0.01 M hydroquinone is presented. The curve shows two peaks at potentials of 0.14 V and 0.50 V, corresponding to the reduction of BQ/HQ and the oxidation of HQ/BQ on the Pt electrode, respectively. The curve indicates that the cathodic peak current is significantly smaller than the anodic one. So, the HQ/BQ redox reaction is irreversible as expected [100]. The oxidation overpotential of HQ can be determined at the point $E_{ox} = 0.35$ V on Pt. In the case of the photoanodes (HA TiO_2-NTs, HA TiO_2-NTs/CoOOH 40 mC/cm^2, HA TiO_2-NTs/CoOOH 100 mC/cm^2), no redox pair HQ/BQ was observed due to the unsuitable electronic alignment.

The situation changes when the samples are exposed to light in photoelectrochemical tests on TiO_2 modified electrodes. In the case of the HA TiO_2 NTs measured without the hole scavenger, the calculated charge extraction efficiency (CEE) is in the range of several per cent (Fig. 10D). However, Titania nanotubes decorated by CoOOH exhibit higher photocurrent generation, and the CEE rises to two-fold times (68 % for 40 mC/cm^2 and 96 % for 100 mC/cm^2 of CoOOH), seen in Fig. 10E-F. The proposed mechanism of water photoelectrocatalysis is presented in Fig. S11. In this work, the photogenerated hole can either: (I) oxidise Co^{2+} to Co^{3+} (Eq. 10) or (II) directly oxidise water (Eq. (10) [100]. Furthermore, in the (I) case, Co^{3+} has two possible pathways. The first (two-step pathway) involves oxidising water and reducing to Co^{2+} and then oxidising to obtain Co^{2+} maintaining at a constant potential of 0.4 V vs Ag/AgCl/3M KCl (Eq. (7)-(8). In the second possible pathway, Co^{3+} can oxidise HQ to BQ and regenerate to Co^{2+} [101,102]. This pathway has only one step, making it faster than a two-step pathway, especially noticeable for a higher amount of deposited cocatalyst, becoming photocurrent activity for HA TiO_2-NTs/CoOOH 100 mC/cm^2 is just associated with the current of HQ/BQ oxidation reaction (Fig. 10F). In the (II) case, active products of water oxidation, such as $^{\bullet}OH$ radicals [103], are deemed less significant due to the lack of an electron acceptor. It should not be neglected that $^{\bullet}OH$ radicals may not react with HQ. Nevertheless, they are more beneficial in photocatalysis for removing organic pollutants.

The second charge carrier generated in TiO_2 material is an electron in the conduction band. In this context, two most probable pathways may be proposed: it can either form a superoxide radicals $O_2^{\bullet-}$ from adsorbed oxygen on the surface of photoanode (Fig. S12) or the electron from CB (e_{CB}^-) can reduce BQ to HQ [100]. Interestingly, reaction rate constants (k) are of the order $k \sim 10^{10} M^{-1} s^{-1}$ [3,10,11]. In fact, during photooxidation of CoOOH it leads to the continuous generation of oxygen, which provides the reactions within an oxygen-rich environment. Thus, the probability of reduction reaction with $O_2^{\bullet-}$ surpasses that of interaction with an e_{CB}^-. However, it should be noted that $O_2^{\bullet-}$ radical in aqueous electrolytes can generate other various Reactive Oxygen Species (ROS) or even form a singlet oxygen ($^1O_2$) [104]. Nevertheless, comparing their reaction rate constants [3,13,14] and considering that the singlet oxygen lifetime is up to 2 microseconds, these possibilities are not considered decisive in the overall mechanism. In this work, analysing the curves in Fig. 9, it is proposed that the main factor hindering the decrease in photocurrents is the superoxide radical activity. Therefore, it is suggested that the mechanism of BQ reduction to HQ occurs with the involvement of superoxide radical $O_2^{\bullet-}$.

In summary, in the absence of HQ, oxygen causes shielding of the perovskite excitation surface. The cathodic activity observed after turning off the light is linked to the reduction of oxidized Co^{3+} to Co^{2+}/Co^{3+} by the remaining photoelectrons in the conduction band (CB). When HQ is present, there is no discernible cathodic activity when the illumination is switched off. The initial reaction of HQ oxidation to BQ by Co^{3+} results in a swift return to Co^{3+}, further reducing BQ/HQ by $O_2^{\bullet-}$, create the beginning components: Co^{2+}, HQ and O_2. Therefore, no decrease in photocurrent activity or the emergence of cathodic activity is observed.

To evaluate photoelectrode durability, chronoamperometric measurements were conducted over 3.5 h at 0.5 V vs. Ag/AgCl. TiO_2/CoOOH maintained stable photocurrent, while TiO_2/Co_3O_4 exhibited photocurrent decline (Fig. S12). Post-treatment XPS analyses confirmed these trends (see Fig. S13). The O 1s peak shift from 531.0 eV to 530.0 eV suggests changes in surface chemistry, possibly due to $Co^{3+} \rightarrow Co^{2+}$ reduction or defect formation. While such shifts are often linked to oxygen vacancies, recent literature [114] warns that XPS alone is insufficient to confirm their presence. Given the concurrent photocurrent drop,

these changes are more likely to indicate structural degradation rather than beneficial defect formation. In contrast, for CoOOH, Favaro [116] and Wiegmann [116] show that O 1 s features at ~ 533 eV emerge under oxygen evolution conditions and correspond to the formation of *OOH/peroxo-like intermediates at active catalytic sites. These findings support our assignment of the observed ~ 530.8 eV O 1 s shift in CoOOH as a signature of active surface oxygen species, aligned with enhanced photocurrent and catalyst stability. Thus, once more, electrolyte-permeable cobalt oxyhydroxide is found to act better than dense /non-permeable to electrolyte Co_3O_4 used for photoanode TiO_2 activity, similarly to their activity towards BiVO$_4$ photoanode electrochemical behavior [45].

The measurement regarding the efficiency of CoOOH-modified photocatalytic studies for the discoloration of an aqueous solution of methylene blue (MB). The obtained UV–Vis spectra in the range of 500–800 nm are presented in Fig. 11 A–C. It is observed that the shape of the curves and the position of the maximum absorbance remain unchanged, with only a gradual decrease in the absorbance values of each photoanode. This indicates no changes in pH in the solution or the formation of nanochromes. The maximum absorption of the initial MB at a concentration of 10^{-5} M was recorded at a wavelength of 662 nm. Subsequently, the changes in concentration over time, C/C$_0$(t), both without and with illumination, are shown in Fig. 11D. For the HA TiO_2-NTs electrode, a decrease in the concentration of the MB solution by 18.0 % was observed compared to the blank MB solution. In the case of samples containing the CoOOH cocatalyst, a decline in concentration of 5.5 % was already noted after 20 min under dark conditions. Furthermore, after 2h of light radiation, there is a decrease in C/C$_0$ of 45.4 % for 40 mC/cm^2 and 31.3 % for 100 mC/cm^2.

Based on the above observations, two degradation pathways can be identified. The first involves the adsorption of MB molecules onto the surface. As previously discussed, CoOOH is a permeable cocatalyst [45], possessing a relatively larger surface area than dense Co_3O_4, and can act as an adsorbent in dark conditions, like in [117,118]. Hence, the noticeable decrease in the first 20 min in Fig. 11D. As suggested [119], the adsorption mechanism of cobalt oxides for MB depends on pH and/or electrostatic interactions between the oxide surface and MB molecules in the solution. In our study, MB molecules exhibit a positive charge (cationic dye), suggesting electrostatic interactions due to the presence of numerous hydroxyl groups (negative charge) in the cobalt oxyhydroxide material. The main mechanisms of adsorption are hydrogen bonding and cation-π interactions, described in [118].

The second pathway is correlated to photocatalytic degradation, caused by photogenerated electron-hole couple agents, as mentioned earlier. In general, holes can oxidize water to species such as: *OH, H_2O_2, $O_2^{\bullet-}$, $^1O_2$ [114,120]. Here, the most probable process is oxidation water from electrolyte to *OH, see in Eq. (10). It is known from the literature that hydroxyl radicals are the key element in the photodegradation of MB [121–123]. On the other hand, it is important to mention that hydroxyl groups can be adsorbed on the Titania nanotubes surface [28]. As shown in the literature [124], the hole trapping of Ti^{4+}–(OH) is a fast process lasts in 10 ns to obtained Ti^{4+}–(*OH) (Eq. (11)), which can oxidize organic pollutants (slow process, approximately 100 ns). The third option is the interaction $O_2^{\bullet-}$ with MB molecule to obtain leuco-methylene blue (LMB) and other products (Eq. (12)) [124]. The overall reaction in photocatalytic degradation of MB using HA TiO_2 NTs as catalyst is the sum of these three elements to obtain carbon dioxide and water (Eq. (13)) [124,125].

$$H_2O + h^+ \rightarrow {}^{\bullet}OH + H^+ \quad (10)$$

$$Ti^{4+}(OH) + h^+ \rightarrow Ti^{4+}({}^{\bullet}OH) + H^+ \quad (11)$$

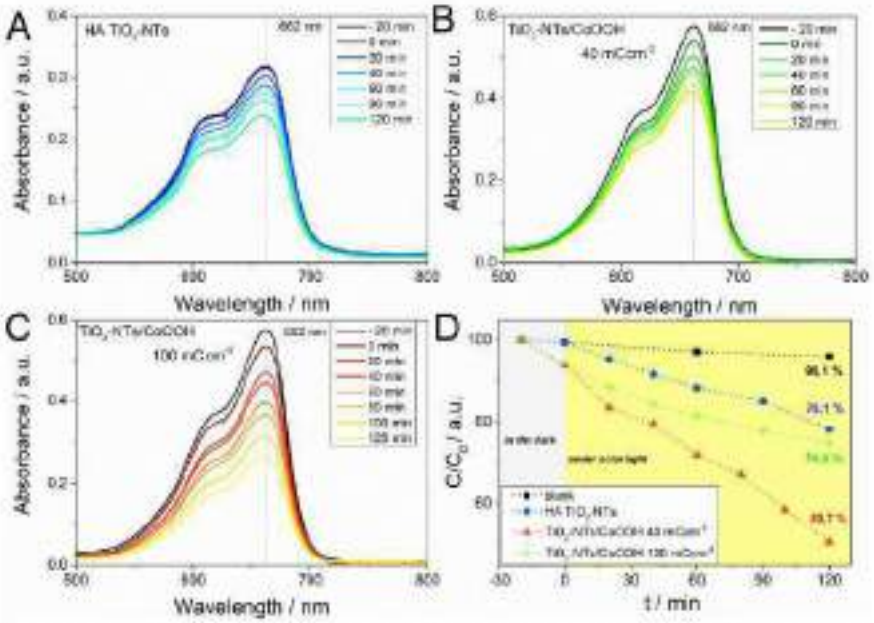

Fig. 11. Photodegradation of methylene blue by (A) HA TiO_2-NTs, (B) HA TiO_2-NTs/CoOOH (40 mC cm^{-2}) and (C) HA TiO_2-NTs/CoOOH (100 mC cm^{-2}).

$$O_2^{\bullet-} + MB \rightarrow LMB \xrightarrow{O_2} degradedproducts \quad (12)$$

$$^{\bullet}OH + H^{+} (^{\bullet}OH) + O_2^{\bullet-} \xrightarrow{MB} CO_2 + H_2O + byproducts \quad (13)$$

$$Co^{3+} + MB \rightarrow degradedproducts \quad (14)$$

The situation is a bit different when TiO_2 nanotubes are decorated with the CoOOH catalyst. In the case of a small amount (40 mC/cm^2), a faster decolouration of the MB solution in light was observed compared to HA TiO_2-NTs. Thus, it is evident that, besides the degrading species (Eq. (12)), Co^{3+} effectively assists in the removal of organic compounds [1,30,31] (Eq. (14)). However, for a larger amount of deposited electrocatalyst, the photodegradation efficiency is lower, but still better than for pure nanotubes. As previously shown based on Figs. 9, 10, the photoactivity of the HA TiO_2-NTs/CoOOH 100 mC/cm^2 electrode is lower compared to pure nanotubes, but the decolouration of MB using light is better. Therefore, it can be speculated that cobalt oxyhydroxide is a more effective catalyst in the photodegradation of MB than pure TiO_2. Hence, the combination of these two materials leads to enhanced performance, as observed in the HA TiO_2-NTs/CoOOH (40 mC/cm^2) sample.

4. Summary

In summary, electrochemical deposition has proven to be an effective method for controlling the size and distribution of cobalt nanoparticles on the TiO_2 NTs photoanode. Subsequent modification leads to the formation of cobalt oxide (Co_3O_4) and cobalt oxyhydroxide (CoOOH) cocatalysts. Structural characterization by XPS and FTIR confirms the composition and chemical states of the obtained materials. Among the modified electrodes, TiO_2 NTs/Co_3O_4 exhibits inferior electrocatalytic and photoelectrocatalytic performance compared to TiO_2 NTs/CoOOH. Notably, for the TiO_2 NTs/CoOOH electrode with a cobalt loading of 100 mC/cm^2, the overpotential at a current density of 0.1 mA/cm^2 is reduced by 0.6 V. The corresponding Tafel slope of 157 mV/dec suggests a one-electron transfer process with a transfer coefficient (α) of approximately 0.5. This cocatalyst promotes the OER. Mechanistic studies revealed that CoOOH facilitates proton-assisted electron transfer (PAET), accelerating oxygen evolution and also generating superoxide species that can temporarily inhibit the cocatalyst. This explains the observed photocurrent decay and the appearance of cathodic current. Adding a hole scavenger (hydroquinone) eliminated these effects, maintaining a high steady photocurrent by overcoming the kinetic limitations of water oxidation. Methylene blue degradation tests indicated a dual mechanism for the TiO_2 NTs/CoOOH system: initial dye adsorption on the porous CoOOH layer, followed by enhanced photocatalytic degradation via hydroxyl radicals and active Co^{4+} species. The CoOOH-modified photoanodes achieved greater dye removal than TiO_2 NTs alone, demonstrating enhancement due to cocatalyst activity. Overall, the controlled electrodeposition of cobalt onto TiO_2 NTs (followed by selective oxidation to CoOOH) significantly enhances water oxidation efficiency and broadens the photocatalytic functionality of the photoanode. The TiO_2 NTs/CoOOH electrode, in particular, exhibits superior performance due to efficient charge carrier utilization (proton-assisted hole transfer) and adaptive semiconductor–catalyst interaction. These findings provide valuable guidance for optimizing cocatalyst morphology and loading to advance solar energy conversion and environmental remediation technologies. In the case of photoelectrochemical oxidation, this work shows the significant impact of superoxides in photocatalytic processes. Through the proton-assisted electron transfer, oxygen evolution can be accelerated. These oxygen species can block the permeable cocatalyst, resulting in high photoactivity, as revealed by decreasing photocurrent generation and the appearance of cathodic activity. To avoid this situation and maintain a high, constant photocurrent over time, it is necessary to add a hole scavenger, which finally overcomes the kinetic limitations towards OER. The decolouration of the MB solution partially proceeds via direct oxidation, being adsorbed on the photocatalyst's surface, supported by the permeable cocatalyst and its electrostatic forces. On the other hand, the remaining dye is mainly photocatalytically degraded by the produced hydroxyl radicals but also by active Co^{4+} centres.

In conclusion, the electrochemical deposition of cobalt onto TiO_2 nanotubes via a controlled electrocrystallization process represents an effective strategy for surface modification aimed at enhancing the oxygen evolution reaction (OER). The introduction of cobalt-based cocatalysts significantly improves both electrocatalytic and photoelectrocatalytic performance. Among the studied materials, the TiO_2 NTs/CoOOH electrode demonstrates superior photoactivity, attributed to proton-assisted electron transfer and efficient charge carrier dynamics. This study highlights the importance of optimizing cocatalyst loading and morphology to enhance photocatalytic efficiency, offering promising prospects for applications in renewable energy conversion and environmental remediation[1].

Declaration of generative AI and AI-assisted technologies in the writing process

During the preparation of this manuscript, the authors did not employ generative AI or AI-assisted technologies. The Grammarly software was used solely for English language minor changes. The authors take full responsibility for the content of the article.

CRediT authorship contribution statement

Mariusz Wasilek: Writing – review & editing, Writing – original draft, Visualization, Methodology, Formal analysis, Data curation, Conceptualization. **Anna Lisowska-Oleksiak:** Writing – review & editing, Writing – original draft, Supervision, Methodology, Investigation, Funding acquisition, Formal analysis, Conceptualization.

Declaration of competing interest

The authors declare that they have no known competing financial interests or personal relationships that could have appeared to influence the work reported in this paper.

Acknowledgements

Financial support from the Faculty of Chemistry, Gdańsk University of Technology, under the SB 037/37 program is gratefully acknowledged. We sincerely thank Professor Anna Zielińska-Jurek (Gdańsk University of Technology) for providing access to the XRD and UV–Vis spectroscopy facilities. We also acknowledge Dr. Grzegorz Gajowiec (Gdańsk University of Technology) for SEM and EDX analyses, and Dr. Marcin Łapiński (Gdańsk University of Technology) for performing the XPS measurements.

Appendix A. Supplementary data

Supplementary data to this article can be found online at https://doi.org/10.1016/j.apsusc.2025.164076.

Data availability

Data will be made available on request.

References

[1] J.M. Macak, S. Albu, [illegible], A. Ghicov, P. Schmuki, Smooth and/or TiO2 nanotubes annealing and structure, Phys. Status Solidi 203 (2006) 3069–3073, https://doi.org/10.1002/pssa.200622114.

[2] G.D. Sulka, Introduction to nanofabrication of metals, Nanostructured Anodic Met, Oxides (2020) 1–34.

[3] S. Arifin, B.M. Yusuf, L.J. Minggu, M.B. Kassim, Improvement of TiO2 nanotube for photoelectrochemical water splitting: Review, Int. J. Hydrogen Energy 46 (2021) 38996–39024.

[4] Y.-H. Wang, Y.-M. Hsu, C.-C. Chang, G.E. Ortiz, P.E. Ujaravia, P.-U. Asuquo, S.U. Offiah, 2019 Conference Series: Earth and Environmental Science A review on the influence of doping TiO2 with metals/non-metals in improving its photocatalytic activity for Chromium(VI) reduction of Se/P/TiO2 Anode Material for Li-Ion Battery Application A review on the influence of doping TiO2 with metals/non-metals in improving its photocatalytic activities, (n.d.).

[5] B. Ambil, T. Matthews, T. Ohwaki, E. Aviz, Y. Tago, Visible-light photocatalysis in nitrogen-doped titanium oxides, Science 293 (2001) 269–271.

[6] J.E. Paul, S. Rao, A.J. Bard, Novel carbon doped TiO_2 nanotube arrays with high aspect ratios for efficient solar water splitting, Nano Lett. 9 (2009) 24–30.

[7] X. Peng, J. Fu, X. Zhang, Y. Li, M. Huang, K. Hou, W.K. Ho, Carbon-doped self-ramified urchin-like platinum for visible photocatalysis, Nanoscale Horizons. Lett. 5 (2018) 1203–1207.

[8] G. Schlegel, M. Wollgarten, A. Gunn, S. Omelchenko, M. Mirkhalaf, M. Bannister, D. Mikhailova, Bismuth modified nitrogen-doped TiO_2 nanotubes as improved anodes for Li-ion batteries, Batter. & (2020) 81.

[9] C. Yang, S. Shang, X. Yao Li, Fabrication of ultra-doped TiO2 nanotube array as a conductive interlayer of PbO2 anode for efficient electrochemical oxidation of organic pollutants, Sep. Purif. Technol. 136 (2021) 116935.

[10] Z. Gong, D. Ding, T. Li, G. Ning, Hydrogen TiO2 nanotubes photoanode for enhanced photoelectrochemical water splitting, Appl. Surf. Sci. 443 (2018) 435–439.

[11] A. Chirvo, B. Eckhardt, F. Rizzo, P. Schmidt, Photoresponse in the visible range from Cr doped TiO_2 nanotubes, Chem. Phys. Lett. 453 (2008) 202–206.

[12] M. Wrobel, M. Szkoda, G. Gajowiec, M. Gazda, E. Kusiak, M. Grzeszek, A. Lisowska-Oleksiak, Hydrothermal cobalt doping of titanium dioxide nanotubes towards photocatalytic activity enhancement, Nanot. 2021, Vol. 14, Page 1507 14 (2021) 1507. Doi: 10.3390/MA14061507.

[13] Y. Feng, L.C. Yin, Y. Liu, K. Rui, M. Tu, J. Guo, S.Y.H. Liow, M.R. Herbowne, Cobalt doped black TiO2 nanotubes array as a stable anode for oxygen evolution and electrochemical wastewater treatment, ACS Catal. 8 (2018) 4278–4287.

[14] E. Szeifi, J. Cooper, M. Bayo Simeratzidis, M. Pilch, T. Kosmala, J. Deryl, G. D. Sulka, Photoelectrochemical properties of BiOBrF-modified anodic TiO_2 layers decorated with Au/Pd by galvanic solar photocatalysis, J. Phys. Chem. C 127 (2023) 9951–9963.

[15] Y. Su, Y. Dong, Effect of structure on the photocatalytic activity of Re-doped TiO2 nanotubes, Appl. Surf. Sci. 257 (2011) 9751–9755.

[16] C. Wu, H. Du, W. Fu, L. Wang, J. Gong, Tuned structure of palladium-doped hollow TiO2 nanosphere as highly efficient electrocatalyst for hydrogen evolution reaction, Int. J. Hydrogen Energy 46 (2021) 1820–1830.

[17] E. Oshchepkov, A. Gebreselassie, E. Wolter, B. Xiao, T.J. Schaafsma, Electrocatalysts and perspectives of oxide-based catalysts for the oxygen evolution reaction, Catal. Sci. Technol. 3 (2013) 3000–3021.

[18] B. Huang, W. Yang, F. Wei, B. Shen, H. Chen, Co3O4-modified Sn-TiO2 nanoheterojunction anodic layer deposition for improved visible-light photoelectrochemical performance, ACS Appl. Mater. Interfaces 7 (2015) 423–431.

[19] A.S. Tazikeh, W.N. Su, S.A. Dahoumane, K.M. Chen, B.J. Hwang, Photoelectrochemical water splitting at low applied potential using a NiOOH coated cadmium (Sn, Se) chalcogenide photoanode, J. Mater. Chem. A 3 (2015) 5049–5061.

[20] A. Jia, M. Rao, J. Ao, T. Shen, Fe-implantation Fe2O3/Co-Pi co-decorated Cu-Pi to enhance nanoporous BiVO4 for photoelectrochemical water splitting, J. Semicond. 38 (2017) 063004.

[21] L. Wang, D. Monaj, A. Tsanis, O.Y. Sharaveliuskaia, T. Jacob, B.S. Hinking, B. Bozzini, Ultrasmall Co_3O_4 nanoparticles as a highly efficient 'true' secondary in operando catalyst for water splitting, ACS Catal. 7 (2017) 4758–4767.

[22] M.W. Kanan, D.G. Nocera, In situ formation of an oxygen-evolving catalyst in neutral water containing phosphate and Co^{2+}, Science 321 (2008) 1072–1075.

[23] M. Zarei, A. Fazlali, M. Grzeszczuk, M. Jarolim, G.R. Salazar-Alvarez, Nanoporous anodic titanium dioxide layers as potential drug delivery systems: drug release kinetics and mechanism, Colloids Surf. B Biointerfaces 145 (2016) 497–504.

[24] M.D. Hoang, M. Sillen, V. Lingua, H. Mikaeeli, O. Mozhen, M. Mojtaba, Porous tin Nanodendrite Anodic TiO2: How the Morphology Really Matters for the Photodegradation of Caffeine?, Coatings 2022, Vol. 12, Page 1002 12 (2022) 1002. Doi: 10.3390/COATINGS12071002.

[25] P. Ribeiro, N.F. Nguyen, S. Ke, F. Schmidt, Aligned metal oxide nanostructures: Investigation of anodic TiO2 nanotubes' formation and properties, Nanomade Horiz. 1 (2016) 445–466.

[26] X. Wang, L. Yao, S. Zhang, X. Wang, Ultralong and bifunctional TiO2 nanotubes achieved by an optimized two-step anodization for efficient dye-sensitized solar cells, ACS Appl. Mater. Interfaces 6 (2014) 1361–1365.

[27] L. Piveteau, K. Gordeyenko, J. Kovtyukhova, J. Bell, E. Skrabalak, Sodide route toward aqueous photocolloids of UV-functionalized TiO2 nanotubes, ACS Appl. Mater. Interfaces 12 (2020) 3225–3235.

[28] K. Nowakowska, M. Szkoda, G. Gajowiec, K. Jurek, G. Trykowski, A. Lisowska-Oleksiak, Hydrothermal modification of TiO2 nanotubes in water and alkaline metal electrolytes (LiOH, NaOH, KOH) – Direct evidence for photocatalytic activity enhancement, Electrochim. Acta 426 (2022) 140803.

[29] K. Kowalkińska, J. Bolesław, J. Kapusta-Kołodziej, A. Jaskuła, Fourier-filtered cyclic voltammetry: A review of theory and applications, Chem. Eng. J. 404 (2021) 126405.

[30] A. Kudelski, A. Grzegorzek, B. Chmiel-Talarek, J. Tamkovich, M. Bigdeloo, R. Felix, A. Szymczyk, A. Ziolkiewicz-Kruk, M. Skarska, T. Jedrzejewski, TiO_2-C composites to synthesized via facile surfactant-assisted method as a part of low energy consuming LED-based photocatalytic system for environmental applications, J. Photochem. Photobiol. A Chem. 407 (2021) 113028.

[31] D. Kuda, K. Trzciński, M. Lopianski, M. Gazda, M. Szkoda, A.P. Nowak, M. Sibiński, The new method of ZnO/ZnS synthesis as the cuprous nanostructure substrate with enhanced stability and photoelectrochemical performance, Sci. Rep. 13 (2023) 21269 | Doi: 10.1038/s41598-023-48208-9.

[32] A.G. Aragon, W. Kowalik-Klimczak, T. Szeluk, K. Zarębska, J. Wilson-Salamonska, M. Skompska, Synchronized application of N-doped TiO2/CdS/polyCoTAPc electrochemical composite for photocatalytic degradation of 4-chlorophenol under visible light illumination, Appl. Surf. Sci. 514 (2020) 145944.

[33] A. Fujiwara, K. Ishida, G. Grobéty, T. Burchhardt, G. Cavelti, M. Lobsh, J. Gonzalez, A. Kotanko, P. Stolkarchevici, Specialties of oxygen functional groups on the carbon support controls the electrocatalytic activity of cobalt oxide nanoparticles in the oxygen evolution reaction, ACS Appl. Mater. Interfaces 13 (2021) 8140–8150.

[34] J. Liu, T. Yang, N.R. Williams, Activation of peroxymonosulfate by oxygen vacancies-enriched cobalt-doped black TiO2 nanotubes for the removal of organic pollutants, Environ. Sci. Technol. 55 (2021) 6872–6880.

[35] V. Bruckman, J. Chamorro, F. Bello, G. Terán, C. Gonzalez, W. Schuhmann, F. Kessler, Hardening cobalt-oxide–cobalt-perfide electrochemistry with solid-electrolyte overlayer, Anal. Chem. 90 (2018) 7341–7348.

[36] X.T. Su, L. Yan, S. Zhang, L. Wang, J.-J. Zou, S. Ke, L. Pan, X. Zhang, L. Wang, J. Zou, Rational design and construction of co-catalysts for enhanced wet-based photo-electrochemical oxygen evolution: a comprehensive review, ACS. Sci. 9 (2019) 1801709.

[37] D.J. Autrey, I.A. Hussien, H.B. Tabak, Electrooxidation of arsenic, silver and palladium, Trans. Faraday Soc. 64 (1968) 192–201.

[38] T. Tan, J. Yang, Y. Wu, Q. Zhou, J. Li, G. Lu, Coupling polyoxometalate with Co_3O_4 on BiVO4 photoanodes towards efficient photoelectrochemical water oxidation, Int. J. Hydrogen Energy 49 (2024) 851–858.

[39] J. Zhou, T. Liu, T. Parker, M. Engelhard, J. Qiu, Interfacial properties of gold and cobalt oxyhydroxide in plasmon mediated oxygen evolution reactions, J. Phys. Chem. C (2020) 119–1124.

[40] X. Zhang, H. Zhang, Q. Zhang, Q. Zhang, C. Wu, J. Yu, Y. Wu, H. An, H. Wang, Y. Zou, C. Dao, J. Chen, D.G. Ye, S. Si, X. Wang, J. Xie, High-rpt CoS_2 in cobalt oxyhydroxide for efficient water oxidation, Nat. Commun. 15 (2024) 1–10.

[41] S. Takeuchi, T. Sato, K. Tanaka, S. Abe, D. Chenlou, K. Sato, T. Yui, M. Yagi, Bipolar inorganic ion collector of nanoscopic species creating highly efficient heterogeneous electrocatalysts for water oxidation on cobalt oxyhydroxide nanoparticles, ACS Appl. Mater. Interfaces 9 (2017) 39850–39861.

[42] T. Chen, J.J. Concepcion, K. Hu, W. Yang, T.C. Meyer, Guaranteed 0 atm proton transfer in the O_2 – O bond forming step in water oxidation, Proc. Natl. Acad. Sci. U. S. A. 107 (2010) 7225–7229.

[43] Y. Ren, Y. A. Y. Yan, M. Yuan, J. Ding, Y. Li, J. Yan, S.F. Liu, Self-assembled CoO/H air 3D 2 for enhanced photoelectrochemical water oxidation, (2020). Doi: 10.1016/j.jechem.2020.11.036.

[44] W. Yang, D. Shen, T. Duan, H. Li, J. Li, Y. Li, Enhanced photoelectrochemical water splitting through reversible atomic separation and transfer in TiO_2 hydrides-anion nanowire arrays, ACS Appl. Energy Mater. 7 (2024) 4412–4420.

[45] S. Li, Y. Li, J. Zhang, X. Liu, S. Zhang, L. Zhang, X. rong zeng, Charge separation at $BiVO_4/Co_3O_4$ and $BiVO_4/CoOOH$ interfaces: difference between dense and permeable electrodes, Appl. Surf. Sci. 624 (2023) 156985.

M. Wróbel and A. Lisowska-Oleksiak

Applied Surface Science 711 (2025) 161870

[146] M.N. Ayub, U. Shahzad, M.F. Rabbani, M. Saeed, M.M. Khan, M.H. Baloach, Recent advances in under-electrolysis based on nanostructured inorganic-metal-free and metal-oxyhydroxides for hydrogen energy production, Int. J. Hydrogen Energy 97 (2025) 507–527, https://doi.org/10.1016/j.ijhydene.2024.11.446.
[147] P. Wang, X. Xu, Y. Li, L. Gu, L. Li, H. Liu, N. Cong, Tailoring lattice oxygen in in-situ evolved CoOOH for industrial-scale water oxidation, Appl. Catal. B Environ. 340 (2024), https://doi.org/10.1016/j.apcatb.2024.123238.
[148] M. Wagler, Triple-a general purpose peak fitting program, Urs Inst0001-0898 (2000) 1128–1128, https://doi.org/10.1107/S0108768100008408.
[149] A.C. Frank, P.T.A. Sumodjo, Electrodeposition of cobalt from citrate containing baths, Electrochim. Acta Complete (2014) 7%–22, https://doi.org/10.1016/0013-4686(74)85033-1.
[150] S.S. Abd El Rehim, S.M. Abd El Wahaab, M.A.M. Ibrahim, M.M. Dankeria, Electrodeposition of cobalt from aqueous citrate baths, J. Chem. Technol. Biotechnol. 73 (1998) 369–375, https://doi.org/10.1002/(SICI)1097-4660(199812)73:4<369::AID-JCTB975>3.0.CO;2-S.
[151] M. Pourbaix, H.S. Thiele, Atlas sur la Electrochimie and Electrocatalyse, Wiley Interscience New York, 1963, p. 125.
[152] D. Gerngross, D. Hilt, I. Shvetsopas, B. Schnabler, Electrochemical methanation: Part I. General considerations, J. Electrocat. Chem. Interfacial Electrochem 388 (1995) 329–348, https://doi.org/10.1016/0022-0728(95)03918-9.
[153] A.M. Glenn, A. Lisowska-Oleksiak, C.A. Vincent, The Effects polymer electrolyte membrane Electrochim. Acta 43 (1998) 2481–2491, https://doi.org/10.1016/S0013-4686(97)10094-8.
[154] A. Mikhey, L. Heusing, Electrochemical oxidation and growth of nano- and microparticles: some theoretical and experimental aspects, Electrochim. Acta 49 (2004) 2003–2012, https://doi.org/10.1016/j.electacta.2003.12.016.
[155] I.G. Casella, M. Gatta, Study of the electrochemical deposition and properties of ruthenium oxide/carbon nanotube composites, J. Electroanal. Chem. 534 (2002) 31–38, https://doi.org/10.1016/S0022-0728(02)01302-2.
[156] J.T. Mefford, A.R. Akbashev, L. Zhang, M.C. Clark, Correction: Correlated catalyst activity of doped p-Co3O4 single crystal cuboid particles in alkaline electrolysis, J. Phys. Chem. C 123 (2019) 18930–18931, https://doi.org/10.1021/acs.jpcc.9b06548.
[157] J. Yang, D. Wang, H. Han, C. Li, Roles of cocatalysts in photocatalysis and photoelectrocatalysis, Acc. Chem. Res. 46 (2013) 1900–1909, https://doi.org/10.1021/ar300227e.
[158] O. Alev, A. Kılıç, Ç. Çoladır, S. Büyükköse, 2.2. Gerçek, Gas sensing properties of p-Co3O4/n-TiO2 nanoheterostructures, Sensors (switzerland) 18 (2018), https://doi.org/10.3390/s18093098.
[159] F. Qin, J. Wang, H. Li, F. Fan, R. Song, J. Chen, Y. Fan, S. Zhang, Electrochemically enhanced activation of Co3O4/TiO2 nanoheterojunction anode for peculiar toward high catalytic activity, low energy consumption, and long lifespan performance, J. Colloid Interface Sci. 606 (2022) 836–850, https://doi.org/10.1016/j.jcis.2021.08.040.
[160] E.J. Wallace, M.A. Anton, W. Liu, E. Nazaris-Drolves, A. Kuzma, D. Nesporova, S. R. Nikkas, P. Peter, F.E. Hajos, Electrodeposited cobalt-phosphate electrocatalysts for efficient oxygen evolution reaction and supercapacitors, Results Chem. 5 (2023) 100875, https://doi.org/10.1016/j.rechem.2023.100875.
[161] A.Ul. Rahee, C.B.A. Gad, G.A.S. Shiliwaan, M.J.Z ub, Combined TPR, XRD, and FTIR studies on the reduction behavior of Co3O4 nanocatalysts, Chem. Phys. 269 (2021) 126367, https://doi.org/10.1016/j.cattod.2020.126367.
[162] B.D. Schaidler, J. Stanaway, Electrochemical Nucleation and growth, Beryst. Electrochem (1969) 512–559, https://doi.org/10.1002/9783527626434.ch10.
[163] P. Gawo, M. Champion, S. Douglas, D. Hugo, T. Jiangchang, W. Yue, L. Yongping, T. Shaogang, L. Yingchun, S. Jing, P. Hongbo, L. Qiheng, S. Jiaqing, Unveiling effective cation substitution in spinel Co3O4 nanosheets for high-performance oxygen evolution reaction, J. Colloid Interface Sci. 641 (2023) 714–720, https://doi.org/10.1016/j.jcis.2023.03.103.
[164] H. Yang, E. Ge, J. Hu, Q.Li, D. Tang, M. Fu, M. Li, X.A.C. Candidates, Effect of amorphous g-C 3 N 4 substrate on catalytic oxidation of CO over Co 3 O 4, Appl. Surf. Sci. 401 (2017) 355–363, https://doi.org/10.1016/j.apsusc.2016.12.226.
[165] C. United S.1.30 P. Lawrence Berkeley National Lab. (LBNL), Berkeley, Materials Data on Ti by Materials Project, (2020), Inst. 10.17188/1206269.
[166] J. Swanson, Crystal structure, 2 nd edition. Vol. 1 by R. W. G. Wyckoff, Am. Mineralogist. 49 (1964) 1258–1259, https://doi.org/10.1107/s0365110x64003261.
[167] M. Sakalis, A. Lisowska-Oleksiak, E. Stavrik, Optimization of boron-doping process of titania nanotubes via electrochemical control toward enhanced photoactivity, J. Solid State Electrochem. 20 (2016) 1769–1774, https://doi.org/10.1007/s10008-016-3180-6.
[168] L. Zhang, J. Wang, T. Deng, S. Wang, A novel fluorescent "turn-on" aptasensor based on nitrogen doped graphene quantum dots and hexagonal cobalt oxyhydroxide nanodiscs to detect tetracycline, Anal. Bioanal. Chem. 412 (2020) 1543–1551, https://doi.org/10.1007/s00216-019-02343-6.
[169] J. Wang, Y. Bai, C. Cui, Z. Zhang, S. Li, J. Fan, Y. Zhang, G. Tu, J. Wang, Z. Li, Preference of Bipositive nCo(OH) 2 nanodots to graphene nanoribbons for boosting dual-oxygen evolution performance, J. Mater. Sci. 54 (2019) 7003–7011, https://doi.org/10.1007/s10853-019-03431-y.
[170] M. Zhang, M. De Respinis, H. Frei, Time-resolved observations of water oxidation intermediates on a cobalt-oxide nanoparticle catalyst, Nat. Chem. 6 (2014) 362–367.
[171] F. Zhang, C. Yuan, X. Lu, L. Zhang, Q. Che, Z. Xiaogang, Facile growth of nanowire-on-3-D-nanosheet array on Ni foam for high performance electrochemical supercaps, J. Power Sources 203 (2012) 230–236, https://doi.org/10.1016/j.jpowsour.2011.11.081.
[172] C. Rajesh, J.S. Ziemak, D.H. Petering, Resonance Raman Studies of H2O-Co(II) Hemerythrin and Co(II)Hemerythrin Hydroxides at two temperature Vibrational Studies of Co-OH, and -H2O-OH, J. Am. Chem. Soc. 120 (1984) 3829–3836, https://doi.org/10.1021/ja00316a.
[173] R.T. Sivo, J.F. Hunt, Q. Quan, N. Zhang, Y.J. Xu, H.M. Cuan, Electrocatalysis for the oxygen evolution reaction: recent development and future perspective, Chem. Soc. Rev. 46 (2017) 337–365, https://doi.org/10.1039/c6cs00328a.
[174] Y. Li, W. Qin, F. Qin, H. Fang, V.G. Hadjiev, D. Litvinov, J. Bao, Identification of cobalt oxides with surface reconstruction and facet-induced enhanced spectroscopy, J. Phys. Chem. C 120 (2016) 4511–4516, https://doi.org/10.1021/acs.jpcc.5b11186.
[175] S.J. Yoo, E.J. Elzinga, P.M.J. Sherwood, XPS studies of adsorbed metal ions exposed to anaerobic synthetic sediment for dynamic redox manipulation and ageing, J. Am. Chem. Soc. 131 (2009) 999–1005, https://doi.org/10.1021/ja807.
[176] T. Okuda, T. Kishi, T. Nishi, Raman spectrum of anatase, TiO2, J. Raman Spectrosc. 7 (1978) 321–324, https://doi.org/10.1002/jrs.1250070606.
[177] V.G. Hadjiev, M.N. Iliev, I.V. Vergilov, The Raman spectra of Co3O4, J. Phys. C Solid State Phys. 21 (1988) L199, https://doi.org/10.1088/0022-3719/21/7/007.
[178] D. Eustace, R. Bendel, J. Stuard, Optical and physical properties of cobalt oxide films electrodeposited in bicarbonate aqueous media, J. Phys. Chem. B 110 (2006) 6874–6880, https://doi.org/10.1021/jp056906.
[179] C. Ruan, Y. Huang, H. Arandiyan, J. Chen, X. Wang, Y. Chen, Advanced in oxygen evolution reaction electrocatalysts via direct oxygen-oxygen radical coupling pathway, Adv. Mater. 31 (2019) 2418064, https://doi.org/10.1002/adma.201902398.
[180] S. Wang, Q. Jiang, S. Jin, F.F. Tao, H.M. Chen, D. Zhang, P. Song, Identifying the geometric catalytic active sites of crystalline cobalt oxyhydroxides for oxygen evolution reaction, Nat. Commun. 11 (2020) 1–13, https://doi.org/10.1038/s41467-020-19445-6.
[181] M.C. Biesinger, B.P. Payne, A.P. Grosvenor, L.W.M. Lau, A.R. Gerson, R.S. C. Smart, Resolving surface chemical states in XPS analysis of first row transition metals, oxides and hydroxides: Cr, Mn, Fe, Co and Ni, Appl. Surf. Sci. 257 (2011) 2717–2730, https://doi.org/10.1016/j.apsusc.2010.10.051.
[182] J. Lojewska, W. Miśkowski, T. Tyrniewski, R. Dziembaj, Active state of model cobalt foil catalyst studied by SEM, TPR, TPO, DTG and TG, Catal. Today 69 (2001) 409–416, https://doi.org/10.1016/S0920-5861(01)00409-6.
[183] C.H. Wu, R. Gross, H. Rhizor, M.B. Sahawneh, Auxiliary-pressure X-ray photoelectron spectroscopy study of cobalt foil model catalyst under CO, H2, and their mixtures, ACS Catal. 7 (2017) 1185–1192, https://doi.org/10.1021/acscatal.6b03033.
[184] A. Lemoine, R. Ameloot, G. Ulrych Gilbraith, L. Weiler, J. Gilchrist, L. Gordon Greenaway, I. Rueda, D. Fidanza, Surface Reactivity and Surface Characterization of the Layered pH10-Co(OH)2 Material: an Experimental and Computational Study, J. Phys. Chem. C 125 (2021) 8078–8561, https://doi.org/10.1021/acs.jpcc.1c00941.
[185] L. Syam Sudhu, M.K. Singh, A.M.S. Pramod, A.C.W. Jones, The cobalt oxide based composite nanomaterial: synthesis and its biomedical and engineering applications: Cobalt Catalyst, Appl. (2019), https://doi.org/10.37591/JOMSR.2019.5.2.
[186] L. Zhong, T. Kropp, W. Rudel, O. Brose, R. Tschakert, R. Schlögl, M. Shivhulka, S. Zaharieva, Correlation between activity and oxidation state of cobalt oxide catalysts for CO preferential oxidation, ACS Catal. 9 (2019) 8105–8116, https://doi.org/10.1021/acscatal.9b02082.
[187] Y. Hou, B. Avrutsky, E.J. Gonzalez, B. Chang, R. Wen, T. Hussain, P.H. Ross, Y. Li, T. Liu, Observing the electrochemical oxidation of Co metal at the solid–liquid interface using ambient pressure X-ray photoelectron spectroscopy, J. Phys. Chem. B 125 (2021) 665–671, https://doi.org/10.1021/acs.jpcb.0c09642.
[188] J. Yang, H. Liu, W.N. Martens, R.L. Frost, Synthesis and characterization of cobalt hydroxide, cobalt oxyhydroxide, and cobalt oxide nanodisks, J. Phys. Chem. C 114 (2010) 111–119, https://doi.org/10.1021/jp9069402.
[189] C. Alia, S.C. Sarma, S.C. Peter, M.S. Saha, Competing effect of CoO—cobalt alloy and oxygen-deficient defects toward high oxygen evolution activity in Co3O4 spinels in alkaline medium, ACS Appl. Energy Mater. 3 (2020) 5939–5947, https://doi.org/10.1021/acsaem.0c00307.
[190] Y. Tang, S. Zhao, F. Li, J. Chen, S. Wang, L. Gu, J. Xu, X. Zhang, Highly efficient pivotal-strand catalysis of toluene over Co3O4/SiO2 pre-heterojunction: the crucial role of interface defects and band structure, Appl. Catal. B Environ. 317 (2022) 121709, https://doi.org/10.1016/j.apcatb.2022.121709.
[191] H. Subramonian, B. Kongkanand, S. Dwaraknadham, M. Secanellpland, Reducing the energy band gap of cobalt hydroxide nanosheets with silver atoms and enhancing their electrical conductivity with silver nanoparticles, ACS Omega 6 (2021) 20189–20811, https://doi.org/10.1021/acsomega.1c01958.
[192] S. Nishida, M. Puma, W. Hanak, How to correctly determine the band gap energy of modified semiconductor photocatalysts based on UV–Vis spectra, J. Phys. Chem. Lett. 4 (2013) 4811–4817, https://doi.org/10.1021/jz.
[193] M.G.K. Sridhar, B.G. Seshadri, Measurement method for carrier concentration in TiO2 via the Mott–Schottky approach, Thin Solid Films 519 (2011) 2105–2110, https://doi.org/10.1016/j.tsf.2010.10.071.
[194] M. Strobel, A. Abo-Hamad, J. Hüttenhofer, A. Lisowska-Oleksiak, Exploring the role of carbon cloth in carbon nanotube, g-C3N4 in enhancing photoelectrocatalytic properties of TiO2 nanotubes for water electrolysis, Appl. Surf. Sci. 605 (2022) 154798, https://doi.org/10.1016/j.apsusc.2022.154798.
[195] M. Rezaei, A. Arsalan, M.H. Hassan, B. Palizvada, A.B. Bagtash, L. Pinto, K. Sakaveevi, G. Sailo, L. Liu, A. Bourdo, Thermal reformation of

electrochemically anodized cobalt thin film and nanowire arrays, Appl. Surf. Sci. 586 (2015) 162570, https://doi.org/10.1016/j.apsusc.2022.154870.
[96] D. Upadhyay, R. Rao Sir, A. Wattiaux, P.S. Jha, Two-dimensional chalcogenide cobalt oxychalcogenide as a cycle life sensor, Appl. Surf. Sci. 478 (2019) 908–916, https://doi.org/10.1016/j.apsusc.2019.02.027.
[97] M. Zhang, iR Compensation for electrocatalytic studies: considerations and recommendations, ACS Energy Lett. 8 (2023) 1962–1968, https://doi.org/10.1021/acsenergylett.3c00066.
[98] R. Bacsik, Photoelectrochemical methods for the determination of the band edge position of TiO_2-based nanomaterials, Adv. Phys. Chem. 2011 (2011), https://doi.org/10.1155/2011/278708.
[99] Y.V. Geerlich, T. V. Bhuvaw, Chapter 4 Photoelectrochemistry of Semiconductors: Sculpted Nanomaterials (9) (2005) 205–320. Doi: 10.1016/S0899-0786(05)80027-X.
[100] K. Tsuchiya, N. Ishida, K. Iwahori, M. Sakurai, S. Lisowska-Oleksiak, enhanced photoelectrochemical performance of inorganic-organic hybrid nanostring of $ZrTiO_4$ and PEDOT:PSS, Appl. Surf. Sci. 363 (2016) 703–711, https://doi.org/10.1016/j.apsusc.2015.12.142.
[101] M.R. Nellist, F.A.L. Laskowski, J. Lee, F.J. Wells, S.W. Boettcher, Semiconductor-electrocatalyst interface theory, experiment, and application to photoelectrochemical water splitting, Ann. Chem. Res. 49 (2016) 733–740, https://doi.org/10.1021/acs.accounts.5b00496.
[102] F.-J. Wilk, P. Liu, S.W. Boettcher, Theory and simulation of discontinuous metal semiconductor electrodes for solar water splitting, (2014). Doi: 10.1103/PhysRevLett.112.248304.
[103] F. Nozaki, Water Photo-Oxidation over TiO_2—History and Reaction Mechanism, Catal. 2022, Vol. 12, Page 1507 12 (2022) 1507. Doi: 10.3390/CATAL12121507.
[104] D. Chatterjee, S. Dasgupta, Visible light induced photocatalytic degradation of organic pollutants, J Photochem Photobiol C Photochem Rev 6 (2005) 186–205, https://doi.org/10.1016/J.JPHOTOCHEMREV.2005.09.001.
[105] I.F. Stange-Soares, M.P. Soares-Hermes, Electrocatalysis of the hydrogen/heterogeneous redox couple at platinum electrodes renewed by colloidal film of poly (5-6-ethylenedioxythiophene). Synth. Met. 175 (2013) 50–61, https://doi.org/10.1016/j.synthmet.2013.04.027.
[106] J.M. Wessel, H. Truckhaya, A. Glazier, R. Yamada, K. Iizuka, S. Beeaff, P. Schwaller, TiO2 nanotubes: Self-organized electrochemical formation, properties and applications, Curr. Opin. Solid State Mater. Sci. 11 (2007) 3–18, https://doi.org/10.1016/j.cossms.2008.04.004.
[107] L.F. Pan, X.Q. Wu, M.D. Dao, Y.T. Gu, Cobalt hydroxide film deposited on glassy carbon electrode for electrocatalytic oxidation of hydrazine, Electrochim. Acta 52 (2007) 3650–3659, https://doi.org/10.1016/j.electacta.2006.10.027.
[108] R.E. Doty, A.T. Stone, D.R. Veblen, Defects and fronthic probing the surface chemistry of heterogenite (CoOOH) by dissolution using hydroxylamine and trans-fluvetic acid, J. Phys. Chem. S 120 (2021) 6998–6997, https://doi.org/10.1021/acs.jpcc.6b00900.
[109] D. Pareja, E. Isabo-Bielen, O. Ruiz-de, J.A.Becerra-Alonso and J.A-Cyclo-xylene based ferromagnetism of electron and superoxide radical bound to heterogeneous photocatalytic systems, J. Photochem. Photobiol. A Chem. 407 (2021) 113057, https://doi.org/10.1016/J.JPHOTOCHEM.2020.113057.
[110] M. Zamalloa, A.R. Gerk, A. Lewandowska-Andralojc, R. Halverd, Y. Zang, J. Khalil, A.S. Miller, electron transfer by coated heterojunction ceramic photocatalyst for two-electron transfers, J. Phys. Chem. A 117 (2013) 8360–8367, https://doi.org/10.1021/jp405116x.
[111] P.S. Rao, B. Hayes, Experimental determination of the redox potential of the superoxide radical eO_2^-, Biochem. Biophys. Res. Commun. 53 (1973) 965–971, https://doi.org/10.1016/0006-291X(73)91189-1.
[112] P. Wilkinson, J.G. Seaman, Rate constants for the decay and reaction of the lowest electronically excited singlet state of molecular oxygen in solution, J. Phys. Chem. Ref. Data 19 (1990) 699–999, http://doi.org/10.1063/1.555859.
[113] F. Galle, Chemical basis of reactive oxygen species reactivity and involvement in neurodegenerative diseases, Int. J. Mol. Sci. 21 (2020), https://doi.org/10.3390/ijms21218427.
[114] H. Idriss, On the wrong assignment of the XPS O1s signal at 531.8 eV attributed to oxygen vacancies in photo- and electro-catalysts for water splitting and other materials applications, Surf. Sci. 712 (2021) 121894, https://doi.org/10.1016/j.susc.2021.121894.
[115] M. Favaro, J. Yang, S. Nappini, E. Magnano, F.M. Toma, E.J. Crumlin, J. Yano, I. D. Sharp, Understanding the oxygen evolution reaction mechanism on CoO_x using operando ambient pressure X-ray photoelectron spectroscopy, J. Am. Chem. Soc. 139 (2017) 8960–8970, https://doi.org/10.1021/jacs.7b03211.
[116] I. Weinstock, H. Sheves, F. Barlowski, J. Sherlock, G. Qin, M. Sivan, M. Barman, F. Patel, O. Savchuk, J. Lifshitz, J. Dean, P. Allington, F. Varun, O. M. Nayaveen, Operando identification of the reversible skin layer in CoBO4 as a three-dimensional reaction zone for oxygen evolution, ACS Catal. 12 (2022) 3256–3266, https://doi.org/10.1021/acscatal.1c05109.
[117] S.R.T. Qeeda, D. Nowarchi, M.S. Elias, A.M. Ghaleb-nezhad, Recent Advancements in Cyclodextrin-Based Adsorbents for the Removal of Hazardous Pollutants from Water, Polym. 2022, Vol. 14, Page 2341 14 (2022) 2341. Doi: 10.3390/POLYM14122341.
[118] A. Debbi, T. Sehili, B.S.P. Pereira, H. Ghaut, J. Georgin, Y. Boulsi, K. Bouhra, M. Mansouri, I. Aufaux, T. Lanfranz, A.A. Alsaiddi, A. Abdallah A. S Abouzeid-ness, A. Lamiri, A Statistical Physics Approach to Understanding the Adsorption of Methylene Blue onto Cobalt Oxide Nanoparticles, Molecules 30 (2024) 912, https://doi.org/10.3390/MOLECULES30040912/S1.
[119] C. Michael, S. Sandhya, P. Gajanan, P. Manoj, K. Subrata, D. Kumar, Synthesis of nanosized doped cobalt oxide (Co3O4) nanoparticles by organic-inorganic-metal and enhanced photocatalytic properties in the visible region, J. Mater. Sci. Eng 07 (2018) 1000459, https://doi.org/10.4172/2169-0022.1000459.
[120] S. Xu, Y. Li, J. Li, L. Wu, Q. Zong, J. Zhou, Effect of CoOOH loading on the photoelectrocatalytic performance of NiO nanorod array film, Appl. Surf. Sci. 364 (2016) 585–590, https://doi.org/10.1016/J.APSUSC.2015.12.206.
[121] A. Wahila, J.W. Qu, G.S. Herne, J. Rosenstock, J.E. Nordlee, Oxidation and photo-oxidation of oxides on TiO2 surfaces, J. Phys. Chem. C 112 (2008) 9873–9879, https://doi.org/10.1021/jp710196t.
[122] A. Iannifelt, E.J. Pelan, Anatase-rich surface local structure of TiO2 and its influence on the water photocatalytic process, J. Phys. Chem. Lett. 5 (2014) 2103–2117, https://doi.org/10.1021/jz500470n.
[123] A. Tadjarodi-Javadi, E. Ravadiki, J.W. Schwab, W. Linnell, L.S. Ghiasi, A. Zabihi-s, Preparation and characterization of nanoparticle (Au) and bimetallic (Ag/Au) modified titania photocatalysts activated by visible light, Appl. Catal. B Environ. 101 (2011) 594–604, https://doi.org/10.1016/J.APCATB.2010.12.012.
[124] H.S.C. Dharma, J. Jaafar, N. Widiastuti, S. Matsuyuni, S. Rajabsadeh, M.H. D. Othman, M.A. Rahman, N.SM. Jafri, S.S. Salleheen, A.H. Nasr, N.H. Alias, A review of titanium dioxide (TiO_2)-based photocatalyst for oilfield produced water treatment, membranes (Basel). Membranes 13 (2023) 343, https://doi.org/10.3390/membranes13030343.
[125] A.A. Clifford, M.A. Waters, 502. mechanisms of organic compounds by cerium salts. Part V. Kinetic and product studies of the oxidation of some carboxylic acids, J. Chem. Soc. (1965) 2796–2804, https://doi.org/10.1039/JR9650002796.

V.3 Supplementary Information

SUPPLEMENTARY INFORMATION

Tailoring TiO_2 Nanotubes Photoanodes with Electrodeposited Co_3O_4 and CoOOH Cocatalysts for Enhanced Electrocatalytic and Photoelectrocatalytic Oxygen Evolution

Mariusz Wrulich, Anna Lasowska-Oleksiak *

Department of Chemistry and Technology of Functional Materials, Faculty of Chemistry, Gdańsk University of Technology, Gdańsk 80-233, Poland;

*ako@pg.edu.pl

Keywords: TiO_2 nanotubes, water splitting, photoelectrooxidation, cobalt oxyhydroxide, OER

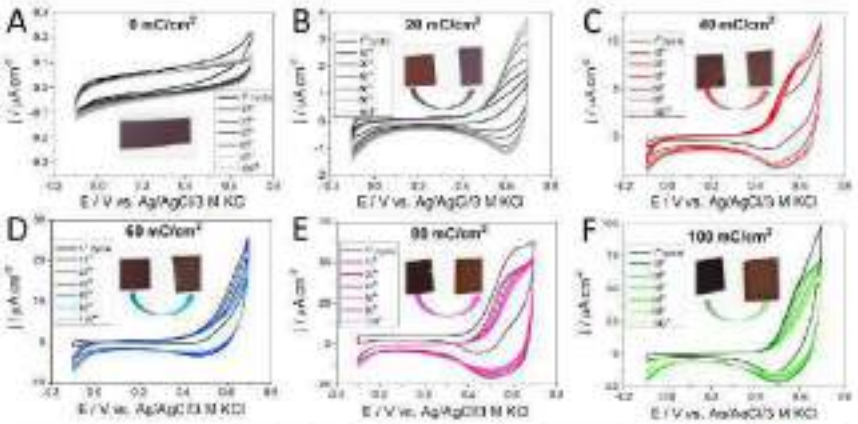

Figure S1. Cyclic voltammetry for Ti/ TiO_2-NTs with cobalt metal surface deposits of A) 0 mC cm^{-2}, B) 20 mC cm^{-2}, C) 40 mC cm^{-2}, D) 60 mC cm^{-2}, E) 80 mC cm^{-2}, F) 100 mC cm^{-2} in 0.1 M NaOH buffered electrolyte (pH = 10).

It's worth noting that with an increasing amount of cobalt deposited onto the TiO_2-NTs surface, the anodic activity is higher in the range of 0.55 V, dedicated to cobalt electrooxidation. Fig. S1 also includes images of electrodes with cobalt species (left) and with CoOOH (right). The colour change from blackish to brownish is visible during successive CV cycles.

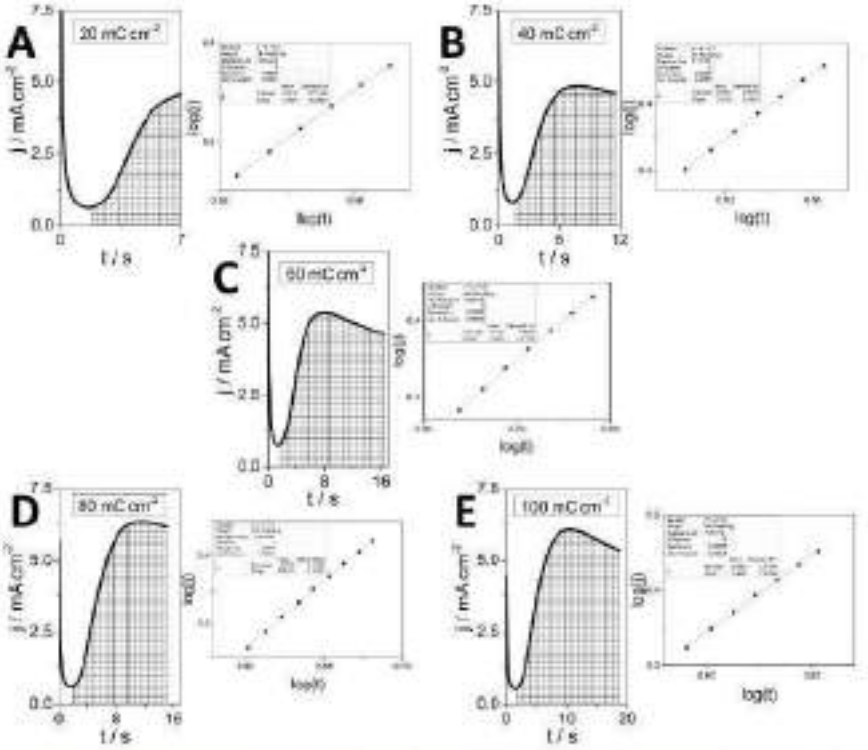

Figure 52. Chronoamperometry curve for cobalt nucleation on ITO-NTs with amounts of: A) 20 mC cm⁻², B) 40 mC cm⁻², C) 60 mC cm⁻², D) 80 mC cm⁻², E) 100 mC cm⁻² in cobalt bath at 30 °C.

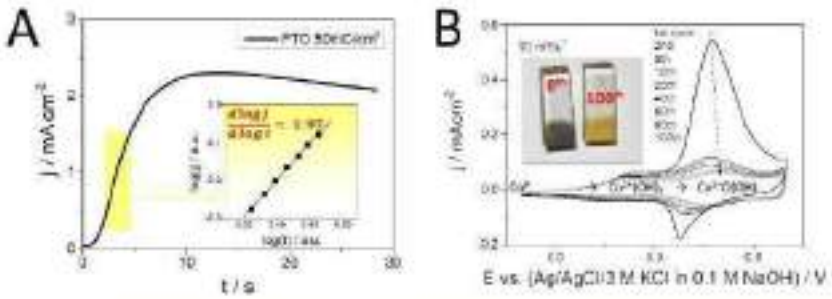

Figure 53. A) Chronoamperometry curve for cobalt nucleation on fluorine-doped tin oxide (FTO) glass (50 mC cm⁻²) in cobalt bath at 30 °C; B) Cyclic voltammetry curve after cobalt deposition in 0.1 M NaOH buffered electrolyte (pH = 10).

2

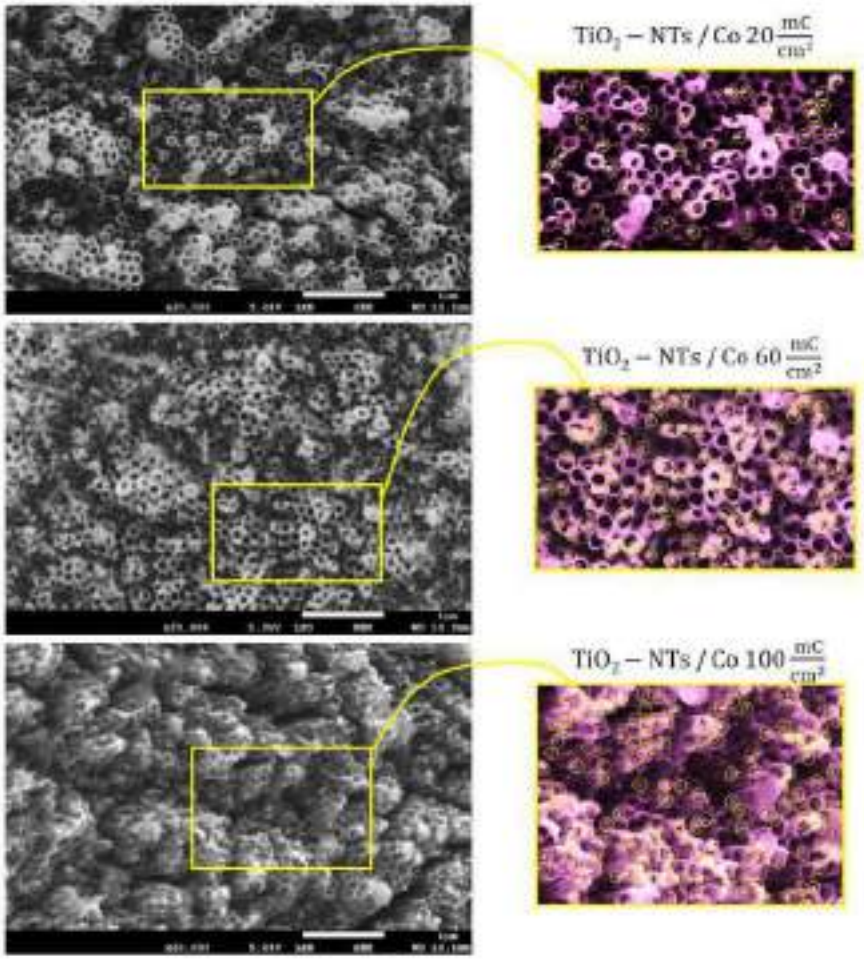

Figure 54 Electrochemical deposition of cobalt onto HA TiO_2-NTs with varying amounts: A) 20 mC cm^{-2}, B) 60 mC cm^{-2}, C) and D) 100 mC cm^{-2}.

Table 51. Different vibration signals of electrodes HA TiO_2-NTs with and without cocatalysts based on Co_3O_4 and CoOOH.

No	Region (wavenumber / cm^{-1})	Assignments / Characteristic group frequencies	Ref.
1	3550 ÷ 3230 3600 ÷ 3100	Broad, medium band of ν_s(OH) – stretching vibration of the hydroxyl group (intermolecular in TiO_2) Broad, weak band of water of crystallisation in solid–state spectra	[1] [2]

3

2	2963±2	Sharp band of $\nu_{as}(CH_3)$ – asymmetric stretching vibration of the methyl group	[3]
3	2876±2	Sharp band of $\nu_{s}(CH_3)$ – symmetric stretching vibration of the methyl group	[3]
4	2926±2	Sharp band of $\nu_{as}(CH_2)$ – asymmetric stretching vibration of the methylene group	[3]
5	2854±2	Sharp band of $\nu_{as}(CH_2)$ – symmetric stretching vibration of the methylene group	[3]
6	1725	Sharp band of ν(O=C–OH) – stretching vibration of the saturated aliphatic carboxylic acid group, hydrogen–bonded	[4]
7	1645	Weak band of δ(Ti–OH) – bending vibration of the hydroxyl group	[1]
8	1583	Sharp band of double bond (Co=O) in the crystal structure Sharp weak band of $\delta_{as}(–COO^-)$ – asymmetric deformation band, characteristic for trisodium citrate	[5] [6]
9	1467	Medium band of $\delta_{as}(CH_3)$ – asymmetric deformation band of the methyl group	[2]
10	1410	Sharp weak band of $\delta_{s}(–COO^-)$ – symmetric deformation band, characteristic for trisodium citrate	[6]
11	1372	Medium band of $\delta_{s}(CH_3)$ – symmetric deformation band of the methyl group	[2]
12	1282	Sharp band of δ(C=O) – bending vibrations Medium/weak band of $\tau(CH_2)$ – twisting vibrations	[2]
13	1120	Medium/weak band of $\rho(CH_3)$ – rocking vibrations Medium/weak band of $\rho(CH_2)$ – rocking vibrations Medium/weak band of ν(C–O–C) – asymmetric stretching vibrations	[2]
14	1070	Medium/weak band of ν_{as}(C–O) – asymmetric stretching vibrations Vibrations of $Ti–O–CH_2CH_3$ group	[7] [8]
15	1040	Medium/weak band of ν(C–C) – stretching vibrations Vibrations of $Ti–O–CH_2CH_3$ group	[8]
16	982	Weak band of δ(Co-OH) – bending vibrations of the hydroxyl group terminated with cobalt	[9]
17	928	Medium/weak band of ν(Ti–O–Ti) – strechting vibrations of Ti-O group Weak band of π(Ti–OH) – wagging vibrations of the hydroxyl group terminated with titanium	[10] [11]
18	830	Medium/weak band of ν(Ti–O–Ti) – strechting vibrations of Ti-O group	[1]
19	780	Medium/weak band of ν(Ti–O–Ti) – strechting vibrations of Ti-O group	[12]
20	652	Transverse optical phonons of tetrahedral ($Co^{2+}O_4$) cobalt ions in the normal spinel-type lattice	[13]
21	558	Transverse optical phonons of octahedral ($Co^{3+}O_6$) cobalt ions in the normal spinel-type lattice	[13]

4

Table S2. Binding energies (in eV) for $^{2+}$Co element selected from the deconvolution of XPS spectra for HA TiO_2-NTs electrodes with deposited cobalt, oxygen or cobalt oxyhydroxide.

HA TiO_2-NTs / cobalt state	with Co	with Co_3O_4/ 40 mC cm^{-2}	with Co_3O_4/ 160 mC cm^{-2}	with CoOOH/ 40 mC cm^{-2}	with CoOOH/ 160 mC cm^{-2}
Co^0 $2p_{3/2}$	777.3	-			
Co^0 $2p_{1/2}$	792.2	-			
Co^{2+} $2p_{3/2}$	781.7	781.2	781.7	781.4	781.8
Co^{2+} $2p_{1/2}$	797.7	797.1	797.3	797.4	797.5
Co^{3+} $2p_{3/2}$	780.2	779.8	780.0	780.1	779.7
Co^{3+} $2p_{1/2}$	796.0	795.0	795.0	795.4	795.2
Sat. $2p_{3/2}$	786.6	786.6	786.8	786.4	784.4
Sat. $2p_{1/2}$	802.9	803.0	803.2	803.6	803.2

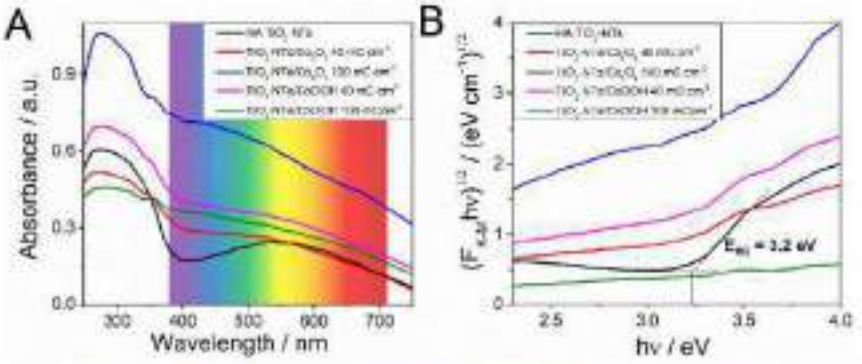

Figure S5. A) Absorbance spectra and B) Tauc plot for TiO_2-NTs with and without cocatalysts.

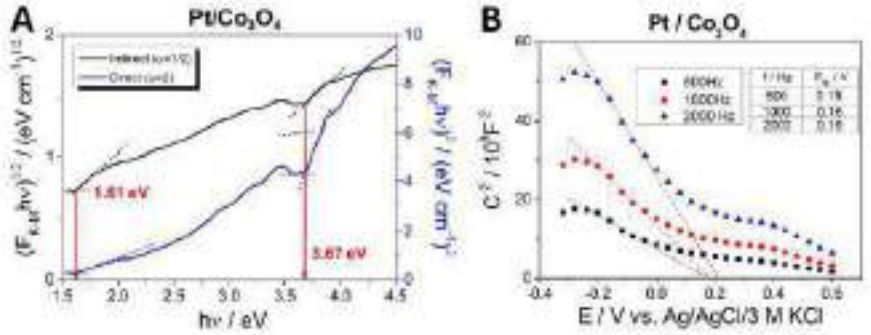

Figure S6. A) Tauc plot and B) Mott–Schottky plot obtained for Pt/Co_3O_4.

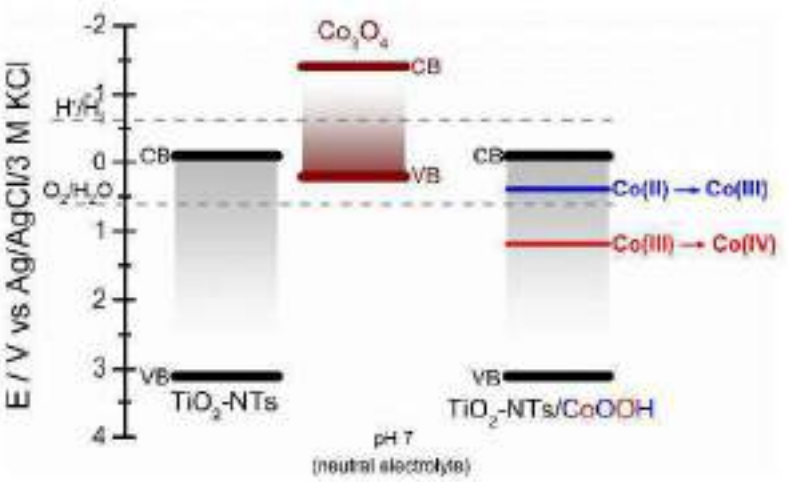

Figure S7. Band Gap alignment for electrodes: TiO2-NTs/Co_3O_4 and TiO2-NTs/CoOOH.

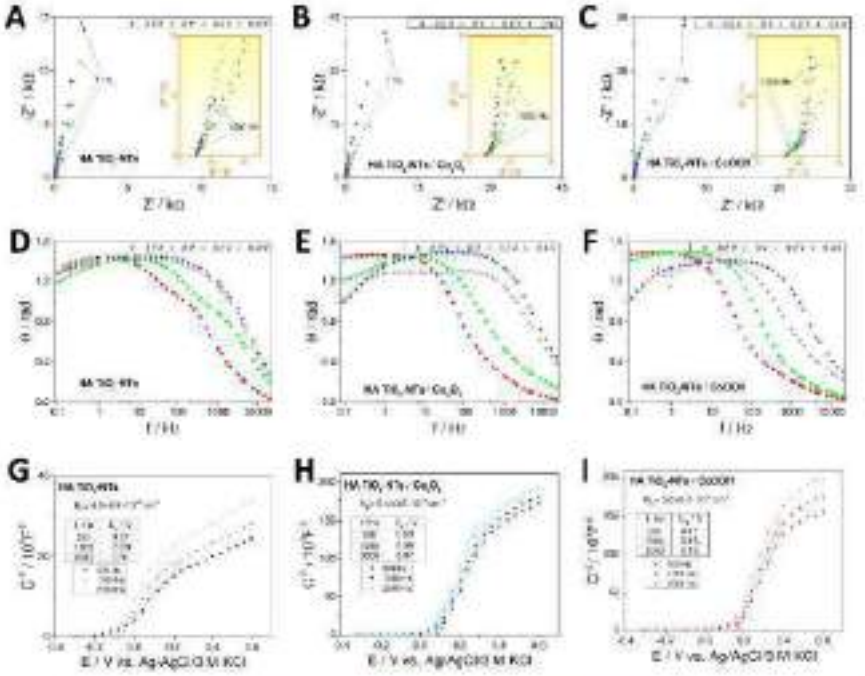

Figure S8. Complex plane impedance, Bode plots and Mott–Schottky plots obtained for EIS TiO_2-NTs without (A, D, G) and with CoOOH (B, E, H) or CoOOH (C, F, I) cocatalyst measured in the frequency range 20 kHz to 0.1 Hz.

6

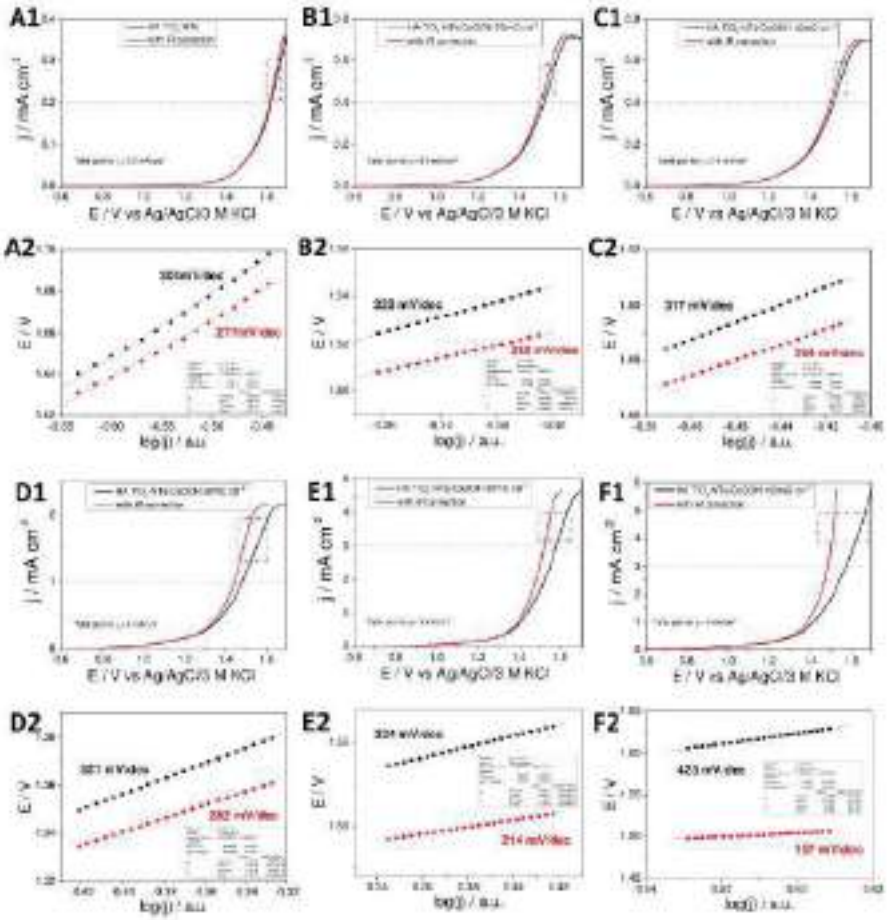

Figure 59. Linear sweep voltammetry curve without (black line) and with (red line) iR correction and their Tafel plots for IEA TiO_2-NTs without (A1, A2) and with CoOOH cocatalysts 20 mCcm^{-2} (B1-B2), 40 mCcm^{-2} (C1-C2), 60 mCcm^{-2} (D1-D2), 80 mCcm^{-2} (E1-E2), 100 mCcm^{-2} (F1-F2).

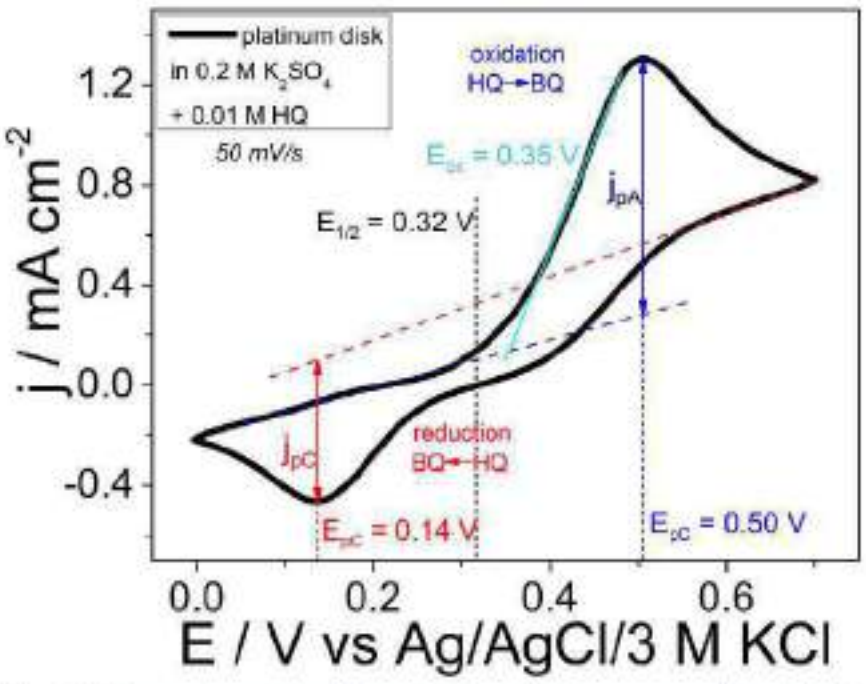

Figure S10. Cyclic voltammetry curve for an electrochemically reversible redox process on a platinum disc in 0.2 M K_2SO_4 with the presence of 0.01 M hydroquinone, a sweep polarization rate of 50 mV/s.

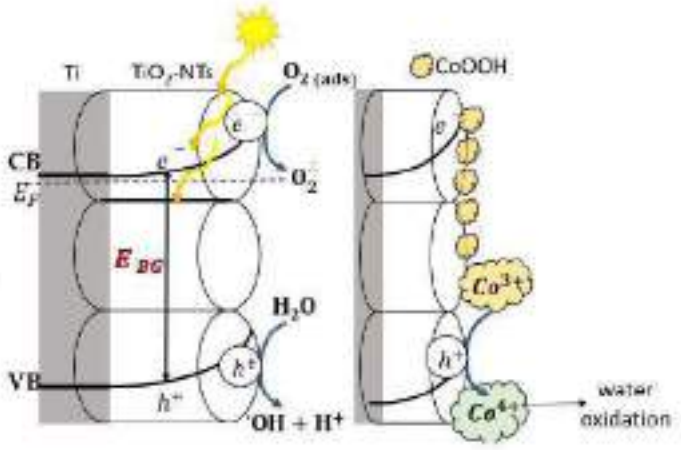

Figure S11. The proposed mechanism of water photoelectrochemical oxidation for HA TiO_2-NTs with a cobalt oxyhydroxide cocatalyst, the presence of BQ/HQ is omitted intentionally.

8

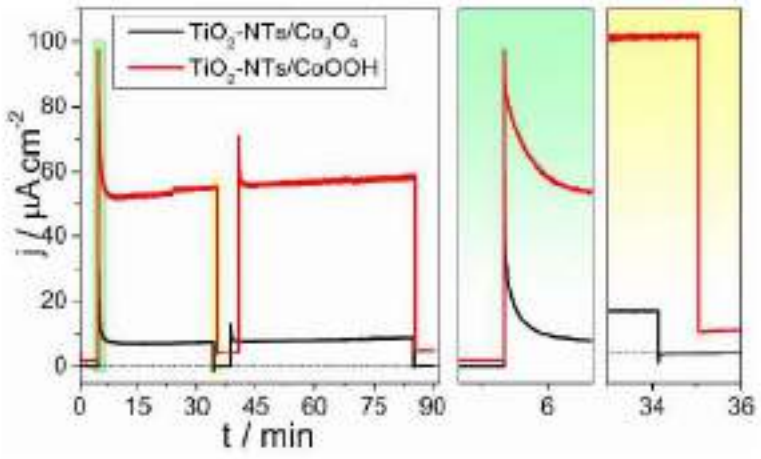

Figure S12. Photocurrent stability comparison of TiO_2-NTs/CoOOH and TiO_2-NTs/Co_3O_4 electrodes under and in the lack of solar illumination, measured at 0.5 V.

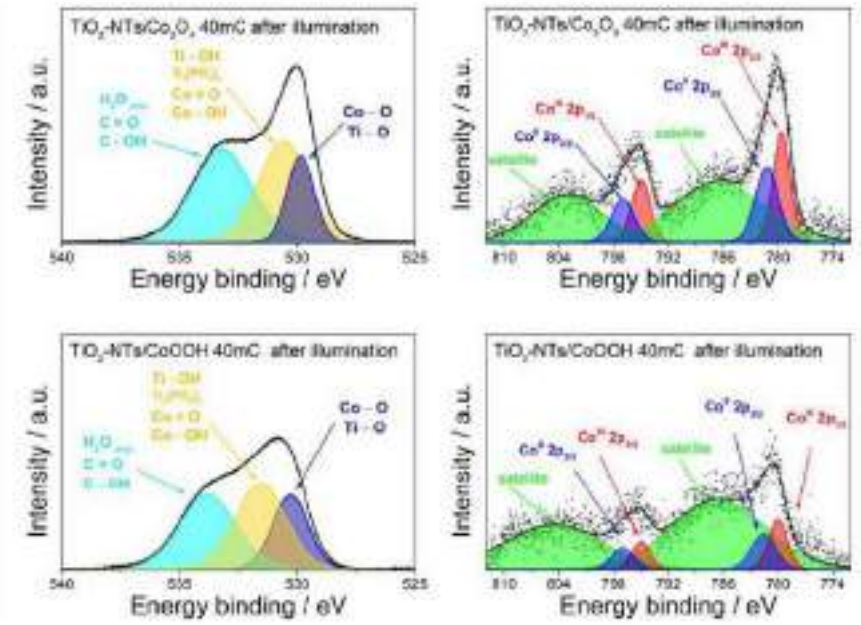

Figure S13. Deconvolution of oxygen 1s and cobalt 2p peaks in the XPS spectra of H4 TiO_2-NTs with Co_3O_4 and CoOOH cocatalysts.

9

Literature:

[1] H.T. Chunate, J. Khamwannah, A.A.A. Aliyu, S. Tantavisut, C. Puncreobutr, A. Khamkongkaeo, C. Tongyam, K. Tumkhanon, T. Phetrattanarangsi, T. Chanamuangkon, T. Sitthiwanit, D. Decha-Umphai, P. Pongjirawish, B. Lohwongwatana, Titania Nanotube Architectures Synthesised on 3D-Printed Ti-6Al-4V Implant and Assessing Vancomycin Release Protocols, Materials (Basel). 14 (2021). https://doi.org/10.3390/MA14216576.

[2] G. Socrates, Infrared Characteristic Group Frequencies. Tables and Charts, 1994. https://doi.org/10.1016/0003-2670(94)80274-2.

[3] P.A. Connor, K.D. Dobson, A.J. McQuillan, Infrared Spectroscopy of the TiO 2 /Aqueous Solution Interface, (1999). https://doi.org/10.1021/la980855d.

[4] B.R.C. De Menezes, F. V. Ferreira, B.C. Silva, E.A.N. Simonetti, T.M. Bastos, L.S. Cividanes, G.P. Thim, Effects of octadecylamine functionalization of carbon nanotubes on dispersion, polarity, and mechanical properties of CNT/HDPE nanocomposites, J. Mater. Sci. 53 (2018) 14311–14327. https://doi.org/10.1007/s10853-018-2627-3.

[5] L. Zhang, J. Wang, J. Deng, S. Wang, A novel fluorescent "turn-on" aptasensor based on nitrogen-doped graphene quantum dots and hexagonal cobalt oxyhydroxide nanoflakes to detect tetracycline, Anal. Bioanal. Chem. 412 (2020) 1343–1351. https://doi.org/10.1007/s00216-019-02361-5.

[6] H. Pan, X. Wang, S. Xiao, L. Yu, Z. Zhang, Preparation and characterization od TiO2 nanoparticles surface- modified by octadecyltrimethoxysilane, Indian J. OfEngineering &Materials Sci. 20 (2013) 561–567.

[7] J. Tan, L. Yang, Q. Kang, Q. Cai, In Situ ATR-FTIR and UV-Visible Spectroscopy Study of Photocatalytic Oxidation of Ethanol over TiO2 Nanotubes, Anal. Lett. 44 (2011) 1114–1125. https://doi.org/10.1080/00032719.2010.507296.

[8] T. Hirakawa, C.K. Nishimoto, A. Komano, M. Otsuka, N. Negishi, H. Miyaguchi, Y. Seto, K. Takeuchi, Experimental study for adsorption and photocatalytic reaction of ethyl methylphosphonate molecule as organophosphorus compound adsorbed at the surface of titanium dioxide under UV irradiation in ambient condition, Res. Chem. Intermed. 47 (2021) 1563–1579. https://doi.org/10.1007/s11164-020-04389-0.

[9] F. Zhang, C. Yuan, X. Lu, L. Zhang, Q. Che, Z. Xiaogang, Facile growth of mesoporous Co 3 O 4 nanowire arrays on Ni foam for high performance electrochemical capacitors, J. Power Sources. 203 (2012) 250–256.
https://doi.org/10.1016/j.jpowsour.2011.12.001

[10] S.K.S. Patel, N.S. Gajbhiye, Intrinsic room-temperature ferromagnetism of V-doped TiO2(B) nanotubes synthesized by the hydrothermal method, Soild State Cimmunications. 151 (2011) 1500–1503. https://doi.org/10.1016/j.ssc.2011.06.021.

[11] J. Tan, L. Yang, Q. Kang, Q. Cai, In situ ATR-FTIR and UV-visible spectroscopy study of photocatalytic oxidation of ethanol over TiO2 nanotubes, Anal. Lett. 44 (2011) 1114–1125. https://doi.org/10.1080/00032719.2010.507296.

[12] M. Szkoda, K. Trzciński, A.P. Nowak, E. Coy, L. Wicikowski, M. Łapiński, K. Siuzdak, A. Lisowska-Oleksiak, Titania nanotubes modified by a pyrolyzed metal-organic framework with zero valent iron centres as a photoanode with enhanced photoelectrochemical, photocatalytical activity and high capacitance, Electrochim. Acta. 278 (2018) 13–24. https://doi.org/10.1016/J.ELECTACTA.2018.05.015.

[13] Y. Li, W. Qiu, F. Qin, H. Fang, V.G. Hadjiev, D. Litvinov, J. Bao, Identification of Cobalt Oxides with Raman Scattering and Fourier Transform Infrared Spectroscopy, J. Phys. Chem. C. 120 (2016) 4511–4516. https://doi.org/10.1021/ACS.JPCC.5B11185.

Chapter VI

Exploring the role of carbon nitrides (melem, melon, g-C_3N_4) in enhancing photoelectrocatalytic properties of TiO_2 nanotubes for water electrooxidation

VI.1 Methods in Brief and Key Results

The article aims to determine whether carbon nitrides with a low degree of polycondensation can act as effective, metal-free cocatalysts on titanium dioxide nanotube photoanodes, and to identify which structural motifs and terminal groups control activity in both the dark and under simulated sunlight. To that end, the authors synthesise melem and melon alongside graphitic carbon nitride (g-C3N4) by controlled thermal treatment of melaminę (yellow), and then subject all three to protonation and oxidative exfoliation in concentrated sulphuric acid to produce a second set of powders with altered terminal functionality (white). These six powders are characterised in detail by X-ray diffraction, X-ray photoelectron spectroscopy, infrared spectroscopy and ultraviolet-visible spectroscopy, which together confirm tri-s-heptazine frameworks and a distribution of terminal groups that include amino, hydroxyl, hydroxylamine, nitroso and carbonyl units. The structural suite shows that the white powders develop elongated, porous crystallites that spread more uniformly on the nanotube surface than the as-calcined yellow powders. Spectroscopy corroborates the evolution from amino-terminated species to materials containing more hydroxylamine and carbonyl-like groups, and ultraviolet-visible measurements show a systematic blue shift in the main absorption feature after acid modification. Impedance analysis, processed with both single-frequency and whole-spectrum approaches, then establishes that all six carbon nitrides behave as p-type semiconductors and provides flat-band positions that are used to construct the band line-up with the n-type TiO_2 nanotubes, leading to a plausible Z-scheme route for charge transfer within the heterojunction, as diagrammed on page twelve. In operation, the presence of carbon nitrides lowers the threshold potential for oxygen evolution and alters the kinetic response in the dark, with the most pronounced effects observed with melem-based coatings. The authors trace this behaviour to the direct participation of pendant amino groups, which undergo stepwise electrooxidation from amine to hydroxylamine, nitroso, and nitro species, thereby mediating electron and proton transfer when the light is off. In the anodic region, the white, acid-modified materials consistently outperform their yellow counterparts, and the best-performing configuration is acid-treated melem on hydrothermally conditioned nanotubes, which achieves a Tafel slope of 83 mV/dec in the dark

and the lowest onset for oxygen evolution among the set. Under illumination, the same junctions show higher photocurrents than bare nanotubes, which the band diagram rationalises in terms of improved separation of photocarriers and a Z-scheme-like pathway that preserves strong oxidising holes in the titania while enabling the carbon nitrides to act as electron sinks - summary depicted in Figure 15. The results presented in the publication demonstrate that changing the purity of the initial titanium substrate during anodization (from 99.5% 0.25 mm thickness to 99.99% 0.127 mm thickness) significantly affects performance. Consequently, the photocurrent for HA TiO_2-NTs increased from 39.5 μA/cm^2 to 114 μA/cm^2 (nearly threefold).

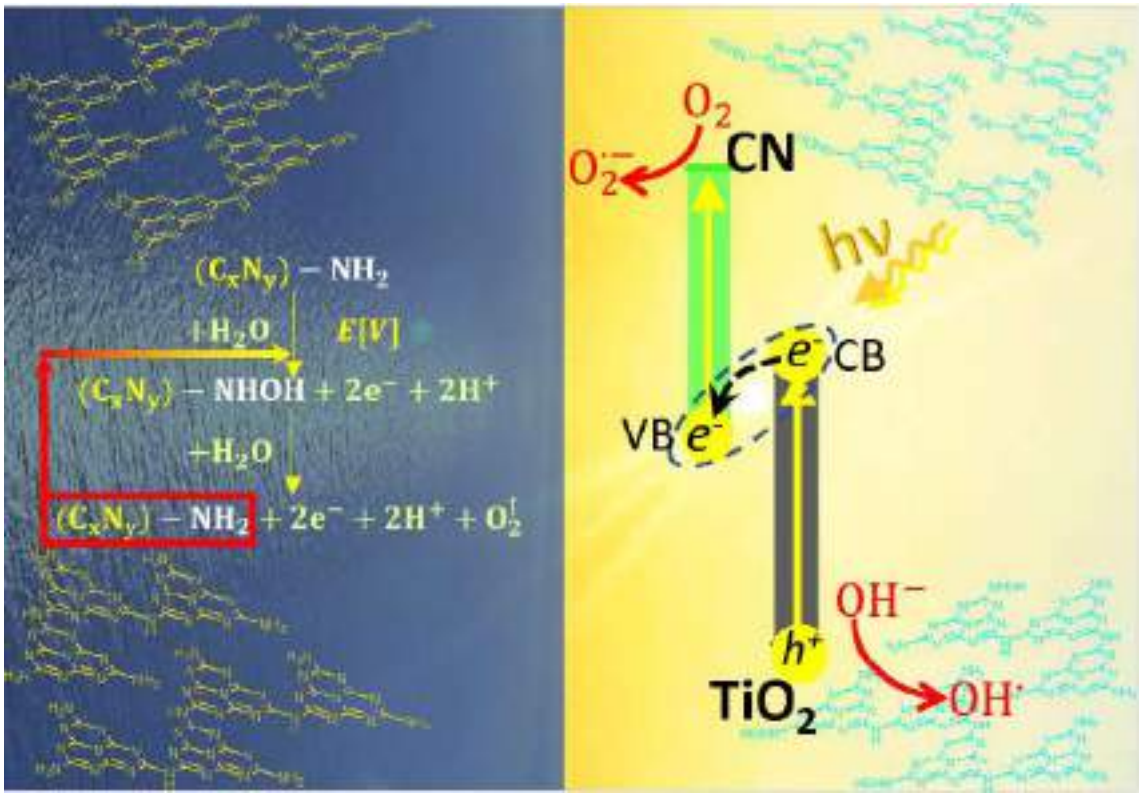

Figure 15. Graphical abstract.

The most novel and consequential aspect is the demonstration that low polycondensation melem and melon, once protonated and lightly oxidised by sulphuric acid, are not only viable but in certain cases superior co catalysts for oxygen evolution on titanium dioxide nanotubes, and that amino groups on these organic semiconductors can function as active electron mediators in electrocatalysis. This is supported by the systematic link the paper draws between synthetic route, terminal group chemistry, semiconductor type and band

alignment, and macroscopic activity, with specific evidence provided by the structural tables and figures, the impedance-derived flatband values, the kinetic analysis from linear sweeps and the comparative performance plots.Together these results deliver a coherent processing to structure to property to performance narrative and open a new lane for using inexpensive, metal free, low temperature carbon nitrides as functional interlayers in water electro oxidation and photoelectrochemical devices.

VI.2 Publication

Applied Surface Science 680 (2025) 161394

Contents lists available at ScienceDirect

Applied Surface Science

journal homepage: www.elsevier.com/locate/apsusc

Full Length Article

Exploring the role of carbon nitrides (melem, melon, g-C_3N_4) in enhancing photoelectrocatalytic properties of TiO_2 nanotubes for water electrooxidation

Mariusz Wrzalich *, Anna Slawinska, Sapajan Ibragimov, Anna Lisowska-Oleksiak *

Faculty of Chemistry, Department of Chemistry and Technology of Functional Materials, Gdansk University of Technology, Narutowicza 11/12, 80-233 Gdansk, Poland

ARTICLE INFO

Dedicated to the memory of Professor Zofia Stasicka (1932-2024).

Keywords:
TiO_2 nanotubes
Carbon nitrides
Melem
Melon
g-C_3N_4
Water splitting

ABSTRACT

Carbon nitrides (CNx), synthesized from melamine at temperatures 600 °C or 620 °C with their derivatives prepared by acidic protonation and exfoliation using H_2SO_4 are tested as co-catalysts for oxygen evolution reaction (OER) modifying anodic titania nanotubes (TiO_2-NTs) surface. Materials exhibit crystalline structures and contain tri-s-triazine rings with different terminal groups (-NH_2, -NHOH, -NO_2, -OH, =O), which are important for their catalytic and photoelectrocatalytic performance. These materials exhibit p-type semiconductor behaviour. Heterojunctions formed by n-type TiO_2 and p-type carbon nitrides were tested using linear sweep voltammetry (LSV) in the dark and under illumination in the potential range allowing the water oxidation reaction to proceed. It is demonstrated, that the presence of -NH_2 functional groups play a considerable role in OER kinetics in the dark. Changes in photocurrent at the anodic potential range are discussed considering Z-scheme heterojunction formation governed with the catalytic activity of -NH_2/-NHOH pending groups. Acid-treated melem in junction with Titania nanotubes emerges as the best co-catalyst for anodic water oxidation in the dark, with a Tafel slope of 83 mV/dec. This research encourages further exploration of melem and melon co-catalysts for improved electro- and photoelectrocatalytic applications.

1. Introduction

Photoelectrocatalytic water splitting is one of the most promising artificial photosynthesis approaches to convert sunlight into sustainable hydrogen energy [1]. Green hydrogen, produced from water through electrolysis and potentially driven by sunlight, is key to achieving carbon neutrality by 2060 [2–4]. The efficiency of electrolysis depends critically on the electrode materials, searching for non-precious metal catalysts for the cathodic hydrogen evolution reaction (HER) and the anodic oxygen evolution reaction (OER) is an active area of research [5,6]. The OER, in particular, remains a bottleneck in the process, and developing efficient photoanodes remains challenging. Historically, the first photoanode was a rutile TiO_2 single crystal presented by Honda and Fujishima more than half a century ago [7]. Since then, extensive research has focused on enhancing the photoactivity of wide-bandgap TiO_2 through non-metal doping, metal doping, or controlled morphologies [8–12]. One approach to improving the photocatalytic efficiency of photoanodes for water splitting involves using titanium dioxide nanotubes (TiO_2-NTs) decorated with co-catalysts and creating Z-scheme (Z/S-type) semiconductor junctions with controlled bandgap alignment [8–11]. These co-catalysts and semiconductors often contain transition metals, which are unsuitable for large-scale applications due to environmental concerns and high costs [12–14]. Therefore, metal-free, cost-effective, and environmentally safe carbon-based semiconductors are desirable alternatives for constructing efficient photoanodes [6,15].

Recently (2024) several review papers have been published on carbon nitrides as materials for application in environmental protection [16] and solar light energy conversion to chemical reaction energy, like CO_2 reduction [17], nitrogen reduction, oxygen evolution reaction, hydrogen evolution reaction, organic pollutants oxidation and disposal, thus materials suitable for overall water splitting [8,18]. The most common synthesis route for carbon nitride (CN), particularly graphitic carbon nitride (g-C_3N_4), involves the thermal polycondensation of precursors such as urea, thiourea, melamine, or cyanuric acid under controlled temperature and atmospheric conditions [19–21]. Other methods, such as hydrothermal, solvothermal, sol-gel, microwave-assisted heating, or chemical vapour deposition, also yield g-C_3N_4 powders [20,22,23]. These synthesis techniques produce unique nanostructures with high surface area, excellent chemical stability, and

* Corresponding authors.
E-mail addresses: mariusz.wrzalich@pg.edu.pl (M. Wrzalich), alo@pg.edu.pl (A. Lisowska-Oleksiak).

https://doi.org/10.1016/j.apsusc.2024.161394
Received 14 August 2024; Received in revised form 28 November 2024; Accepted 2 December 2024
Available online 4 December 2024

enhanced light absorption properties. Recent studies allow to generation of carbon nitrides as a soft photocatalyst for overall water-splitting [24]. When combined with TiO_2 NTs, g-C_3N_4 can significantly enhance the photoelectrocatalytic performance of the composite material [25,26]. Carbon nitrides serve as efficient charge carriers and electron sinks, facilitating the separation and transfer of photogenerated charge carriers in the TiO_2 matrix. This leads to enhanced photocatalytic activity and improved efficiency in applications such as water splitting, pollutant degradation, and photoelectrochemical (PEC) technology [27–29]. As highlighted in a review article on g-C_3N_4 nanomaterials, achieving practical PEC water splitting requires the development of efficient, stable, environmentally friendly, and low-cost photoelectrode materials, which can be realized using carbon nitrides [30].

Over the past decade, numerous studies have demonstrated the photocatalytic properties of g-C_3N_4 as an organic semiconductor in various photoelectrode systems [31–33]. Many examples of g-C_3N_4 combined with other semiconductors exist [34–36]. As summarized in a review of the state-of-the-art carbon nitride research, the mechanisms of photocatalysis enhancement are often linked to the heterojunctions formed between the components of the photoelectrode, such as Type II heterojunctions, co-catalyst-assisted systems, Type I heterojunctions, or Z-scheme architectures. For example, it has been demonstrated that g-C_3N_4 decorated with CoO can function as a p-n junction, and when combined with $CoFe_2O_4$, it forms a Z-scheme heterojunction, resulting in remarkable photoanode performance [37]. Carbon nitrides modified using electrophoresis and silver and gold plasmic functionalization were proposed for photoelectrocatalytic water oxidation in OER [38]. Ethanol oxidation under visible light irradiation on Pt nanoparticle-modified g-C_3N_4 is reported as efficient both in the dark and under solar illumination [4]. Numerous other examples of successful exploitation of carbon nitrides as photocatalysts are mainly related to high polycondensation degree CNs [39–46].

Less-known carbon nitride materials include white crystalline melem monomers, yellow oligomers (2,5,8-triamino-tri-s-triazine) [47–49], and melon (poly(amino (imino)heptazine) [45–47], which are intermediate compounds formed during the condensation reaction (with ammonia evolution by-product, Fig. 1C) of melamine at lower temperatures (e.g. for melem, above 360 °C [50–52]) or shorter thermal polycondensation time. However, these materials often exhibit lower catalytic, photocatalytic, and photoelectrocatalytic properties due to their small surface area, low electrical conductivity, and rapid charge recombination [34]. To enhance the photoactivity of these CNs, the formation of heterojunctions is beneficial [42], as it effectively reduces the recombination of electron–hole pairs ($h^+ - e^-$) upon solar excitation, especially through p-n junctions [53]. Furthermore, melem and melon can be modified into 2D materials with higher specific surface areas, making them more dispersible on TiO_2–NT surfaces. Four main methods are used to exfoliate CN compounds: ultrasonication, thermal polymerization, hydrothermal oxidation, and acid-mediated chemical processes [54–56]. The latter involves two steps: intercalation and redox reactions induced by strong oxidizing acids, such as concentrated sulphuric or nitric acid [52]. The optical and electrochemical properties of carbon nitride photocatalysts can be fine-tuned by modifying their chemical composition (C/N ratio, type, and number of functional groups), morphology (nanostructures, crystallinity, specific surface area), and through the selection of suitable junctions (to facilitate electron/hole separation). Optimizing these parameters is key to achieving the most effective surface characteristics for specific applications.

This study compares the catalytic and photocatalytic properties of six different carbon nitrides used as co-catalysts in photoanodes with TiO_2 nanotubes. The materials investigated include melem (an oligomer), melon, and g-C_3N_4, along with their derivatives obtained through treatment with sulfuric acid. We specifically focus on melem and melon, which are obtained at lower stages of polycondensation, as their large-scale synthesis could offer energy savings, aligning with the principles of the 3R framework: economy, efficiency, and environmental sustainability [57]. Carbon nitrides are variously reported as either p-type or n-type semiconductors [58]. This makes it essential to correctly identify their nature, as flat band potential (E_{fb}) values are critical for understanding band gap alignment in heterojunctions. Here, we employ electrochemical impedance spectroscopy (EIS) and electrical equivalent circuits to determine the majority carriers in the synthesized CNs, confirming their p-type character. The role of functional groups, particularly amine groups (-NH_2), in charge transfer during the four-electron water oxidation reaction, where nitrogen in pending groups is identified as a key electron transfer agent is shown. We propose a mechanism for electron mediation during catalytic water oxidation. Among the six examined carbon nitride co-catalysts, two newly developed compounds, melem oligomer and chemically acid-modified melon, show the most significant potential for application in photoelectrochemical (PEC) systems and dark-phase water electrolysis. To our knowledge, this is the first report on the potential use of low-polycondensation degree carbon nitrides in water splitting technologies.

2. Experimental section

2.1. Preparation of the TiO_2–NTs electrode

To prepare the electrodes, Ti foil was cut into 2 cm square pieces and subjected to pressing with a force of 2 kN/m. Next, the samples underwent degreasing in an ultrasonic bath with acetone and isopropyl alcohol (1:1 ratio) at 40 °C for 20 min, followed by rinsing with distilled water. Both metal plates were placed in a two-electrode glassy cell with a 2 cm gap between them for the anodization process. The cell was filled with 50 ml of an electrolyte solution containing ethylene glycol, NH_4F (0.5 g), H_2O (2.5 ml), and H_3PO_4 (1.75 ml). Titania nanotubes were synthesized by applying a constant voltage of 40 V for 2 h at 20 ± 1 °C. After anodization, thorough rinsing provided calcination in a furnace at 450 °C with a heating rate of 2.5 °C/min. Cooling to room temperature allowed for the formation of TiO_2–NTs. Subsequently, the electrodes were transferred to an autoclave lined with PTFE and filled with water (20 ml per 50 ml chamber volume) for hydrothermal annealing at 100 °C for 24 h. Following drying, hydrothermally annealed (HA) TiO_2–NTs were obtained.

2.2. Preparation of the CN powders

The carbon nitride was prepared by thermal polycondensation of melamine powder ($C_3H_6N_6$, purchased by Thermo Scientific chemicals, 99% purity) as previously described [19]. The process was conducted in semi-closed conditions at temperatures: 400 °C and 525 °C for either 2 h or 6 h, in a tubular furnace. Obtained CN powders were called melem Yellow (400 °C, 2 h), melon Yellow (525 °C, 2 h), and g-C_3N_4 Yellow (double calcination at 525 °C, 2 h). Subsequently, these powders were further modified in the following processes. One gram of carbon nitride was introduced into a flask containing 40 ml of concentrated sulphuric acid and stirred for 4 h. Later, the contents of the flask were poured into a 250 ml flask filled with water and stirred for another 20 h. After this time, the flask was placed in an ultrasonic bath for 4 h. Subsequently, the suspension was washed with distilled water until reaching pH 7. It was again subjected to 4-hour vibrations in the ultrasonic bath. After evaporation of a less temperature of the water from the solution, powders of melem White, melon White and g-C_3N_4 White were obtained. Finally, here obtained 6 different powders and labelled them as

Y400M – Yellow powder of melem (400 °C, 2 h); Y525M – Yellow powder of melon (525 °C, 2 h); Y525G – Yellow powder of g-C_3N_4 (twice at 525 °C, 2 h); W400M – White powder of melem (400 °C, 2 h); W525M – White powder of melon (525 °C, 2 h); W525G – White powder of g-C_3N_4 (twice at 525 °C, 2 h). Yellow and White carbon nitrides were tested concerning their photocatalytic methylene blue decolouration.

2.3. Preparation of the HA TiO_2-NTs/CN electrode

The drop-casting method was used to prepare Titania nanotube electrodes with a carbon nitride–based co-catalyst. To create the desired coating, a mixture (mixture A) was prepared by combining the binder, isopropanol, and distilled water in a volumetric ratio of 1:5:14, with 10 mg of carbon nitride per 1 ml of solution. Nafion perfluorinated resin solution (5 wt% in a mixture of lower aliphatic alcohols and water) obtained from Sigma Aldrich was used as a binder. Subsequently, 50 µl of mixture A was combined with 50 µl of isopropanol, creating mixture B. From this mixture, 25 µl was extracted and deposited onto hydrothermally annealed TiO_2-NTs to form a carbon nitride layer on the surface. The TiO_2- NTs surface was onto which the layer was deposited measured 0.5 cm^2, ensuring a coverage of 50 µl of mixture B per 1 cm^2. The layers were then left to evaporate for 24 h in the dark. Six electrodes were prepared using the procedures described above. Each electrode marked with the symbol TiO_2-NTs/CN, as: TiO_2-NTs/Y400M, TiO_2-NTs/Y525M, TiO_2-NTs/Y525G, TiO_2-NTs/W400M, TiO_2-NTs/W525M, TiO_2-NTs/W525G.

2.4. Chemicals, materials and apparatus

All chemical reagents and materials used in synthesizing TiO_2 nanotubes, carbon nitrides, and electrochemical tests were of analytical grade: NH4F, Na_2SO_4, H_2SO_4 (95% concentrated), H_3PO_4 (85 % concentrated), ethylene glycol (purchased from CHEMPUR, Piekary Śląskie, Poland), melamine powder ($C_3H_6N_6$, purchased from Thermo Scientific Chemicals, 99% purity), and Nafion perfluorinated resin solution (5 wt% in a mixture of lower aliphatic alcohols and water), purchased from Sigma Aldrich, and Ti foils (99.5% metals basis, Alfa Aesar, Kandel, Germany). The electrical conductivity of the water used during synthesis and experimental tests was 0.5 µS/cm.

In this work, numerous experimental studies were employed, including SEM (Scanning Electron Microscopy), elemental analysis, XRD (X-ray Diffraction), XPS (X-ray Photoelectron Spectroscopy), FTIR (Fourier-transform infrared spectroscopy), UV-Vis spectroscopy, EIS (Electrochemical impedance spectroscopy), CV (cyclic voltammetry), LSV (linear sweep voltammetry) and MB (methylene blue) decolourization. The electrode morphologies were characterized using the JSM-7100F field emission SEM (JEOL, Tokyo, Japan) with a beam accelerating voltage of 1 kV. The crystal structure and phase composition of the synthesized carbon nitrides were analyzed via XRD for powders using CuKα emission with λ = 1.5406 Å (Rigaku MiniFlex 600 X-ray diffractometer). The elemental analysis of the chemical composition of carbon nitrides was performed using a Vario El Cube CHNS analyser from Elementar, which involves high-temperature oxidative combustion of samples, was employed. The gaseous combustion products are purified and separated into the individual components (nitrogen, carbon dioxide, sulphur dioxide, water vapour) in absorption columns, and detected in the measurement cell of a TCD detector (thermal conductivity detector). The XPS analyses were performed using a PHI VersaProbe II scanning XPS system with monochromatic Al Kα (1486.6 eV) X-rays, focused to a 100 µm spot and scanned over an area of 400 µm × 400 µm. The photoelectron take-off angle was 45°, with the analyser pass energy set to 117.50 eV (0.5 eV step size) for survey scans, and 46.95 eV (0.1 eV step size) for high-resolution spectra in the C 1 s, O 1 s, N 1 s, and S 2p regions. A dual-beam charge compensation system, using 7 eV Ar^+ ions and 1 eV electrons, maintained a stable surface potential regardless of sample conductivity. All XPS spectra were referenced to the unfunctionalized, saturated carbon (C–C) C 1 s peak at 285.0 eV. The analytical chamber pressure was maintained below 2 × 10^{-7} mbar. Spectral deconvolution was performed using PHI MultiPak software (v.9.9.0), with background subtraction done via the Shirley method. Attenuated Total Reflectance Fourier Transformation of Infrared Radiation (ATR-FTIR) analysis was carried out using a Nicolet iS10 apparatus (Thermo Fisher Scientific, Waltham, MA, USA). The optical characteristics (absorbance curve and band gap energy) were examined using a UV–Vis spectrophotometer (Thermo Fisher Scientific, Evolution 220 Tablet Control Module, USA) with a dual silicon photodiodes detector. Barium sulphate salt was used as a reference standard (blank probe). Visualizations of the molecular orbitals energy levels diagrams presenting HOMO-LUMO electron transition were created using the Chemissian program. The structures of melem and its derivatives, along with their orbitals, were created using the Chemcraft program [67]. Electrochemical and photoelectrochemical tests were studied using a potentiostat–galvanostat system, comprising an Autolab PGStat10 with an FRA module from Eco Chemie B.V. and Autolab PGSTAT 30 from Metrohm Autolab B.V. (Utrecht, Netherlands). In CV, LSV tests three electrode cells were utilized, with TiO_2- NTs/CN as the working electrode (WE), platinum mesh as the counter electrode (CE), and Ag/AgCl/3 M KCl electrode as the reference electrode (RE) immersed in 0.2 M Na_2SO_4 electrolyte purged with high purity argon gas. The temperature was maintained at 20 ± 1 °C using a Julabo F-12 thermostat (Seelbach, Germany). EIS measurements were conducted over a frequency range of 20 kHz to 0.1 Hz with ten points per decade and an amplitude of 10 mV point-to-point in the AC signal. The procedure of fitting functions to the values obtained from impedance measurements was carried out using the EIS Spectrum Analyser program, following Powell's algorithm over 1200 iterations [50]. In photoelectrochemical measurements, the same three-electrode system and conditions were maintained with the high transmittance quartz window. Illumination was provided by a xenon lamp (Osram XBO 150 from Quantum Design, Darmstadt, Germany) generating a light intensity of 100 mW/cm^2, equipped with an air mass (AM) 1.5 filter and an automatic shutter operating on a 5-second cycle. The investigation of the photocatalytic aspect of CN powders on MB decolourization was conducted in a blank glass reactor under the lamp illumination described above, with a magnetic stirrer (150 rpm, CHEMLAND, Stargard, Poland). The reactor was filled with a 50 ml water-based solution containing 1.0 µM MB and 10 mg of CN powder. Tests were performed for 20 min in the dark to establish adsorption processes and for 2 h under solar light illumination. A 0.75 ml sample of the suspension was taken after every 30-minute interval and analysed using a UV–Vis spectrophotometer (UV5100, METASH, Shanghai, China).

3. Results and discussion

3.1. SEM images

Fig. 1 presents SEM images obtained for bulk materials: Yellow CN powders (1A–C) before treatment, White CN powders (1D–F) after H_2SO_4 treatment, and heterojunction HA TiO_2–NTs/White powder (1G–L). The Yellow locus of melem, melon, and g-C_3N_4 exhibit irregularly shaped particles of several micrometers in size. In contrast, the White powders are elongated cuboids with hexagonal bases, lengths of several micrometers and diameters from approximately 300 nm to around 1 µm. The shapes demonstrate regularity and high crystallinity. Generally, the White powders have significantly smaller macroscopic grains than the Yellow ones.

Before the powder deposition onto Titania nanotubes, the material was finely ground and dispersed in mixture B to obtain thin co-catalyst layers. As shown in Figure S1, the surface of TiO_2–NTs covered with Yellow powders (melem and melon) has relatively large CN grains. Obtaining a thin layer, apart from the Y525G, was difficult. For heterojunctions TiO_2–NTs/White CN, the surface is predominantly covered with elongated grains of White powder (Fig. 1 G–I). Fig. 1G and 1H show that the W400M and W525M materials possess numerous pores, likely resulting from the sulphuric (VI) acid treatment. However, when using W525G powder, thin-layered elongated structures are observed, seemingly a result of the exfoliation of larger grains. It can be conclusively stated that the modification of Yellow powders with sulphuric acid (VI) leads to the formation of smaller structures, which are more

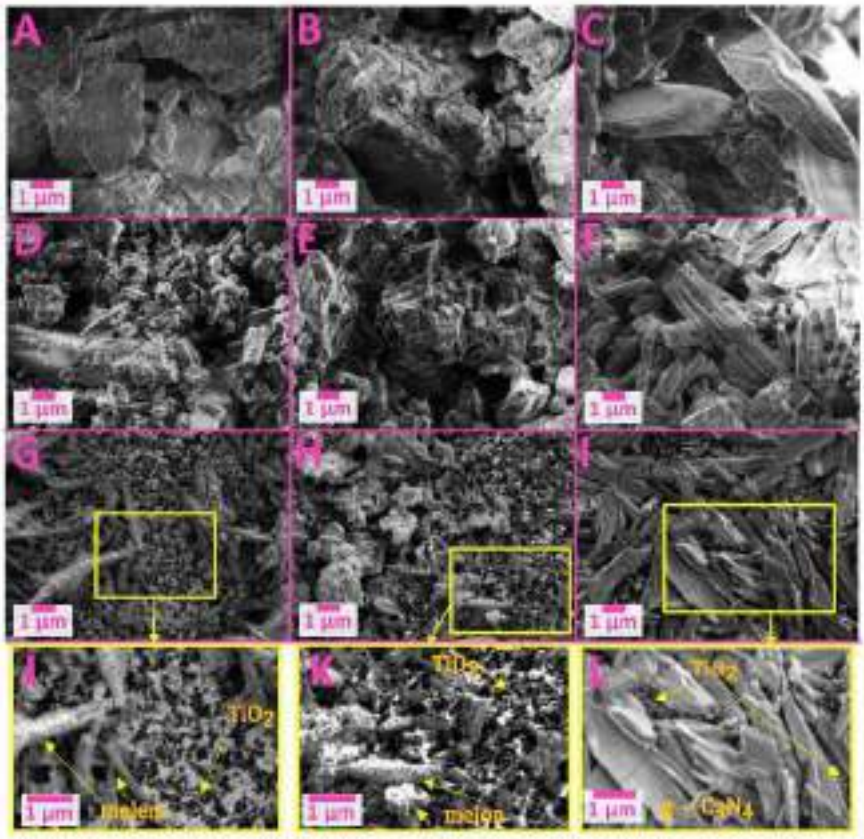

Fig. 1. Top-view SEM images at x10 000 magnification for Yellow CN powders (A–C), White CN powders (D–F), $TiNT_{as}$ NTs/White CN at x10 000 (G–I) and x20 000 (J–L) magnification, respectively (in each row CN: melem, melon and g-C_3N_4).

advantageous for photocatalytic application.

3.2. Elemental analysis

The elemental composition (carbon, nitrogen, hydrogen, and sulphur) was analysed by elemental analysis. Their atomic composition was established to identify the obtained products, and the results are presented in Table 1. The remaining content in the samples (labelled as 'others') is associated with oxygen and silicon, resulting from the calcination of powders in ceramic crucibles in the presence of oxygen. XPS studies confirmed the presence of these elements, see in section 3.4 and Table S1. It is worth noting that during the modification of Yellow CN with acid, the silicon content does not increase, only the oxygen and sulphur. Therefore, in the case of White CN powders, the remaining content will mainly be determined by the oxygen.

Table 1
Carbon, nitrogen, sulphur and hydrogen elements analysis in White and Yellow powders.

	N / % at.	C / % at.	H / % at.	S / % at.	Others / % at.	C/N
YMRM	46.25	29.20	23.34	0.00	1.19	0.63
WMRM	39.61	25.05	31.38	0.25	3.21	0.63
YSEM	46.05	29.09	23.75	0.00	1.46	0.63
WSEM	39.80	25.53	32.54	0.24	0.82	0.63
YMRG	46.07	29.30	23.42	0.00	1.21	0.64
WMRG	39.16	25.26	32.84	0.31	2.43	0.64

The carbon with molecular formula $C_6N_7(NH_2)_3$ has an analytical atomic composition of N (45.46%), C (27.27%), and H (27.27%) with a carbon-to-nitrogen ratio of 0.60 [50]. In this study, the obtained contents were N (46.25%), C (29.20%), and H (23.34%), with a C/N ratio of 0.63. These values are close to and consistent with the results obtained by others. Melon, with the stoichiometry $C_6N_9H_{3.17}$ [60], with a C/N ratio of 0.66, matches the composition obtained in this work. For carbon nitride, g-C_3N_4, the ratio was slightly lower by 0.03 than the standard value, i.e., 0.72. Nevertheless, these values are consistent with those reported by other authors [61].

The obtained yellow powders after calcination in a crucible differed slightly in their shades of Yellow. Melem was lightly yellow with a white shadow (bright beige), melon was yellow, and g-C_3N_4 was an intense

yellow-orangish. The yield of the products obtained through this process was approximately: 50% melem, 30% melon, and 20% g-C_3N_4.

3.1. XRD analysis

Carbon nitrides have a crystal structure similar to graphite/graphene-like compounds [62,63], with their hexagonal rings formed by triazine or heptazine (tri-s-triazine) [47,56]. The XRD patterns of carbon nitrides are presented in Fig. 3A, covering the range of 10° ÷ 60°. The analysis of the two typical signals for carbon nitrides will be discussed in detail, as shown in Fig. 3B (10° ÷ 15°) and Fig. 3C (25° ÷ 32°).

For Yellow CN powders, identification is easier than for White powders. In the S400M sample, the structure of melem was confirmed, characterized by the planes: (011), (002), (012), (111), (102), (021), (20-2), (21-2), (21-3) and (200) located at 2θ values of 12.3°, 13.4°, 16.5°, 18.2°, 19.5°, 25.8°, 28.0°, 27.6°, 30.2° and 31.1°, respectively [50,64]. It is noteworthy that during the thermal treatment of melamine melam—a dimer of melamine formed through condensation—can be synthesized [65]. However, no melon was detected in the XRD pattern, indicating that the melem structure does not exist in these CN materials calcined at 400 °C. Generally, poly(triazine imide) compounds can be obtained through thermal treatment, but this requires corrosive salt melts [47,50].

Due to the heating conditions, melem molecules can undergo polycondensation at higher temperatures, forming various types of melon [66]. The first melon compound was found by Berzelius and named by Liebig [67]. Franklin suggested [68], that depending on the amount of hydrogen, melem molecules can form bigger polyazine-like structures with different combinations of heptazine rings. Melem can be joined through nitrogen atoms, forming a cyclic arrangement [69], a linear polymer chain [69], a zigzag melamine structure [47,56] or planar oligomers with triangular heptazine cores that have alternating orientations [62,70]. Therefore, melem compound is referred to as polymeric carbon nitride rather than graphitic carbon nitride, as is often found in the literature [47,56]. More precisely, a melon should be referred to as poly (amino-imino)heptazine. For the material labelled as Y525M, the registered signals at 12.9°, 17.3°, 21.6° and 27.3° correlate to (210), (310), (3-20) and (002) the Miller indices [71]. This confirms that the compound is identified as melon [72].

Obtaining a fully polycondensed melon compound – poly(heptazine imide), popularly known as graphitic carbon nitride, is not straightforward under one-stage heat treatment conditions [47,56]. The remaining amounts of non-polymerised melem or long linear/zigzag polymer chain of melem are the main obstacles to full conversion into heptazine-based g-C_3N_4 [66,73]. In this work, the thermal treatment process was repeated after thorough grinding in a mortar and pestle. The Y525G powder reveals a sharp peak centred at 27.3° corresponding to the (002) plane, which is likewise the characteristic interlayer in graphite [62,63], see Fig. 3C. However, in Fig. 3B, two small peaks at 12.5° and 13.8° are observed. As said above, at around 2θ = 13°, the peak is correlated to the (001) plane for graphitic structure, notwithstanding that the g-C_3N_4 peak is about 13° [15,74]. The change in double intensity signal may mainly result from the thermal process. The crystal structure of carbon nitrides strictly depends on the effects of heating time and temperature [72], but also on the quenching process itself [75]. This may occur as the formation of two different phases (α and β) during the crystallization process, beyond the graphitic CN phase [76]. However, as the literature suggests, it is more likely to determine the presence of pure melon, g-C_3N_4, or a mix of them, and whether they form 2D or 3D structures, which is challenging [50,66,77]. According to Table 1, the Y525G material contains less amount of hydrogen than Y525M. This effect is higher crystallinity of g-C_3N_4 material, which is observed as a smaller FWHM (full width at half maximum) value for the 27.3° peak [75]. The sharper peak indicates a higher number of graphene-like layers stacked per crystallite, particularly evident for W525G (Fig. 3B). However, there is no significant change observed in the distance between these layers. As shown by Tyborski [78], in such a case, a triclinic unit cell is formed with slightly less than 90° lattice constant (γ < 90°). This distortion causes two planes of small displacement of 3Å (100) and (-100). Accordingly, those CN layers exhibit a shift relative to each other. Therefore, this is the A-B configuration of alternated stacking tri-s-heptazine layers. That can reduce the impact of the repulsive forces created by the π-electron clouds of adjacent layers [79]. Nevertheless, the distortion may be caused by the presence of silica or sulphur in the structure [79–81] or even sodium or potassium intercalation [82], but the amount of these elements is negligible. Overall, we can assume that Y525G is a g-C_3N_4 composed with a 3D structure.

For white carbon nitrides (CNs), it has been observed that treatment with sulphuric acid (VI) increases the crystallite size. Additionally, increased crystallinity is observed through the appearance of additional

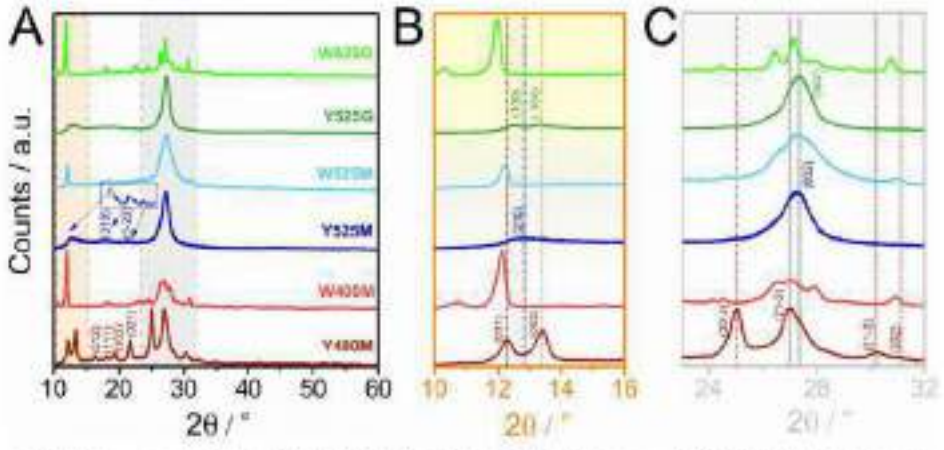

Fig. 3. XRD patterns of carbon nitrides (Y400M, W400M, Y525M, W525M, Y525G, W525G) in the range of (A) 10° ÷ 60°, (B) 10 ÷ 16 and (C) 24 ÷ 32°.

peaks 24.6°, 24.7°, 24.4° and 30.9°, 31.0°, 30.7° (Fig. 2C), corresponding to melem, melon, g-C_3N_4 after sulphuric acid treatment. The set of two smaller peaks can be associated with interstitial defects. The application of a high acid concentration during the exfoliation process (protonation) significantly affected the powders [65]. According to literature, the exfoliation of carbon nitrides through protonation with sulphuric acid treatment leads to the incorporation of sulphates into the structure, resulting in the expansion of the crystal lattice (increased interplane distance), which occurs by the shift of the peak maximum towards lower angles [52,63,64]. Here, in White CN the remaining amount of sulphur is below 0.4 at. %. Thus, protonation will likely cause a main change in the White powders' structure and allow chemical interaction with sulphate anions by forming new layered compounds. Nevertheless, the acid may cause strong oxidation of functional groups, forming new intermolecular interactions in the material. To our knowledge, no published reports exist on the structural identification of the W400M and W525M XRD maxima.

3.4. XPS analysis

Fig. 3A-S presents the deconvolution of the XPS spectra for C 1 s, N 1 s, and O 1 s for the following samples: (A-C) Y400M, (D-F) Y525M, (G-I) Y525O, (J-L) W400M, (M-N—O) W525M, and (P-R) W525O. The surface elemental composition derived from the fitting of XPS data for all analysed carbon nitrides is summarised in Table S1. The full spectra, ranging from 0 eV to 1200 eV, are shown in Figure S2. The deconvolution of the C 1 s spectra revealed four distinct components. The peak at binding energy (E_B) 285.0 eV corresponds to adventitious carbon C–C bonds and/or sp^2 hybridised C = C bonds (a thin layer of carbonaceous material typically presents on the surface of samples exposed to air) [66]. The peak at 286.4 eV is associated with C–O groups, predominantly due to surface contamination, likely covered by hydrocarbons, hydroxyl groups [56–58]. The most intense peak, observed at 288.5 eV, is attributed to N-C = N bonds [59–61]. Additionally, a shake-up feature at 294.2 eV is linked to sp^2 carbon, especially in its aromatic forms, further confirming the presence of these bonding configurations [59,62].

The nitrogen spectra display three prominent peaks. The first, at 398.6 eV, is indicative of C-N = C bonds within aromatic structures [59]. The second peak, at 400.1 eV, corresponds to nitrogen in a three-coordinated neighbourhood N-(C_3), while the third peak at 401.3 eV is ascribed to –NH, $–NH_2$ bonds [59,63] serving as a linker of cores or terminal groups of the polymer, respectively. A clear trend was observed in Fig. 3 for both yellow and white carbon nitrides as the polymer chain length increases (as reflected by a higher C/N ratio, see Table 1), the signal intensity at 288.5 eV in the C 1 s spectrum, and at E_B of 399.0 eV in the N 1 s spectrum, also increases. This suggests a higher concentration of C = N bonds, characteristic of aromatic ring structures in carbon nitrides. Such observations support the conclusion that the proposed synthesis yields carbon nitride derivatives (melem, melon, g-C_3N_4) with defined stoichiometries.

Regarding the oxygen spectra, distinct variations were identified. For the yellow powders, the spectrum fits well to a single component at 535.8 eV, corresponding to O-S, O-C bonds, and/or –OH groups, or adsorbed H_2O [59,66]. However, in the white powders, an additional signal at 531.4 eV appears, particularly visible in Fig. 3S, suggesting the presence of O = C organic bonds. Furthermore, a slight broadening of the C 1 s spectrum towards higher binding energies is seen in Fig. 3D, while a significant increase in the intensity of the N 1 s spectrum is observed in Fig. 3R. These changes indicate that the modification of carbon nitrides with sulphuric acid alters the local carbon environment around nitrogen atoms, leading to the formation of a new O = C bond, which is absent in the yellow carbon nitride samples. A comprehensive analysis of the terminal groups within the polymer chains, as outlined in Section 3.5, shows that shifts from typical $–NH_2$ groups to = O or –OH groups significantly affect the optical properties (the yellow-to-white colour shift, discussed in Section 3.6) as well as the electrochemical properties, which are a central focus of this study. The sulphur S 2p signal was also examined. No S 2p signal was detected in the Yellow CNs, whereas a weak signal was observed in the white samples, as shown in Supplementary Information, Figure S3. The S 2p spectra were fitted with a doublet structure, featuring a doublet separation of 1.16 eV between the $2p_{3/2}$ and $2p_{1/2}$ peaks. The primary $2p_{3/2}$ peak, located at 168.5 eV, is indicative of SO_4^{2-} ions [67,68].

3.5. FTIR analysis

FTIR spectra of materials obtained during thermally initiated polycondensation of melamine are similar to those described in the literature [69] and shown in Fig. 4. In each case, characteristic vibration bands associated with the presence of primary and secondary amino groups are recorded (maximum 3074 cm^{-1}, 3078 cm^{-1}, 3090 cm^{-1} – Y400M, Y525M and Y525O, respectively), as well as those indicating the presence of heterocyclic rings containing nitrogen atoms (range from about 1625 to 1070). All vibration values along with literature references are provided in the supplementary, see Table S2. The melem spectrum shows a strong deformation band of the primary N-H group of 1576 cm^{-1} [3,69]. In the remaining materials, this band is accompanied by a second one approximately 1550 cm^{-1}, indicating condensation and formation of secondary aromatic bonds. In each case, bands indicating the presence of heptazine units are also visible, characterised by two sharp signals around 806 cm^{-1} which should be related to short chains and 790 cm^{-1} arising from bending modes of the tri-s-heptazine units and can relate to long chains.

Further modification of the materials included their prolonged contact with sulphuric acid (18.4 M, 4 h; 2.6 M, 24 h). In the first stage, a rapid salt formation reaction occurs. Most of the available amino groups become protonated, and a new cubic in the structure is created based on hydrogen bonds and electrostatic interactions. The materials become proton donors. In the next step, dilution, the presence of air and ultrasound promote further reactions such as hydrolysis and redox. As a consequence, the number of amine groups forming salts with sulphuric acid decreases due to supramolecular bonds between heptazine units and cyanuric/melamic (or cyanuric) acids units, as well as inclusions of sulphate ions SO_4^{2-} formed during the reduction of sulphuric acid (VI), confirmed by XPS analysis Figures S3.

Comparing the recorded IR spectra before and after acid treatment, significant changes can be observed. The main bands responsible for N-H stretching vibrations are sharpened. No broadening or shifting of the aforementioned bands is observed, which may indicate that the dominant form is the salt formation via a protonated amino group (positively charged) and SO_4^{2-} anions with the ability to form the bridge assembly. Stretching vibrations of hydroxyl groups are recorded in the same range. Nevertheless, they may be covered by the main N-H bands or indicate a shift in the ketone-enol equilibrium toward the more stable ketone tautomers, as evidenced by the strengthening of the 1753 cm^{-1} band for W400M and W525O and the appearance of a shear strain around 1756 cm^{-1}. The vibration region of the heterocyclic skeleton is also significantly modified. For materials obtained at 525 °C, the N-H strain bond ceases to be visible at about 1535 cm^{-1}. The C-N stretching bands of the aromatic amine group also undergo significant changes. The C-N stretching band at about 1311 cm^{-1} is extinguished, which may indicate a partial transformation into hydroxyl groups. Following the above, structural formulas of the obtained compounds based on carbon nitrides are proposed in Fig. 1. Due to the complexity of the studied system, it is difficult to confirm unequivocally the presence of SO(VI)/S (VI) residues from sulphuric acid treatment by FTIR. However, their presence is confirmed by elemental and XPS analysis. In conclusion, the main features of FTIR spectra of g-C_3N_4 derived from melamine are consistent with those presented in previous studies [101].

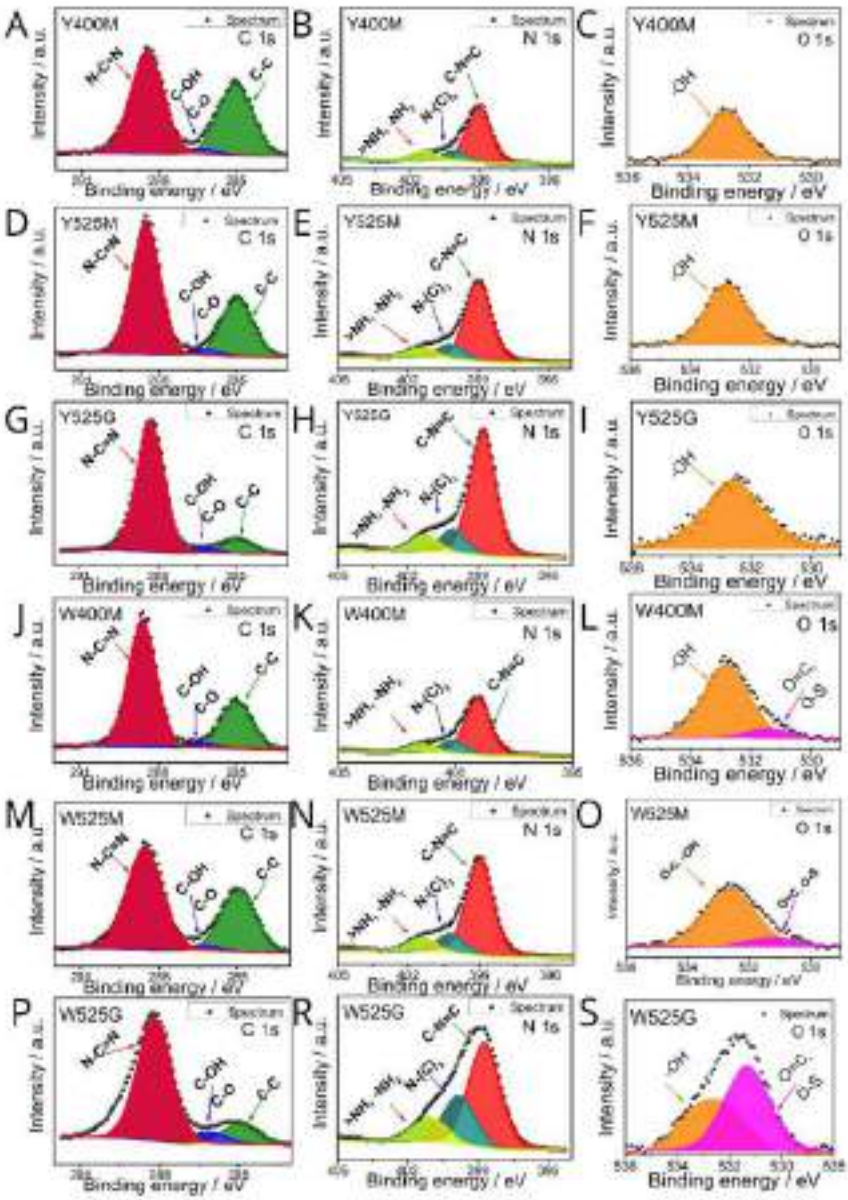

Fig. 6. The XPS deconvoluted spectra of C 1 s, N 1 s and O 1 s for (A-C) Y400M, (D-F) Y525M, (G-I) Y525G, (J-L) W400M, (M-O) W525M, (P-S) W525G samples, respectively.

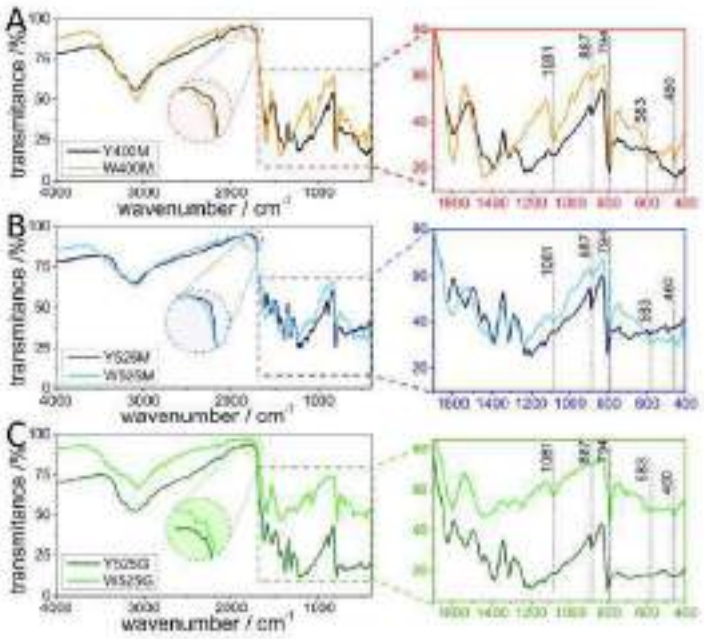

Fig. 4. FTIR Spectra obtained for carbon nitrides (A) Y400M, W400M, (B) Y525M, W525M, and (C) Y525G, W525G.

3.6. UV–Vis spectroscopy measurements

Titania nanotubes and carbon nitrides were characterized by UV–Vis spectroscopy. Fig. 5A-B depicts Tauc plots and Fig. 5C-D shows the absorbance spectra for HA TiO_2-NT and carbon nitrides. In the case of absorbance spectra, Titania nanotubes show bilight at wavelengths (λ) in two regions: 1.) the sharp band in UV and 2) the wide band in VIS (black line). In the first region, a typical photoabsorption (~ 400 nm) for titanium dioxide is observed, which arises from intrinsic VB (valence band) to CB (conduction band) electron transitions [79,102,103]. The second broad maximum (λ = 527 nm) is mainly correlated with the morphology of TiO_2-NTs mainly due to the Fabry–Perot interference phenomenon [104].

However, for carbon nitrides, in the UV range, we can distinguish carbon–nitrogen (C/N) groups such as sp^2 σ bonding, sp^2 π bond and lone pair on the bridging nitrogen. The π → π* electronic transition is due to the extensive π-conjugated aromatic system and is visible in the absorbance spectra for λ > 400 nm [104]. The absorption edge is redshifted when a larger CN molecule is obtained (more connected heptazine groups) for Yellow powders, see Fig. 6C. However, during sulphuric acid treatment, CN obtained additional hydroxyl, hydroxylamine or nitroso terminal groups as shown above in Fig. 5. These structures can change the maximum peak wavelength towards blueshift, see Fig. 7 [105].

Additionally, UV–Vis spectrum analysis is carried out in the gas phase using Time-dependent Density Functional Theory (TDDFT) for a better understanding of the electronic transition states of each substituent –OH and = O compared to $–NH_2$. Optimized structures of melem $–NH_2$ and substituted –OH, =O were obtained using B3LYP density functional [106,107] employing all-electron correlation–consistent polarized basis set augmented with diffuse functions: AUG-Cc-pVTZ [110,111] in Gaussian 16 software [112]. To verify that optimized geometry is local minima, we have performed vibrational analysis to ensure that there are no imaginary frequencies. A tight SCF convergence criterion was used for all calculations. In the excited-state calculations, 30 possible singlet vertical excited states were considered for melem (NH_2) and its substitutional derivatives (–OH, =O). The corresponding donor electronic transitions, structures, and molecular orbitals are illustrated in Figure S4. The optimized structures of melem and its substitutional derivatives possess Cs symmetry, and their Highest Occupied Molecular Orbital (HOMO) is a non-bonding (n) orbital located on the nitrogen lone pair in the ring structure. The lowest Unoccupied Molecular Orbital (LUMO) is a π* antibonding orbital located on the C–N bond or the C–O bond in melem and the substitutional derivatives (–OH, =O), respectively. Since the electron transition from the non-bonding (n) orbital to the antibonding π* orbital requires lower energy compared to the transition from bonding π orbitals to the π* antibonding orbital, this results in light absorption at lower frequencies and higher wavelengths of 316.11 nm, 330.97 nm, and 285.73 nm, respectively. However, these transitions are symmetry forbidden and therefore do not appear in the UV–Vis spectra, or they appear with lower oscillator strengths. On the other hand, π → π* transitions were observed, where the maximum wavelength (λmax) absorbed by melem and its substitutional derivatives (–NH_2, –OH, =O) is 204 nm, 195 nm, and 192 nm, respectively. From the molecular orbitals, it can be seen that these transitions are primarily π → π* in nature.

The TD-DFT calculation was performed to examine the role of pending groups on the UV–VIS absorption properties of the carbon nitride group. The TD-DFT calculation was conducted on a low molecular weight representative of the studied species, namely melem. Figure S7 shows the spectra deduced from the TD-DFT calculations. The theoretically deduced spectra confirm that the blue shift observed in

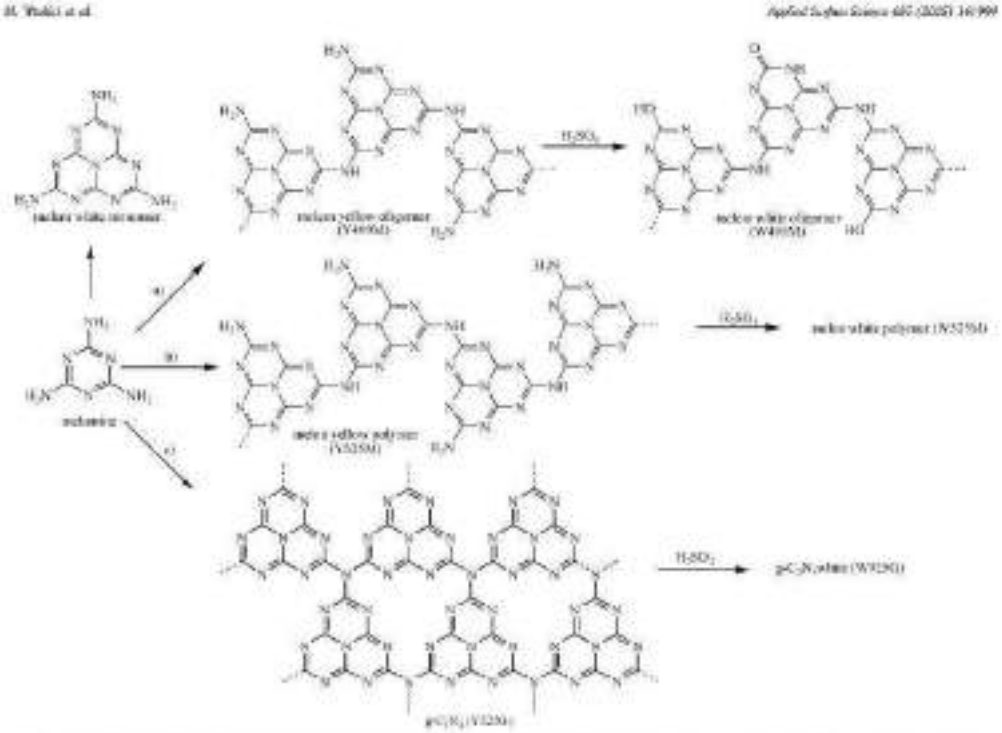

Fig. 6. Schematic representation of Yellow and White carbon nitrides (melon, carbon and g-C_3N_4) synthesized from melamine via thermal treatment followed by reaction with sulphuric acid.

Yellow CNs depends on the presence of pending groups, and the yellow colour (with a maximum absorption around ~ 420 nm) is attributed to the presence of $-NH_2$ in the carbon nitrides. Sulfuric acid treatment of carbon nitrides causes the oxidation of amine groups to $-NHOH$, which is reflected as a change in the UV–Vis spectra. The maximum absorption shifts towards higher frequencies/lower wavelengths in the UV region. Therefore, it can be concluded that modification with sulphuric acid causes changes in the terminal groups of melem, because of the observed hypsochromic effect in the experimental measurements (Fig. 6C-D) and theoretical calculations (Fig. 7).

Based on the Tauc plot (Fig. 8A–B), the bandgap energy (E_{BG}) can be determined using the Kubelka-Munk function [113]. For photoanode Titania nanotubes E_{BG} is equal to 3.20 eV [102]. In the case of carbon nitrides, we observe a significantly lower bandgap value. For carbon nitrides/melem/sulphuric acid treatment (Y400M, Y525M, Y525G), the E_{BG} values are 2.78, 2.77, and 2.75 eV, respectively. Meanwhile, for the modified powders (W400M, W525M, W525G), the E_{BG} values are 3.01, 2.96, and 3.01 eV and are presented in Table 2. Titania nanotubes are generally recognised as indirect n-type semiconductors [103,113,114]. A further EIS study was used to investigate the semiconductor type of carbon nitrides, see section 3.6. This is necessary to build the proper bandgap alignment.

3.7. EIS measurements

The EIS measurements were performed to investigate the type of semiconducting carbon nitride CN nanotubes and estimate the position of the flat band potential (E_{FB}). First, electrodes were prepared by depositing from suspension containing powders (mixture B, described in 2.3. paragraph) onto Pt-disc electrode and dried under air. Then electrodes were immersed in 0.2 M Na_2SO_4 and characterised using electrochemical impedance spectroscopy in the 3-electrode cellat 20 °C. The obtained EIS results are presented in Figure 9A. The results of EIS measurements allowed for determination of the flat band position, using formula (1):

$$-Z'' = \frac{1}{2\pi f C} \quad (1)$$

for all synthesized materials, applying the Mott-Schottky relationship for an AC signal with 10 mV amplitude at a frequency of 1000 Hz, where Z'' is the imaginary part of impedance (Ω), f is the frequency of the AC signal (Hz) and C as is the value of capacitance (F) [113–117]. The electrode materials were polarized from −0.1 V to 0.6 V, with the rest potential of semiconducting materials ~ 0.3 V vs. Ag/AgCl/3 M KCl electrode. At the contact between the semiconductor CN and the Pt, a Schottky barrier exists, which produces a changeable capacitance [115]. Measured capacitance C, represented by Equation (1) is representing both C_{SC} (the space charge capacitance) and C_{DL} (the double layer capacitance) connected in series, where C_{DL} value is much smaller than C_{SC} value ($C_{SC} \ll C_{DL}$). To determine the value of flat band potential (E_{FB}) from Mott–Schottky relationship (2) was used:

$$\frac{1}{C_{SC}^2} = \frac{2}{\varepsilon_r \varepsilon_0 q N_x}\left(E - E_{FB} - \frac{k_B T}{|q|}\right) \quad (2)$$

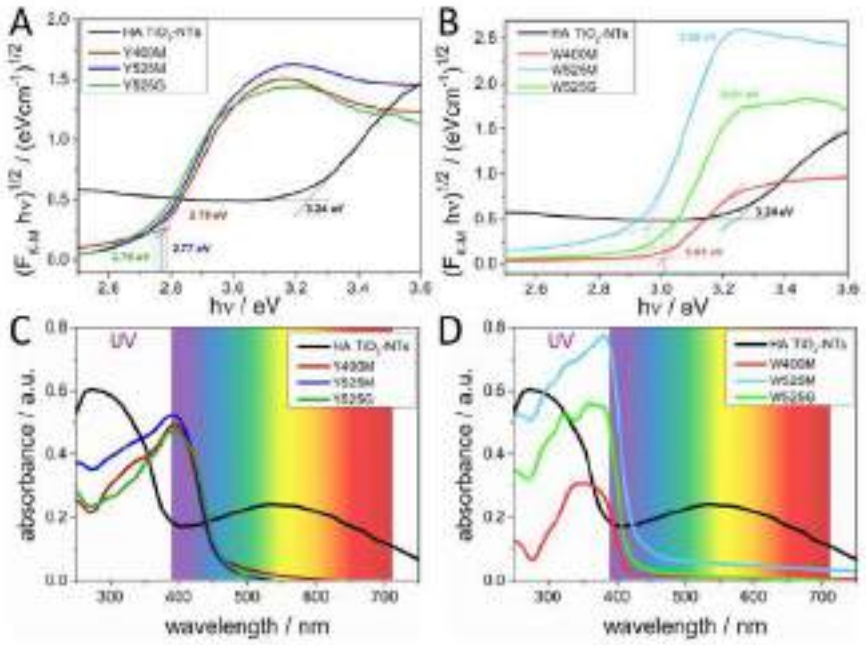

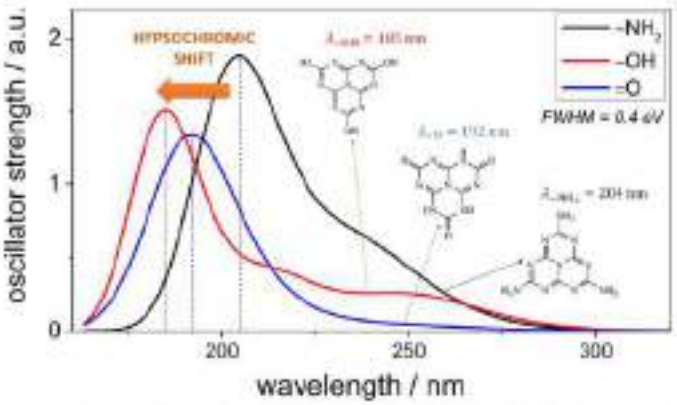

Table 2

	TiO_2-NTs	W400M	W600M	W525M	N525M	P525G	W525G
E_{gap} (eV)	3.24	2.79	3.45	2.77	2.99	2.78	3.01

Where symbols mean: ε_r – relative permittivity, ε_0 – vacuum permittivity, q_e – the elementary charge, N_A – the acceptor density, k_B – the Boltzmann constant, T – the temperature [116,117]. The obtained values of (C_{SC}^{-2}) vs. E for all carbon nitride materials measured at 1000 Hz are depicted in Figure S7.

All Yellow carbon nitride materials: Y400M, Y525M, Y525G and White ones: W400M, W525M W525G, which were modified in sulphuric acid, behave similarly representing the slope $[(\Delta(1/C_{SC}^2)/\Delta E]$ with the negative values, which is typical for p-type semiconductors.

In the case of melem and melon, the structure obtained contains numerous amino groups, which can act as proton acceptor (electron donor) groups [118], as described in the FTIR section (3.4). Thus, the presence of $-NH_2$ groups is considered to promote n-type conductivity in carbon nitrides (CNx). Such a structure could be crucial for achieving the p-type conductivity when terminal $-NH_2/NH_2$ groups in CNx structure undergo substitution with electron-accepting groups. This situation occurs in the case under study. The synthesis is conducted under so-called semi-closed conditions, which allowed the introduction of –OH and C – O groups into the structure, which are very likely responsible for the p-type conductivity of the carbon nitrides being studied. In the case of g-C_3N_4, the heptazine rings may lower-en electron deficiency, which contributes to the attention of the attractive interactions between adjacent CN planes. This results in a noticeable difference in the change of unit cell parameters, as discussed in the XRD section (3.2). However, it is often stated that g-C_3N_4 are n-type semiconductors [27,119,120]. Remembering that TiO_2 nanotubes belong to the group of n-type semiconductors (with E_{fb} of –0.05 V confirmed in [108]), the creation of a heterojunction with a reduced tendency to electron/hole recombination exists. Estimated values of d_{SC} for carbon nitrides are collected in Table 3.

However, interfacial properties of studied electrodes were characterized by more complex equivalent circuits than simple capacitance connected in series with electrolyte resistance R_{El}, as $R_{El}C$. The electrical equivalent circuit proposed to simulate electrical interfacial properties of TiO_2–NTs/CN is built of two parallel circuits combining resistance and capacitance as constant phase elements (*CPE*) with electrolyte resistance in series, as

$$R_{El}(R_1\ CPE_1)(R_2\ CPE_2),$$

which is shown in Figure S6. The CPE is represented by two parameters Q and n according to the expression [33]

$$Z = \frac{1}{Q(j\omega)^n} \tag{S1}$$

where $0 < n < 1$, Q are frequency independent constants and represent CPE [121]. Constant n is related to rotation of the impedance plot with angle α where $\alpha = |1 - n|90^\circ$. Brug et al. [122], gave us an empirical formula (4) allowing to exclude capacitance from CPE element, as:

$$Z(\omega) = R_\Omega + \frac{1}{Q(j\omega)^n} \tag{4}$$

The relation between n, Q and C is given in equation (5) as

$$Q = R_\Omega^{\frac{n}{1-n}} C^n \tag{S5}$$

and for more complex systems, where combined faradaic current exist obeys equation (6):

$$Q = \left(\frac{1}{\mathcal{A}_0} + \frac{1}{R_{ct}}\right)^{1-n} \cdot C \tag{6}$$

The given formula allows to evaluation of the capacitance value independent of the frequency of the AC signal with all consequences of such simplification [123]. Results of the fitting procedure for all obtained EIS-measured carbon nitrides are presented in Table S3–S6. As can be seen, Q_1 values change with potential, as one expects for semiconductor experiments C_{SC}. On the other hand, Q_2 is almost potentially independent or probably is related to Nafion-membrane barrier usage. Thus, assuming that Q_1 represents C_{SC} capacitance was excluded using Brug's approach. Using equation (6), obtained values are used for Mott–Schottky analysis by equation (2) and corrected value of semiconductor flat bands crude estimation, see Fig. 8.

In the analysis above, both linear fitting methods using equation (2) resulted in a decreasing function, indicating that each of the carbon nitrides obtained is an each of the p-type semiconductor materials. A comparison of the estimated values of E_{fb} using Brug's approach and using simple calculation from impedance data at a single frequency (1000 Hz) shows a difference of approximately 0.2 V (see Table 3), which is within expected limits [117]. The complexities in extracting C_{sc} in the studied cases arise from the intricate interfacial structure, the presence of faradaic minimal charge transfer reactions, and the varying degrees of polycondensation within each sample. Additionally, as the samples are attached to the metal support using a Nafion membrane, the precise extraction of E_{fb} is more challenging, making accurate measurement of C_{sc} difficult. Therefore, the E_{fb} values determined via Brug's approach were selected to establish the bandgap alignment, as illustrated in Fig. 9. The position of the band results from the assumption that the flat band potential for a p-type semiconductor is close (–0.1 V) to the valence band (VB) and for an n-type semiconductor it is close to the conduction band [117]. The position of the flat band potential E_{fb} was determined based on the Mott-Schottky analysis of the impedance function, see Table 3.

Fig. 9 shows the positions of the VB and CB bands for both semiconductors that make up the electrode material, specifically for TiO_2 nanotubes (NT) and the examined carbon nitrides (CNx). Charge transfer (CNx connections in photocatalysis and photoelectrocatalysis are summarized in the review article [16]. The most commonly considered junctions are the (n-p) heterojunction and the Z-scheme junction. The difference between them lies in the way photogenerated charge is transported. Both semiconductors are illuminated, and electrons transferred from the VB of TiO_2 to the CB of TiO_2 can move to the VB of carbon nitrides. Meanwhile, the holes generated in the VB of TiO_2 serve as an oxidizing agent for H_2O. This is how the Z-scheme functions, and in the studied case, it is highly likely that this mechanism is responsible for the observed increase in photocurrents for modified TiO_2 compared to pure TiO_2 nanotubes.

Moreover, when two semiconductors with opposite charge carriers are combined in a single electrode, charge recombination is expected to be less likely. However, the formation of a Z-scheme semiconductor photoanode primarily accounts for the observed increase in photocurrent. A schematic representation of the Z-scheme is provided, with a conclusion emphasizing that the synergistic effects of optimal bandgap alignment and opposite-sign charge carriers at the solid-state interface are crucial for enhancing photocurrent. The role of $-NH_2$ (amine) groups

Table 3
Estimated values of flat band potential E_{fb} [vs. Ag/AgCl/3M KCl] with ± 0.01 V accuracy, using data from 1 000 Hz and whole range (20 kHz ÷ 0.1 Hz) – Brug's approach vs. Ag/AgCl/3M KCl and RHE-electrode, obtained for carbon nitrides films deposited onto Ti-disc support.

	Y400M	W400M	Y525M	W525M	Y525G	W525G
E_{fb}[V vs Ag/AgCl – 1000 Hz]	1.33	1.34	0.75	0.95	0.73	0.85
E_{fb}[V vs Ag/AgCl] – Brug	1.31	1.38	0.64	0.80	0.50	0.73
E_{fb}[V vs RHE] – Brug	2.28	2.05	1.23	1.44	1.34	1.37

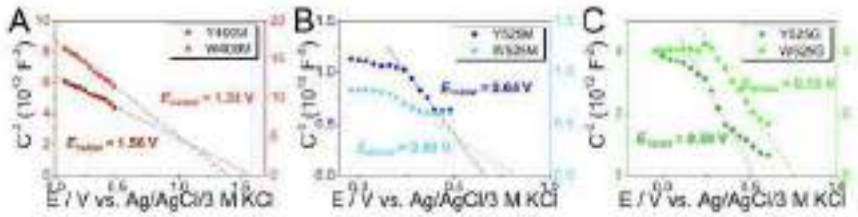

Fig. 8. Mott–Schottky plots obtained for (A) melem, (B) melon and (C) $g\text{-}C_3N_4$ materials, measured from −0.16 V to 0.6 V in the range of 20 kHz to 0.1 Hz (calculated from a whole range of the frequency using Brug's approach, equation (1)).

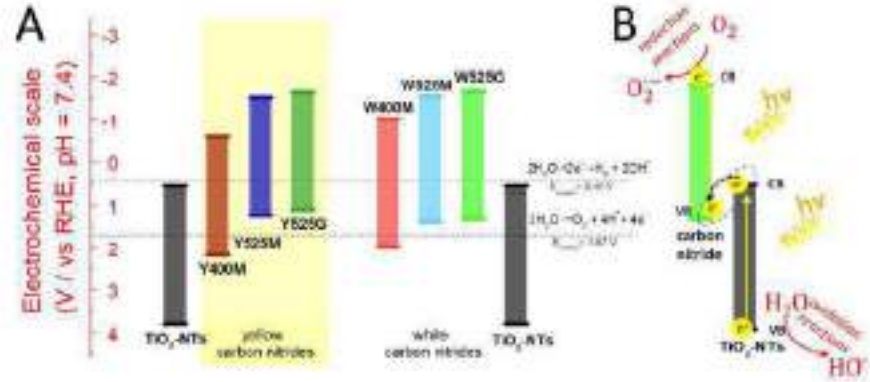

Fig. 9. (A) The band gap alignment for HA TiO_2-NTs/carbon nitrides and (B) Z-scheme junction.

in the electrooxidation process, particularly in the dark, is taken into account. These groups likely act as active sites facilitating electrooxidation reactions when photoactivity is not prominent. This contribution is essential for sustaining redox reactions independently of light, adding another dimension to the functionality of the anode. We are not aware of any other examples of amino groups acting as electron mediators in electrocatalysis in the electro-oxidation process, which may indicate the role of the CN semiconductor plane in this process.

3.3. CV, LSV in the dark

In Fig. 10, the LSV polarization curves of the heterojunction electrodes composed of TiO_2-NTs and carbon nitrides (Yellow and White) are shown, along with the LSV curve of pure TiO_2-NTs. The general features of LSV curves are presented in Fig. 10A and 10D. Titania nanotubes modified with melon, melem, and $g\text{-}C_3N_4$ are used to identify the threshold potential E_{th} that responds to water molecule oxidation (refer to Table 4).

The position of E_{th} changes slightly after modifying Ti anode nanotubes, resulting in a decrease in the reaction overpotential. Additionally, new electrode activity is observed in a broad potential range, which is directly related to the amount of $-NH_2$ groups in Yellow and White modifiers. The quantity of $-NH_2$ groups depends on the degree of polycondensation. Since complete polycondensation is not achievable, some $-NH_2$ groups still exist in $g\text{-}C_3N_4$. During anodic polarization, the $-NH_2$ pending groups from carbon nitrides undergo oxidation, which is evident as a pre-wave (Fig. 10 B, E). The reverse scan on the cathodic branch of the polarization curve is not detected. The product of the electrooxidation can be –NHOH hydroxylamine group, –NO nitroso compound and finally $-NO_2$ nitro group, with water molecule serving as a source of oxygen atoms. Thus, limiting the current j_L of observed processes is related to the amount of $-NH_2$, which is transformed to –NHOH, –NO and even likely finally to $-NO_2$. Further polarization leads to the OER process with varied kinetics, depending on the type of the TiO_2–NTs modifier.

The polarization curves in Fig. 10 C and 10F display all polarization curves within a high anodic potential range for both pure TiO_2-NTs and modified electrodes. The threshold potentials E_{th} and b coefficients ("Tafel slope") identifying the change in the potential for a tenfold increase in current [mV/dec] are collected in Table 4. It is important to note that the parameter b (Tafel slope) is related to a more complex electrode reaction mechanism rather than just activation control as presented in Tafel or Butler-Volmer equations. All TiO_2–NTs electrodes modified with CN White species treated in H_2SO_4, exhibit better parameters for the OER process in the dark in comparison with their Yellow (without H_2SO_4 treatment) counterparts. As one can see diminishing of OER overpotentials is equal to 0.03 V for the majority of the electrodes and 0.04 V for TiO_2–NTs /W400M. The kinetics of OER reaction is seen to be related to the type of TiO_2–NTs modifier chemistry and the presence of $-NH_2$ terminal groups, which are identified in PTIR spectroscopy, see p. 3.5.

Oxidation of the $-NH_2$ by sulphuric acid involves the reduction of S (+VI) to S(+IV) species, which are identified by XPS analysis. The most significant changes in OER in the dark were recorded for melem – with the highest amount of $-NH_2$ groups, but also combined S(IV)/S(VI) residual species (Fig. 10B). The participation of amino groups has a significant impact on the kinetics of the reaction in dark conditions. Generally, during electrooxidation the $-NH_2$ group can be transformed

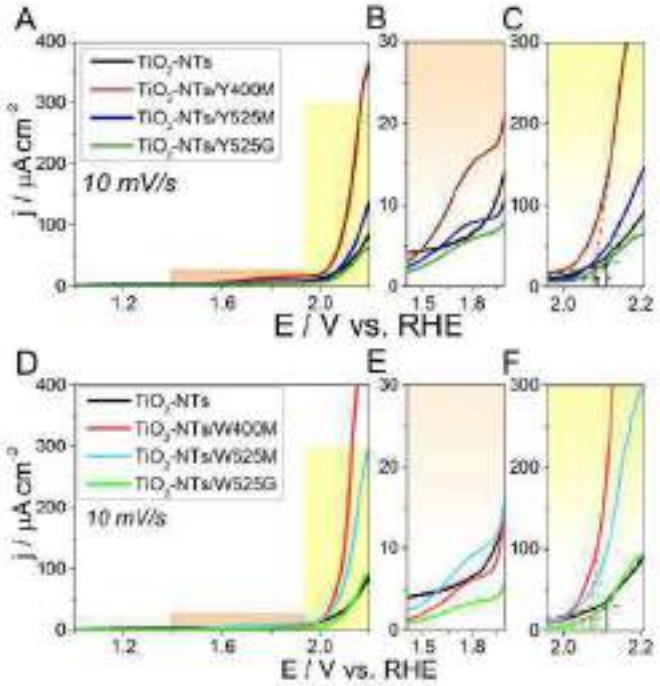

Fig. 10. Linear sweep voltammetry curve for (A–C) Yellow and (D–F) White carbon nitrides.

Table 4
The parameters calculated from LSV curves in the dark for OER: threshold potential E_{th} vs. RHE, Tafel slope b and photocurrent density j_{ph} obtained from polarization of the heterojunctions TiO_2-NTs/CN electrodes.

	TiO_2-NTs	Y400M	W400M	Y525M	W525M	Y525G	W525G
E_{th} (V)	2.11	2.08	2.07	2.09	2.10	2.08	2.08
$b\left(\frac{mV}{dec}\right)$	479	131	93	198	128	242	163
$j_{ph}\left(\frac{\mu A}{cm^2}\right)$	113	61	170	49	140	147	142

to –NHOH, –NO and finally $–NO_2$ as mentioned above. The pendant group with a nitrogen atom is supposed to act as an electron mediator, catalysing the OER reaction in the dark and under irradiation too. The OER four-electron process can be represented by the following equation (7):

$$2H_2O \rightarrow 4e^- + 4H^+ + O_2\uparrow \quad (7)$$

in this process, changes of nitrogen valence from N(–III) theoretically up to N(+V) can serve as the catalytic centre. Possible electron transfer might be illustrated as follows:

$$(C_xN_y) - NH_2 + H_2O \rightarrow (C_xN_y) - NHOH + 2e^- + 2H^+ \quad (8)$$

$$(C_xN_y) - NHOH + H_2O \rightarrow (C_xN_y) - NO_2 + 2e^- + 2H^+ + O_2\uparrow \quad (9)$$

The surface amino groups ($–NH_2$) first oxidized to hydroxylamine (–NHOH) moiety, are regenerated in reaction (8) with simultaneous oxygen evolution. One molecule of water oxidation involves 4 electrons and protons to take part in it. It has been demonstrated that the pendant groups play the most crucial role in the oxygen evolution reaction, making electrocatalysis possible without the need for transition metals' centres. The mechanism of H_2O oxidation via the 4-electron process is indeed intriguing and could play a significant role in understanding the energy conversion process, especially in the context of artificial photosynthesis and solar energy harvesting.

It is very likely that the hydrogen bonding of water molecules with oxygen from the NHOH groups accelerate the water oxidation reaction. Thus, again the highest number of pending amino $–NH_2$ groups undergoing oxidation, allows for better kinetics of oxygen evolution reaction to take place. The slope b from TiO_2-NTs/W400M equals 93 [mV/dec] – the smallest value succeeded for studied heterojunctions, see Table 4 and Figure S5. In the case of White samples content of –OH groups increase due to oxalic acid oxidative activity. Functional hydroxy –OH groups likely promote water oxidation, possibly through hydrogen bond formation with H_2O molecules. The role of functional groups in Yellow and White samples in water splitting is one of the key factors for both

anodic process and cathodic reaction [123]. Hydroxylation of the carbon nitrides in White powder, even if only partial, can explain differences in reaction kinetics measured as polarization curve slope b. All TiO_2-NTs electrodes decorated with White co-catalysts W400M, W525M, and W525G exhibit lower Tafel slopes in comparison with their Yellow precursors Y400M, Y525 M, Y525G recorded in the dark (Table 4).

3.9. LSV under electrodes' illumination

Before the creation of the TiO_2-NTs/CN heterojunction, carbon nitride powders were examined using the methylene blue decolorization test to investigate their photocatalytic properties. It was confirmed that all materials exhibited good properties towards MB decolorization, see Figure S5. Notably, White powders, with their larger energy gaps and strong UV light absorption, exhibited higher photocatalytic activity compared to the Yellow ones. This can be explained by the larger number of terminal hydroxyl groups, which are favourable for the photodegradation process [124–126]. Given these results, a synergistic effect is expected for TiO_2-NTs heterojunctions with CNs, particularly in enhancing their photoelectrocatalytic properties.

One of the ways towards photocatalytic and photoelectrocatalytic response enhancement relies upon Z-type heterojunction formation in which combining two semiconductors of the opposite type of charge carriers is expected to facilitate electron-hole separation. These kinds of Z-scheme band alignments known also as traditional type II heterojunction can be beneficial for the acceleration of both anodic and cathodic photoreactions as it shown for WO_3/C_3N_4 heterojunctions [127]. Another type of photogenerated charges transfer is realized in p-n heterojunction in which carbon nitrides can easily shift photoelectrons from CB (CN) to CB of TiO_2–NTs or CBs of CN (Y, W) are positioned at lower energy. Similarly, holes may be transfered from VB of TiO_2–NTs to VB of CN (Y, W) in p-n heterojunction. However, these transfers are less probable, rather holes stay where they are produced [128,129].

In this study, indirect n-type TiO_2-NTs and p-type carbon nitrides were used as a layer-by-layer heterojunctions as photoanode (Titania nanotubes at the bottom side and CNs as the top ones). The photocurrent is measured at the potential range (Fig. 11), where one would expect not only photoelectrochemical activity of the heterojunction towards water electrooxidation but very likely catalytic redox activity of $-NH_2$/$-NHOH$ centres as described in section 3.7. Although the band positions indicate the possibility of photocurrent increase for TiO_2–NTs /CNs, a significant increase is observed for the composite electrode with Y525G, carbon nitride of high degree of polycondensation. For anatase and carbon, no specific increase was observed, see Fig. 11.

However, White CN are acting positively and the photocurrent is higher for TiO_2–NTs in heterojunction in series: TiO_2 –NTs/W400M > TiO_2 –NTs/W525M > TiO_2 –NTs/W525G. From such observation one may conclude that amount of pending $-NH_2$ groups again is seen to be important for photoelectrocatalytic effects, not only band position and the possible increase in redox activity of heterojunctions. On the other hand, additional activity in the case of

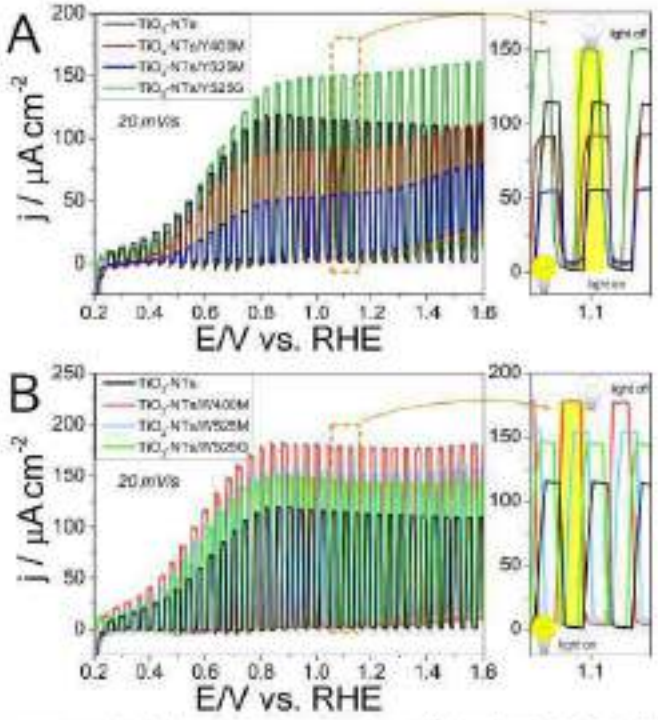

Fig. 11. Linear sweep voltammetry curves obtained under pulse illumination of electrodes comprising heterojunctions TiO_2–NTs/ (A) Yellow carbon nitrides or (B) White carbon nitrides, sweep rate of 20 mV/s.

H_2SO_4 treated CN species may have its origin in the presence of residual sulphur amount. XPS analysis of the presence of sulphur as S(IV) valence species bonded with oxygen. Sulphur (IV) can consume generated holes on Titania under illumination and then oxidized to S(VI) may act as an additional redox centre. These S(IV)/S(VI) centres, chemically attached to planes CN take part in water oxidation and an increase of photocurrent is observed for all White samples. The proposed reaction of photooxidation of water likely involves also sulphur centres as co-catalysts and White species are more active in comparison with Yellow species.

4. Conclusions

The study shows that synthesized transition metal-free co-catalysts are competitive in catalytic properties for anodic water oxidation and photoelectrocatalysis compared to their metal containing counterparts. Studies focus on matching up novel compounds of sulfuric acid modified melamine-derived melem and melon with g-C_3N_4 as reduced overpotential of OER reaction reaches up to 0.04 V for TiO_2NTs modified by White melem. The Tafel slope for TiO_2/W400M is excellent equal to 0.85 mV/dec for TiO_2–NTs/WM400 which is improved in comparison with the sample is including g-C_3N_4.Moreover, the highest photocurrent enhancement is demonstrated for titania modified with acid treated carbon nitrides of lower polycondensation degree melem and melon-like W400M W525M materials. The high crystallinity of these compounds was confirmed through SEM images and XRD studies. The study proposed a mechanism for the synergistic photoanode's activity, discussing it in the context of electronic band positions at 2-scheme heterojunction and the presence of pending chemical groups capable of exhibiting catalytic activity towards the oxygen evolution reaction (OER). Key groups identified include $-NH_2$, $-NHOH$, additional OH groups, or even residuals of S(IV) species, all of which enhance this activity. A mechanism of catalytic H_2O oxidation reaction involving 4-electrons is given and the amino-terminal $-NH_2$ group is proposed to undergo oxidation forming $-NHOH$ moiety in the first stage donating 2-electrons. In the second 2-electron stage $-NHOH$ turns back to the amino group $-NH_2$ with oxygen molecule evolution. Thus, the catalytic centre of the amino group can be successfully regenerated. This mechanism is very likely to take place in the dark and under solar illumination. The mechanism of H_2O oxidation via the 4-electron process using the pending amino group, electronically supported via carbon nitride planes, as a catalytic centre could play a significant role in understanding the energy conversion process, especially in the context of artificial photosynthesis and solar energy harvesting.

The p-type conductivity of semiconducting carbon nitrides has been confirmed for all White and Yellow CNs. Studies have shown that sulphuric acid (VI) modification of carbon nitrides changes the amino substituents according to theoretical calculations and UV-VIS experimental results, leading to improved photoelectrocatalytic and non-light-driven water electrooxidation properties for TiO_2–NTs/CN heterojunctions compared to yellow powders. Additionally, methylene blue decolorization tests indicated that the White powders also exhibited superior performance, up to 98.2 % decolorization of MB. The presented studies have shown that the use of compounds with a lower degree of polycondensation, both White and Yellow, enables improved performance parameters of anodes and photoanodes in the oxygen evolution reaction. This result should encourage the use of melem and melon, especially White melon, instead of g-C_3N_4 carbon nitrides, as they require less energy in high-temperature synthesis processes. In these studies, we demonstrated that less-condensed CN materials, such as melem and melon specially H_2SO_4-treated White derivatives are excellent candidates for photocatalytic and photoelectrocatalytic applications in oxygen evolution reactions and water splitting technologies.

Declaration of generative AI and AI-assisted technologies in the writing process

During the preparation of this work, the authors did not use any AI or AI-assisted technologies. The 'Grammarly' program and ChatGPT were used for English polishing. The authors take full responsibility for the content of the published article.

CRediT authorship contribution statement

Mariusz Wolski: Writing – review & editing, Writing – original draft, Visualization, Methodology, Formal analysis, Data curation, Conceptualization. **Anna Słowierowska:** Writing – review & editing, Writing – original draft, Visualization, Formal analysis, Conceptualization. **Sapojin Ilenganso:** Visualization, Formal analysis, Data curation. **Anna Lisowska-Oleksiak:** Writing – review & editing, Writing – original draft, Visualization, Formal analysis, Conceptualization.

Declaration of competing interest

The authors declare that they have no known competing financial interests or personal relationships that could have appeared to influence the work reported in this paper.

Acknowledgement

Financial support from Gdańsk University of Technology Poland by 17/1/2021/IDUB/III.4c/Tc grant under the Technetium Talent Management Grants program is gratefully acknowledged. We are deeply grateful for the significant contributions to Dr Mateusz Marzec (AGH University of Kraków) for his expertise in XPS analysis, to Professor Anna Zielińska-Jurek and MSc Marta Rosenkiewicz (Gdańsk University of Technology) for their help and provision of XRD and UV-VIS spectroscopy instruments and data collection, and to Dr Grzegorz Gajowiec (Gdańsk University of Technology) for providing the SEM images.

Appendix A. Supplementary data

Supplementary data to this article can be found online at https://doi.org/10.1016/j.apsusc.2024.161999.

Data availability

Data will be made available on request.

References

[1] C. Ding, J. Shi, Z. Wang, C. Li, Photoelectrocatalytic water splitting: significance of cocatalysts, electrolyte, and interfaces, ACS Catal. 7 (2017) 675–688, https://doi.org/10.1021/acscatal.6b02181.

[2] K. Nishiyama, T. Yamada, M. Nakabayashi, Y. Maehara, M. Yamaguchi, Y. Kunisada, H. Taniguchi, Y. Segawa, H. Tokudome, S. Akiyama, T. Watanabe, K. Naruokawa, K. Obazawa, N. Nishiwaki, T. Tokuda, T. Hamasaki, S. Ikeuchi, Photocatalytic solar hydrogen production from water on a 100-m2 scale, Nature 598 (2021) 304–307, https://doi.org/10.1038/s41586-021-03907-3.

[3] M. Barreiro, G.A. Grant, G.I. Lebedev, V. Sadtchenko, C. Sella, J.L. Ware, A. Bard, C. Miranda, L. Degtyarenko, D. Berman, Advances in photo-assisted seawater splitting powered by green ion-cable carbon nitride photoelectrodevices, J. Mater. Chem. A 11 (2023) 21591–21600, https://doi.org/10.1039/D3TA04041C.

[4] J.R. Choi, Modelling of carbon offset networks for process systems to achieve net zero emissions, Computer Aided Chemical Engineering 52 (2024) 1003–1008, https://doi.org/10.1016/B978-0-443-15274-0.50173-6.

[5] S. Hu, Z. Zhang, Y. Zeb, J. Chen, J.W. Shi, The progress of g-C3N4 in photocatalytic H2 evolution: from fabrication to modification, Coord. Chem. Rev. 503 (2024) 215649, https://doi.org/10.1016/j.ccr.2023.215649.

[6] S.F. Rhodewalt, J.L. Fennimore, F. Harders, L.H. Mascaro, Carbon nitrides in photoelectrochemical water splitting: state of the art and perspectives beyond water splitting, ACS Appl. Energy Mater. 7 (2024) 8221–8255, https://doi.org/10.1021/acsaem.4c00855.

[7] A. Fujishima, K. Honda, Electrochemical photolysis of water at a semiconductor electrode, Nature 238 (1972) 37–38, https://doi.org/10.1038/238037a0.

[8] F. Chen, J. Yu, M. Jaroniec, Ab-initio visible 2-electron photocatalysis, adv. Mater. 35 (2014) 4983–4986, https://doi.org/10.1002/adma.201401650.

[9] T. Hu, B. Zhu, B. Cheng, J. Yu, W. Ho, W. Macyk, 2D/2D/0D TiO2/C3N5/TiO2 S-Scheme composite S-scheme photocatalyst with enhanced CO2 reduction activity,

Appl Catal B Environ 272 (2020) 119006. https://doi.org/10.1016/j.apcatb.2020.119006.
[10] H. Sopha, M. Motola, M. Sopčić, J.M. Macak, Recent advances in TiO2 nanotube layers – A mini review of the latest developments in nanotube preparation and applications in photocatalysis and microwave shielding, Nano Select 2 (7–8) (2020) 1309–1340. https://doi.org/10.1002/nano.202000048.
[11] G.D. Sulka, J. Kapusta Kołodziej, A. Brzózka, M. Jaskuła, Fabrication of nanoporous TiO2 by electrochemical oxidation, Electrochim. Acta 55 (2010) 4359–4367. https://doi.org/10.1016/j.electacta.2009.12.055.
[12] Z. Dong, D. Ding, T. Li, C. Ning, Ni-doped TiO2 nanotubes photoanode for enhanced photoelectrochemical water splitting, Appl Surf Sci 443 (2018) 325–332. https://doi.org/10.1016/j.apsusc.2018.03.040.
[13] T. Hirata, L. Wang, R. Hara, P. Schmuki, In situ Cr doped modified TiO2 nanotubes with increased photocurrent response, Electrochim. Acta 332 (2019) 135–142. https://doi.org/10.1016/j.electacta.2019.12.140.
[14] M. Wrobel, M. Sibinski, G. Gojzewski, M. Guzik, E. Jartych, M. Lisowski, A. Lisowska-Oleksiak, Hydrothermal solvothermal modification of titanium dioxide nanotubes towards photocatalytic activity enhancement, Materials 14 (2021) 1507. https://doi.org/10.3390/ma14061507.
[15] X. Wang, H. Maeda, A. Thomas, K. Takanabe, G. Xin, J.M. Carlsson, K. Domen, M. Antonietti, A metal-free polymeric photocatalyst for hydrogen production from water under visible light, Nat. Mater. 8 (2009) 76–80. https://doi.org/10.1038/nmat2317.
[16] D. Bhanderi, P. Lakhani, C.K. Modi, Graphitic carbon nitride (g-C3N4) as an emerging photocatalyst for sustainable environmental applications: a comprehensive review, RSC Sustain. 2 (2024) 265–307. https://doi.org/10.1039/D3SU00306B.
[17] A. Kezia, S. Park, The synthesis and key features of 2D carbon nitride (C3N4) and its CO2 photoreduction, Chem. Eng. J. 485 (2024) 150018. https://doi.org/10.1016/j.cej.2024.150018.
[18] M. Joseph, M. Kumar, S. Sudha, C. Subramaniam, S.N. Sreedhr, A review on the advancements of graphitic carbon nitride based photoelectrodes for photoelectrochemical water splitting, Energy Adv. 3 (2024) 90–98. https://doi.org/10.1039/D3YA00266A.
[19] S.K. Yen, Z.L. Li, J.G. Lee, Wettability/dissolution performance of gC3N4 fabricated by electrolyte bonding solutions, Langmuir 28 (2000) 16697–16701. https://doi.org/10.1021/la3030202.
[20] A. Hafez, K. Dessoki, H.E. Abbasy, A.S. Shawky, N. Kamdeld, Structural, optical, and photocatalytic properties of non-reduced g-C3N4 nanosheets, Appl. Phys. A 130 (2024) 1–9. https://doi.org/10.1007/s00339-023-07065-8.
[21] Y. Liao, S. Zhu, J. Shi, Z. Sun, C. Yin, C. Zou, X. Lou, D. Zhang, Tailoring the morphology of gC3N4 by self-assembly towards high photocatalytic performance, Chem. nrChem. 9 (2014) 3418–3426. https://doi.org/10.1002/chem.201204064.
[22] M. Nasrollahi, A. Pishkenari, P.M. Anbarsooz, High-quality visible light-driven photocatalytic activity of WO3 /g-C3N4 heterostructure catalysts synthesized by a novel corrosive microwave irradiation route, J. Mater. Sci. Mater. Electron. 30 (2019) 3204–3214. https://doi.org/10.1007/s10854-018-00602-6.
[23] T.A. Miller, A.S. Aasyr, T.M. Suter, A. Sella, F. Deiana, P.P. McMillan, Carbon nitrides: synthesis and characterization of a new class of functional semiconductors, PCCP 19 (2017) 15035–15056. https://doi.org/10.1039/C7CP00717D.
[24] B.J. Ng, L.K. Putri, W.C. Chong, S.P. Chai, Breaking boundaries of self-photocatalysis: overcoming limitations of carbon nitride as a single-light absorber for overall water splitting, J. Mater. Chem. A 12 (2024) 21971–24004. https://doi.org/10.1039/D4TA03410F.
[25] T. Nurkolis-Ismo, E. Setiyanpoire, M. Sitra, P. Sujatmikoesiyo, Investigation of the Ag species and synergy of Ag TiO2 and g-C3N3 for the enhancement of photocatalytic activity under UV–Visible light irradiation, Appl. Surf. Sci. 575 (2022) 151615. https://doi.org/10.1016/j.apsusc.2021.151615.
[26] M. Liu, J. Hou, X. Liu, F. Wang, S. Shi, W. Fu, H. Dai, H. Xie, Coupling photocatalytic fuel cell based on S-scheme g-C3N4/TiO2 photoanode with H2O2 activation for p-chloronitrobenzene degradation and simultaneous electricity generation under visible light, Separation and Purification Technology 309 (2023) 123108. https://doi.org/10.1016/j.seppur.2022.123108.
[27] A. Mishra, A. Mehta, S. Basu, N.P. Shetti, K.R. Reddy, T.M. Aminabhavi, Graphitic carbon nitride (g- C3N4)-based metal-free photocatalysts for water splitting: a review, Carbon 149 (2019) 693–721. https://doi.org/10.1016/j.carbon.2019.04.332.
[28] X. Liu, B. Ma, C. Zhuang, B. Hu, J. Chen, X. Liu, X. Wang, Recent developments of doped g-C3N4 photocatalysts for the degradation of organic pollutants, Crit. Rev. Environ. Sci. Technol. 51 (2021) 751–790. https://doi.org/10.1080/10643389.2020.1745405.
[29] C. Marchal, T. Cottineau, M.G. Méndez-Medrano, C. Colbeau-Justin, V. Caps, V. Keller, Au/TiO2–gC3N4 nanocomposites for enhanced photocatalytic H2 production from water under visible light irradiation with very low quantities of sacrificial agents, Adv. Energy Mater. 8 (2018) 1702142. https://doi.org/10.1002/aenm.201702142.
[30] L. Wang, W. Si, Y. Tang, F. Hu, D. Regulacio, J. Hu, T. Lippert, S.X. Liu, J. Liang, Graphitic carbon nitride (g-C3N4)-based nanowell heterojunction nanostructured materials for photoelectrochemical water splitting, Carbon Energy 2 (2020) 229–250. https://doi.org/10.1002/cey2.46.
[31] I. Papailias, T. Giannakopoulou, N. Todorova, D. Demotikali, T. Vaimakis, C. Trapalis, Effect of processing temperature on structure and photocatalytic properties of g-C3N4, Appl. Surf. Sci. 358 (2015) 278–286. https://doi.org/10.1016/j.apsusc.2015.06.047.
[32] X. Liu, Q. Wang, D. Cui, Preparation and photocatalytic properties of g-C3N4/TiO2 hybrid composite, J. Mater. Sci. Technol. 26 (2010) 825–830. https://doi.org/10.1016/S1005-0302(10)60140-1.
[33] S. Dhiravel, J.N. Vishnu, S. Tulsidas Jacob, A. Chinnathambi, M.B. Ronash, K. Sole Mansoor, Photocatalytic activity of zinc oxide nanorods incorporated graphitic carbon nitride catalyst, J. Taiwan Inst. Chem. Eng. (2023) 105002. https://doi.org/10.1016/j.jtice.2023.105002.
[34] S.P. Bhattacharya, H.L.S. Santos, I.F. Teixeira, J.L. Bott-Neto, P.S. Fernandes, G. H. Moreno, Nickel-modified polymeric carbon nitride for improving TiO2-based photoanode photoelectrochemical evaluation and mechanistical insights, Mater. Today Nano 18 (2022) 100190. https://doi.org/10.1016/j.mtnano.2022.100190.
[35] L. He, J. Liu, Y. Liu, B. Cai, B. Hu, M. Wang, S. Tian, T. Song, S. Wu, Z. Zhang, Z. Peng, M. Fu, Titanium dioxide incorporated carbon nitride nanosheets derived from ultrasound mediated organic acid composite as a multifunctional electrocatalyst for hydrogen and oxygen evolution reaction and oxygen reduction reaction, Appl. Catal. B 340 (2024) 123179. https://doi.org/10.1016/j.apcatb.2023.123179.
[36] M. Benelmir, O. Arabeyre Iratni, A. Guesmioui, N. Ouagueni, A. Ouldkaci, C. Mansour, D. Barreau, Tailoring oxygen evolution performance of carbon nitride systems fabricated by electrophoretic through Ag and Au plasma functionalization, Chemical Engineering Journal 448 (2022) 137645. https://doi.org/10.1016/j.cej.2022.137645.
[37] M. Benelmir, O. Arabeyre Iratni, A. Guesmioui, N. Ouagueni, A. Ouldkaci, J. Verbeeck, C. Mansour, D. Barreau, Functionalization of graphitic carbon nitride systems by cobalt and cobalt-iron oxides boosts solar water oxidation performances, Appl. Surf. Sci. 610 (2023) 156082. https://doi.org/10.1016/j.apsusc.2022.156082.
[38] M. Brugia, M. Benelmir, S.A. Rizzi, A. Guesmioui, D. Barreau, O.I. Lebedev, C. Mansour, Graphitic carbon nitride as a promising visible-light-activated support boosting platinum nanoparticle activity in mixed-electrolyte electrolysers, ChemSusChem 17 (2024) e202401491. https://doi.org/10.1002/cssc.202401491.
[39] J. Jia, Y. Song, S. Li, Q. Zhao, S. Quan, G. Chen, Novel phosphorus doped carbon nitride modified TiO2 nanotube arrays with improved photoelectrochemical performance, Nanoscale 7 (2015) 16260–16268. https://doi.org/10.1039/C5NR04301B.
[40] E. Vereshchagina, M. Benelmir, O.A. Rizzi, A. Guesmioui, O.I. Lebedev, D. Barreau, C. Mansour, Graphitic carbon nitride structures on carbon cloth containing silver and cerium dispersed MoO3 for photocatalytic oxygen evolution, ChemSusChem (2024) e202402048. https://doi.org/10.1002/cssc.202402048.
[41] H. Liu, M. Shen, P. Zhou, Z. Guo, S. Liu, W. Yang, M. Guo, M. Chen, H. Guan, N. P. Rutkevov, Y. Yu, X. Dai, X. Sun, Locking modes with conjugated bithiadiazole bonds in donor photocatalytic chlorines of carbon nitride for overall water splitting, Nanoscale 13 (2021) 9311–9321. https://doi.org/10.1039/D1NR01340C.
[42] D. Tang, L.L. Li, G. Shen, S. Zhang, Boosting charge kinetics in metal-free g-C3N4/carbon hybrid photocatalysts for highly efficient visible-light driven hydrogen evolution, Appl. Surf. Sci. 510 (2020) 145340. https://doi.org/10.1016/j.apsusc.2020.145340.
[43] W. Mellaldin, V. Mantzila, J. Fierlinger, P. Pfeiz, M. Rit, J. Semelkova, L. Gembalová, M. Kormunda, E. Pesek, M. Bell, G. Sirbu nanocarbon, Effect of Ag modification on TiO2 and carbon/g-C3N4 composite on photocatalytic performance, Sci. Rep. 12 (2022) 1–20. https://doi.org/10.1038/s41598-022-20844-6.
[44] H. Tavares, E. Amelia, E. Asepogu, Y. Ito, M. Tamura, E. Kwei, Electrolytic oil for enhanced photocatalytic of carbon catalyst with MoO3, Appl. Catal. B 279 (2020) 119368. https://doi.org/10.1016/j.apcatb.2020.119368.
[45] Y. Hou, Q. Dong, F. Yu, L. Wang, Y. Xia, K. Li, M. Hou, Size-tailored synthesis of crystalline carbon nitride nanosheets from nitrogen-rich melon for efficient photocatalytic hydrogen evolution with simultaneous highly selective oxidation of benzyl alcohol, ACS Appl. Mater. Interfaces 14 (2022) 13438–13450. https://doi.org/10.1021/acsami.2c01402.
[46] H. Wilczak, M. Leszczyńska, E. Dziuba, E. Kubica, A study on ingredients in the high-pressure melamine production process, Materials 16 (2023) 5700. https://doi.org/10.3390/ma16165700.
[47] F.S. Rinaldi, Y. Zheng, Z. Schwarz, C. Mesaljuana, W. Schuch, L. Wang, H. J. Snaith, Power-free carbon nitride materials — design strategies for electrochemical devices, Nat. Rev. Mater. 2 (2017) 1–17. https://doi.org/10.1038/natrevmats.2017.45.
[48] S. Dyjak, W. Kiciński, A. Huczko, Thermally driven radiation conversion in CoNiAl-graphitic ternary polymer towards carbonate, large scale synthesis of g-C3N4, J. Mater. Chem. A 3 (2015) 8621–8631. https://doi.org/10.1039/C5TA00861J.
[49] C. Li, J. Li, Y. Wang, J. Liu, M. Ma, E. Liu, C. Shen, Z. Wang, J. Qi, L. Zhang, N. Hou, W. Deng, Y. Wang, Recent developments in heterojunction structure tuning of graphitic carbon nitride for highly efficient photocatalysis, J. Environ. 48 (2022). https://doi.org/10.1016/j.jece.2022.107170.
[50] L. Tang, X. Zeng, L. Jing, S. Kuangyang, Y. Guoliang, L. Gan, H. Jiahong, Y. Dengfu, S. Yuanchun, Proto-triazine rich polymeric sheets of graphitic carbon nitride as a photocatalyst, ACS Omega 3 (2018) 12597–12607. https://pubs.acs.org/doi/10.1021/acsomega.8b01507.
[51] E. Skorlak, H. Schaefe, J. Kaczmarski, J. Ryl, A. Jaszcka-Olekszo, Tricolor nanotubes infiltrated with the conducting polymer PEDOT modified by Prussian blue - a novel type of organic-inorganic heterojunction characterized with

enhanced photoactivity. RSC Adv. 8 (2018) 28028–28036. https://doi.org/10.1039/C8RA05170K.
[50] J. Gu, L. Zhang, B. He, Y. Yan, Chemical exfoliation of graphitic carbon nitride for efficient heterogeneous photocatalysis. J. Mater. Chem. A 1 (38) (2013) 11766–11775. https://doi.org/10.1039/C3TA12005G.
[51] Y. Li, M.Q. Wang, X.J. Ren, S. Jia, M. Xu, D. Long, L. Pu, Tuning and General oxidation graphene-like carbon nitride nanosheets for superior photocatalytic activity, Green. Ind. 42 (2019) 10521–10535. https://doi.org/10.1016/j.CEJA.2019.05.150.
[52] J. Huang, M. Ruan, X. Yan, X. Dai, J. Ruhlich, F. Abdin, B. González, S. Barlim, H. Lund, N. Steinfeldt, T. Peppel, A.A. Siegfried, H. Jiao, J. Strunk, Fabricated polymeric carbon nitride nanosheets for photocatalytic applications, ACS Appl. Nano Mater. 7 (2024) 7462–7482. https://doi.org/10.1021/acsanm.4c00135.
[53] LPR 3.0 – LPR19 RSV/RS/XXI/19/1, https://portal.gov.pl/wp-content/uploads/2019/09/LPR-3.0-LPR19-RSV-RS-XXI-19-1-ogloszenie-konkursowe.pdf (accessed October 31, 2024).
[54] J. Ang, J. Chen, C. Feng, H. Jia, J. Sun, Transforming g-C3N4 from amphoteric to n-type semiconductor: the impact and role of protrude defect passivation in photocatalytic molecular oxygen activation, J. Alloys Compd. 850 (2021) 156658. https://doi.org/10.1016/J.JALLCOM.2020.156658.
[55] Chemcraft, Graphical software for visualization of quantum chemistry computations. Version 1.8 build 682, https://chemcraftprog.com/index.html (accessed August 6, 2024).
[56] A.J. Bard/series, G.A. Ragsdale, S.E. Feldberger, Progress in electroactive research, Nova Science Publishers, New York, 2005, pp. 89–103, accessed November 7, 2024 (accessed November 7, 2024). http://www.loc.gov/catdir/toc/fy0703/2006933611.html.
[57] B. Jürgens, E. Irran, J. Senker, P. Kroll, H. Müller, W. Schnick, Melem (2,5,8-triamino-tri-s-triazine), an important intermediate during condensation of melamine rings to graphitic carbon nitride: synthesis, structure determination by x-ray powder diffractometry, solid-state NMR, and theoretical studies, J. Am. Chem. Soc. 125 (2003) 10288–10300. https://doi.org/10.1021/JA034708N.
[58] T. Kouzuma, The first synthesis and characterization of cyanuric high polymers, Macromol. Chem. Phys. 202 (2001) 19–25. https://doi.org/10.1002/1521-3935(20010101)202:1<19::AID-MACP19>3.0.CO;2-C.
[59] J. Zhang, X. Chen, K. Takanabe, K. Maeda, K. Domen, J.D. Epping, X. Fu, M. Antonietti, X. Wang, Synthesis of a carbon nitride structure for visible-light catalysis by copolymerization, Angew. Chem. 49 (2010) 441–444. https://doi.org/10.1002/anie.200905968.
[60] T. Wang, X. Chen, J. Thomas, X. Fu, M. Antonietti, Metal-containing carbon nitride compounds: a new functional organic-metal hybrid material, Adv. Mater. 21 (2009) 1609–1612. https://doi.org/10.1002/adma.200803222.
[61] L. Zhang, H. Liu, J. Duan, X. Chen, X. Guo, F. Zhao, T. Sun, S. Shi, Metal-free g-C3N4 photocatalyst by cellulose acid assistance for selective aerobic oxidation of benzyl alcohol under visible light, Mater. Res. Bull. 59 (2014) 64–70. https://doi.org/10.1016/j.materresbull.2014.06.023.
[62] L. Lei, W. Wang, Y. Huang, J. Li, R. Bosque-Valles, H. Wang, Q. Li, H. Fu, Tailoring chemical structure and intermolecular interaction of carbon intermediates for highly efficient photocatalytic hydrogen evolution of g-C3N3, Appl. Surf. Sci. 503 (2020) 144104. https://doi.org/10.1016/J.APSUSC.2019.144104.
[63] B. Sirota, S.A. Miller, Mellamine and derivatives of cyclotriaz, Chem. Rev. 58 (1958) 351–372. https://doi.org/10.1021/cr50020a004.
[64] C. Jia, B. Kirkland, J. Xiaoteer, D. Bhowal, R. Dwaraki, T. Jacob, Structure and spectral properties of polymeric carbon nitrides from symmetric triazine, Chem. Mater. 33 (2021) 1547–1556. https://doi.org/10.1021/acs.chemmater.0c03745.
[65] J. Liebig, Ueber einige Stickstoffverbindungen, Annalen der Physik. 110 (1834) 339–415. https://doi.org/10.1002/ANDP.18341100303.
[66] E.C. Franklin, The ammono carbonic acids, J. Am. Chem. Soc. 44 (1922) 486–509. https://doi.org/10.1021/ja01424a009.
[67] C.E. Redemann, H.J. Lucas, Some derivatives of cyanuric acid and probable structure of melam, melam and melon, J. Am. Chem. Soc. 62 (1940) 842–846. https://doi.org/10.1021/ja01861a030.
[68] T. Ota, H. Kiuchi, M. Shiozaki, Y. Miyake, H. Ishii, Y.S.A. Tetsuro, K. Kimi, Growth and characterization of melem hydrate crystals with hydrogen bonded honeycomb network, Phys. chem. Chem. Phys. 24 (2022) 13982, https://doi.org/10.1039/D2CP00644A.
[69] Y. Miyake, G. Sato, K. Matsumoto, N. Tsuboi, K. Kimi, Synthesis of carbon nitride oligomer as a precursor of melem with improved fluorescence quantum yield, Mater. Adv. 2 (2021) 4000–4005. https://doi.org/10.1039/D1MA00275C.
[70] T. Tyborski, C. Merschjann, S. Orthmann, F. Yang, M.-C. Lux-Steiner, T. Schedel-Niedrig, Crystal structure of polymeric carbon nitride and the determination of its process-dependent structural modifications, J. Phys. Condens. Matter 25 (2013) 395402. https://doi.org/10.1088/0953-8984/25/39/395402.
[71] C. Merschjann, S. Tyborski, T. Tyborski, K. Kailasam, S. Orthmann, D. Hollmann, T. Schedel-Niedrig, A. Thomas, S. Lochbrunner, Geminate recombination in polymeric carbon nitrides, Adv. Mater. 46 (2015) 7992, https://doi.org/10.1002/adma.201503992.
[72] F. Yan, S.K. Cullen, D.M. Collins, J.T.S. Irvine, Structural investigation of graphitic carbon nitride via XRD and neutron diffraction, Chem. Mater. 27 (2015) 2612–2618. https://doi.org/10.1021/acs.chemmater.5b00451.
[73] A. Dontsov, T. Arkhipova, I. Ramanathan, S. Ramakrishnan, Quantitative and real-time structural dynamics of graphitic carbon nitride nanostructures: enhanced photocatalytic activity and electrochemical hydrogen production, ACS Omega 4 (2019) 9478–9485. https://doi.org/10.1021/ACSOMEGA.9B00374.
[74] S. Matsumoto, E.Q. Xie, F. Izumi, On the validity of the formation of crystalline carbon nitrides, C3N4, Diamond Relat. Mater. 1 (1992) 1175–1182. https://doi.org/10.1016/0925-9635(92)90063-X.
[75] D. Negru, F. Gaiseru, S. Cosmin, Combined DFT/IR computational and experimental studies on g-C3N5: new insight into structure optical, and vibrational properties, Molecules 15 (2021) 4549, https://doi.org/10.3390/ma14164549.
[76] H. Wang, X. Zhang, J. Xie, J. Zhang, P. Ma, B. Pan, Y. Xie, Structural distortion in graphitic-C3N4 realizing an efficient photoreactivity, Nanoscale 7 (2015) 5132–5136. https://doi.org/10.1039/C4NR07454A.
[77] S. Wang, Y. Yang, S. Wang, X. Wang, Defected carbon nitride nanosheets with activated n → π* transition and polarized internal properties for photocatalytic CO2 reduction, J. Catal. 402 (2021) 366–376. https://doi.org/10.1016/J.JCAT.2021.10.010.
[78] S. Wierzbicka, M. Kobiela, T. Tylus, M. Szkoda, Comparative studies of g-C3N4 and C3N3S2 organic semiconductors—synthesis properties, and application in the catalysis oxygen reduction, Molecules 28 (2023) 2468, https://doi.org/10.3390/molecules28062468.
[79] T. Xiong, W. Cen, Y. Zhang, F. Dong, Bridging the g-C3N4 interlayer for enhanced photoreactivity, ACS Catal. 6 (2016) 2462–2472. https://doi.org/10.1021/acscatal.5b02650.
[80] Y. Chen, Y. Ying, W. Weiwei, L. Weihua, D. Weilin, J. TingTing, Y. Shichai, Y. Yinyhong, Preparation of g-C3N4 and its temperature-sensing properties, J. Mater. Sci. Mater. Electron. 33 (2022) 4790–4799. https://doi.org/10.1007/s10854-021-07664-z.
[81] X. Zhang, H. Liao, X. Li, R. Shang, Y. Zhu, Y. Zhou, Graphitic carbon nitride nanosheets made by different methods as electrode material for supercapacitors, ionics 28 (2022) 1–9. https://doi.org/10.1007/s11581-021-04199-2.
[82] R. Wang, S. Song, Q. Zhang, Y. Jin, Q. Zhang, Selection of protonated g-C3N4 nanosheets as promising proton conductive materials, Chem. Commun. 55 (2019) 7414. https://doi.org/10.1039/C9CC03237H.
[83] L. Encinacorta, S.A. Korili, A. Gil, J.M. López-de-Luzuriaga, M. Monge, Effect of gold nanoparticles on SiO2/g-C3N4 catalyst for the degradation of nanofilic, Appl. Surf. Sci. 573 (2022) 151586. https://doi.org/10.1016/J.APSUSC.2021.151586.
[84] H. Deiseroad, G.I.N. Waterhouse, A. Beniac-Brown, K.T.C. Ingham, J. Thompson, G. V. Sim, High-resolution XPS of organic polymers: the scienta ESCA300 database (Beamer, G., Briggs, D.), J. Chem. Educ. 70 (1993) 825. https://doi.org/10.1021/ED070P825.5.
[85] L. Du, B. Cao, S. Xu, Q. Su, Strong ferromagnetism of g-C3N4 achieved by atomic modulation, Nat. Commun. 14 (2023) 1–8. https://doi.org/10.1038/s41467-023-36116-2.
[86] X. Chen, X. Wang, G. Fang, A review on C1s XPS-spectra for some kinds of carbon materials, Fullerenes, Nanotubes and Carbon Nanostruct. 23 (2015) 1005–1052. https://doi.org/10.1080/1536383X.2015.1079402.
[87] V.W.H. Lau, C.T. Au, B. Paul Wijaya, M. Lotsch, Gan X-ray photoelectron spectroscopy characterize photocatalytically relevant defects in graphitic carbon nitride? re-examining peak assignment and quantification using model compounds, Chem. Mater. 33 (2021) 9762–9774. https://doi.org/10.1021/acs.chemmater.1c03910.
[88] J.C. Ying, J.F. chen, Arranged for highly efficient photocatalytic degradation, ads 10 (2019) 106, https://doi.org/10.1186/s13068-017-0793-1.
[89] S. Hellgren, R.T. Hamish, S. Johnels, L. Hedman, J. Penny, Interpretation of X-ray photoelectron spectra of carborundum like films: New insights from in situ XPS, Carbon 130 (2018) 842–850, https://doi.org/10.1016/J.CARBON.2018.01.017.
[90] D.D. Rondon, M.J. Stout, XPS analysis of thin organic systems, Surf. Interface Anal. 43 (2011) 1463–1470. https://doi.org/10.1002/sia.3551.
[91] W. Lee, R. Wang, I. Zhou, H. Hsu, Efficiently photocatalytic activities of novel metal free g-C3N4 under simulated solar irradiation removal efficiency, influence factors, and reaction mechanism, Water Air Soil Pollut. 225 (2014) 1–15. https://doi.org/10.1007/s11270-013-2180-y.
[92] C.D. Wagner, C.J. Powell, J.W. Allison, J.R. Rumble, NIST X-ray Photoelectron Spectroscopy Database 1, Version 5 (1991). https://www.nist.gov/publications/nist-x-ray-photoelectron-spectroscopy-database-1-version-2 (accessed June 27, 2024).
[93] A.A. Yadav, S.W. Kang, Y.M. Hunge, Photocatalytic degradation of Rhodamine B using graphitic carbon nitride photocatalyst, J. Mater. Sci. Mater. Electron. 32 (2021) 19577–19585. https://doi.org/10.1007/s10854-021-06466-y.
[94] M.C. Biesinger, L.W.M. Lau, A.R. Gerson, R.St.C. Smart, Resolving surface chemical states in XPS analysis of first row transition metals, oxides and hydroxides: Sc, Ti, V, Cu and Zn, Appl. Surf. Sci. 257 (2010) 887–898. https://doi.org/10.1016/J.APSUSC.2010.07.086.
[95] V.B. Cist, Handbook of Monochromatic XPS Spectra, Volume 1 - The Elements and Native Oxides, XPS international, LLC, 1999. https://www.researchgate.net/publication/313218018_Handbook_of_Monochromatic_XPS_Spectra (accessed June 27, 2024).
[96] R. Kurtaran, D. Ensari, D. Avcı, A. Ekinci, A. Ricci, Explosives XPS for the classification of nitrites and polynitrites, RSC Adv. 4 (2014) 7898–7906. https://doi.org/10.1039/C3RA47198C.
[97] B. Zhu, P. Xia, W. Ho, J. Yu, Isoelectric point and adsorption activity of porous g-C3N4, Appl. Surf. Sci. 344 (2015) 188–195, https://doi.org/10.1016/J.APSUSC.2015.03.064.
[100] J. Wen, J. Xie, X. Chen, X. Li, A review on g-C3N4-based photocatalysts, Appl. Surf. Sci. 391 (2017) 72–123. https://doi.org/10.1016/J.APSUSC.2016.07.030.

[101] J. Wang, S. Wang, A critical review on graphitic carbon nitride (g-C3N4)-based materials: preparation, modification and environmental application, Coord. Chem. Rev. 453 (2022) 214338, https://doi.org/10.1016/j.ccr.2021.214338.
[102] E. Coy, Mimoun, Ha, Dudchak, P. Gluchowski, O. Tynkevych, M. Pinková, A. Piątkowska, K. Siuzdak, A. Zhelkubich-Jurek, Heterojunction of (N, F) co-doped C3N4 and 2D TiO2 for improved sonocatalysis and environmental photocatalytic degradation, Surf. Interfaces 31 (2022) 102030, https://doi.org/10.1016/j.surfin.2022.102030.
[103] M. Wudzki, M. Szkoda, O. Gajkowski, K. Antoń, G. Trykowski, A. Lisowska-Oleksiak, Hydrothermal modification of TiO2 nanotubes in water soft alkali metal electrolytes (LiNO3, NaNO3, KNO3) – Direct evidence for photocatalytic activity enhancement, Electrochim. Acta 436 (2022) 141482, https://doi.org/10.1016/j.electacta.2022.141482.
[104] J. Su, G. Zhang, N. Li, Z. Huang, X. Wang, Y. Han, J. Hou, F. Jiang, S. Guo, Self-supporting 3D carbon nitride with reactive n → π* electronic transition for enhanced solar hydrogen production, Adv. Mater. 33 (2021) 2100–4361, https://doi.org/10.1002/adma.202104361.
[105] Z. Nemat, Ghe P.H. Hamnia, J.M. Rueff, J. Fraxedas, Adjusting CO2 interaction of chitosan by functional group engineering, ChemistryOpen 13 (2024) e202400093, https://doi.org/10.1002/open.202400093.
[106] A.D. Becke, Density-functional thermochemistry. III. The role of exact exchange, J. Chem. Phys. 98 (1993) 5648–5652, https://doi.org/10.1063/1.464913.
[107] P.J. Stephens, F.J. Devlin, C.F. Chabalowski, M.J. Frisch, Ab initio calculation of vibrational absorption and circular dichroism spectra using density functional force fields, J. Phys. Chem. 98 (1994) 11623–11627, https://doi.org/10.1021/j100096a001.
[108] C. Lee, W. Yang, R.G. Parr, Development of the Colle-Salvetti correlation-energy formula into a functional of the electron density, Phys. Rev. B Condens Matter 37 (1988) 785–789, https://doi.org/10.1103/PhysRevB.37.785.
[109] J.E. Peralta, J. Wilt, M. Strain, Accurate spin-dependent electron liquid correlation energies for local spin density calculations: a critical analysis, Can. J. Phys. 58 (1980) 1326–1337, https://doi.org/10.1139/p80-198.
[110] R.J. Harrison, T.H. Dunning, Fluorine affinities of the first-row atoms revisited. systematic basis sets and wave functions, J. Chem. Phys. 94 (1991) 6196–6206, https://doi.org/10.1063/1.460364.
[111] T.H. Dunning, Gaussian basis sets for use in correlated molecular calculations. I. The atoms boron through neon and hydrogen, J. Chem. Phys. 90 (1989) 1007–1023, https://doi.org/10.1063/1.456153.
[112] J.M.F. M. J. Frisch, G. W. Trucks, H. B. Schlegel, G. E. Scuseria, M. A. Robb, J. R. Cheeseman, G. Scalmani, V. Barone, G. A. Petersson, H. Nakatsuji, X. M. M. Caricato, A. V. Marenich, J. Bloino, B. G. Janesko, R. Gomperts, B. Mennucci, H. P. Hratchian, J. V., D.J. Fox, Gaussian 16, Revision C.01, Gaussian, Inc., Wallingford CT (2016).
[113] P. Vidossich, M. Fiorin, M. Alfonso-Prieto, J.M. Carbó, J.M. Poblet, C. Rovira, How reliable are DFT predictions of the oxidative power of metal-oxo species? A performance test on a case study of H-abstraction reactivity by chromium-oxo species and their peroxido precursors, J. Phys. Chem. Lett. 1 (2010) 1017–1021, https://doi.org/10.1021/jz100128h.
[114] M. Sachanidou, E. Kougoulos, E. Dracopoulos, D. Tsoutsouva, Reducing the energy band gap of cobalt hydroxide nanosheets with silver atoms and enhancing their electrical conductivity with silver nanoparticles, ACS Omega 8 (2023) 20084–20091, https://doi.org/10.1021/acsomega.3c01802.
[115] F. Valle-Pérez-Noriega, M. García-Belinchón, I. Mora-Seró, J. Bisquert, Characterization of nanostructured hybrid and organic solar cells by impedance spectroscopy, PCCP 13 (2011) 9083–9118, https://doi.org/10.1039/C0CP02984K.
[116] S.M. Yu, E.E. Ng, Physics of semiconductor devices, Wiley, 2006, 53–0471143235.
[117] A. Lasia, Electrochemical impedance spectroscopy and its applications, Springer, 2014, 10.1007/978-1-4614-8933-7.
[118] D. Selvakumar, D.G. Ghugal, R.D. Tanwar, M. Ramanuj, Extended P-conjugated n-type hexazine-mixed graphitic carbon nitride for photodegradation and charge storage applications, Sci. Rep. 9 (2019) 1–12, https://doi.org/10.1038/s41598-019-43515-0.
[119] M.J. Ong, S.L. Tan, Y.H. Ng, S.T. Tung, S.P. Chai, Graphitic carbon nitride (g-C3N4)-based photocatalysts for artificial photosynthesis and environmental remediation: are we a step closer to achieving sustainability? Chem. Rev. 118 (2018) 7108–7329, https://doi.org/10.1021/acs.chemrev.8b00705.
[120] C. Hu, D. Li, R. Liu, R. Xu, S. Sohni, S. Tung, S. Lei, J. Tang, M. Pan, Z. Huang, T. Smith, Direct Z-scheme construction of g-C3N4 quantum dots / TiO2 nanotube for efficient photocatalysis, Chem. Eng. J. 430 (2022) 132886, https://doi.org/10.1016/j.cej.2021.132886.
[121] P. Zoltowski, On the theory of capacitance of layers not exhibiting constant phase element behaviour, J. Electroanal. Chem. Interfacial Electrochem. 443 (1998) 149–154, https://doi.org/10.1016/S0022-0728(97)00567-7.
[122] G.J. Brug, A.L.G. van der Eeden, M. Sluyters-Rehbach, J.H. Sluyters, The analysis of electrode impedances complicated by the presence of a constant phase element, J. Electroanal. Chem. Interfacial Electrochem. 176 (1984) 275–295, https://doi.org/10.1016/S0022-0728(84)80383-9.
[123] J. Feng, G. Liu, S. Yuan, T. Ma, Influence of functional groups on water splitting in carbon nanotube/graphitic carbon nitride composites: a theoretical mechanism study, Phys. Chem. Chem. Phys. 19 (2017) 9997–10003, https://doi.org/10.1039/C6CP08225B.
[124] I. Khan, K. Saeed, I. Zekker, B. Zhang, A.H. Hendi, A. Ahmad, N. Ahmad, N. Zaib, H. Ahmad, I.A. Shah, F. Shah, I. Khan, Review on methylene blue: its properties, uses, toxicity and photodegradation, Water 14 (2022) 242, https://doi.org/10.3390/w14020242.
[125] M.I. Din, R. Khalid, J. Najeeb, Z. Hussain, Fundamentals and photocatalysis of methylene blue dye using various nanoparticles: a critical review, J. Chin. Pract. (4) (2021) 104847, https://doi.org/10.1016/j.jclepro.2021.126847.
[126] V. Nosaka, A. Nosaka, Understanding hydroxyl radical (•OH) generation processes in photocatalysis, ACS Energy Lett. 1 (2016) 356–359, https://doi.org/10.1021/acsenergylett.6b00174.
[127] Z. Song, Q. Chen, T. Sun, K. Cheng, Z. Xie, Q. Kang, Constructing Z-scheme WO3/C3N4 heterojunction with an enhanced internal electric field and accelerated water oxidation kinetics for robust CO2 photoreduction, J. Mater. Chem. A 12 (2024) 14436–14450, https://doi.org/10.1039/D4TA01994A.
[128] J. Yan, H. Wu, H. Chen, Y. Zhang, F. Zhang, S.F. Liu, Fabrication of TiO2/C3N4 heterojunction for enhanced photocatalytic Z-scheme overall water splitting, Appl. Catal. B. 191 (2016) 134–137, https://doi.org/10.1016/j.apcatb.2016.03.030.
[129] Y. Zhang, S. Pan, J. Pang, Z. Guo, Enclosed TiO2/g-C3N4 composites prepared by hydrothermal-assisted thermal polymerization with enhanced visible light photocatalytic activity, Res. Chem. Intermed. 47 (2021) 1969–1983, https://doi.org/10.1007/s11164-020-04378-0.

VI.3 Supplementary Information

SUPPLEMENTARY INFORMATION

Exploring the role of carbon nitrides (melem, melon, g-C_3N_4) in enhancing photoelectrocatalytic properties of TiO_2 nanotubes for water electrooxidation

Mariusz Wtulich*, Anna Skwierawska, Sapajan Ibragimov, Anna Lisowska-Oleksiak*

Faculty of Chemistry, Department of Chemistry and Technology of Functional Materials, Gdańsk University of Technology, Narutowicza 11/12, 80–233 Gdańsk, Poland
*corresponding authors: mariusz.wtulich@pg.edu.pl, alo@pg.edu.pl

Keywords: TiO_2 nanotubes, carbon nitrides, melem, melon, g-C_3N_4, water splitting

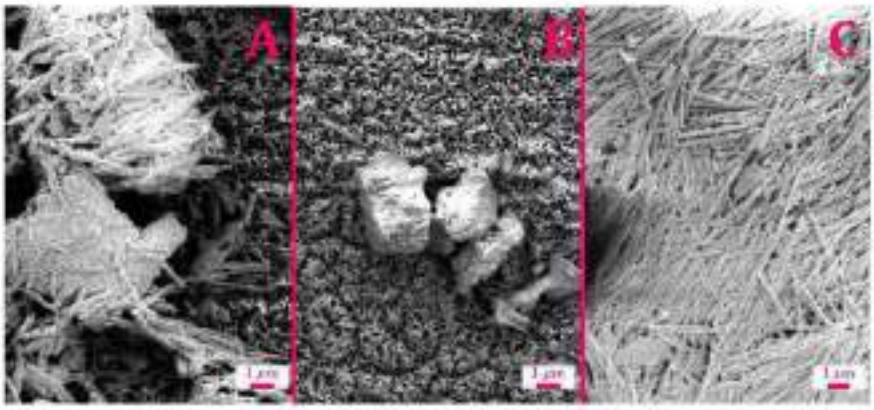

Figure S1. SEM images for (A) TiO_2-NTs/Y400M, (B) TiO_2-NTs/Y525M and (C) TiO_2-NTs/Y525G.

Table S1. Surface composition (atomic %) determined by fitting XPS spectra for all analyzed samples.

	C				N			O		S
Binding energy [eV]	285.0	286.4	288.5	294.2	399.0	400.1	401.5	531.4	532.8	168.5
Compounds / Bonds	C-C C=C	C-N C-O	N-C=N	shake-up	C-N=C	N-C_3	C-NH	O=C O-S	O-C -OH O-S	SO_4^{2-}
Melem Yellow	12.0	1.4	29.7	1.1	32.3	6.4	4.4	0.2	6.6	0.0
Melem White	17.7	1.5	24.7	0.4	24.2	9.7	4.2	1.3	9.6	0.6
Melon Yellow	12.7	1.7	28.6	1.0	32.0	5.6	4.2	0.2	6.8	0.0
Melon White	15.1	1.3	27.1	0.4	27.6	8.4	4.0	1.2	8.3	0.4
g-C_3N_4 White	4.2	1.6	34.7	1.5	43.8	7.1	5.5	1.3	0.3	0.0
g-C_3N_4 Yellow	4.2	2.4	26.1	5.4	32.8	13.5	7.5	5.9	1.6	0.6

1

-

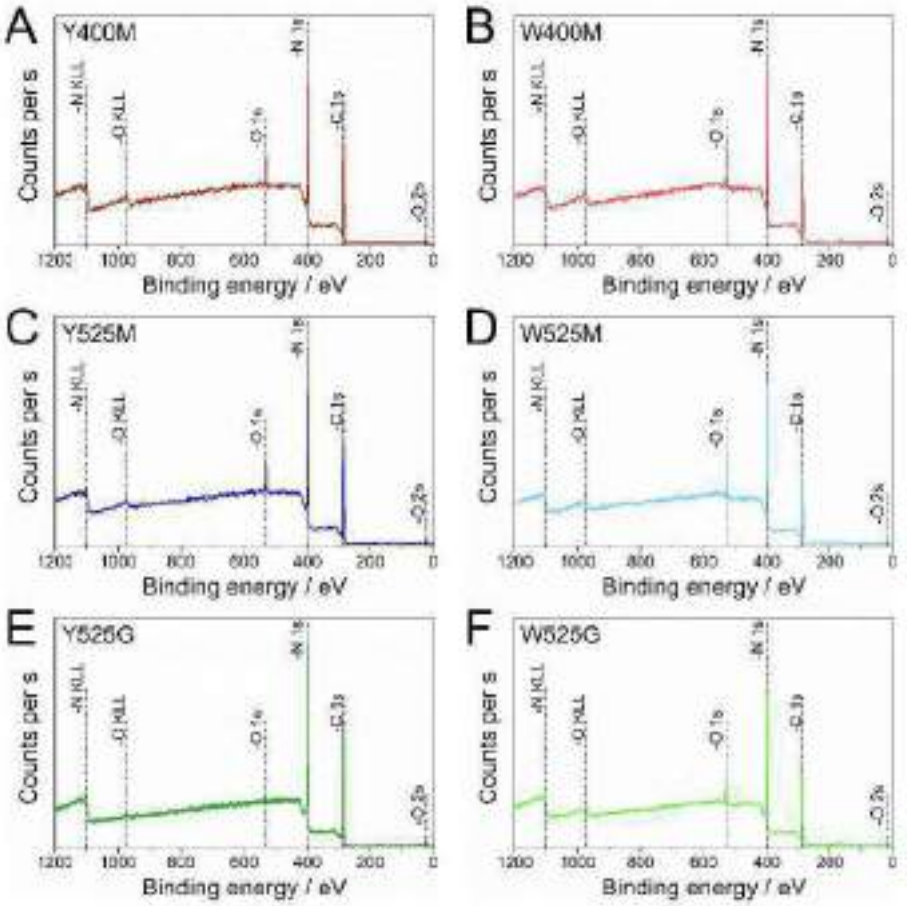

Figure S2. Deconvolution of carbons 1s, nitrogen 1s, oxygen 1s, sulphur 2p and silicon 2p peaks in the XPS spectra of melem yellow (Y400M).

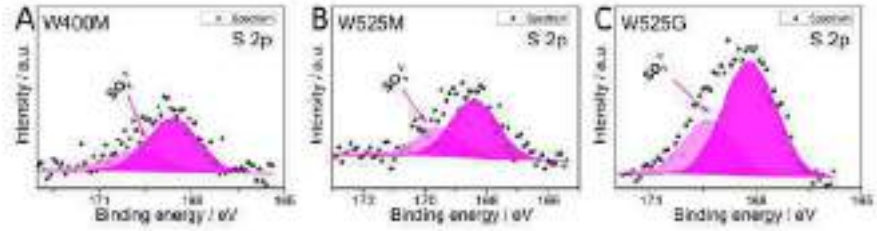

Figure S3. Deconvolution of S 2p peak in the XPS spectra of (A) White melem, (B) melon and (C) g-C_3N_4.

2

Table S2. FTIR spectra analysis. Different vibration signals of carbon nitride powders (Y400M, W400M, Y525M, W525M, Y525G, W525G).

Y400M		W400M		
Wavenumber (cm^{-1})	Band type	Wavenumber (cm^{-1})	Band type	references
3470	ν(N-H, OH)		ν(N-H, OH)	[1–11]
3424		3264		
3251				
3074		3070		
2810		2825		
2127	ν(C=N=O)	2120	ν(C=N=O)	
1744	ν(O-NH-O)	1756	ν(O-NH-O)	
1593	ν(C–N/C=N) heterocyclic skeletons	1596	ν(C–N/C=N) heterocyclic skeletons	
1444		1437		
1393		1398		
1311		1306		
1227		1252		
1199		1150		
1072	Si–O–Si asym-metric stretching	1079	Si–O–Si asym-metric stretching	
977	Si–OH	972	Si–OH	
886	γ(heptazine unit)	882	γ(heptazine unit)	
793	γ(heptazine unit) Si–O symmetric stretching	789	γ(heptazine unit) Si–O symmetric stretching	
		580	SO_3 umbrella	
448	Si–O–Si bending	459	Si–O–Si bending -O-S=O scissor	
Y525M		W525M		
Wavenumber (cm^{-1})	Band type	Wavenumber (cm^{-1})	Band type	
3240	ν(N-H, OH)	3293	ν(N-H, OH)	
3152		3076		
3078		2810		
2123	ν(C=N=O)	2120	ν(C=N=O)	
1625	ν(C–N/C=N) heterocyclic skeletons	1600	ν(C–N/C=N) heterocyclic skeletons	
1537		1455		
1455		1399		
1392		1314		
1227		1235		
1201		1202		
1130		1147		
1069		1081		
1008		973		
888	γ(heptazine unit)	890	γ(heptazine unit)	
802		790		
691		693		
641		577		
580		490		
560		444	Si–O–Si bending	

3

			-O-S=O scissor
493			
Y525G		W525G	
Wavenumber (cm^{-1})	Band type	Wavenumber (cm^{-1})	Band type
3238	ν(N-H, OH)	3264	ν(N-H, OH)
3146		3066	
3070		2828	
2980			
2124	ν(C=N=O)	2127	ν(C=N=O)
1748	ν(O-NH-O)	1753	ν(O-NH-O)
1624	ν(C=N/C=N) heterocyclic skeletons	1597	ν(C=N/C=N) heterocyclic skeletons
1533			
1450		1444	
1389			
1312		1310	
1227		1243	
1200		1150	
1129			
1071		1081	
888	γ(heptazine unit)	978	
801		888	γ(heptazine unit)
725		791	
691		703	
644			
583		586	
460		459	

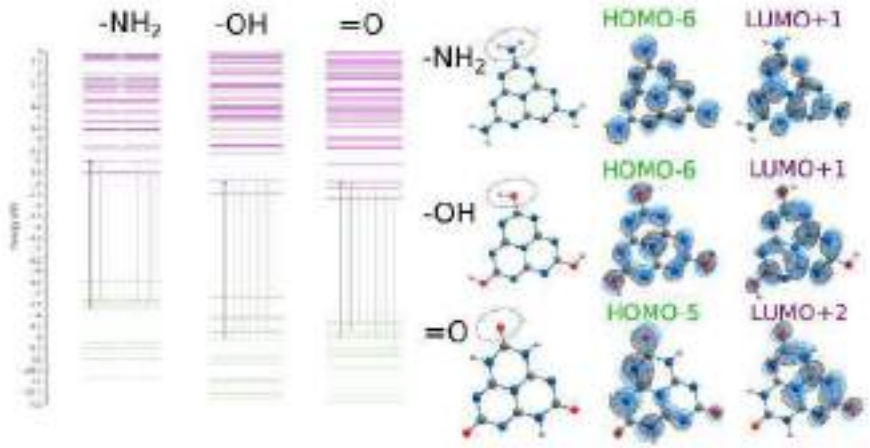

Figure 54. Results for the most probable electron transition, computer-calculated energy diagrams for melem with different terminal groups ($-NH_2$, -OH, =O) and molecular orbitals.

4

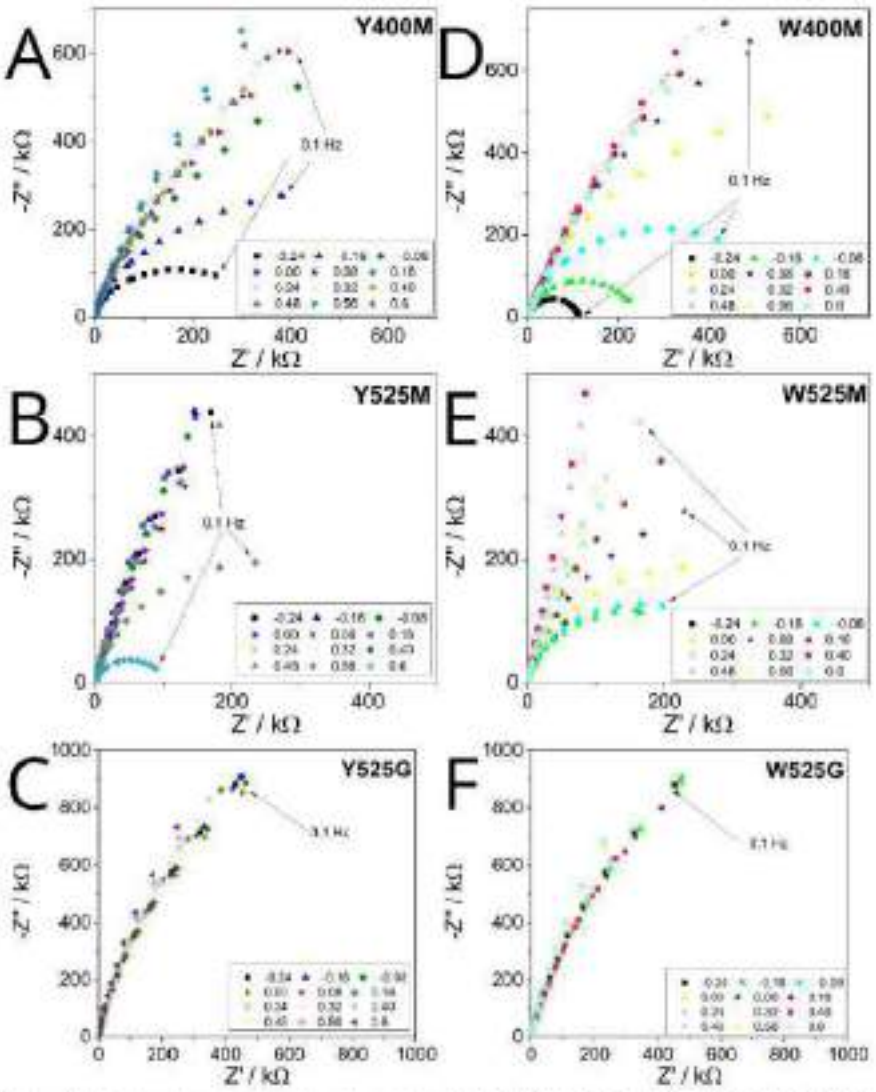

Figure S5. Complex plane impedance for carbon nitrides (Y400M, W400M, Y525M, W525M, Y525G, W525G) deposited onto platinum disc electrode in the frequency range 20 kHz to 0.1 Hz.

The impedance function was fitted with a chi-squared (χ^2) value on the order of 10^{-4} to 10^{-3}. The percentage error in the calculated circuit parameter values remained below 6%, with the highest error observed in the R_2 parameter. For the (Q, n) parameters characterizing the

5

constant phase element (CPE), the error was consistently under 1%, which is essential for accurate capacitance evaluation via Brug's function. The results following the fitting process are presented in Tables S3–S8.

Table S3. Obtained values of R_s, CPE$_1$ (Q_1,n_1) and CPE$_2$ (Q_2,n_2) for the proposed electrical circuit for W400M.

E / V	R_s / Ω	R_1 / Ω	R_2 / Ω	Q_1	n_1	Q_2	n_2
0.44	2.58E+02	3.69E+06	2.62E+03	1.89E-06	8.02E-01	4.42E-06	1.00E+00
0.4	2.59E+02	3.91E+06	2.89E+03	1.82E-06	8.05E-01	4.27E-06	1.00E+00
0.36	2.59E+02	3.90E+06	2.89E+03	1.74E-06	8.08E-01	4.23E-06	1.00E+00
0.32	2.60E+02	3.64E+06	3.00E+03	1.67E-06	8.11E-01	4.15E-06	1.00E+00
0.28	2.59E+02	3.38E+06	2.77E+03	1.61E-06	8.12E-01	4.18E-06	1.00E+00
0.24	2.59E+02	3.15E+06	3.00E+03	1.54E-06	8.15E-01	4.07E-06	1.00E+00
0.2	2.60E+02	3.05E+06	2.58E+03	1.50E-06	8.16E-01	4.01E-06	1.00E+00
0.16	2.60E+02	2.85E+06	2.35E+03	1.45E-06	8.19E-01	3.88E-06	1.00E+00
0.12	2.61E+02	2.47E+06	2.07E+03	1.40E-06	8.21E-01	3.85E-06	1.00E+00
0.08	2.61E+02	2.19E+06	2.22E+03	1.40E-06	8.21E-01	3.66E-06	1.00E+00
0.04	2.60E+02	1.76E+06	2.23E+03	1.39E-06	8.23E-01	2.86E-06	1.00E+00

Table S4. Obtained values of R_s, CPE$_1$ (Q_1,n_1) and CPE$_2$ (Q_2,n_2) for the proposed electrical circuit for W525M.

E / V	R_s / Ω	R_1 / Ω	R_2 / Ω	Q_1	n_1	Q_2	n_2
0.44	1.45E+02	9.95E+08	1.51E+02	3.32E-06	8.89E-01	4.07E-06	1.00E+00
0.4	1.45E+02	1.70E+07	1.50E+02	3.20E-06	8.94E-01	3.89E-06	1.00E+00
0.36	1.45E+02	1.56E+07	1.45E+02	3.12E-06	8.97E-01	3.98E-06	1.00E+00
0.32	1.44E+02	6.70E+06	1.38E+02	3.08E-06	8.97E-01	4.14E-06	1.00E+00
0.28	1.44E+02	3.49E+06	1.26E+02	3.08E-06	8.94E-01	4.47E-06	1.00E+00
0.24	1.43E+02	2.22E+06	1.18E+02	3.15E-06	8.89E-01	4.80E-06	1.00E+00
0.2	1.43E+02	1.56E+06	1.04E+02	3.22E-06	8.82E-01	5.25E-06	1.00E+00
0.16	1.43E+02	1.23E+06	1.00E+02	3.20E-06	8.80E-01	5.38E-06	1.00E+00
0.12	1.43E+02	9.09E+05	1.02E+02	3.16E-06	8.81E-01	5.36E-06	1.00E+00
0.08	1.43E+02	7.08E+05	1.00E+02	3.16E-06	8.80E-01	5.42E-06	1.00E+00
0.04	1.43E+02	5.39E+05	9.35E+01	3.21E-06	8.77E-01	6.27E-06	1.00E+00

Table S5. Obtained values of R_s, CPE$_1$ (Q_1,n_1) and CPE$_2$ (Q_2,n_2) for the proposed electrical circuit for W525G.

E / V	R_s / Ω	R_1 / Ω	R_2 / Ω	Q_1	n_1	Q_2	n_2
0.44	1.36E+02	3.06E+06	5.18E+00	2.01E-06	8.72E-01	1.19E-06	1.00E+00
0.4	1.41E+02	3.04E+10	2.19E+00	1.99E-06	8.68E-01	4.57E-06	1.00E+00
0.36	1.37E+02	3.02E+06	4.13E+00	1.94E-06	8.65E-01	1.62E-06	1.00E+00
0.32	1.38E+02	2.96E+06	3.48E+00	1.86E-06	8.66E-01	1.88E-06	1.00E+00
0.28	1.37E+02	3.12E+06	3.27E+00	1.76E-06	8.67E-01	1.93E-06	1.00E+00
0.24	1.40E+02	2.98E+06	3.00E+00	1.62E-06	8.75E-01	1.91E-06	9.97E-01
0.2	1.42E+02	3.30E+06	1.95E+04	1.62E-06	8.77E-01	1.42E-06	1.00E+00
0.16	1.43E+02	3.29E+06	2.67E+04	1.53E-06	8.81E-01	1.23E-05	1.00E+00
0.12	1.44E+02	3.32E+06	3.82E+04	1.48E-06	8.85E-01	9.56E-06	1.00E+00
0.08	1.45E+02	3.33E+06	4.30E+04	1.43E-06	8.89E-01	8.24E-06	1.00E+00
0.04	1.45E+02	3.31E+06	4.28E+04	1.40E-06	8.92E-01	7.82E-06	1.00E+00

6

Table S6. Obtained values of R_{el}, CPE_1 (Q_1,n_1) and CPE_2 (Q_2,n_2) for the proposed electrical circuit for Y400M.

E / V	R_{el} / Ω	R_1 / Ω	R_2 / Ω	Q_1	n_1	Q_2	n_2
0.44	1.36E+02	5.31E+06	1.00E+03	1.52E-06	8.80E-01	1.51E-05	9.50E-01
0.4	1.34E+02	5.83E+06	1.10E+03	1.41E-06	8.83E-01	5.00E-05	9.50E-01
0.36	1.35E+02	6.58E+06	2.26E+03	1.30E-06	8.91E-01	2.11E-05	9.50E-01
0.32	1.36E+02	8.53E+06	1.35E+04	1.24E-06	8.94E-01	1.19E-05	9.50E-01
0.28	1.36E+02	8.80E+06	1.90E+04	1.14E-06	9.01E-01	1.01E-05	9.50E-01
0.24	1.37E+02	8.78E+06	1.91E+04	1.07E-06	9.05E-01	7.11E-06	1.00E+00
0.2	1.37E+02	7.83E+06	2.49E+04	1.03E-06	9.08E-01	6.82E-06	1.00E+00
0.16	1.37E+02	7.40E+06	2.97E+04	9.91E-07	9.11E-01	5.98E-06	1.00E+00
0.12	1.37E+02	6.84E+06	2.88E+04	9.49E-07	9.15E-01	5.70E-06	1.00E+00
0.08	1.37E+02	6.35E+06	1.72E+04	8.96E-07	9.18E-01	7.72E-06	1.00E+00
0.04	1.31E+02	1.67E+06	1.88E+02	3.94E-06	8.54E-01	8.00E-06	1.00E+00

Table S7. Obtained values of R_{el}, CPE_1 (Q_1,n_1) and CPE_2 (Q_2,n_2) for the proposed electrical circuit for Y525M.

E / V	R_{el} / Ω	R_1 / Ω	R_2 / Ω	Q_1	n_1	Q_2	n_2
0.44	1.32E+02	3.06E+06	1.29E+02	3.30E-06	8.90E-01	6.70E-06	1.00E+00
0.4	1.29E+02	1.00E+09	8.76E+05	7.30E-06	9.99E-01	0.00E+00	0.00E+00
0.36	1.29E+02	9.99E+08	7.02E+00	5.68E-06	8.19E-01	9.25E-06	9.50E-01
0.32	1.32E+02	4.10E+06	7.46E+04	3.82E-06	8.59E-01	5.00E-05	1.00E+00
0.28	1.29E+02	9.21E+06	1.22E+05	4.18E-06	8.43E-01	3.05E-05	9.50E-01
0.24	1.27E+02	9.57E+06	8.21E+04	4.39E-06	8.34E-01	7.11E-05	9.50E-01
0.2	1.27E+02	5.26E+06	8.06E+04	4.59E-06	8.28E-01	7.05E-05	9.50E-01
0.16	1.27E+02	3.75E+06	6.30E+04	4.54E-06	8.29E-01	6.94E-05	9.50E-01
0.12	1.29E+02	2.12E+06	6.62E+01	4.10E-06	8.40E-01	2.07E-05	9.50E-01
0.08	1.29E+02	2.13E+06	6.50E+01	4.05E-06	8.40E-01	2.00E-05	9.50E-01
0.04	1.30E+02	2.41E+06	6.46E+01	3.92E-06	8.43E-01	1.93E-06	9.50E-01

Table S8. Obtained values of R_{el}, CPE_1 (Q_1,n_1) and CPE_2 (Q_2,n_2) for the proposed electrical circuit for Y525G.

E / V	R_{el} / Ω	R_1 / Ω	R_2 / Ω	Q_1	n_1	Q_2	n_2
0.44	1.28E+02	1.80E+05	2.87E+06	5.37E-06	8.02E-01	2.50E-06	9.80E-01
0.4	1.28E+02	2.04E+05	3.32E+06	4.96E-06	8.04E-01	2.42E-06	9.75E-01
0.36	1.27E+02	2.17E+05	3.77E+06	4.69E-06	8.06E-01	2.28E-06	9.73E-01
0.32	1.27E+02	3.11E+05	3.98E+06	3.79E-06	8.16E-01	2.34E-06	9.86E-01
0.28	1.27E+02	4.51E+05	4.36E+06	3.12E-06	8.27E-01	2.49E-06	1.00E+00
0.24	1.27E+02	7.12E+05	5.55E+06	2.61E-06	8.40E-01	2.85E-06	1.00E+00
0.2	1.27E+02	6.72E+05	4.80E+06	2.58E-06	8.39E-01	2.67E-06	1.00E+00
0.16	1.27E+02	7.31E+05	4.68E+06	2.42E-06	8.43E-01	2.70E-06	1.00E+00
0.12	1.28E+02	7.43E+05	4.31E+06	2.32E-06	8.46E-01	2.69E-06	1.00E+00
0.08	1.29E+02	7.27E+05	4.00E+06	2.24E-06	8.48E-01	2.67E-06	1.00E+00

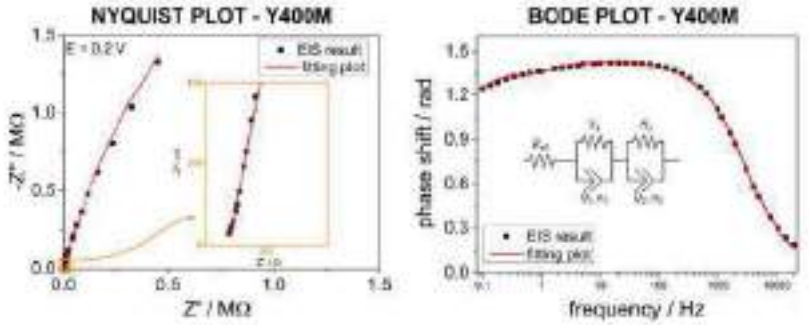

Figure S6. Examples of experimental results form EIS spectra and fitted curves for Nyquist and Bode plots.

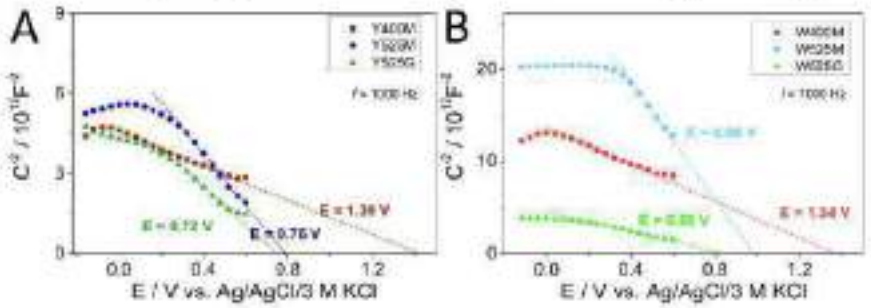

Figure S7. Mott–Schottky plots obtained for (A) Yellow and (B) White) carbon nitrides, measured from −0.16V to 0.6V for 1000 Hz (calculated from one frequency eq. 3).

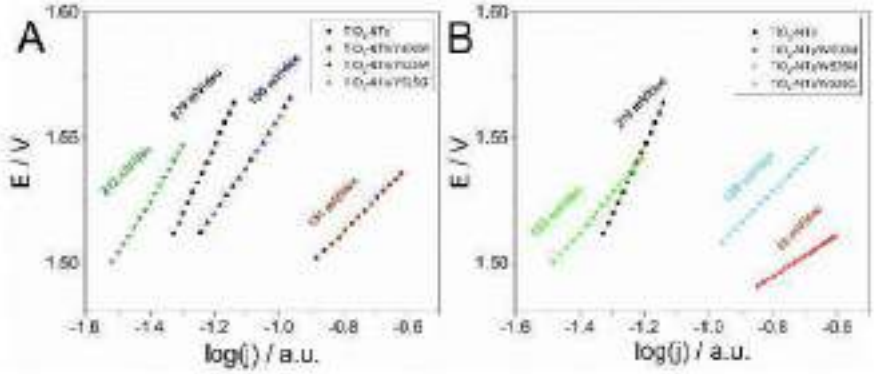

Figure S8. Tafel plots obtained from LSV curves with IR correction for TiO_2-NTs electrode without and with cocatalysts: (A) Yellow and (B) White carbon nitrides.

8

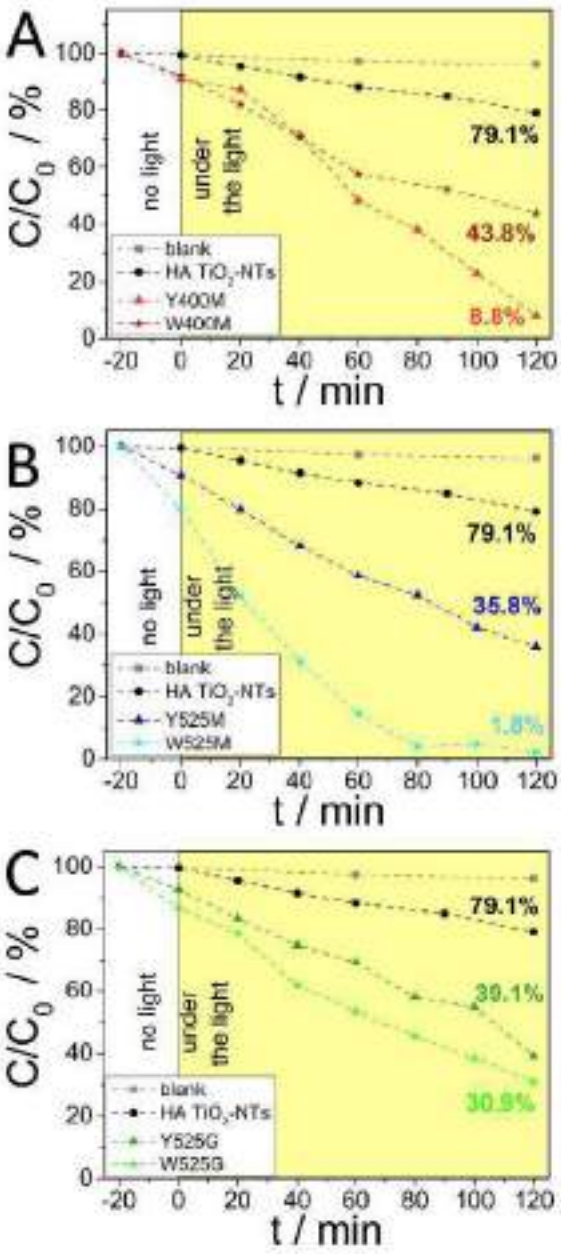

Figure 89. The photocatalytic performance of TiO_2-NTs and carbon nitriden (A) Y400M, W400M, (B) Y525M, W525M and (C) Y525G and Y525M in decolourization of MB before and under solar light illumination with a 1.5 AM filter, measured by UV-Vis spectroscopy at 662 nm.

9

References:

[1] N. Liu, T. Li, Z. Zhao, J. Liu, X. Luo, X. Yuan, K. Luo, J. He, D. Yu, Y. Zhao, From Triazine to Heptazine: Origin of Graphitic Carbon Nitride as a Photocatalyst, ACS Omega 5 (2020) 12557–12567. https://doi.org/10.1021/ACSOMEGA.0C01607/ASSET/IMAGES/LARGE/AO0C01607_0009.JPEG.

[2] Q. Dong, N. Mohamad Latiff, V. Mazánek, N.F. Rosli, H.L. Chia, Z. Sofer, M. Pumera, Triazine- And Heptazine-Based Carbon Nitrides: Toxicity, ACS Appl Nano Mater 1 (2018) 4442–4449. https://doi.org/10.1021/ACSANM.8B00708/SUPPL_FILE/AN8B00708_SI_001.PDF.

[3] Y. Li, F. Gong, Q. Zhou, X. Feng, J. Fan, Q. Xiang, Crystalline isotype heptazine-/triazine-based carbon nitride heterojunctions for an improved hydrogen evolution, Appl Catal B 268 (2020) 118381. https://doi.org/10.1016/J.APCATB.2019.118381.

[4] M. Soto-Herranz, M. Sánchez-Báscones, A. Hérnandez-Giménez, J.I. Calvo-Díez, J. Martín-Gil, P. Martín-Ramos, Effects of Protonation, Hydroxylamination, and Hydrazination of g-C3N4 on the Performance of Matrimid®/g-C3N4 Membranes, Nanomaterials 2018, Vol. 8, Page 1010 8 (2018) 1010. https://doi.org/10.3390/NANO8121010.

[5] X. Yuan, K. Luo, N. Liu, X. Ji, C. Liu, J. He, G. Tian, Y. Zhao, D. Yu, Cluster-model DFT simulations of the infrared spectra of triazine-based molecular crystals, Physical Chemistry Chemical Physics 20 (2018) 20779–20784. https://doi.org/10.1039/C8CP01550C.

[6] B. V. Lotsch, W. Schnick, New Light on an Old Story: Formation of Melam during Thermal Condensation of Melamine, Chemistry – A European Journal 13 (2007) 4956–4968. https://doi.org/10.1002/CHEM.200601291.

[7] Y. Yi, J. Wang, Y. Niu, Y. Yu, S. Wu, K. Ding, Exploring the evolution patterns of melem from thermal synthesis of melamine to graphitic carbon nitride, RSC Adv 12 (2022) 24311–24318. https://doi.org/10.1039/D2RA03337B.

[8] T. Saplinova, V. Bakumov, T. Gmeiner, J. Wagler, M. Schwarz, E. Kroke, 2,5,8-Trihydrazino-s-heptazine: A Precursor for Heptazine-based Iminophosphoranes, Z Anorg Allg Chem 635 (2009) 2480–2487. https://doi.org/10.1002/ZAAC.200900311.

[9] P. Wu, J. Wang, J. Zhao, L. Guo, F.E. Osterloh, Structure defects in g-C3N4 limit visible light driven hydrogen evolution and photovoltage, J Mater Chem A Mater 2 (2014) 20338–20344. https://doi.org/10.1039/C4TA04100C.

[10] R. da F. Bez, J. da S. Salla, S.M. de Amorim, E. Rodríguez-Castellon, M.O. Guerrero-Pérez, J.P. Winiarski, K. Krambrock, R. de F.P.M. Moreira, R.A. Peralta, Construction and characterization of intramolecular tri-s-triazine heterostructures, J Mater Sci 58 (2023) 11500–11526. https://doi.org/10.1007/S10853-023-08745-4/FIGURES/1.

[11] B.H. Stuart, Infrared Spectroscopy: Fundamentals and Applications, Infrared Spectroscopy: Fundamentals and Applications (2005) 1–224. https://doi.org/10.1002/0470011149.

[12] Chemcraft, Graphical software for visualization of quantum chemistry computations. Version 1.8, build 682, n.d. https://chemcraftprog.com/citation.html (accessed August 6, 2024).

General Conclusions

This dissertation demonstrates how titanium dioxide nanotube photoanodes can be advanced in a controlled manner by combining hydrothermal conditioning, cobalt-doping, cobalt cocatalyst formation, and metal-free carbon nitride species within a single measurement and comparison framework. Hydrothermal annealing of calcined TiO_2-NTs in a sealed Teflon chamber represents a significant advance. Treatment in distilled water (i) removes residual fluorine and phosphorus, (ii) makes the array more homogeneous and less stratified, which strictly influences TiO_2 stress, (iii) shifts the band edges, lowering the threshold potential for OER and (iv) increases almost 2-fold the photocurrent under simulated sunlight (from 20.7 $\mu A/cm^2$ to 39.5 $\mu A/cm^2$). The field review and the experimental results together indicate that a systematic study of calcined anodic nanotubes treated hydrothermally without a subsequent heat step had not been reported before, and this work establishes that route as an effective post-treatment for both performance and surface purity.

Cobalt introduced at very low levels (0.4 at.%) via hydrothermal treatment validates the theoretical expectation of a small amount of substitution in anatase. The flatband potential shifts in the favourable direction, the overpotential for oxygen evolution in the dark decreases, visible light absorption increases, and the photocurrent under solar illumination rises (by 2.6 times). This provides direct experimental support for band-edge tuning and an enhanced carrier density resulting from gentle cobalt doping in anodic nanotube arrays prepared for photoelectrochemical work.

In the PhD dissertation, it also showed a controllable route to deposit metallic cobalt on TiO_2-NTs from a citrate bath and identified the nucleation pathway (2d with a progressive growth), with XPS confirming the metallic state after deposition. Analysis of XPS, Raman spectroscopy and UV-Vis allows to prove the successful obtained Co_3O_4 and CoOOH materials. For the TiO_2-NTs/CoOOH electrode with a cobalt loading of 100 mC/cm^2, the overpotential at 0.1 mA/cm^2 decreased by 0.6 V. A mechanism has been proposed to explain how CoOOH accelerates the oxygen evolution reaction more efficiently than Co_3O_4. CoOOH stores and shuttles photogenerated holes; it supports rapid cycling among cobalt valence states, takes up protons, and facilitates the formation of the oxygen-

oxygen bond. Its porous and electrolyte-permeable architecture allows rapid mass transport and efficient accumulation and transfer of holes, leading to a lower overpotential and a larger steady photocurrent than for compact cobalt oxide layers at a matched cobalt loading. The study also explains the role of proton-assisted electron transfer and the temporary blocking effect of superoxide, and shows how a hole scavenger restores a high, stable photocurrent.

The dissertation also introduces new metal-free carbon nitride materials. Melem and melam were synthesised and modified in sulphuric acid, and the resulting products were studied alongside g-C_3N_4. These low-polycondensation materials show p-type behaviour. They carry amino and related groups that can participate directly in oxygen-evolution chemistry, and when placed on nanotube arrays, they form beneficial junctions that operate in a Z-scheme-like system. The best melem white (melem modified by H_2SO_4) reduces overpotential and increases photocurrent beyond that obtained with g-C_3N_4. The work proposes and supports an amino-group-mediated pathway for water oxidation that can operate in the dark and under illumination.

Taken together, the results convert a fragmented set of modification tactics into a single map that links processing, structure, surface chemistry, and band alignment to the two key performance metrics of photocurrent and overpotential under solar light. The outcome is a set of practical rules. Clean and relax the nanotube electrolyte interface with hydrothermal annealing in water to remove impurities and to reduce strain. Introduce cobalt only in trace amounts by the same route to shift band edges and to raise carrier density without creating deep traps. Use cobalt oxyhydroxide rather than dense cobalt oxide so the interface can accept and transport holes and protons with minimal mass-transport penalties. Deploy thin and chemically tuned carbon nitride interlayers, in particular the new sulphuric acid protonated melem and melam, when band alignment and permeability favour charge separation and Z scheme-like transfer. When implemented together, these measures deliver stable photoanodes that generate higher photocurrents at lower overpotentials and move titanium dioxide nanotube arrays closer to practical solar-driven water oxidation.

The current density values for all photoanodes are summarised in Table 6 (measured at 100 seconds via chronoamperometry at 0.5 V vs. Ag/AgCl).

Table 5. Photocurrent density (j_{ph}) and enhancement factor of TiO_2-NTs photoanodes referenced to Chapters 3–6.

	Photoanode	j_{ph} ($\mu A/cm^2$)	Enhancement Factor	Chapter
	titanium 0.25 mm thick, 99.5%			
1	TiO_2-NTs	20.7	-	3
2	HA TiO_2-NTs (in H_2O, 24 h)	39.5	1.91	3
3	HA TiO_2-NTs (in $LiNO_3$, 24 h)	20.0	0.97	3
4	HA TiO_2-NTs (in $NaNO_3$, 24 h)	23.3	1.13	3
5	HA TiO_2-NTs (in KNO_3, 24 h)	32.3	1.56	3
6	Co-TiO_2-NTs	33.3	1.61	4
7	HA TiO_2-NTs/Co_3O_4 40mC/cm^2	39.0	1.88	5
8	HA TiO_2-NTs/CoOOH 100mC/cm^2	54.1	2.61	5
	titanium 0.127 mm thick, 99.99%			
9	HA TiO_2-NTs	114.0	-	6
10	HA TiO_2-NTs/melem yellow	92.0	0.81	6
11	HA TiO_2-NTs/melam yellow	55.0	0.48	6
12	HA TiO_2-NTs/g-C_3N_4 yellow	150.0	1.32	6
13	HA TiO_2-NTs/melem white	177.0	1.55	6
14	HA TiO_2-NTs/melam white	155.0	1.36	6
15	HA TiO_2-NTs/g-C_3N_4 white	144.0	1.26	6

The thesis also points to further research directions, as each individual modification can serve as a building block for combined strategies, the effects of which can be verified within identical protocols or applied to other electrodes. The thesis also presents an attempt to anodise tantalum to the Ta_2O_5 form, which, according to the literature, can be converted into visible-light-active nitride phases, expanding the material base for future photoanodes. Combined electrochemical and preliminary mechanical studies demonstrate that managing stress and permeability at the nanoscale improves durability and points to the potential for practical industrial applications.

Scientific achievements

Publication Record

1. **M. Wtulich,** M. Szkoda, G. Gajowiec, M. Gazda, K. Jurak, M. Sawczak, A. Lisowska-Oleksiak*,
   Hydrothermal Cobalt Doping of Titanium Dioxide Nanotubes towards Photoanode Activity Enhancement, Materials 2021, 14(6), 1507. https://doi.org/10.3390/ma14061507

   IF2021: 3.748; MNiSW: 140

2. **M. Wtulich***, M. Szkoda, G. Gajowiec, K. Jurak, G. Trykowski, A. Lisowska-Oleksiak*,
   Hydrothermal modification of TiO_2 nanotubes in water and alkali metal electrolytes ($LiNO_3$, $NaNO_3$, KNO_3) – Direct evidence for photocatalytic activity enhancement, Electrochimica Acta 2022, 426, 140802. https://doi.org/10.1016/j.electacta.2022.140802

   IF2022: 6.6; MNiSW: 100

3. **M. Wtulich***, A. Schmidt (formerly A. Skwierawska), S. Ibragimov, A. Lisowska-Oleksiak*,
   Exploring the role of carbon nitrides (melem, melon, g-C_3N_4) in enhancing photoelectrocatalytic properties of TiO_2 nanotubes for water electrooxidation, Applied Surface Science 2025, 685, 161994. https://doi.org/10.1016/j.apsusc.2024.161994

   IF2025: 6.9; MNiSW: 140

4. **M. Wtulich**, A. Lisowska-Oleksiak*,
   Tailoring TiO_2-NTs with Electrodeposited Cobalt-Based Cocatalysts: Insights into OER and Photoelectrocatalytic Processes, Applied Surface Science 2025, 714, 164376 (30 Dec 2025). https://doi.org/10.1016/j.apsusc.2025.164376

   IF2025: 6.9; MNiSW: 140

Conferences

	Venue & dates	*Authors*	*Conference (full name)*	*Participation type*	*Title of contribution*
1	Mikulov, Czech Republic, 18-21.04.2021	**M. Wtulich*** M. Szkoda A. Lisowska-Oleksiak	29th Regional (Annual) Meeting of the International Society of Electrochemistry	Active – oral presentation	Hydrothermal modification of titania nanotubes towards photoanodes enhancing activity under solar light illumination
2	Kraków, Poland, 06-09.06.2021	**M. Wtulich*** M. Szkoda A. Lisowska-Oleksiak	6th International Symposium on Surface Imaging/Spectroscopy at the Solid/Liquid Interface (ISSIS)	Active – oral presentation	Hydrothermal Annealing of Titanium Dioxide Nanotubes – the Influence of the Processing Conditions
3	Prague, Czech Republic, 15-19.08.2022	**M. Wtulich*** S. Ibragimov M. Bobrowski A. Lisowska-Oleksiak	1st Regional Meeting of the International Society of Electrochemistry	Active – oral presentation	Electrochemically produced CoO_x onto anodised titania nanotubes tested as a photoanode in K_2SO_4 aqueous electrolyte
4	Ogrodzieniec, Poland, 04-06.09.2022	**M. Wtulich** O. Chronowska M. Szkoda A. Lisowska-Oleksiak	7th Forum Smart Energy Conversion & Storage	Active – poster presentation	Electrodeposition of cobalt oxy(hydroxide) on TiO_2-NTs as a cocatalyst for the OER
5	Strasbourg, France, 29.05-02.06.2023	A. Maszczak* **M. Wtulich** A. Lisowska-Oleksiak	European Materials Research Society (E-MRS) – Spring Meeting 2023	Passive – poster presentation	Enhanced photoelectroactivity of hydrothermally annealed titania nanotubes covered with melamine-derived CxNy nanomaterial
6	Toruń, Poland, 18-22.09.2023	**M. Wtulich** A. Maszczak A. Lisowska-Oleksiak	65th Congress of the Polish Chemical Society	Active – oral presentation	Eksfoliowany melem i g-C_3N_4 kwasem siarkowym jako kokatalizator nanorurek TiO_2 do zastosowań fotokatalitycznych
7	Augustów, Poland, 16-19.04.2024	A. Lisowska-Oleksiak* **M. Wtulich**	16th Symposium “Fast Ion Conductors”	Passive – oral presentation	Strategies towards titania photoanode activity enhancement
8	Augustów, Poland, 16-19.04.2024	**M. Wtulich** A. Maszczak A. Schmidt (formerly A. Skwierawska) A. Lisowska-Oleksiak	16th Symposium “Fast Ion Conductors”	Active – poster presentation	Exploring the role of carbon nitrides (melem, melon, g-C_3N_4) in enhancing photoelectrocatalytic properties of TiO_2 nanotubes
9	Augustów, Poland, 16-19.04.2024	M. Wtulich A. Mirowska (formerly: A. Laska) M. Szkodo M. Gazda A. Lisowska-Oleksiak	16th Symposium “Fast Ion Conductors”	Active – poster presentation	Optimising TiO_2 nanotubes photoanodes for solar activity: Interplay of mechanical and electrochemical properties via hydrothermal annealing

Teaching Conferences

No	*Venue & dates*	*Authors*	*Conference (full name)*	*Participation type*	*Title of contribution*
1	Gdańsk, Poland, 07-08.06.2023	**M. Wtulich**	8th National Conference on Academic Didactics "IDEATORIUM"	Active – poster presentation	*Fizykoiny – zastosowanie grywalizacji w nauczaniu fizyki w szkole średniej*
2	Gdańsk, Poland, 01–07.09.2023	**M. Wtulich**	48th Congress of Polish Physicists (Polish Physical Society)	Active – poster presentation	*Fizykoiny – zgamifikowana metodyka nauczania fizyki w liceum*

Post-conference Publication *(related to teaching at secondary schools)*

2nd National Scientific Conference of Secondary Schools, June 3-4, 2025, Warszawa, Poland,
ISBN: 978–83–975515–0–3

- F. Sajnaj, **M. Wtulich**, *Nanocząstki tlenku cynku syntezowane zieloną herbatą jako wzmacniacz plonowania roślin*
- K. Drausal, **M. Wtulich**, *Zeroemisyjny Samolot Przyszłości*
- M. Pawłowski, **M. Wtulich**, *Nanocząstki miedzi jako katalizatory rozkładu zanieczyszczeń organicznych w wodach*
- M. Kolosova, **M. Wtulich**, *Ekodeskorolka do przewozu lekkiego cargo*
- T. Lorek, **M. Wtulich**, *Magazyny Energii Elektrycznej z Glonów Cladophora*

Scientific projects

- 2021–2022 **LIDER X** (code: LIDER/15/0088/L-10/18/NCBR/2019)
  Project: *Integrated prototype of a photo-supercapacitor for energy storage obtained as a result of solar radiation conversion.*
  Funder/institution: National Centre for Research and Development.
  Principal Investigator: Asst. Prof. Mariusz Szkoda, PhD
  Your role: Young Scientist.
  Type: research grant.

- 2021–2022 **Mini-grant for young academics**
  Project (2021): *Hydrotermalna modyfikacja nanorurek TiO_2 – fotoanod aktywnych w świetle słonecznym.*
  Project (2022): *Elektrochemiczne osadzanie związków: Co_xO_Y i CoO(OH) na nanorurkach TiO_2 badanych jako fotoanoda w elektrolitach wodnych.*
  Funder/institution: Gdańsk University of Technology, Faculty of Chemistry.
  Grant manager/PI: Prof. Anna Lisowska-Oleksiak.
  Your role: grant holder (young academic).
  Type: mini-grant supporting the development of young academics.

- 2023 — **IDUB ‘Technetium’**
  Project: *Nanostrukturalne kompozytowe fotoanody na bazie TiO_2 i grafeno-podobnego azotku węgla.*
  Funder/institution: Gdańsk University of Technology, IDUB.
  Grant manager/PI: Prof. Anna Lisowska-Oleksiak.
  Your role: Young Scientist.
  Type: talent management grant (IDUB).

Other projects

- 2022 **IDUB ‘Uranium’**
  Project: *Chemia bez granic: warsztaty fizykochemiczne dla uczniów szkół ponadgimnazjalnych*.
  Funder/institution: Gdańsk University of Technology, IDUB.
  Grant manager/PI: Prof. Ewa Wagner-Wysiecka.
  Your role: co-ordinator and contractor.
  Type: institutional outreach/education grant (IDUB).

Awards and Distinctions

- **Best teaching poster** – competition award (2023)
  Fizykoiny – zgamifikowana metodyka nauczania fizyki w liceum
  48th Congress of Polish Physicists (Polish Physical Society)

- **Honorary distinction in the FarU award competition** (2023)
  Event organiser and coordinator of Trójmiejskie Wykłady Profesorskie
  2nd edition of Fahrenheit Universities Award (FarU)

- **PROM -** Scholarship for the best PhD students carrying out PhD projects in international cooperation,
  Polish National Agency for Academic Exchange (NAWA) (2023)

- **FRANCIUM** – Supporting Outstanding Doctoral Candidates (IDUB)
  Awarded twice — 10.2021–09.2022 and 10.2022–09.2023.
  Excellence Initiative – Research University (IDUB)

- **5th Open Polish Championships for Teachers and Education Staff in Swimming** (Białystok, 01.04.2023):
  - 1st place – 50 m backstroke,
  - 1st place – 100 m individual medley.

- **Academic Championships of Poland in Swimming** (Lublin, 15-16.04.2023)
    - 2nd place in the overall classification among Technical Universities.

Public Engagement and Science Outreach

- 19 March 2021 — Presentation for *Wirtualny Dzień Otwarty PG* (Virtual Open Day, Gdańsk University of Technology).

- 21–22 March 2022 — Speaker at the *Open Days at the Faculty of Chemistry*, Gdańsk University of Technology: *„Polimerowe magazyny energii”* (Polymer-based energy storage).

- 25–27 May 2023 — Laboratory leader and workshop host at *Bałtycki Festiwal Nauki* (Baltic Science Festival): *„Nie taka chemia straszna, jak ją malują – warsztaty dla młodych chemików.”*

- 11 October 2023 — Event organiser and coordinator of *Trójmiejskie Wykłady Profesorskie*.

- 21 March 2024 — Laboratory leader at *Ogólnopolski Dzień Otwarty PG* (National Open Day, Gdańsk University of Technology).

- 23–26 May 2024 — Laboratory leader at *Bałtycki Festiwal Nauki* (Baltic Science Festival).

Teaching and Academic activity

<u>Academic Employment</u>

- 11.2022 – 05.2023 — Consultant for Gdańsk University of Technology students, *“ŁATFIZNA. Easy Learning of Physics”*, Centre for Modern Education, Gdańsk University of Technology.

- 05.2023 – 09.2023 — Senior Student Affairs Officer, Centre for Modern Education, Gdańsk University of Technology.

- 10.2024 – 12.2024 — Assistant Lecturer (supporting the teaching of physics) for Gdańsk University of Technology students, project *“Petarda1”*, employed by the Vice-Rector for Education, Gdańsk University of Technology.

- 10.2025 – 12.2025 — Assistant Lecturer (supporting the teaching of physics) for Gdańsk University of Technology students, project *“Petarda2”*, employed by the Vice-Rector for Education, Gdańsk University of Technology.

Teaching Activities

- **Course:** Conducting Polymers (Laboratory class)
  Hours: 30
  Date: 03.2021–06.2021

- **Course:** Conducting Organic Materials (Laboratory class)
  Hours: 15
  Date: 07.10.2021–02.12.2021

- **Course:** Conducting Polymers (Laboratory class)
  Hours: 15
  Date: 28.02.2022–25.04.2022

- **Course:** Electrochemical Methods in Biomedical Applications (Laboratory class)
  Hours: 15
  Date: 11–12.2022

- **Course:** Conducting Polymers (Laboratory class)
  Hours: 15
  Date: 03–04.2023

- **Course:** Conducting Organic Materials (Laboratory class)
  Hours: 15
  Date: 09.10.2023–20.11.2023

- **Course:** Chemistry (Laboratory class)
  Hours: 15
  Date: 22.02.2024–13.06.2024

Author Contribution Statements

GDAŃSK UNIVERSITY OF TECHNOLOGY

Gdańsk, 17.09.2025 r.

mgr inż. Mariusz Wtulich
Katedra Chemii i Technologii Materiałów Funkcjonalnych
Wydział Chemiczny Politechniki Gdańskiej
ul. Gabriela Narutowicza 11/12, 80-233 Gdańsk

Co-author Contribution Declaration

Jako współautor poniższych prac:

1) **M. Wtulich**, M. Szkoda, G. Gajowiec, M. Gazda, K. Jurak, M. Sawczak, A. Lisowska-Oleksiak, *Hydrothermal cobalt doping of titanium dioxide nanotubes towards photoanode activity enhancement*, Materials 14 (2021), 1507, DOI: 10.3390/MA14061507;

2) **M. Wtulich**, M. Szkoda, G. Gajowiec, K. Jurak, G. Trykowski, A. Lisowska- Oleksiak, *Hydrothermal modification of TiO_2 nanotubes in water and alkali metal electrolytes ($LiNO_3$, $NaNO_3$, KNO_3) – Direct evidence for photocatalytic activity enhancement*, Electrochimca Acta 426 (2022) 140802, DOI: 10.1016/J.ELECTACTA.2022.140802;

3) **M. Wtulich**, A. Skwierawska, S. Ibraginov, A. Lisowska-Oleksiak, *Exploring the role of carbon nitrides (melem, melon, g-C_3N_4) in enhancing photoelectrocatalytic properties of TiO_2 nanotubes for water electrooxidation*, Applied Surface Science 685 (2025) 161994, DOI: 10.1016/J.APSUSC.2024.161994;

4) **M. Wtulich**, A. Lisowska-Oleksiak, *Tailoring TiO_2 nanotubes photoanodes with electrodeposited Co_3O_4 and CoOOH cocatalysts for enhanced electrocatalytic and photoelectrocatalytic oxygen evolution*, Applied Surface Science 714 (2025) 164376, DOI: 10.1016/j.apsusc.2025.164376;

I hereby declare that my individual scientific contribution to the preparation and publication of the aforementioned works comprised: performing computations; analysing and interpreting experimental results; preparing all samples (synthesis, optimisation, and methodological development); visualising data and preparing figures from multiple techniques (XRD, FTIR, XPS, UV–Vis, EIS, CA, CV, LV, and related methods); and drafting, reviewing, and editing the manuscript, as well as preparing responses to reviewers' comments.

Mariusz Wtulich

(signature)

GDAŃSK UNIVERSITY OF TECHNOLOGY

Gdańsk, 4.11.2025 r.

Prof. Anna Lisowska-Oleksiak D.Sc., Ph.D.
Department of Chemistry and Technology of Functional Materials
Faculty of Chemistry
Gdańsk University of Technology
Gabriela Narutowicza 11/12
80-233 Gdańsk

Co-author Contribution Declaration

As a co-author of the following papers:

1. Mariusz Wtulich, Anna Lisowska-Oleksiak*, *Tailoring TiO_2 nanotubes photoanodes with electrodeposited Co_3O_4 and CoOOH cocatalysts for enhanced electrocatalytic and photoelectrocatalytic oxygen evolution*, Applied Surface Science 714 (2025) 164378. https://doi.org/10.1016/j.apsusc.2025.164378.

2. Mariusz Wtulich *, Anna Slowierawska, Sapojan Ibragimov, Anna Lisowska-Oleksiak*, *Exploring the role of carbon nitrides (melem, melon, g-C_3N_4) in enhancing photoelectrocatalytic properties of TiO_2 nanotubes for water electrooxidation, Applied Surface Science* ***685 15(2025) 161994.*** https://doi.org/10.1016/j.apsusc.2024.161994.

3. Mariusz Wtulich *, Mariusz Szkoda, Grzegorz Gajowiec, Kacper Jurak, Grzegorz Trykowski, Anna Lisowska-Oleksiak *, Hydrothermal modification of TiO_2 nanotubes in water and alkali metal electrolytes ($LiNO_3$, $NaNO_3$, KNO_3) – Direct evidence for photocatalytic activity enhancement, Electrochimica Acta 426 10 (2022) 140802. https://doi.org/10.1016/j.electacta.2022.140802.

4. Mariusz Wtulich, Mariusz Szkoda, Grzegorz Gajowiec, Maria Gazda, Kacper Jurak, Miroslaw Sawczak, Anna Lisowska-Oleksiak*, *Hydrothermal Cobalt Doping of Titanium Dioxide Nanotubes towards Photoanode Activity Enhancement*, Materials 14 (2021), 1507. https://doi.org/10.3390/ma14061507

I hereby declare that in the publications listed above (1–4), which form part of the doctoral dissertation of Mr. Mariusz Wtulich, M.Sc. Eng., my contribution included supervision of the research, formulation of the research subject, provision of the necessary instrumental facilities, participation in the interpretation of the results, writing of the initial version of the manuscript, as well as revision of the work following the reviewers' comments.

I give my consent and appreciation for the above-mentioned papers to be included by **Mr. Mariusz Wtulich M.Sc. Eng.**, as part of his doctoral dissertation in the form of a thematically consistent collection of research articles published in peer-reviewed scientific journals.

Anna Lisowska-Oleksiak
(signature of co-author)

GDAŃSK UNIVERSITY OF TECHNOLOGY

Gdańsk, 30.10.2025 r.

dr inż. Grzegorz Gajowiec
Department of Materials Science and Engineering
Institute of Manufacturing and Materials Technology
Faculty of Mechanical Engineering and Ship Technology
Gdańsk University of Technology
Gabriela Narutowicza 11/12
80-233 Gdańsk

Co-author Contribution Declaration

As a co-author of the following papers:

1) M. Wtulich, M. Szkoda, **G. Gajowiec**, M. Gazda, K. Jurak, M. Sawczak, A. Lisowska-Oleksiak, *Hydrothermal cobalt doping of titanium dioxide nanotubes towards photoanode activity enhancement*, Materials 14 (2021), 1507, DOI: 10.3390/MA14061507;

2) M. Wtulich, M. Szkoda, **G. Gajowiec**, K. Jurak, G. Trykowski, A. Lisowska-Oleksiak, *Hydrothermal modification of TiO_2 nanotubes in water and alkali metal electrolytes ($LiNO_3$, $NaNO_3$, KNO_3) – Direct evidence for photocatalytic activity enhancement*, Electrochimca Acta 426 (2022) 140802, DOI: 10.1016/J.ELECTACTA.2022.140802;

I hereby declare that my individual scientific contribution to the preparation and publication of the above-mentioned works comprised: performing scanning electron microscopy (SEM) and energy-dispersive X-ray spectroscopy (EDX) measurements; analysing and interpreting the resulting data; and assisting in the preparation of additional figures to accompany responses to selected reviewers' comments.

At the same time, I give my consent for the above-mentioned papers to be included by **Mariusz Wtulich** as part of his doctoral dissertation in the form of a thematically consistent collection of research articles published in peer-reviewed scientific journals.

.....
(signature of co-author)

GDAŃSK UNIVERSITY OF TECHNOLOGY

Gdańsk, 05.11.2025 r.

prof. dr hab. inż. Maria Gazda
Institute of Nanotechnology and Materials Engineering
Faculty of Applied Physics and Mathematics
ul. Gabriela Narutowicza 11/12
80-233 Gdańsk

Co-author Contribution Declaration

As a co-author of the following paper:

M. Wtulich, M. Szkoda, G. Gajowiec, **M. Gazda**, K. Jurak, M. Sawczak, A. Lisowska-Oleksiak, *Hydrothermal cobalt doping of titanium dioxide nanotubes towards photoanode activity enhancement*, Materials 14 (2021), 1507, DOI: 10.3390/MA14061507;

I hereby declare that my individual scientific contribution to the preparation and publication of the above-mentioned work included X-ray diffraction (XRD) analyses and pattern interpretation, participation in the discussion of the results, and contribution to the preparation and revision of the manuscript text.

At the same time, I give my consent for the above-mentioned paper to be included by **Mariusz Wtulich** as part of his doctoral dissertation in the form of a thematically consistent collection of research articles published in peer-reviewed scientific journals.

M. Gazda

(signature of co-author)

GDAŃSK UNIVERSITY OF TECHNOLOGY

Gdańsk, 30.10.2025 r.

mgr inż. Sapajan Ibragimov
Katedra Chemii i Technologii Materiałów Funkcjonalnych
Wydział Chemiczny Politechniki Gdańskiej
Gdańsk University of Technology
Gabriela Narutowicza 11/12
80-233 Gdańsk

Co-author Contribution Declaration

As a co-author of the following paper:

M. Wtulich, A. Skwierawska, **S. Ibragimov**, A. Lisowska-Oleksiak, *Exploring the role of carbon nitrides (melem, melon, g-C_3N_4) in enhancing photoelectrocatalytic properties of TiO_2 nanotubes for water electrooxidation*, Applied Surface Science 685 (2025) 161994, DOI: 10.1016/J.APSUSC.2024.161994;

I hereby declare that my individual scientific contribution to the preparation and publication of the aforementioned works comprised: drafting the section on TD-DFT methodology, conducting simulations and analysing the results, proofreading the manuscript, and assisting in the preparation of responses to selected reviewers' comments.

At the same time, I give my consent for the above-mentioned papers to be included by **Mariusz Wtulich** as part of his doctoral dissertation in the form of a thematically consistent collection of research articles published in peer-reviewed scientific journals.

.....
(signature of co-author)

GDAŃSK UNIVERSITY OF TECHNOLOGY

Gdańsk, 30.10.2025 r.

dr hab. inż. Mirosław Sawczak, prof. IMP PAN
Zakład Fotoficyki, Ośrodek Techniki Plazmowej i Laserowej
Instytut Maszyn Przepływowych PAN
ul. Generała Józefa Fiszera 14,
80-231 Gdańsk

Co-author Contribution Declaration

As a co-author of the following paper:

M. Wtulich, M. Szkoda, G. Gajowiec, M. Gazda, K. Jurak, **M. Sawczak**, A. Lisowska-Oleksiak, *Hydrothermal cobalt doping of titanium dioxide nanotubes towards photoanode activity enhancement*, Materials 14 (2021), 1507, DOI: 10.3390/MA14061507;

I hereby declare that my individual scientific contribution to the preparation and publication of the above-mentioned works consisted of:

performing Raman measurements, as well as the analysis and interpretation of the obtained results.

At the same time, I give my consent for the above-mentioned papers to be included by **Mariusz Wtulich** as part of his doctoral dissertation in the form of a thematically consistent collection of research articles published in peer-reviewed scientific journals.

Mirosław Sawczak
(signature of co-author)

Gdańsk, 22.10.2025

dr hab. inż. Anna Maria Schmidt
Department of Chemistry and Technology of Functional Materials
Faculty of Chemistry
Gdańsk University of Technology
Gabriela Narutowicza 11/12
80-233 Gdańsk

I, the undersigned, Anna Maria Schmidt (formerly Anna Maria Skwierawska), hereby declare that I made a substantial and creative contribution to the preparation of the publication entitled: "Exploring the role of carbon nitrides (melem, melon, g-C_3N_4) in enhancing photoelectrocatalytic properties of TiO_2 nanotubes for water electrooxidation." DOI: 10.1016/j.apsusc.2024.161994.

My contribution to the publication included, in particular: the analysis and interpretation of FTIR and UV–Vis spectra, the preparation and graphical development of figures illustrating the obtained research results, participation in drafting and editing the initial version of the manuscript.

Furthermore, I hereby confirm that the contribution of MSc Eng. Mariusz Wtulich to the above-mentioned publication was significant, independent, and essential to the successful completion of the research work.

Anna Schmidt

Signature

GDAŃSK UNIVERSITY OF TECHNOLOGY

Gdańsk, 30.10.2025 r.

dr hab. inż. Mariusz Szkoda, prof. PG
Department of Chemistry and Technology of Functional Materials
Faculty of Chemistry
Gdańsk University of Technology
Gabriela Narutowicza 11/12
80-233 Gdańsk

Co-author Contribution Declaration

As a co-author of the following papers:

1) M. Wtulich, **M. Szkoda**, G. Gajowiec, M. Gazda, K. Jurak, M. Sawczak, A. Lisowska-Oleksiak, *Hydrothermal cobalt doping of titanium dioxide nanotubes towards photoanode activity enhancement*, Materials 14 (2021), 1507, DOI: 10.3390/MA14061507;

2) M. Wtulich, **M. Szkoda**, G. Gajowiec, K. Jurak, G. Trykowski, A. Lisowska- Oleksiak, *Hydrothermal modification of TiO_2 nanotubes in water and alkali metal electrolytes ($LiNO_3$, $NaNO_3$, KNO_3) – Direct evidence for photocatalytic activity enhancement*, Electrochimica Acta 426 (2022) 140802, DOI: 10.1016/J.ELECTACTA.2022.140802;

I hereby declare that my individual scientific contribution to the preparation and publication of the above-mentioned work consisted of:

- in publication no. 1: assistance in the synthesis of TiO_2 nanotubes, proofreading of the manuscript, and helping to prepare responses to some of the reviewers' comments;
- in publication no. 2: assistance in describing the photoelectrochemical properties and in preparing responses to some of the reviewers' comments.

At the same time, I give my consent for the above-mentioned papers to be included by **Mariusz Wtulich** as part of his doctoral dissertation in the form of a thematically consistent collection of research articles published in peer-reviewed scientific journals.

Szkoda

(signature of co-author)

NICOLAUS COPERNICUS UNIVERSITY IN TORUŃ
Faculty of Chemistry

RESEARCH UNIVERSITY

Gdańsk, 30.10.2025 r.

dr hab. Grzegorz Trykowski
prof. UMK
trykil@umk.pl +48 603-691-129

Co-author Contribution Declaration

As a co-author of the following papers:

1) M. Wtulich, M. Szkoda, G. Gajowiec, K. Jurak, **G. Trykowski**, A. Lisowska- Oleksiak, *Hydrothermal modification of TiO_2 nanotubes in water and alkali metal electrolytes ($LiNO_3$, $NaNO_3$, KNO_3) – Direct evidence for photocatalytic activity enhancement*, Electrochimca Acta 426 (2022) 140802, DOI: 10.1016/J. ELECTACTA.2022.140802;

I hereby declare that my individual scientific contribution to the preparation and publication of the above-mentioned work consisted of the analysis of TiO2 nanotubes samples with instrumental methods and interpretation results.

At the same time, I give my consent for the above-mentioned papers to be included by **Mariusz Wtulich** as part of his doctoral dissertation in the form of a thematically consistant collection of research articles published in peer-reviewed scientific journals.

Grzegorz Trykowski
(signature of co-author)

NICOLAUS COPERNICUS UNIVERSITY IN TORUŃ Faculty of Chemistry
Gagarina Street 7, 87-100 Toruń, Poland, tel. +48 56 611 43 02, e-mail: wydział@chem.umk.pl
chem.umk.pl/en

GDAŃSK UNIVERSITY OF TECHNOLOGY

Gdańsk, 30.10.2025 r.

dr inż. Kacper Jurak
Katedra Inżynierii Materiałów Funkcjonalnych
Instytut Technologii Maszyn i Materiałów
Wydziału Elektroniki, Telekomunikacji i Informatyki Politechniki Gdańskiej
Gdańsk University of Technology
Gabriela Narutowicza 11/12
80-233 Gdańsk

Co-author Contribution Declaration

As a co-author of the following papers:

1) M. Wtulich, M. Szkoda, G. Gajowiec, M. Gazda, **K. Jurak**, M. Sawczak, A. Lisowska-Oleksiak, *Hydrothermal cobalt doping of titanium dioxide nanotubes towards photoanode activity enhancement*, Materials 14 (2021), 1507, DOI: 10.3390/MA14061507;

2) M. Wtulich, M. Szkoda, G. Gajowiec, **K. Jurak**, G. Trykowski, A. Lisowska- Oleksiak, *Hydrothermal modification of TiO_2 nanotubes in water and alkali metal electrolytes ($LiNO_3$, $NaNO_3$, KNO_3) – Direct evidence for photocatalytic activity enhancement*, Electrochimca Acta 426 (2022) 140802, DOI: 10.1016/J. ELECTACTA.2022.140802;

I hereby declare that my individual scientific contribution to the preparation and publication of the aforementioned works comprised: performing X-ray photoelectron spectroscopy (XPS) measurements; analysing and interpreting the resulting data; proofreading the manuscript; and assisting in the preparation of responses to reviewers' comments.

At the same time, I give my consent for the above-mentioned papers to be included by **Mariusz Wtulich** as part of his doctoral dissertation in the form of a thematically consistent collection of research articles published in peer-reviewed scientific journals.

Kacper Jurak
(signature of co-author)